Organic Rankine Cycle Waste Heat Recovery Systems for Aircraft Engines

Krempus, D.

DOI
10.4233/uuid:5e565f99-a9f4-4208-95e9-2c542fd720f8

Publication date
2025

Document Version
Final published version

Citation (APA)
Krempus, D. (2025). *Organic Rankine Cycle Waste Heat Recovery Systems for Aircraft Engines*. [Dissertation (TU Delft), Delft University of Technology]. https://doi.org/10.4233/uuid:5e565f99-a9f4-4208-95e9-2c542fd720f8

ORGANIC RANKINE CYCLE WASTE HEAT RECOVERY SYSTEMS FOR AIRCRAFT ENGINES

Dissertation

for the purpose of obtaining the degree of doctor
at Delft University of Technology,
by the authority of the Rector Magnificus prof. ir. T.H.J.J. van der Hagen,
chair of the Board for Doctorates,
to be defended publicly on
Thursday 6 February 2025 at 10:00 o'clock.

by

Dabo KREMPUS

Master of Science in Aerospace Engineering,
University of Stuttgart, Germany,
born in Vienna, Austria.

Composition of the doctoral committee:

Rector Magnificus,	Chairperson
Prof. dr. ir. P. Colonna di Paliano,	Delft University of Technology, *promotor*
Dr. ir. R. Vos,	Delft University of Technology, *promotor*
Dr. C. M. De Servi,	Delft University of Technology, *co-promotor*
Independent members:	
Prof. dr. ir. L. L. M. Veldhuis,	Delft University of Technology
Prof. dr. T. Grönstedt,	Chalmers University of Technology, Sweden
Prof. Dr.-Ing. J. Friedrichs,	Technical University of Braunschweig, Germany
Dr. S. Evans,	Pratt & Whitney, USA
Prof. dr. R. Pecnik,	Delft University of Technology, reservelid

The research presented in this dissertation has been performed at the Flight Performance and Propulsion Section, Department of Flow Physics and Technology, Faculty of Aerospace Engineering. This work is part of the research project "Airborne Thermal Energy Harvesting for Aircraft" (ARENA), funded by the Applied and Engineering Sciences Division (TTW) of the Dutch Organization for Scientific Research (NWO), Open Technology Program of the Ministry of Economic Affairs, Grant No. 17906.

Cover design by Fabian Krempus ♥

ISBN 978-94-6366-997-9

An electronic version of this dissertation is available at
http://repository.tudelft.nl/.

CONTENTS

SUMMARY

Since the advent of commercial aviation, advancements in propulsion system technology have been the main cause of the reduction of fuel consumption. Modern turbofan engines typically achieve a thermal efficiency of approximately 50%, implying that roughly half of the chemical energy released by fossil fuel combustion is lost to the environment as hot exhaust gas.

For gas turbine engines of stationary power plants, it is common practice to use bottoming units based on the Rankine cycle to recover part of this energy and increase thermal efficiency by up to 20%. The concept of the combined-cycle engines is also suitable for applications with low power capacity, however, organic compounds instead of water must be used as the working fluid of the bottoming unit. The combined-cycle concept is in principle also suitable for aircraft engines, however, adding an organic Rankine cycle (ORC) waste heat recovery system to an aircraft gas turbine engine is challenging because the thermodynamic benefit is counterbalanced by the increased aircraft mass and drag. The few studies conducted so far on combined-cycle aircraft engines indicate a possible net benefit on fuel consumption, however, these results are based on low-fidelity models, neglecting or only partially considering the effect of the new engine configuration on aircraft design and performance.

The work documented in this dissertation aims to provide reliable information on the feasibility of the combined-cycle engine concept based on complex system models, enabling the optimization of preliminary designs and formulating design guidelines. For this purpose, a simulation framework that considers the interaction of the gas turbine, the bottoming unit, and the aircraft was developed. This software package is named *ARENA framework*, and it can provide the preliminary design of combined-cycle engines optimized for minimized fuel consumption while considering their effect on aircraft design and performance.

ARENA was used to model the effect of this novel technology on the fuel consumption of three exemplary aircraft adopting different combined-cycle configurations and mission scenarios. These cases are 1) a medium-range aircraft employing a combined-cycle auxiliary power unit (CC-APU) instead of a conventional APU to provide power on the ground, 2) a medium-range turboelectric aircraft employing combined-cycle turboshaft engines (CC-TS) in place of conventional turboshaft engines, and 3) a medium-range partial-turboelectric aircraft replacing conventional turbofan engines with combined-cycle turbofan engines (CC-TF). All combined-cycle engine configurations are based on an ORC waste heat recovery unit implementing a non-recuperated cycle, using cyclopentane as the working fluid, whereby the ORC turbogenerator converts the recovered heat into electrical power. The simulated CC-APU engine consumes approximately 50% less fuel to provide ground power compared to a conventional APU, which corresponds to mission fuel savings of approximately 0.6%. The power output of the CC-APU engine is 250 kW, of which 60 kW are provided by the ORC turbogenerator. The opti-

mized ORC unit features a mass-specific power of 1.5 kW/kg and an efficiency of 15%, while the overall combined-cycle efficiency is 34%. The fuel savings calculated in the case of the CC-TS engine are 1.5%, if compared to a single-cycle turboshaft engine. The combined power output is 5.4 MW of which 340 kW are contributed by the ORC turbogenerator. The optimized ORC unit mass-specific power is 1.3 kW/kg and its efficiency at cruise is 17%, while the CC-TS engine efficiency is 53%. The CC-TF engine burns 4% less fuel if compared to a single-cycle engine. It contributes 60% of the cruise thrust and 2.6 MW of shaft power of which 570 kW are provided by the ORC turbogenerator. The shaft power is converted to thrust by the electrical distributed propulsion system. The optimized ORC unit has a mass-specific power of 1 kW/kg and an efficiency of 18%. The performance difference between the CC-TS and CC-TF engines is mainly due to different condenser integration architectures. The condensers of the CC-TF engine are integrated into the engine bypass duct downstream of the fan, whereas the condensers of the CC-TS engine are placed into ram-air ducts. The combination of pressure rise and thermal energy input into the bypass air stream increases the propulsive efficiency and the specific thrust of the CC-TF. According to these preliminary studies, the optimized CC-TS and CC-TF engines have no appreciable impact on the lift-to-drag ratio of the aircraft and the maximum take-off mass only increases by a few percent.

It can be concluded that according to the results of this work, the thermodynamic benefit of adopting an ORC system to recover the thermal energy of the exhaust of gas turbines onboard aircraft can outweigh the penalties of the increased aircraft mass and drag. However, the uncertainty due to modeling limitations and simplifying assumptions suggests that further research and development are needed before decisions regarding the development of this engine concept can be taken. Such a drastic change in engine configuration would only be justifiable if the fuel consumption reduction is larger than what was estimated. Further performance improvements may be possible if advanced heat exchanger technology is considered. Furthermore, as well known from theory and practice regarding ORC power plant technology, the identification of an optimal organic working fluid (pure or mixture) may result in considerable performance and operational improvements. Another research direction worth investigating is the optimization of the design of the combined-cycle engine to minimize environmental impact and not fuel consumption. Preliminary considerations show that the benefit of waste heat recovery in this case may be even larger.

SAMENVATTING

Sinds de komst van de commerciële luchtvaart zijn de technologische ontwikkelingen op het gebied van voortstuwing de belangrijkste drijvende kracht geweest achter de vermindering van het brandstofverbruik. Moderne turbofanmotoren behalen een thermodynamische efficiëntie van ongeveer 50%, wat inhoudt dat ongeveer de helft van de chemische energie die vrijkomt bij de verbranding van fossiele brandstoffen verloren gaat aan de omgeving als hete uitlaatgassen.

Voor gasturbinemotoren van stationaire elektriciteitscentrales is het gebruikelijk een deel van deze energie terug te winnen door toepassing van een systeem op basis van de Rankine-cyclus. Applicaties met lage vermogenscapaciteit, zoals voor voertuigen, vereisen het gebruik van organische verbindingen in plaats van water als werkvloeistof voor de Rankine-cyclus. Het toepassen van dergelijke organische Rankine-cyclus (ORC) systemen op vliegtuigmotoren blijkt uitdagend omdat de thermodynamische voordelen worden tegengewerkt door een toename van de massa en de luchtweerstand van het vliegtuig. De weinige studies die zijn uitgevoerd naar vliegtuigmotoren met een gecombineerde cyclus (combined-cycle) op basis van een gasturbine en een ORC-systeem laten een gunstig effect op het brandstofverbruik van deze technologie zien. Deze resultaten zijn echter gebaseerd op verschillende niveaus van modelgetrouwheid en houden slechts gedeeltelijk rekening met de invloed op het ontwerp en de prestaties van het vliegtuig.

Het werk dat in dit proefschrift wordt gedocumenteerd, heeft als doel betrouwbare informatie te verschaffen over de haalbaarheid van het “combined-cycle” concept op basis van complexe systeemmodellen, die de optimalisatie van voorlopige ontwerpen mogelijk maken en ontwerprichtlijnen kunnen formuleren. Hiertoe werd een simulatieraamwerk ontwikkeld dat de interactie tussen de gasturbine, het ORC-systeem en het vliegtuig in beschouwing neemt. Deze software heet het ARENA-raamwerk en kan motoren met een “combined-cycle” ontwerpen die geoptimaliseerd zijn voor minimaal brandstofverbruik, waarbij rekening wordt gehouden met hun effect op het ontwerp en de prestaties van het vliegtuig.

ARENA wordt gebruikt om het effect van deze nieuwe technologie op het brandstofverbruik te modelleren voor drie gevallen met verschillende “combined-cycle” motorconcepten en missiescenario’s. Deze gevallen zijn: 1) een middellange afstandsvliegtuig dat een hulpaggregaat [auxiliary power unit (APU)] met gecombineerde cyclus (CC-APU) gebruikt in plaats van een conventionele APU om vermogen op de grond te leveren, 2) een middellange afstandsvliegtuig met een turboelektrisch voortstuwingssysteem waarbij de gasturbine een combineerde cyclus gebruikt (CC-TS) in plaats van een conventionele gasturbine, en 3) een middellange afstandsvliegtuig met turboelektrische voortstuwing waarbij de turbofan wordt vervangen door een turbofan met een gecombineerde cyclus (CC-TF). Alle drie de configuraties maken gebruik van ORC systemen zonder recuperator met cyclopentaan als werkvloeistof en de ORC-turbogenerator zet de terugge-

wonnen warmte om in elektrische energie.

De CC-APU, de eerste toepassing, verbruikt ongeveer 50% minder brandstof om vermogen op de grond te leveren in vergelijking met een conventionele APU. Dit vertaalt zich in een brandstofbesparing van 0.6% over een gemiddelde missie. Het gecombineerde geleverde vermogen is 250 kW, waarvan 60 kW wordt geleverd door de ORC-turbogenerator. Het geoptimaliseerde ORC-systeem heeft een massaspecifiek vermogen van 1.5 kW/kg en een efficiëntie van 15%, terwijl de algehele "combined-cycle" efficiëntie 34% is. De CC-TS motor, de tweede toepassing, resulteert in een brandstofbesparing van 1.5%. Het gecombineerde geleverde vermogen is 5.4 MW, waarvan 340 kW wordt bijgedragen door de ORC-turbogenerator. Het geoptimaliseerde ORC-systeem heeft een massaspecifiek vermogen van 1.3 kW/kg en een efficiëntie van 17%, terwijl de CC-TS motor efficiëntie 53% is. De CC-TF motor, de derde toepassing, resulteert in een brandstofbesparing van 4%. Het CC-TF systeem levert 60% van de stuwkracht tijdens de kruisvlucht en 2.6 MW aan asvermogen voor de elektrische voortsuwing, waarvan 570 kW wordt geleverd door de ORC-turbogenerator. Het geoptimaliseerde ORC-systeem heeft een massaspecifiek vermogen van 1.0 kW/kg en een efficiëntie van 18%.

Het prestatieverschil tussen de CC-TS en CC-TF concepten is het gevolg van verschillende condensorintegratie-configuraties. De condensors van de CC-TF zijn geïntegreerd in het omloopkanaal van de motor achter de fan, terwijl de condensors van de CC-TS zijn geïntegreerd in aparte luchtkanalen. De combinatie van drukverhoging en de toevoeging van warmte aan de omloopstroom verhoogt de voortstuwingsefficiëntie en specifieke stuwkracht van de CC-TF. De geoptimaliseerde CC-TS en CC-TF concepten hebben geen merkbare impact op de lift-tot-weerstandsverhouding van het vliegtuig en het maximale startgewicht van het vliegtuig neemt slechts met enkele procenten toe.

De conclusie is dat het thermodynamische voordeel van het toepassen van ORC-systemen op gasturbinemotoren van vliegtuigen zwaarder kan wegen dan de nadelen van een toename van de massa en luchtweerstand van het vliegtuig. Echter, de onzekerheid als gevolg van modelbeperkingen en vereenvoudigende aannames suggereert dat verder onderzoek en ontwikkeling nodig zijn voordat beslissingen over de ontwikkeling van dit motorconcept kunnen worden genomen. Een dergelijke ingrijpende verandering in motorconfiguratie zou alleen gerechtvaardigd zijn als de brandstofverbruiksreductie groter is dan wat werd geschat. Verdere prestatieverbeteringen kunnen mogelijk worden bereikt met geavanceerde warmtewisselaarstechnologie. Bovendien, zoals bekend uit theorie en praktijk met betrekking tot ORC-technologie voor stationaire elektriciteitscentrales, kan de identificatie van een optimale organische werkvloeistof (puur of mengsel) resulteren in aanzienlijke prestatie- en operationele verbeteringen. Een andere onderzoekslijn die het onderzoeken waard is, is de optimalisatie van het ontwerp van de "combined-cycle" motor om de milieu-impact te minimaliseren en niet het brandstofverbruik. Voorlopige overwegingen tonen aan dat het voordeel van warmteterugwinning in dit geval zelfs groter kan zijn.

1

INTRODUCTION

The easiest way to reduce greenhouse gas emissions due to aviation is to fly less. However, this insight does not earn you a PhD.

Dabo Krempus

THIS dissertation presents research on a novel propulsion system concept aiming at reducing aircraft mission fuel consumption. In this chapter, first, an overview of aircraft engine emissions and a justification for designing engines for minimum fuel burn is provided. Secondly, a brief history of the technological evolution of aircraft engines and examples of state-of-the-art engines are given. This is followed by an overview of research on advanced propulsion system concepts envisaged for next-generation aircraft. Based on this literature review the motivation of this work is presented. Lastly, an outline of the content of this dissertation is provided.

1.1. AIRCRAFT ENGINE EMISSIONS

The combustion of fossil fuels results in the emission of carbon dioxide (CO_2), water (H_2O), nitrous oxides (NO_x), unburned hydrocarbons (HC), carbon monoxide (CO), and soot. Additionally, aircraft engines emit noise.

The reduction in fuel consumption is currently driven by commercial interest. In the year 2022, the cost of fuel and oil accounted for approximately 30% of total airline operating costs.[1] However, growing concerns over air quality and noise emissions in the vicinity of airports lead to standards and recommended practices (SARPs) issued by the International Civil Aviation Organization (ICAO)[2] [1]. These SARPs set limits to allowable

[1] International Air Transport Association (IATA), Unveiling the biggest airline costs, https://www.iata.org/en/publications/newsletters/iata-knowledge-hub/unveiling-the-biggest-airline-costs/, accessed on 14 June 2024

[2] ICAO SARPs are not legally binding. Nevertheless, governments and supranational organizations, like the European Union, integrate them into their domestic legislation, thereby elevating them to certification standards.

landing and take-off (LTO) cycle emissions of nitrous oxides (NO_x), unburned hydrocarbons (HC), carbon monoxide (CO), and soot, as well as noise emissions. The reduction of LTO-cycle emissions is mainly due to improvements in combustor technology. Improvements in thermal efficiency of gas turbine engines, if achieved with an increase in turbine inlet temperature, increase NO_x emissions. In the year 2017 the ICAO for the first time issued SARPs for the emission of CO_2 during cruise [2]. Nevertheless, current research suggests that roughly two-thirds of the climate impact of aviation is due to non-CO_2 related emissions such as the emissions of NO_x and water [3]. At high altitude NO_x engages in chemical reactions that produce ozone (O_3) which acts as a greenhouse gas [3]. The emission of water vapor at high altitudes can lead to the formation of contrails and contrail-induced cirrus clouds which cause a net warming effect [3]. To date, no standards are calling for a reduction of non-CO_2 related emissions during cruise. Recognizing the urgency to do so, governments are setting emission reduction goals supported by research funding. For example, the vision of the European Union (EU) for the year 2050 as worked out by the Advisory Council for Aviation Research and Innovation in Europe (ACARE) calls for net-zero CO_2 emissions, a reduction in NO_x, non-volatile particular matter, and contrail cirrus clouds by 90% with respect to the year 2000 for all intra-EU flights and those departing from the EU. The goal of net-zero CO_2 emissions is based on the assumption of using synthetic fuels and hydrogen sustainably produced in the required amounts. Assuming the availability of sustainable aviation fuels, this goal could readily be achieved with current-day engines that are certified to use such fuels. However, the emissions of NO_x and water are proportional to the amount of fuel burned, which, besides the commercial interest, justifies the development of more efficient engines from an environmental point of view. Therefore, the engine concepts presented in this dissertation focus on reducing CO_2 emissions. Engine noise emissions are not considered.

1.2. A BRIEF HISTORY OF AIRCRAFT ENGINE EVOLUTION

Figure 1.1: Photo of Boeing 707-320B ©Mike Freer/Wikimedia Commons/GFDL 1.2

Figure 1.2: Photo of Boeing 787-8 ©H. Michael Miley/Wikimedia Commons/CC-BY-SA-2.0

Figure 1.3: Photo of Airbus A320neo ©BriYYZ/Wikimedia Commons/CC-BY-SA-2.0

The design of current-day airliners strongly resembles that of the first jetliners that entered into service at the end of the 1950s. Since then, technological advancements in the fields of aerodynamics, materials, structures, manufacturing technologies, and propulsion systems strongly reduced aircraft emissions related to fossil fuel combustion and noise generation. However, the main driver of this trend were developments in propulsion system technology. This is highlighted, for example, by comparing the cruise

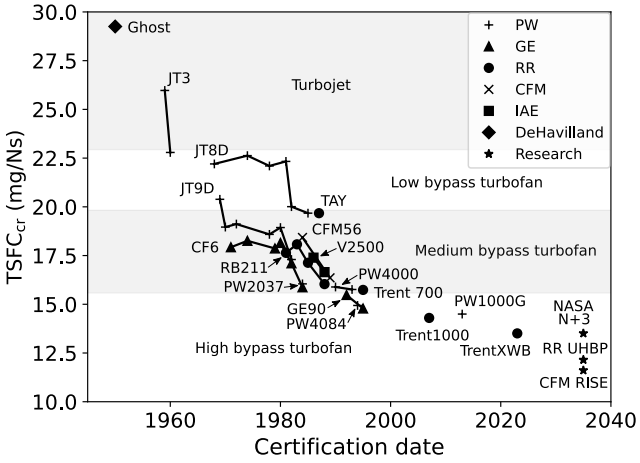

Figure 1.4: Cruise thrust-specific fuel consumption ($TSFC_{cr}$) over engine certification year including the forecasted performance of engines with entry into service in the 2030s. The graph is adapted from Ref. [5] and extended with data from Refs. [5, 7, 8].

thrust-specific fuel consumption ($TSFC_{cr}$) and the cruise lift-to-drag ratio of the Boeing 707 (Fig. 1.1), the first jet-powered commercial aircraft, with values of state-of-the-art aircraft.

The first version of the B707 entered into service in the year 1958 and used Pratt & Whitney JT3C turbojet engines with a $TSFC_{cr}$ of 25.5 mg/Ns [4]. The updated B707-320B with entry into service (EIS) in the year 1962 employed Pratt & Whitney JT3D low-bypass ratio turbofan engines with a $TSFC_{cr}$ of 23.0 mg/Ns [5] and the lift-to-drag ratio is estimated as 17.6 using the method reported in Ref. [6]. For comparison, the lift-to-drag ratio of the Boeing 787-8 (EIS year 2011) (Fig. 1.2) is 18.9.[3] The $TSFC_{cr}$ of the Pratt & Whitney PW1100G-JM geared-turbofan (GTF™) engine that is employed on the Airbus A320neo (EIS year 2016) (Fig. 1.3), and which is in the same thrust class as the JT3D engine, is 14.4 mg/Ns.[4] While improvements to wing aerodynamics were achieved with the introduction of supercritical airfoils and winglets, the tube-and-wing architecture limits the potential gains in lift-to-drag ratio. However, advances in propulsion system technology have reduced $TSFC_{cr}$ by approximately 40%. For a given amount of fuel, the range an aircraft can fly is proportional to the lift-to-drag ratio and inversely proportional to $TSFC_{cr}$. Therefore, based on the numbers above, the fuel savings due to improvements in the lift-to-drag ratio are approximately 7%, and those due to reduced $TSFC_{cr}$ are close to 70%.

[3] Estimated with the method of Ref. [6] and a $TSFC_{cr}$ of 14.3 mg/Ns for the Rolls-Royce Trent 1000 engine [7]

[4] Approximated based on the statement of Pratt & Whitney that the PW1100G-JM engine is 15% more fuel efficient than the previous generation engine, which is represented by the CFM56-5B engine featuring a $TSFC_{cr}$ of 17.0 mg/Ns [7].

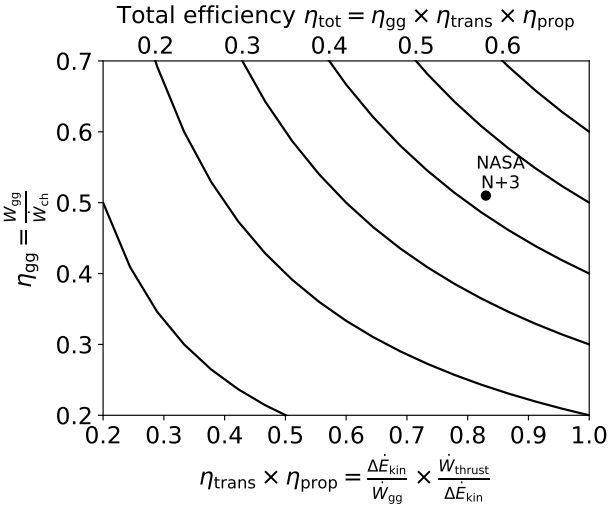

Figure 1.5: Indicative values of engine gas generator efficiency (η_{gg}), the product of propulsive efficiency (η_{prop}) and transmission efficiency (η_{trans}), and total efficiency (η_{tot}) for different engine architectures. The variable $\dot{W}_{ch}$ indicates the chemical power added by the combustion of fuel, $\dot{W}_{thrust}$ is the product of engine net thrust and flight speed, $\dot{W}_{gg}$ is the gas generator power, and $\Delta\dot{E}_{kin}$ is the change in kinetic energy of the core and bypass streams. The efficiencies of the NASA N+3 turbofan engine, which is in the 89 to 133 kN (20.000 to 30.000 lbf) thrust class, are calculated from data provided in Ref. [8]. The graph is adapted from Ref. [5].

Figure 1.4 gives the historical trend of $TSFC_{cr}$ for different engines over their certification date and forecasted values for next-generation engines. Figure 1.5 indicates values of engine propulsive efficiency (η_{prop}), the product of gas generator and transmission efficiency ($\eta_{gg} \times \eta_{trans}$), and total efficiency (η_{tot}) obtained with different engine architectures and the predicted performance of the NASA N+3 turbofan engine [8]. η_{gg} is defined as

$$\eta_{gg} = \frac{\dot{W}_{gg}}{\dot{W}_{ch}} = \frac{0.5\dot{m}_{45}(V_{45,id}^2 - V_\infty^2)}{\dot{m}_{fuel}\mathrm{LHV}}, \tag{1.1}$$

where the numerator is the gas generator power and the denominator is the chemical power added by fuel combustion. $\dot{m}_{45}$ is the high-pressure turbine exit mass flow rate, $V_{45,id}$ the speed obtained when isentropically expanding the gas generator exhaust to ambient pressure, V_∞ is the free stream velocity. $\dot{m}_{fuel}$ is the fuel mass flow rate and LHV is the lower heating value of the fuel. Alternatively, $\dot{W}_{gg}$ can be approximated using the following relation proposed by Guha [9]

$$\dot{W}_{gg} = 0.5\dot{m}_9(V_{9,id}^2 - V_\infty^2) + 0.5\dot{m}_{19}(V_{19,id}^2 - V_\infty^2)\eta_{ke}^{-1}, \tag{1.2}$$

where $\dot{m}_9$ and $\dot{m}_{19}$ are the core and bypass nozzle mass flow rates, and $V_{9,id}$ and $V_{19,id}$ are the nozzle exhaust speeds when isentropically expanded to ambient pressure. η_{ke} is the transmission efficiency of kinetic energy from the core to the bypass stream. It is defined as the product of the low-pressure turbine, the fan, and the bypass nozzle isentropic efficiencies.

η_{trans} is defined as

$$\eta_{\text{trans}} = \frac{\Delta \dot{E}_{\text{kin}}}{\dot{W}_{\text{gg}}} = \frac{F_{\text{net}} V_\infty + 0.5\dot{m}_9 (V_9 - V_\infty)^2 + 0.5\dot{m}_{19}(V_{19}^2 - V_\infty)^2}{0.5\dot{m}_{45}(V_{45,\text{id}}^2 - V_\infty^2)}, \tag{1.3}$$

$\Delta \dot{E}_{\text{kin}}$ is the change in kinetic energy of the core and bypass streams, and F_{net} is the net thrust. η_{prop} is defined as

$$\eta_{\text{prop}} = \frac{\dot{W}_{\text{thrust}}}{\Delta \dot{E}_{\text{kin}}} = \frac{F_{\text{net}} V_\infty}{F_{\text{net}} V_\infty + 0.5\dot{m}_9 (V_9 - V_\infty)^2 + 0.5\dot{m}_{19}(V_{19}^2 - V_\infty)^2}, \tag{1.4}$$

where $\dot{W}_{\text{thrust}}$ is the thrust power. η_{tot} is the product of η_{gg}, η_{trans} and η_{prop}. The bypass ratio (BPR) categories shown in these figures are defined as follows: low BPR if $0 < \text{BPR} < 3$, medium if $3 < \text{BPR} < 7$, and high if $\text{BPR} > 7$. The reduction of TSFC_{cr} is the result of improvements in η_{th} and η_{prop}. The main cause of the increase of η_{th} are higher turbine inlet temperature (TIT), higher compressor OPR, and improvements in turbomachinery efficiencies. The development of high-temperature resistant materials, equiaxed and single crystal alloy turbine blades, thermal barrier coatings, and advancements in turbomachinery aerodynamics contributed to a steady increase of η_{th}. The engine BPR is the main driver for increasing values of η_{prop}. An increase in BPR was made possible with the introduction of wide-chord fan blades made of titanium and composite materials that could sustain the large centrifugal forces at the blade roots and at the same time allow high aerodynamic efficiency. Furthermore, the introduction of turbofan engines that employ a gearbox to decouple the speed of the fan and the low-pressure spool allows optimal aerodynamic designs of both turbomachines, a reduction in low-pressure compressor (LPC) and low-pressure turbine (LPT) stage count, an increase in BPR, and a reduction in fan noise due to a lower fan speed if compared to direct-drive configurations.

The PW1100G-JM is the state-of-the-art engine in the 89 to 133 kN (20.000 to 30.000 lbf) thrust class and it is used on single-aisle medium-range aircraft. It features a bypass ratio (BPR) of 12.5 [7], an overall pressure ratio (OPR) of 50,[5], a fan diameter of approximately 2.2 m [7], and a TSFC_{cr} of 14.4 mg/Ns[4]. For comparison, the state-of-the-art engine in the 356 to 445 kN (80.000 to 100.000 lbf) thrust class used on long-range aircraft is the Rolls-Royce Trent XWB engine. This engine has a BPR of 9.6, an OPR of 50,[6] a fan diameter of approximately 3.0 m [7] and a TSFC_{cr} of approximately 13.5 mg/Ns[7].

1.3. ADVANCED PROPULSION SYSTEM CONCEPTS

Research focuses on advanced propulsion system concepts that reduce mission fuel burn, for reasons outlined in Section 1.1. The state-of-the-art commercial aircraft design fea-

[5] FlightGlobal article, https://www.flightglobal.com/pandw-on-a320neo-more-pressure-less-cooling/99337.article, accessed on 19 February 2024

[6] Rolls-Royce Trent XWB information brochure, https://www.rolls-royce.com/~/media/Files/R/Rolls-Royce/documents/civil-aerospace-downloads/trent-xwb-infographic.pdf, accessed on 12 June 2024

[7] Approximated based on the statement of Rolls-Royce that the Trent XWB engine is 15% more fuel efficient than the Trent 700 engine which has a TSFC_{cr} of 15.9 mg/Ns [7].

tures a tube-and-wing airframe with turbofan engines mounted below the wings. However, similar to the developments in the car industry, there is an interest in an increased degree of electrification of aircraft systems including the propulsion system. Based on the used energy carrier and the mode of power transmission to produce propulsive power, four different propulsion system architectures can be distinguished: I) conventional, II) all-electric, III) hybrid-electric, and IV) turboelectric. Power can be transmitted mechanically or electrically to drive a ducted or un-ducted propulsor. Conventional or state-of-the-art aircraft engines burn a chemical energy carrier stored as a liquid or gaseous fuel and use mechanical power transmission. All-electric aircraft use electrical energy stored in batteries and make use of electrical power transmission. Hybrid-electric aircraft use both electrical and chemical energy carriers and employ a mix of mechanical and electrical power transmission. Turboelectric aircraft only use chemical energy and employ a mix of mechanical and electrical power transmission. An introduction to the topic of electric propulsion systems is provided by Hepperle [10] and Refs. [11, 12] provide an in-depth overview of electrified concepts and how they compare with conventional aircraft architecture. A summary of the advantages and disadvantages of electric propulsion is given in the following, for completeness.

Electric machines are more efficient than gas turbines and can result in higher overall efficiency. Furthermore, the efficiency of electric machines is scale-independent [13]. This can enable new aircraft designs employing distributed propulsion systems consisting of small-scale electrically driven propulsors. Embedding distributed propulsion systems with the fuselage or wing may reduce wetted area and drag compared to a podded turbofan engine producing the same thrust. The drag advantage may be used to reduce the disk loading of the propulsors and increase propulsive efficiency. Propulsive efficiency advantages may also be derived from boundary layer ingestion of wing-mounted or fuselage-mounted systems. Ingesting the boundary layer reduces the average inlet velocity, this lowers intake ram drag and increases net thrust. The design of boundary layer ingesting intakes requires special attention to keep internal losses due to non-uniform flow low [14, 15]. Additionally, aircraft aerodynamics can be modulated for example by employing propulsive flaps for high-lift augmentation [16] and benefits on cruise lift-to-drag ratio may be derived from the aeropropulsive interaction of wing-mounted systems [17, 18]. One engine inoperative scenarios and the resulting thrust asymmetry could be handled more easily with a distributed propulsion system. This may allow downsizing of the powertrain and the vertical tail of the aircraft [19]. In the case of aircraft concepts utilizing batteries as the energy carrier, a direct reduction in emissions can be achieved by using renewably sourced electrical energy. Downsizing of gas turbine engines may be possible if electric power is available during flight phases requiring peak power. Disadvantages of electrical architectures are low values of battery mass-specific energy and electrical component mass-specific power. Furthermore, increased electrical power capacity requires advanced thermal management systems. Embedding the propulsion system within the airframe requires a multidisciplinary approach as previously distinct disciplines become highly coupled. A Class-I sizing method that considers aeropropulsive interaction effects is presented in Ref. [20].

The realization of aircraft configuration II relies on the state of battery technology research. The state-of-the-art lithium-ion battery technology achieves cell-level mass-

specific energy values of around 250 Wh/kg [21]. This value is approximately 50 times lower than the value of kerosene which is 43 MJ/kg = 12 000 Wh/kg. Research on solid-state lithium-sulfur batteries conducted within the NASA SABERS project[8] demonstrated a cell-level mass-specific energy value of 500 Wh/kg. Values of mass-specific energy of up to 1000 Wh/kg may be possible with lithium-air or lithium-sulfur batteries [22]. In any case, the mass-specific energy of the most promising future battery technologies is at least one order lower than that of kerosene. As mission range is proportional to mass-specific energy, the realization of commercially viable all-electric aircraft in the next decades proves difficult. Nonetheless, recent work presented in Refs. [23, 24] suggests that an all-electric aircraft transporting 90 passengers over a range of 800 km is feasible assuming a battery pack-level mass-specific energy of 360 Wh/kg.

On the other hand, aircraft architectures I), III), and IV), as defined above, rely on gas turbine engines (or fuel cells) as the prime movers. Research on gas turbine technology focuses on two main architectures, 1) advanced turbofan engines and 2) unconventional thermodynamic cycle engines. The following two sections summarize the state of the research in these fields. This review benchmarks novel engine concepts against reference engines with varying technology levels. Comparing these concepts to a common benchmark can clarify their potential. However, differing modeling and technology assumptions, and the lack of absolute data, make this challenging.

1.3.1. ADVANCED TURBOFAN ARCHITECTURES

ULTRA-HIGH-BYPASS TURBOFAN ENGINES

It is becoming increasingly difficult to further improve η_{th} of turbofan engines as turbomachinery efficiencies are close to their theoretical limits and a further increase of OPR and TIT is challenged by material temperature constraints and more stringent LTO-cycle emission restrictions. Additionally, the thermodynamic benefits of adopting increasingly higher values of OPR are limited by reduced compressor efficiency resulting from high aerodynamic losses of the short last-stage blades. Raising η_{tot} may be possible with advanced fan technology and highly efficient small gas generators, enabling higher engine bypass ratios and increasing η_{prop}. Improvements in TSFC of 5 to 10% over current-day turbofan engines are predicted by research on ultra-high-bypass ratio turbofan (UHBP) engines [25, 8, 26, 27]. Common technology assumptions are the use of ceramic matrix composite (CMC) material for the combustor and turbine, allowing increased TIT and/or reduced turbine cooling air demand, improved turbine cooling technology, improved turbomachinery efficiency of small-scale machines, high-efficiency low-pressure ratio fans in combination with variable geometry nozzles.

In industry, the UltraFan project of Rolls-Royce aims to develop technology for a UHBP engine that is scalable in the 111 to 489 kN (25.000 to 110.000 lbf) thrust range, and that promises fuel savings of 10% over the top-in-class Trent XWB engine,[9] and is to

[8] NASA Solid-state Architecture Batteries for Enhanced Rechargeability and Safety (SABERS), https://www.nasa.gov/aeronautics/nasas-solid-state-battery-research-exceeds-initial-goals-draws-interest/, accessed on 13 June 2024

[9] Rolls-Royce UltraFan project, https://www.rolls-royce.com/innovation/ultrafan.aspx, accessed on 12 June 2024

enter service in the 2030s. The HyTEC project of NASA[10] focuses on technology development for next-generation small gas generators. The first results of this project are presented by Bennett et al. [25]. They analyzed the benefits that an advanced technology gas generator employed in a next-generation direct-drive turbofan engine can have on the fuel consumption of an Airbus A320-like aircraft. The resulting engine is characterized by a BPR of 10.8 and, after accounting for changes in propulsion system mass, achieves approximately 5% fuel savings compared to a state-of-the-art direct-drive turbofan engine. The impact of advanced core and fan technology on fuel consumption of an Airbus A320-like aircraft was studied by Jones et al. [8]. They considered a fan polytropic efficiency of 97% combined with a fan pressure ratio of around 1.3, a variable-area bypass nozzle, and a reduction gearbox between the low-pressure spool and the fan. The optimized engine design features a BPR of around 24 and a $TSFC_{cr}$ of 13.5 mg/Ns which is approximately 6% lower than the value of the PW1100G-JM engine which is in the same thrust class (see Section 1.2). However, this engine design is based on a fan diameter of 100 in, which is larger than the 81 in of the PW1100G-JM engine. The penalty of the large fan on the landing gear length requirement, aircraft mass, and nacelle drag is not considered. Mastropierro et al. [26] present a turbofan engine design with a geared architecture for a long-range aircraft featuring advanced gas generator and fan technology. The optimized turbofan engine has a BPR of around 17, a fan outer diameter of 2.8 m, and a cruise $TSFC_{cr}$ of 12.6 mg/Ns which is approximately 7% lower than the value of the state-of-the-art Rolls-Royce Trent XWB engine which is in the same thrust class (see Section 1.2). Furthermore, using advanced materials, the engine is 35% lighter compared to a reference engine with entry into service (EIS) year 2000.

OPEN-ROTOR ENGINES

The potential fuel savings of UHBP engines are limited by the resulting increase of nacelle drag. Open-rotor engines, sometimes also referred to as propfan or un-ducted fan engines, may allow a further increase in propulsive efficiency because larger fan diameters can be adopted as a result of the missing fan cowl. Due to the high fuel prices, intensive research on this concept was carried out during the 1970s and 1980s, with a projected entry into service in the 1990s. Towards the end of the 1980s flight tests were carried out by NASA in collaboration with General Electric [28, 29] and by Pratt & Whitney in collaboration with Allison [30] using Boeing 727 and McDonnell Douglas MD-80 aircraft as the testbeds. Fuel savings of 20 to 30% with respect to best-in-class turbofan engines of that time were measured.[11] Compared to the PW1100G-JM, the tested open-rotor engines feature a $TSFC_{cr}$ that is 0 to 14% higher. However, sinking fuel prices towards the end of the 1980s put an end to these efforts. Currently, the open-rotor concept receives renewed attention from the industry, as testified, for example, by the RISE project pursued by the CFM consortium.[12] Only a few academic works were published

[10] Hybrid thermally efficient core (HyTEC), https://www.nasa.gov/directorates/armd/hytec-technical-portfolio/, accessed on 12 April 2024.

[11] The best-in-class engine considered by Refs. [28, 29, 30] was the Pratt & Whitney JT8D-209 turbofan engine generating a maximum thrust of around 82 kN and featuring a bypass ratio of approximately 1.8 and a $TSFC_{cr}$ = 20.50 mg/Ns [7].

[12] Revolutionary Innovation for Sustainable Engines (RISE), https://www.cfmaeroengines.com/rise/, accessed on 11 April 2024.

on this topic in the recent past and all consider the application of this engine configuration to short-range or medium-range aircraft.

Mastropierro et al. [26] present a counter-rotating open-rotor engine design for a medium-range aircraft with technology assumptions for an EIS year of 2050. The optimized open-rotor engine generates approximately 80 kN of thrust at take-off and features a maximum rotor diameter of 4 m, a TSFC at top-of-climb (TOC) of 10.8 mg/Ns, and a TSFC at cruise of 10.4 mg/Ns. The optimized engine features a $TSFC_{cr}$ which is 42% lower than that of a year 2000 reference engine and 28% lower than that of the PW1100G-JM.[13] Furthermore, it is stated that engine mass estimation was conducted but no values are given. In an earlier work Hendricks and Tong [31] performed the conceptual design of a counter-rotating open-rotor engine for a medium-range aircraft with technology assumptions for an EIS year of 2015. Their design features a maximum rotor diameter of 4.5 m and results in an estimated TSFC at TOC of 12.1 mg/Ns. The engine generates approximately 121 kN of thrust at sea-level-static conditions. Compared to a reference turbofan engine with a geared architecture, the same thrust range, and the same technology level, the open rotor engine features a mass that is approximately 50% higher and a TSFC that is 12% lower.[14] Despite the heavier open-rotor architecture and the resulting increase in aircraft operating empty mass, improvements in fuel efficiency reduce the required fuel mass, resulting in an aircraft maximum take-off mass that is similar to an aircraft employing turbofan engines. Similarly, Larsson et al. [32] describes an open-rotor engine design based on technology assumptions for an EIS year of 2020. The engine generates 92 kN of thrust at take-off and features a maximum rotor diameter of 4.2 m. No absolute values for TSFC and engine mass are listed. Nevertheless, it is stated that a reduction in fuel consumption of around 15% is possible if compared to an aircraft employing a projected turbofan engine design featuring a geared architecture based on the same technology assumptions. This estimate includes the effect of increased open-rotor engine mass by 11% and the reduction in aircraft drag due to the smaller nacelle. Notably, the difference between turbofan mass and open-rotor mass is smaller than those projected by Hendricks and Tong [31].

The varying technology assumptions, the use of different reference engines, and partially missing data make it difficult to compare the various open-rotor engine concepts. Nevertheless, a significant fuel-saving potential associated with this engine type was predicted over multiple decades.

BOOSTED TURBOFAN ENGINES

The boosted turbofan concept belongs to the class of hybrid-electric architectures and incorporates electric motors injecting power into the low-pressure or high-pressure spool. The required electrical power is stored in batteries. For example, power injection or extraction can modify the engine operating line during off-design operation. Furthermore, power injection into the low-pressure spool directly contributes to overall thrust. Reducing mission fuel consumption and engine size is possible by providing power to the

[13] The year 2000 reference engine modeled by Ref. [26] features a $TSFC_{cr}$ = 18.0 mg/Ns which is similar to the performance of earlier CFM56 models.

[14] The reference turbofan engine with EIS year 2015 features a TSFC at TOC of 14.2 mg/Ns which is similar to the value of the PW1100G-JM engine that is in the same thrust class.

low-pressure spool during off-design operation [33, 34, 35]. In particular, these advantages apply to high-power operations such as the rolling-take-off (RTO) and TOC. Zhao et al. [34] investigated a boosted turbofan engine with a geared architecture powering an Airbus A320-like aircraft. They identified that injecting a power of 500 kW into the low-pressure spool during RTO lowers the required TIT and therefore turbine cooling demand. As a result, cruise TSFC is reduced by 0.5%. Furthermore, it is stated that power extraction during part-load operation may allow to reduce the amount of compressor handling bleeds. Sielemann et al. [33] present a comprehensive numerical method to design boosted turbofan engines. Using a parametric study they show the impact on TSFC, η_{th}, and cooling air demand that a variation of power injection to the low-pressure spool and OPR can have at different operating points. RTO is identified as the mission phase benefiting the most from electric power injection. However, engine performance can also increase because of power injection during cruise as turbomachinery efficiencies are higher due to the lower aerodynamic loading. Chapman [35] compared the effectiveness of different methods to adjust turbomachinery operating conditions based on variable geometry and highlighted that power injection/extraction can have a similar impact without the need for complicated mechanical designs.

1.3.2. ENGINE ARCHITECTURES BASED ON THERMAL ENERGY RECOVERY

As can be deduced from Fig. 1.5 the total efficiency of even the most advanced engines based on the Brayton cycle is less than 50%. This means that approximately half of the chemical power provided by the combustion of kerosene is wasted in the form of a hot exhaust gas stream. Figure 1.6 gives a qualitative overview of the power utilization of a state-of-the-art turbofan engine. To overcome this limitation, modifications to the thermodynamic cycle which are well-known from a theoretical point of view, and widely applied to improve the efficiency of stationary power plants, are being explored. These include concepts incorporating recuperation and/or intercooling, as well as combined-cycle configurations. The main challenges are related to the weight, volume, added drag, and complexity of implementing these concepts into actual aircraft propulsion systems.

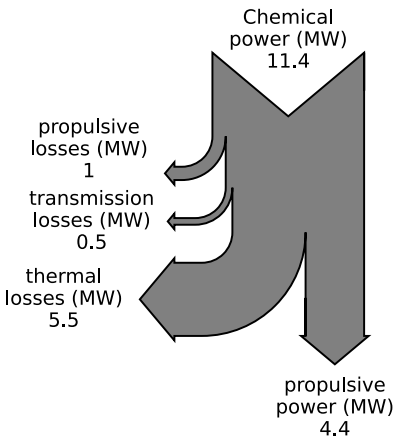

Figure 1.6: Sankey diagram of a turbofan engine with similar performance to the PW1100G-JM.

RECUPERATED TURBOSHAFT ENGINES

The process flow diagram (PFD) of a recuperated turboshaft engine is shown in Fig. 1.7. Recuperators are gas-to-gas heat exchangers placed in the exhaust of gas turbine engines that exchange heat between the exhaust gas and the air at the outlet of the compressor. The application of this concept to turboshaft and turboprop engines was extensively studied in the 1960s as documented by McDonald et al. [36]. Several experimental engines in the power range from 200 to 3000 kW were built and ground tested. The Al-

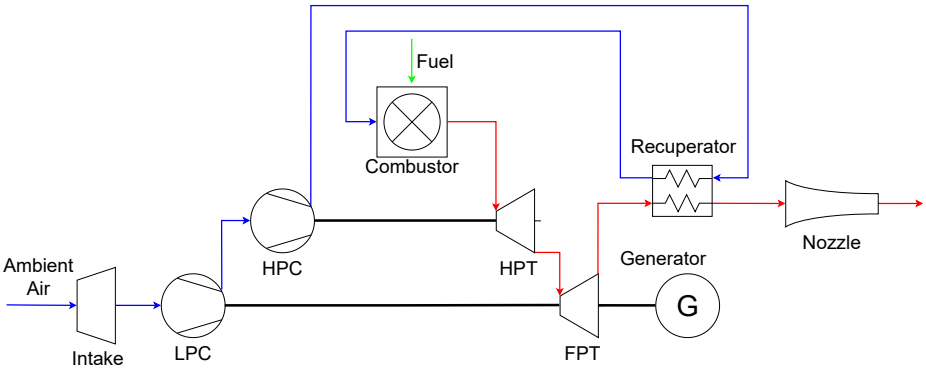

Figure 1.7: Process flow diagram of a recuperated turboshaft engine that powers a generator.

lison T63 turboshaft engine [36, 37] was the only engine to be flight-tested onboard a helicopter. These studies indicated that employing a recuperator can lead to a reduction of power-specific fuel consumption of around 30% if compared to a conventional cycle engine. Engine mass increased by about one-third with the addition of the recuperator. Moreover, as a result of the cooler exhaust gas, a reduction in jet noise and infrared signature were identified as advantages of this engine configuration. The efficiency of recuperated engines benefits from high values of TIT. To achieve high temperatures over the entire operating envelope variable nozzle guide vanes (NGVs) can be adopted in the low-pressure turbine (LPT). However, the effect of continuously elevated temperatures on turbine blade life needs to be considered [38]. Lightweight tubular heat exchangers with effectiveness values ranging from 60 to 75% were determined as the most promising heat exchanger configurations. Plate-fin and primary surface heat exchangers, while cost-effective, often suffer from cracking due to extremely high thermal stresses. However, while technological advancements allowed for ever-increasing values of TIT and OPR, high temperature and pressure remains a major issue for high-performance heat exchangers. At the end of the 1960s, the interest in recuperated engines diminished due to doubts about the long-term structural integrity and reliability of the heat exchanger as well as low fuel prices.

Recent research focuses on applying recuperators to the turboshaft engines of helicopters [39, 40, 38]. Stroh [38] presents the conceptual design of a 300 kW turboshaft engine with EIS year 2020 to replace the simple-cycle turboshaft engines of a Bo-105 helicopter. The design procedure included thermodynamic performance modeling, engine mechanical design, and helicopter mission analysis. Variable NGVs for the LPT are assumed and the penalty of continuously high TIT on turbine blade life is considered. The cross-counterflow elliptical tube recuperator design presented by Schoenenborn et al. [41] is used and different integration architectures are assessed considering the available volume onboard the helicopter. For a 90-minute transport mission fuel savings of around 35% are estimated if compared to the conventional engine. It is highlighted that advantages of recuperated engines are relevant during part-load operations, especially during cruise. Therefore, the potential benefits of this engine type depend on the de-

1

sign mission of the helicopter. Zhang and Gümmer [39] provide an updated review of past recuperator research and re-assess the potential of classical heat exchanger (HEX) layouts assuming state-of-the-art materials and manufacturing technologies. It is concluded, that while traditionally tube bundle heat exchangers were favored due to their low mass, favorable pressure-containing capability, and high reliability, primary surface heat exchangers made of layers of stacked corrugated sheet metal combined with state-of-the-art materials and manufacturing technologies are more appropriate choices for the future. In line with this finding, Zhang and Gümmer [40] performed the design optimization of a primary surface HEX for a 300 kW recuperated turboshaft engine employing HEX mass and effectiveness as the objective functions. For a selection of optimal HEX designs, mission analysis is performed. It is concluded that, for a search-and-rescue mission, fuel savings of around 30% are possible with an optimized HEX mass ranging from 30 to 75 kg and a HEX effectiveness in the range 75 to 90%.

INTERCOOLED-RECUPERATED TURBOFAN ENGINES

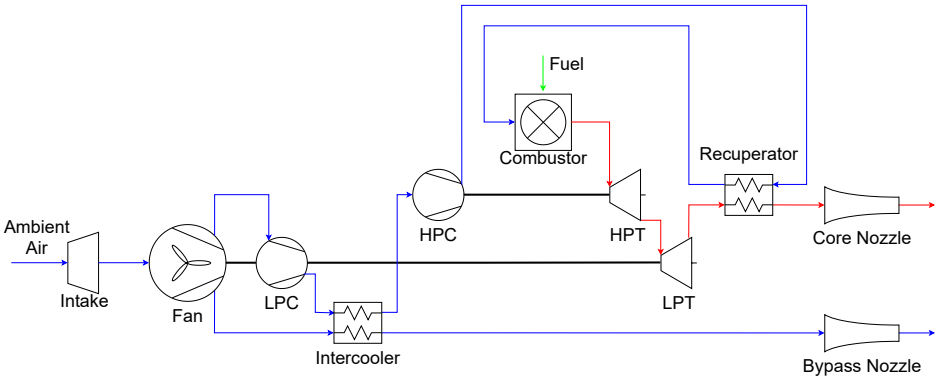

Figure 1.8: Process flow diagram of an intercooled-recuperated turbofan engine.

The recuperated cycle is only practical for OPR values up to about 10. For larger OPR values the temperature difference between the air at the compressor discharge and the exhaust of the gas turbine becomes too small to allow sufficient heat transfer given the size limitations of the recuperator. Therefore, the application of recuperators to engines with higher OPR requires the use of an intercooler. Figure 1.8 shows the PFD of an intercooled-recuperated (ICR) turbofan engine. An intercooler is a HEX placed between the low-pressure and the high-pressure compressors. It cools the compressed air using a gaseous or liquid heat sink. In the case of a turbofan engine, the heat sink is usually the bypass air. However, if liquid hydrogen is the fuel, it could also serve as the heat sink, as considered by Patrao et al. [42].

MTU Aero Engines extensively studied an ICR turbofan engine concept with a take-off thrust of 200 kN using bypass air as the heat sink of the intercooler [43]. This work included designing and testing a cross-counterflow elliptical tube recuperator [41]. A thermodynamic cycle analysis shows that a reduction of TSFC of around 19% is possible if compared to a conventional direct-drive turbofan engine with an EIS year 1995. The

added mass per engine is estimated to be 1000 kg, however, the impact on aircraft fuel consumption is not determined. The resulting engine has a lower OPR than a conventional turbofan engine which reduces NO_x emissions. Similar to recuperated engines, the performance of the ICR engine benefits from high values of TIT over the whole operating range. Therefore, variable geometry NGVs for the LPT should be employed. The TIT at maximum climb is around 1950 K. This allows to design a very compact core and drives the BPR to values around 20. Kyprianidis et al. [44] performed a similar analysis on an intercooled (IC) and ICR turbofan engine concept. The IC engine achieves a reduction in TSFC of 1.5% and mission fuel savings of 3% if compared to a conventional turbofan engine with the same EIS year of 2020. Fuel saving is higher than TSFC reduction as the engine is approximately 6% lighter than the conventional engine. It is highlighted that employing a variable area nozzle for the cooling air side of the intercooler can improve the TSFC during off-design operation. The ICR engine with assumed EIS year 2020 achieves a reduction in TSFC of 18% and mission fuel savings of 22% if compared to a conventional turbofan employed on an aircraft with EIS year 2000. The aircraft with EIS year 2020 is 10% lighter than the aircraft with EIS year 2000, and no reasoning for this weight saving is given. No absolute values of engine mass, TSFC, and thrust are provided. The importance of employing variable geometry LPT NGVs is highlighted and quantified using a parametric study. Patrao et al. [42] investigated the IC and ICR turbofan engine concepts with an assumed EIS year of 2050 using hydrogen as the fuel and as the heat sink of the intercooler. Both engine concepts are compared to a conventional turbofan engine with the same EIS year and technology assumptions generating a take-off thrust of 136 kN. Part of this work is dedicated to identifying optimized HEX duct designs and formulating pressure drop correlations. The IC engine reduces cruise TSFC by approximately 3%, mission fuel mass by 3.6%, and NO_x emissions during cruise by approximately 25%. The ICR engine achieves a reduction in cruise TSFC of 5% and fuel mass savings of 5.5%. Furthermore, a reduction in NO_x emissions similar to the IC engine is estimated. The reference, the IC, and the ICR engine adopt very similar values for the OPR, which is contrary to the results presented by Boggia and Rüd [43] and Kyprianidis et al. [44]. No variable geometry LPT NGVs were assumed in the case of the ICR engine resulting in lower TIT during cruise.

WATER-ENHANCED TURBOFAN ENGINE

The water-enhanced turbofan (WET) engine concept, conceived by MTU Aero Engines, promises not only a reduction of fuel consumption but also a significant reduction of NO_x and water emissions during cruise. A similar concept is studied by Pratt & Whitney within the HySIITE project,[15] however, the status of this project is not documented in open literature.

Figure 1.9 shows the PFD of the WET engine. The WET engine is a combined-cycle engine consisting of a Brayton and a steam cycle. An EIS in the 2030s is targeted for this technology. The concept is compatible with kerosene, synthetic fuels, and hydrogen. The basic thermodynamics of the cycle are explained in Ref. [45]. Water is extracted from

[15] Steam injected, inter-cooled turbine Engine (HySIITE), https://www.prattwhitney.com/en/newsroom/news/2022/02/21/pw-awarded-department-of-energy-project-to-develop-hydrogen-propulsion-technology, accessed on 10 April 2024

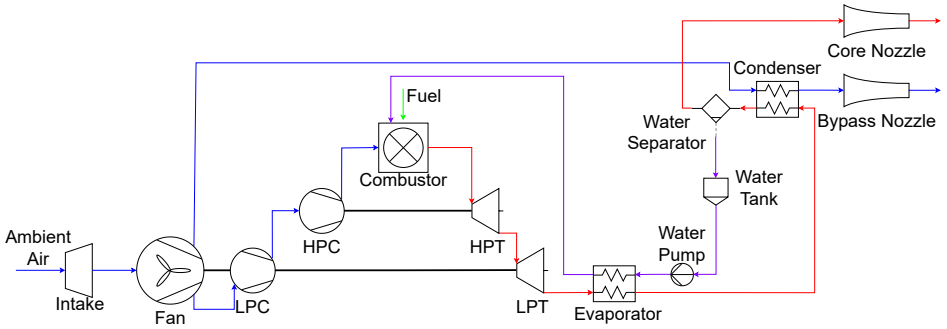

Figure 1.9: Process flow diagram of the water-enhanced turbofan engine concept.

the exhaust gas using a condenser. This water is then pressurized and evaporated in a heat recovery steam generator that exchanges heat with the exhaust gas. The generated steam is injected into the combustion chamber. Steam injection increases the specific heat capacity of the exhaust gas and its mass flow rate enabling more power conversion by the turbine and the realization of a smaller compressor. This improvement in the thermodynamic cycle is estimated to reduce TSFC by around 13% compared to a turbofan engine with equal technology level and using kerosene as the fuel [46]. Accounting for added heat exchanger mass a reduction of 10% in mission fuel consumption for an Airbus A320-like aircraft is expected [46]. Furthermore, due to the high heat capacity of the injected steam, a more homogeneous temperature distribution is achieved during combustion, eliminating temperature peaks, and therefore reducing NO_x emissions. Kaiser et al. [46] estimate a reduction of NO_x emission by 90% with respect to the reference turbofan engine. Additionally, water recovery from the exhaust gas stream strongly reduces its water content and the possibility of contrail formation. Kaiser et al. [46] estimates a reduction of contrail formation of 50%. Overall, the WET engine has the potential to reduce the environmental impact of engine emissions[16] by approximately 40% if compared to the emissions of the reference engine. Advantages of using hydrogen as the fuel were identified by Görtz et al. [47]. Hydrogen may be used as a heat sink in the water condensation process. In addition, to achieve a given water recovery ratio (WRR), defined as the fraction of recovered to injected water, less water needs to be cooled as hydrogen exhaust gas contains approximately three times as much water as kerosene exhaust gas. In conclusion, the WET engine designed for use with hydrogen has a more compact condenser and an approximately 2% lower specific energy consumption if compared to the engine designed for kerosene as the fuel.

COMBINED-CYCLE ENGINE WITH ORGANIC RANKINE CYCLE BOTTOMING UNITS

Organic Rankine cycle (ORC) bottoming units have been successfully integrated into medium-power capacity stationary gas turbines [48]. ORC waste-heat-recovery (WHR) systems have also found application on vessels and have undergone comprehensive

[16] Based on the absolute pulse global warming potential ($APGWP_H$), that considers the radiative forcing of a pulse emission over a given timeframe H. The stated results are based on H = 100 years.

testing to enhance the fuel efficiency of long-haul truck engines [48]. The PFD of a turboshaft engine adopting an ORC bottoming unit is shown in Fig. 1.10.

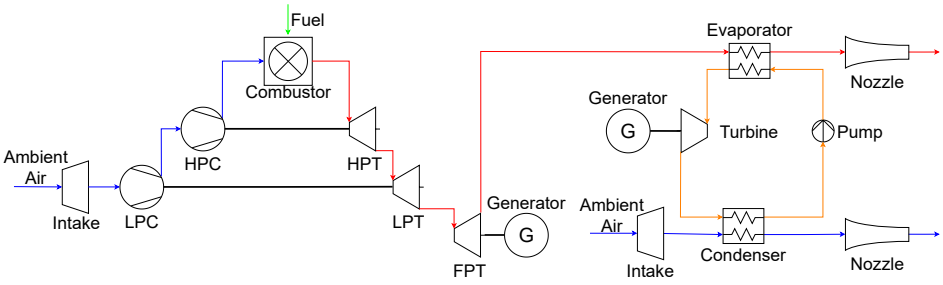

Figure 1.10: Process flow diagram of a turboshaft engine with an air-cooled ORC bottoming unit.

Only a few studies analyzed the effect of recovering otherwise wasted thermal energy from aero-engines with an ORC WHR system. The first investigation on the feasibility of integrating an ORC WHR system with a CFM56 turbofan engine was presented by Perullo et al. [49]. They analyzed a retrofit scenario of adopting a WHR system based on an air-cooled subcritical recuperated ORC configuration using R245fa as the working fluid. In their design, the evaporator is integrated into the walls of the engine core nozzle and the condenser is integrated into the engine air intake lip. The ORC turbogenerator and the pump are integrated into the engine pylon and nacelle, respectively. The ORC system is designed to provide 200 kW of electrical power to the electrically driven air compressor of the environmental control system (ECS). The study is solely based on on-design thermodynamic calculations and component sizing is not included. A mass of 430 kg is assumed for the WHR system per engine and no detailed justification is provided. The fuel-saving potential for a short-range flight is estimated to be 0.9%. Zarati et al. [50] investigated a retro-fitting scenario of integrating an ORC WHR system with a 2 MW-class turboprop engine powering a regional aircraft. A WHR system based on an air-cooled subcritical non-recuperated ORC configuration using R245fa as the working fluid is modeled, including the sizing of both plate-fin heat exchangers. The condenser is housed in a separate ram-air duct and the evaporator is located in the exhaust duct of the engine. Simplified zero-dimensional modeling of the ram-air duct is conducted and it is concluded that the thermal energy transferred from the condensing working fluid to the ram-air generates sufficient thrust to overcome the drag caused by the air intake, duct, and HEX core. On and off-design simulations are carried out and the system is optimized to provide maximum heat recovery during cruise. No details regarding the optimization procedure are given. Furthermore, it is determined that transferring the ORC turbine power directly to the low-pressure shaft of the engine yields the largest fuel savings. Compared to the benchmark engine, the envisaged combined-cycle engine reduces mission fuel mass by 1.7% for a 300 NM trip. The exhaust gas temperature of the engine is 750 K and the ORC turbogenerator provides 100 kW of shaft power. The designed WHR unit has a mass-specific power of 0.33 kW/kg. Additionally, based on the assumption of an ORC turbine mass-specific power of 0.5 kW/kg, the ORC turbine is identified as the major contribution to ORC system mass (70%) followed by the con-

denser (20%). De Servi et al. [51] and Jacob et al. [52] investigated the integration of a supercritical CO_2 WHR system with turbofan engines for long-range aircraft. Both studies consider a recuperated cycle configuration with the heater located in the engine core exhaust duct and the cooler in the engine bypass duct. Suitable WHR system designs to provide a turbine power output of around 1000 kW were identified using parametric studies including HEX sizing. The turbofan engines considered by Jacob et al. [52] and De Servi et al. [51] have an exhaust gas temperature of 615 K and 780 K, respectively. The exhaust gas temperature value chosen by De Servi et al. [51] is considerably higher due to the lower technology level and therefore thermodynamic efficiency of the selected gas turbine engine. Downsizing of the engine due to the contribution of the WHR system was not considered. Despite the similar configurations (high bypass turbofan engine, air-cooled recuperated cycle architecture, CO_2 as the working fluid, same cooler and heater placement), the estimation of the component weights is largely different, therefore the results regarding fuel mass saving potential are opposing. Jacob et al. [52] report a fuel mass reduction of 1.9%, and De Servi et al. [51] report that the efficiency increase of the combined-cycle engine is insufficient to counter the added system weight. The high maximum operating pressure of supercritical CO_2 cycles allows for compact component design. However, the thick tubing required results in high heater mass, reducing the potential benefits of using CO_2 as the working fluid. The addition of an ORC WHR unit to the internal combustion engine of a parallel-hybrid electric drive train for a small general-aviation aircraft was analyzed by Hughes and Olsen [53]. The performance of a WHR unit based on a fuel-cooled subcritical non-recuperated ORC configuration is investigated for five different hydrofluroolefins as the working fluid. In contrast to the studies of Perullo et al. [49] and Zarati et al. [50], the prime mover is downsized so that the combined-cycle hybrid drive train fulfills the specified power requirement. The investigation is carried out for three different aircraft with a power requirement of the combined-cycle engine ranging from $100 - 300$ kW. Component sizing is not performed and the impact of added system weight is investigated using a parametric study. Only the on-design performance of the system is analyzed. For three investigated aircraft types, an ORC mass-specific power above 0.8 kW/kg leads to a fuel burn reduction of around 13%.

1.4. MOTIVATION AND RESEARCH QUESTIONS

The very little research on combined-cycle engines employing ORC bottoming units conducted so far indicates a varying degree of fuel-saving potential ranging from 1 to 13% if compared to simple-cycle engines. Possible reasons for the large spread of these values can be differences in the level of modeling fidelity and modeling assumptions. Furthermore, the benefit of employing an ORC bottoming unit may also depend on the considered application. So far, the impact of this novel propulsion system on aircraft performance was only partially considered, the aspect of airframe integration was only addressed qualitatively, and the impact of the ORC working fluid selection on combined-cycle performance was not investigated. Furthermore, among the non-conventional cycle architectures, the following advantages are identified for combined-cycle engines employing an ORC bottoming unit:

- Increased flexibility, as the recovered power can be used in different ways, such as to boost the gas turbine engine or to drive an electrical generator.
- Increased operational safety, as failure of the ORC system does not lead to failure of the entire engine.
- Increased design freedom, compared to recuperated configurations, because component design and performance can be optimized using the organic working fluid as an additional design variable.
- Possibility to retrofit existing engines by providing bolt-on solutions. However, this option entails two disadvantages compared to an aircraft designed to operate with optimized combined-cycle engines. First, integration with an existing airframe or nacelle imposes additional space constraints on the design of the WHR unit. Second, the thermodynamic cycles of the gas turbine engine and the ORC cannot be optimally matched, resulting in lower combined-cycle efficiency. Therefore, the performance of a retrofitted combined-cycle engine is bound to be lower than that of an optimized system and may not lead to the desired fuel savings.
- Wider range of applicability, for example for thermal management purposes of other onboard systems.

These reasons motivate the research on ORC bottoming units for aircraft gas turbine engines documented in this dissertation. To better understand the benefits that can be derived from employing such systems onboard aircraft, a numerical framework capable of performing thermodynamic analysis of combined-cycle engines and that considers the impact on aircraft design and mission performance needs to be developed. The highly multidisciplinary nature of this problem requires a physics-based modeling approach in combination with numerical optimization algorithms. Methods for HEX and ORC turbomachinery preliminary design are integrated into the design framework to reduce the uncertainty regarding ORC system mass and component performance. This simulation framework is used to answer the following research questions.

The main research question is:

What is the effect on mission fuel consumption of adopting an ORC bottoming unit to aircraft gas turbine engines?

This main question is accompanied by the following sub-research questions:

1. For which combinations of aircraft configurations and missions can the adoption of an ORC bottoming unit for aircraft gas turbine engines be beneficial?
2. What is the impact of an ORC bottoming unit on the optimum design of an aircraft gas turbine engine?
3. What is the optimal configuration for integrating the heat exchangers of the ORC WHR system into aircraft gas turbine engines?
4. What is the impact of an ORC bottoming unit for aircraft gas turbine engines on aircraft design and performance?

5. What is the impact on the combined-cycle power output of selecting mixtures of organic compounds as the working fluid of air-cooled ORC bottoming units for gas turbine engines in the 50 MW power range?

6. What are the design guidelines for airborne ORC bottoming units, given the vastly different environmental conditions, constraints related to mass and volume, and the impact on aircraft aerodynamics, when compared to stationary power plants?

1.5. THESIS OUTLINE

This dissertation is partially based on work presented at conferences and published in peer-reviewed journals. It is organized into 8 Chapters whose content is summarized as follows.

Chapter 2 presents a simplified method to assess the efficiency of a combined-cycle engine adopting an ORC bottoming unit and its impact on mission fuel consumption. The results of using this method to assess the feasibility of three application cases are presented.

Chapter 3 presents a thermodynamic analysis of a stationary combined-cycle power plant consisting of a 35 MW gas turbine engine and an ORC bottoming unit using different organic working fluids and mixtures thereof. Two different ORC architectures are investigated that utilize air as the heat sink. An optimization study is conducted to identify the thermodynamic cycle and working fluid that maximizes combined-cycle power output.

Chapter 4 presents the combined-cycle auxiliary power unit (CC-APU) concept consisting of a turboshaft engine and an ORC bottoming unit. It is analyzed whether the operation of the CC-APU instead of a conventional APU for providing ground power can result in mission fuel savings for a medium-range aircraft. For this purpose, a simulation framework named the ARENA framework was developed. ARENA allows to perform on-design thermodynamic analysis of the gas turbine and the ORC, sizing of the heat exchangers and the ORC turbogenerator, and a simplified mission analysis. The acronym ARENA stands for airborne thermal energy harvesting for aircraft. A non-recuperated fan-air-cooled ORC unit using cyclopentane as the working fluid is considered. The ORC unit and the gas turbine are integrated into the tail of the aircraft and volume limitations are considered as sizing constraints of the heat exchangers. An optimization study is performed to identify the CC-APU design that minimizes mission fuel consumption.

Chapter 5 presents the combined-cycle turboshaft engine (CC-TS) concept consisting of a turboshaft engine and an ORC bottoming unit. The impact on mission fuel consumption of employing CC-TS engines instead of simple-cycle turboshaft engines onboard a medium-range turboelectric aircraft is analyzed. A non-recuperated ram-air cooled ORC unit using cyclopentane as the working fluid is considered. The ORC unit and the ram-air ducts that house the condensers are integrated with the turboshaft engine in nacelles. The volume limitations inside the nacelle serve as sizing constraints for the heat exchangers. For this purpose, the ARENA framework was extended with a ram-air duct model, a model to consider the impact on aircraft design and performance, and a more detailed mission analysis model. The results regarding an optimized CC-TS engine design for minimum mission fuel consumption are presented.

Chapter 6 presents the combined-cycle turbofan engine (CC-TF) concept consisting of a turbofan engine and an ORC bottoming unit. It is investigated whether mission fuel consumption of a medium-range partial-turboelectric aircraft can be reduced if the simple-cycle turbofan engines are replaced with CC-TF engines. A non-recuperated air-cooled ORC unit using cyclopentane as the working fluid is considered. The condensers are placed in the bypass duct of the turbofan engine. The ARENA framework was further extended with a module for nacelle sizing, off-design simulation of the turbofan engine, and on/off-design simulation of the electrically driven ducted-fans. The CC-TF design and the thrust ratio between the CC-TF and the distributed electric propulsion system that results in minimized fuel consumption are identified.

Chapter 7 presents the methodology of a newly developed program for the weight estimation of aeronautical gas turbine engines (WEST). WEST sizes the main engine components using a mix of physics-based models and empirical correlations and considering mechanical design constraints. The tool provides the preliminary design of axial and radial compressors and axial turbines. Thermodynamic cycle data and various geometrical and performance parameters are required as input. WEST provides engine dimensions and component mass estimates as the output.

Chapter 8 outlines the main conclusions resulting from the performed research by answering the stated research questions. Furthermore, recommendations for further development of the ARENA framework and topics for future research activities are provided.

1

BIBLIOGRAPHY

[1] *Annex 16 - Environmental Protection, Volume II: Aircraft Engine Emissions.* International Civil Aviation Organization, 2017.

[2] *Annex 16 - Environmental Protection, Volume III: CO_2 Certification Requirement.* International Civil Aviation Organization, 2017.

[3] D. Lee, D. Fahey, A. Skowron, M. Allen, U. Burkhardt, Q. Chen, S. Doherty, S. Freeman, P. Forster, J. Fuglestvedt, A. Gettelman, R. De León, L. Lim, M. Lund, R. Millar, B. Owen, J. Penner, G. Pitari, M. Prather, R. Sausen, and L. Wilcox, "The contribution of global aviation to anthropogenic climate forcing for 2000 to 2018," *Atmospheric Environment*, vol. 244, p. 117834, 2021, doi: 10.1016/j.atmosenv.2020.117834.

[4] E. Torenbeek, *Synthesis of Subsonic Airplane Design.* Delft University Press, 1982, ISBN: 90-247-2724-3.

[5] B. L. Koff, "Gas turbine technology evolution: A designers perspective," *Journal of Propulsion and Power*, vol. 20, no. 4, pp. 577–595, 2004, doi: 10.2514/1.4361.

[6] E. Torenbeek, "The initial calculation of range and mission fuel during conceptual design," Delft University of Technology, Faculty of Aerospace Engineering, Tech. Rep., 1987, report LR-525.

[7] Jane's Information Group, "Jane's aero-engines," 2022. [Online]. Available: https://shop.janes.com/products/air-space/janes-aero-engines

[8] S. M. Jones, W. J. Haller, and M. T.-H. Tong, "An N+3 technology level reference propulsion system," NASA Glenn Research Centre, Tech. Rep., 2017, NASA-TM-2017-219501.

[9] A. Guha, "Optimisation of aero gas turbine engines," *The Aeronautical Journal*, vol. 105, no. 1049, 2001, doi: 10.1017/s0001924000012264.

[10] M. Hepperle, "Electric flight-potential and limitations," NATO, Tech. Rep., 2012, sTO-MP-AVT-209.

[11] S. Sahoo, X. Zhao, and K. Kyprianidis, "A review of concepts, benefits, and challenges for future electrical propulsion-based aircraft," *Aerospace*, vol. 7, no. 4, 2020, doi: 10.3390/aerospace7040044.

[12] B. J. Brelje and J. R. Martins, "Electric, hybrid, and turboelectric fixed-wing aircraft: A review of concepts, models, and design approaches," *Progress in Aerospace Sciences*, vol. 104, pp. 1–19, 2019, doi: j.paerosci.2018.06.004.

[13] M. D. Moore, "Misconceptions of electric aircraft and their emerging aviation markets," in *AIAA SciTech Forum*, 2014, doi: 10.2514/6.2014-0535.

[14] J. Felder, H. Kim, and G. Brown, "Turboelectric distributed propulsion engine cycle analysis for hybrid-wing-body aircraft," in *47th AIAA Aerospace Sciences Meeting including The New Horizons Forum and Aerospace Exposition*, 2009, doi: 10.2514/6.2009-1132.

[15] J. L. Felder, G. V. Brown, H. DaeKim, and J. Chu, "Turboelectric distributed propulsion in a hybrid wing body aircraft," in *20th ISABE Conference*, 2011.

[16] B. T. Schiltgen and J. Freeman, "Aeropropulsive interaction and thermal system integration within the ECO-150: A turboelectric distributed propulsion airliner with conventional electric machines," in *16th AIAA Aviation Technology, Integration, and Operations Conference*, 2016, doi: 10.2514/6.2016-4064.

[17] A. M. Stoll, J. Bevirt, M. D. Moore, W. J. Fredericks, and N. K. Borer, "Drag reduction through distributed electric propulsion," in *AIAA Aviation Forum*, 2014, doi: 10.2514/6.2014-2851.

[18] R. de Vries and R. Vos, "Aerodynamic performance benefits of over-the-wing distributed propulsion for hybrid-electric transport aircraft," in *AIAA SciTech Forum*, 2022, doi: 10.2514/6.2022-0128.

[19] B. Schiltgen, A. Gibson, M. Green, and J. Freeman, "More electric aircraft: "tube and wing" hybrid electric distributed propulsion with superconducting and conventional electric machines," in *SAE AeroTech Congress*, 2013, doi: 10.4271/2013-01-2306.

[20] R. de Vries, M. Brown, and R. Vos, "Preliminary sizing method for hybrid-electric distributed-propulsion aircraft," *Journal of Aircraft*, vol. 56, no. 6, pp. 2172–2188, 2019, doi: 10.2514/1.C035388.

[21] S. Weston, "Small spacecraft technology state-of-the-art report," NASA Ames Research Center, Tech. Rep., 2024, NASA/TP-2024-0001462.

[22] P. G. Bruce, S. A. Freunberger, L. J. Hardwick, and J. Tarascon, "Li–O2 and Li–S batteries with high energy storage," *Nature materials*, vol. 11, no. 1, pp. 19–29, 2012, doi: 10.1038/nmat3191.

[23] R. E. Wolleswinkel, R. de Vries, M. Hoogreef, and R. Vos, "A new perspective on battery-electric aviation, part I: Reassessment of achievable range," in *AIAA SciTech Forum*, 2024, doi: 10.2514/6.2024-1489.

[24] R. de Vries, R. E. Wolleswinkel, M. Hoogreef, and R. Vos, "A new perspective on battery-electric aviation, part II: Conceptual design of a 90-seater," in *AIAA SciTech Forum*, 2024, doi: 10.2514/6.2024-1490.

[25] M. Bennett, J. W. Chapman, and D. P. Wells, "An approach to evaluating the impact of small-core turbofan technologies on engine and aircraft performance," in *AIAA SciTech Forum*, 2024, doi: 10.2514/6.2024-1372.

[26] F. S. Mastropierro, J. Sebastiampillai, F. Jacob, and A. Rolt, "Modeling geared turbofan and open rotor engine performance for year-2050 long-range and short-range aircraft," *Journal of Engineering for Gas Turbines and Power*, vol. 142, no. 4, p. 041016, 02 2020, doi: 10.1115/1.4045077.

[27] S. Samuelsson, T. Gronstedt, and K. G. Kyprianidis, "Consistent conceptual design and performance modeling of aero engines," in *Proceedings of the ASME Turbo Expo*, 2015, doi: 10.1115/GT2015-43331.

[28] R. D. Hager and D. Vrabel, *Advanced turboprop project*. NASA Lewis Research Center, 1988.

[29] C. Reid, "Overview of flight testing of GE aircraft engines' UDF engine," in *24th AIAA/ASME/SAE/ASEE Joint Propulsion Conference*, 1988.

[30] D. Chapman, J. Godston, and D. Smith, "Testing of the 578–DX propfan propulsion system," in *24th AIAA/ASME/SAE/ASEE Joint Propulsion Conference*, 1989.

[31] E. Hendricks and M. Tong, "Performance and weight estimates for an advanced open rotor engine," in *48th AIAA/ASME/SAE/ASEE Joint Propulsion Conference*, 2012, doi: 10.2514/6.2012-3911.

[32] L. Larsson, T. Grönstedt, and K. G. Kyprianidis, "Conceptual design and mission analysis for a geared turbofan and an open rotor configuration," in *Proceedings of the ASME Turbo Expo*, 2011, doi: 10.1115/GT2011-46451.

[33] M. Sielemann, C. Coïc, X. Zhao, D. Eirini Diamantidou, and K. Kyprianidis, "Multi-point design of parallel hybrid aero engines," in *AIAA/IEEE Electric Aircraft Technologies Symposium (EATS)*, 2020, doi: 10.2514/6.2020-3556.

[34] X. Zhao, S. Sahoo, K. Kyprianidis, J. Rantzer, and M. Sielemann, "Off-design performance analysis of hybridised aircraft gas turbine," *The Aeronautical Journal*, vol. 123, no. 1270, pp. 1999–2018, 2019, doi: 10.1017/aer.2019.75.

[35] J. W. Chapman, "A study of large scale power extraction and insertion on turbofan performance and stability," in *AIAA/IEEE Electric Aircraft Technologies Symposium (EATS)*, 2020, doi: 10.2514/6.2020-3547.

[36] C. McDonald, A. Massardo, C. Rodgers, and A. Stone, "Recuperated gas turbine aeroengines, part i: Early development activities," *Aircraft Engineering and Aerospace Technology*, vol. 80, pp. 139–157, 03 2008, doi: 10.1108/00022660810859364.

[37] E. J. Privoznik, "Allison T63 regenerative engine program," in *24th Annual National Forum of the American Helicopter Society*, 1968.

[38] A. C. Stroh, "Potenzial zukünftiger hubschrauber-triebwerke der 300 kW-leistungsklasse durch einsatz optimierter rekuperativer systeme," Ph.D. dissertation, Technische Universität München, 2015.

[39] C. Zhang and V. Gümmer, "High temperature heat exchangers for recuperated rotorcraft powerplants," *Applied Thermal Engineering*, vol. 154, pp. 548–561, 2019, doi: 10.1016/j.applthermaleng.2019.03.119.

[40] ——, "Multi-objective optimization and system evaluation of recuperated helicopter turboshaft engines," *Energy*, vol. 191, p. 116477, 2020, doi: 10.1016/j.energy.2019.116477.

[41] H. Schoenenborn, E. Ebert, B. Simon, and P. Storm, "Thermomechanical design of a heat exchanger for a recuperative aeroengine," *Journal of Engineering for Gas Turbines and Power*, vol. 128, no. 4, pp. 736–744, 09 2006, doi: 10.1115/1.1850510.

[42] A. C. Patrao, I. Jonsson, C. Xisto, A. Lundbladh, and T. Grönstedt, "Compact heat exchangers for hydrogen-fueled aero engine intercooling and recuperation," *Applied Thermal Engineering*, vol. 243, p. 122538, 2024, doi: 10.1016/j.applthermaleng.2024.122538.

[43] S. Boggia and K. Rüd, "Intercooled recuperated gas turbine engine concept," in *41st AIAA/ASME/SAE/ASEE Joint Propulsion Conference*, 7 2005, doi: 10.2514/6.2005-4192.

[44] K. G. Kyprianidis, T. Grönstedt, S. O. T. Ogaji, P. Pilidis, and R. Singh, "Assessment of future aero-engine designs with intercooled and intercooled recuperated cores," *Journal of Engineering for Gas Turbines and Power*, vol. 133, no. 1, p. 011701, 09 2010, doi: 10.1115/1.4001982.

[45] O. Schmitz, H. Klingels, and P. Kufner, "Aero engine concepts beyond 2030: Part 1—the steam injecting and recovering aero engine," *Journal of Engineering for Gas Turbines and Power*, vol. 143, no. 2, p. 021001, 01 2021, doi: 10.1115/1.4048985.

[46] S. Kaiser, O. Schmitz, P. Ziegler, and H. Klingels, "The water-enhanced turbofan as enabler for climate-neutral aviation," *Applied Sciences*, vol. 12, no. 23, 2022, doi: 10.3390/app122312431.

[47] A. Görtz, J. Häßy, M. Schmelcher, and M. El-Soueidan, "Water enhanced turbofan: Improved thermodynamic cycle using hydrogen as fuel," in *Proceedings of the ASME Turbo Expo*, 2023, doi: 10.1115/GT2023-100807.

[48] P. Colonna, M. Astolfi, J. van Buijtenen, C. Wieland, G. David, F. Garofalo, M. Baresi, H. Öhman, and W. Klink, "Thermal energy harvesting: The path to tapping into a large CO_2-free european power source," Knowledge Center on Organic Rankine Cycle technology, techreport, 2021, accessed, 23 August 2024. [Online]. Available: https://kcorc.org/wp-content/uploads/2022/06/Thermal_Energy_Harvesting_-_the_Path_to_Tapping_into_a_Large_CO2-free_European_Power_Source.pdf

[49] C. A. Perullo, D. N. Mavris, and E. Fonseca, "An integrated assessment of an organic Rankine cycle concept for use in onboard aircraft power generation," in *Proceedings of the ASME Turbo Expo*, 2013, doi: 10.1115/GT2013-95734.

[50] K. Zarati, S. Maalouf, and A. T. Isikveren, "Potential of the bottom organic Rankine cycle to recover energy on turboprop engine architecture," in *23rd ISABE Conference*, 2017.

[51] C. M. De Servi, L. Azzini, M. Pini, A. G. Rao, and P. Colonna, "Exploratory assessment of a combined-cycle engine concept for aircraft propulsion," in *1st Global Power and Propulsion Forum*, 1 2017.

[52] F. Jacob, A. M. Rolt, J. M. Sebastiampillai, V. Sethi, M. Belmonte, and P. Cobas, "Performance of a supercritical CO2 bottoming cycle for aero applications," *Applied Sciences*, vol. 7, p. 255, 3 2017, doi: 10.3390/APP7030255.

[53] M. Hughes and J. Olsen, "Fuel burn reduction of hybrid aircraft employing an exhaust heat harvesting system," *Journal of Propulsion and Power*, vol. 38, pp. 241–253, 9 2022, doi: 10.2514/1.B38393.

2

First-Order Analysis

ABSTRACT

A first-order analysis is performed to identify aircraft applications that could benefit from integrating an ORC bottoming unit with gas turbine engines. First, a simplified method to estimate combined-cycle efficiency is presented. Second, this method is applied to three application cases. The results indicate fuel savings when integrating an ORC bottoming unit with an aircraft auxiliary power unit for providing ground power and to the turboshaft engines of a turboelectric aircraft. Based on these results, detailed analysis is carried out in the following chapters.

2.1. Introduction

The impact of integrating an ORC WHR system with aircraft engines on mission fuel consumption depends on the combined-cycle configuration and the mission scenario. To identify cases that may profit from this new technology a simplified method is developed that enables the estimation of the combined-cycle efficiency, and the impact on mission fuel consumption. The following application cases are analyzed using this method:

1. A combined-cycle power unit (CC-PU) adopting an ORC WHR system providing secondary power during cruise for a more-electric long-range aircraft.

2. A combined-cycle auxiliary power unit (CC-APU) adopting an ORC WHR system providing power for ground operations only of a medium-range aircraft.

3. A combined-cycle turboshaft (CC-TS) engine adopting an ORC WHR system replacing the turboshaft engines of a medium-range turboelectric aircraft.

2.2. Methodology

The methodology consists of two parts. The first part estimates the performance and mass of combined-cycle engines. The second part estimates mission fuel consumption

accounting for changes in fuel efficiency and aircraft mass. These methods are described in the following.

2.2.1. Estimation of Combined-cycle Performance

In the following a method to estimate η_{cc}, the ORC unit power contribution, and the ORC unit mass (m_{orc}) is presented. For this purpose, the impact of the evaporator pressure drop on gas turbine efficiency is neglected. Furthermore, mechanical losses are not accounted for, i.e., thermal efficiencies equal net efficiencies. Therefore, the results obtained with this method may overpredict real system performance.

The following definitions for η_{cc}, the gas turbine efficiency (η_{gt}), the ORC efficiency (η_{orc}), and the recovery factor of the ORC evaporator (χ) are applied. η_{cc} is defines as

$$\eta_{cc} = \frac{\dot{W}_{cc}}{\dot{m}_{fuel}\mathrm{LHV}}, \tag{2.1}$$

where $\dot{W}_{cc}$ is the combined shaft power output of the gas turbine engine and the ORC turbine, $\dot{m}_{fuel}$ the fuel mass flow rate, and LHV the lower heating value of the fuel. η_{gt} is defined as

$$\eta_{gt} = \frac{\dot{W}_{gt}}{\dot{m}_{fuel}\mathrm{LHV}}, \tag{2.2}$$

where $\dot{W}_{gt}$ is the shaft power produced by the gas turbine engine. η_{orc} is defined as

$$\eta_{orc} = \frac{\dot{W}_{orc}}{\dot{Q}_{evap}}, \tag{2.3}$$

where $\dot{W}_{orc}$ is the shaft power provided by the ORC turbogenerator and $\dot{Q}_{evap}$ is the heat extracted from the exhaust gases via the evaporator. χ is defined as

$$\chi = \frac{\dot{Q}_{evap}}{\dot{Q}_{waste}}, \tag{2.4}$$

where $\dot{Q}_{waste}$ is the waste heat available at the exit of the gas turbine. Using these definitions, η_{cc} can be expressed as

$$\eta_{cc} = \eta_{gt} + \eta_{orc}\chi(1-\eta_{gt}). \tag{2.5}$$

The fraction of $\dot{W}_{orc}$ over $\dot{W}_{cc}$ is calculated as

$$\frac{\dot{W}_{orc}}{\dot{W}_{cc}} = 1 - \frac{\eta_{gt}}{\eta_{cc}}. \tag{2.6}$$

m_{orc} is determined by dividing $\dot{W}_{orc}$ with the mass-specific power of the ORC system (e_{orc}). For this purpose, a suitable estimate of e_{orc} is required.

The presented method straightforwardly applies to turboshaft engines. An extension to turbofan engines is possible, considering that $\dot{W}_{cc}$ drives the fan. The net thrust produced by the fan bypass stream ($F_{net,fan}$) is determined using the following definition of the fan propulsive efficiency ($\eta_{prop,fan}$)

$$\eta_{prop} = \frac{F_{net,fan}V_{\infty}}{\dot{W}_{cc}\frac{BPR}{BPR+1}}, \tag{2.7}$$

where V_∞ is the free stream velocity and BPR is the engine bypass ratio. For high bypass ratio engines, where the core stream produces only little thrust the simplification that engine net thrust equals $F_{\text{net,fan}}$ can be applied.

2.2.2. ESTIMATION OF MISSION FUEL CONSUMPTION

The mission fuel consumption is calculated using the Breguet range equation to estimate cruise fuel consumption and using fuel fractions for the non-fuel-intensive flight phases (take-off, climb, descend and landing). The fuel consumption during cruise is the difference between the aircraft mass at the start of cruise ($m_{\text{cr,start}}$) and the mass at the end of cruise ($m_{\text{cr,end}}$). The value of $m_{\text{cr,end}}$ is determined by dividing the zero-fuel mass (m_{zf}) with the fuel fraction for the descend and landing phase ($ff_{\text{cr-ldg}}$). According to data reported by Roskam [1] $ff_{\text{cr-ldg}}$ is set to 0.98. m_{zf} is the sum of the operating empty mass (m_{oe}) and the payload mass (m_{pl}). The value of $m_{\text{cr,start}}$ is determined by rearranging the Breguet range equation that is defined as

$$R_{\text{cr}} = \frac{V_{\text{cr}}}{g \cdot \text{TSFC}_{\text{cr}}} \frac{L}{D}_{\text{cr}} \log \frac{m_{\text{cr,start}}}{m_{\text{cr,end}}}, \tag{2.8}$$

where R_{cr} is the cruise range V_{cr} is the cruise speed, g is the gravitational acceleration, TSFC_{cr} is the cruise thrust-specific fuel consumption, $\frac{L}{D}_{\text{cr}}$ the lift-to-drag ratio during cruise. Subsequently, the maximum take-off mass (m_{mto}) is calculated by dividing $m_{\text{cr,start}}$ with the fuel fraction for the take-off and climb phase ($ff_{\text{to-cr}}$). According to data reported by Roskam [1] $ff_{\text{to-cr}}$ is set to 0.98.

Adding a WHR unit affects the value of TSFC_{cr}, m_{oe}, and $\frac{L}{D}_{\text{cr}}$. TSFC_{cr} is defined as the cruise thrust divided by the fuel mass flow rate. The latter is affected by changes to the engine efficiency. The change in m_{oe} is accounted for by adding m_{orc}. Non-linear effects on m_{oe} that may arise from the need for a larger wing and landing gear are not addressed by this simple method. Similarly, the impact on aircraft aerodynamics of adding the ORC unit is neglected.

2.3. RESULTS

The method to estimate combined-cycle performance presented in Section 2.2.1 is first applied to perform a parametric analysis that shows the effect on η_{cc} of varying η_{orc}, η_{gt}, and χ. Second, the methods presented in Sections 2.2.1 and 2.2.2 are applied to the three case studies introduced in Section 2.1. For these cases, a value of $\eta_{\text{orc}} = 20\%$, which is similar to the value resulting from the ORC system design of Zarati et al. [2], and a range of χ from 0.2 to 0.6 is assumed.

2.3.1. PARAMETRIC ANALYSIS

Figure 2.1 gives results of a parametric study obtained using Eq. 2.5 for different levels of χ. The contour plots shown in this figure can serve to estimate the value of η_{cc} based on assumed values of the input parameters η_{gt}, η_{orc}, and χ, or to estimate required values of the input parameters to achieve a desired level of η_{cc}. These graphs show, that gas turbines with low efficiency benefit more from adding an ORC WHR unit and that higher heat recovery results in higher combined-cycle efficiency. However, higher recovery requires a larger evaporator. The evaporator is integrated into the exhaust duct of

the gas turbine and its size may be constrained. Furthermore, a larger evaporator imposes more pressure drop which increases the backpressure of the turbine. This results in a larger engine and more fuel consumption for a given power or thrust requirement. The value of η_{orc} is a function of the recovered and rejected heat. Similar, to the effect of heat recovery on gas turbine efficiency, heat rejection via the condenser can affect aircraft performance via the pressure drop imposed on the cooling air in case of a ram-air cooled configuration. Therefore, an optimal value of η_{orc} results from a multidisciplinary analysis.

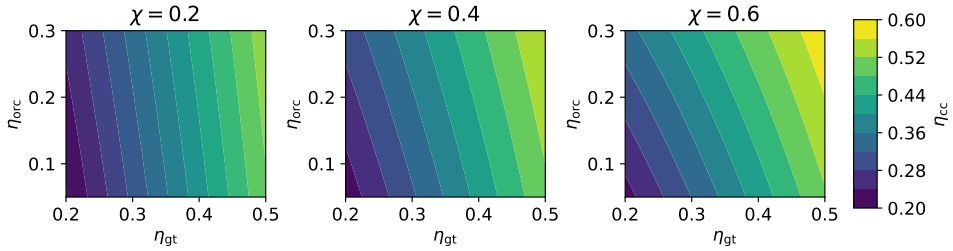

Figure 2.1: Countour plots showing combined-cycle efficiency (η_{cc}) as a function of ORC thermal efficiency (η_{orc}), gas turbine thermal efficiency (η_{gt}) and ORC recovery factor (χ).

2.3.2. Case 1: CC-PU for Power During Cruise

Case 1 considers a combined-cycle power unit (CC-PU) consisting of a turboshaft engine and an ORC bottoming unit with a combined output power of 1 MW. This is approximately the shaft power required during cruise to produce the electrical power for onboard systems of the Boeing 787 [3]. In the case of the 787, this power is provided by engine-mounted generators. The question is whether a CC-PU can provide this power more efficiently than the turbofan engines.

First, the fuel consumption of turbofan engines related to the provision of shaft power ($\dot{m}_{fuel,offtake}$) is estimated. According to Scholz et al. [4] $\dot{m}_{fuel,offtake}$ can be estimated as

$$\dot{m}_{fuel,offtake} = k \times TSFC_{cr} \times \dot{W}, \tag{2.9}$$

where k is the shaft power factor, $TSFC_{cr}$ is the cruise thrust-specific fuel consumption, and $\dot{W}$ is the shaft power. According to Scholz et al. [4] the value of k can be taken as 0.002 N/W and the Rolls Royce Trent 1000 engine used on the Boeing 787 has a $TSFC_{cr}$ of 14.3 mg/Ns [5]. Based on these values and assuming $\dot{W}$ = 1 MW, $\dot{m}_{fuel,offtake}$ amounts to 0.029 kg/s.

Secondly, the fuel consumption of the CC-PU is estimated. A thermal efficiency of the CC-PU's gas turbine of 30% is assumed based on advanced turboshaft engine concepts with a power capacity of around 1 MW studied by Snyder and Tong [6]. Table 2.1 gives the resulting values of η_{cc} determined using Eq. 2.5 and $\dot{m}_{fuel}$ for the provision of $\dot{W}_{cc}$ = 1 MW. These results show that even under the most optimistic assumption of χ = 0.6 the CC-PU fuel consumption is still twice the value of the turbofan engine for the

provision of power off-takes. Therefore, this concept is considered infeasible for providing shaft power during cruise. However, the operation of a CC-PU in operating points other than cruise could entail advantages. For example, the turbofan engines could be relieved from providing secondary power during descent, when they are typically operated close to the idle operating point.

Table 2.1: CC-PU combined-cycle efficiency (η_{cc}) and ORC power fraction $\dot{W}_{orc}/\dot{W}_{cc}$ for different values of ORC heat recovery factor (χ), and values of the resulting fuel mass flow rate ($\dot{m}_{fuel}$) for the provision of 1 MW of shaft power ($\dot{W}_{cc}$). The results are based on η_{orc} = 20% and η_{gt} = 30%.

χ (-)	0.2	0.4	0.6	Ref. Turbofan
η_{cc} (-)	33%	36%	38%	
η_{cc} (-)	32.8%	35.6%	38.4%	$\dot{m}_{fuel,offtake}$ =
$\dot{W}_{orc}/\dot{W}_{cc}$ (-)	9%	16%	22%	0.029 kg/s
$\dot{m}_{fuel}$ (kg/s)	0.071	0.065	0.061	

2.3.3. CASE 2: CC-APU FOR POWER ON GROUND

Case 2 considers a combined-cycle auxiliary power unit (CC-APU) to provide the secondary power required during ground operations of a medium-range aircraft. This analysis assumes an aircraft similar to an Airbus A320neo that according to data of Ref. [7] has an approximate secondary power requirement of 250 kW. This power is provided by the APU that has an efficiency of around 18% [7] which results in a fuel consumption of 0.032 kg/s. The CC-APU's gas turbine efficiency is assumed to be equal to the baseline APU. The question is whether mission fuel consumption can be reduced by employing a CC-APU instead of a simple-cycle APU for providing ground power.

The mission fuel consumption is the sum of the flight phase fuel consumption estimated using the method presented in Section 2.2.2, and the ground phase fuel consumption. The Airbus A320neo has an m_{oe} of 43 520 kg, a $\frac{L}{D}_{cr}$ of 17.9, estimated using a method proposed by Torenbeek [8], and a $TSFC_{cr}$ of 14.4 mg/Ns. $TSFC_{cr}$ is calculated for the CFM LEAP-1A engine based on information reported by the Jane's Information Group [5]. The mission is over a range of 900 NM at a cruise Mach number of 0.78, and a m_{pl} of 19 280 kg. The ground phase fuel consumption is determined by multiplying the fuel mass flow rate of the APU or CC-APU with the total ground operating time. This time is determined to be approximately 41 min according to data of Refs. [9, 10, 11, 12].

Figure 2.2 shows the required improvement of η_{cc} over the baseline APU efficiency ($\Delta\eta_{cc}$) to compensate for the extra fuel consumption incurred by an increase in operating empty mass (Δm_{oe}). In the considered range of Δm_{oe} an almost linear improvement of $\Delta\eta_{cc}$ is required. For an increase in m_{oe} of 100 kg the CC-APU efficiency needs to be approximately 3 absolute percent points higher than the baseline APU efficiency of 18%. Table 2.1 gives the values of η_{cc} determined using Eq. 2.5 and of $\dot{m}_{fuel}$ for the provision of $\dot{W}_{cc}$ = 250 kW. Additionally, this table presents the required minimum ORC mass-specific power ($e_{orc,min}$) to break even with the additional fuel consumption incurred by

the increased operating empty mass. This value is determined assuming that the mass of the CC-APU's gas turbine stays constant and equal to the mass of the baseline APU and that Δm_{oe} is entirely due to the added ORC components. The value of $e_{orc,min}$ stays constant at 0.35 kW/kg for different values of χ due to the almost linear nature of the curve presented in Fig. 2.2.

It is concluded, that the adoption of a CC-APU can reduce mission fuel consumption if the ORC WHR system has a e_{orc} that is larger than 0.35 kW/kg. For comparison, the ORC WHR system design identified by Zarati et al. [2] for a 2 MW turboprop engine has a e_{orc} of 0.33 kW/kg. Zarati et al. [2] assumed a mass-specific power of the ORC turbine of 0.5 kW/kg, and it amounts to approximately 70% of m_{orc}. Optimized ORC turbogenerator designs are likely to achieve higher values of mass-specific power. Therefore, a more detailed investigation of the CC-APU concept, including the design of the ORC turbogenerator, is advised.

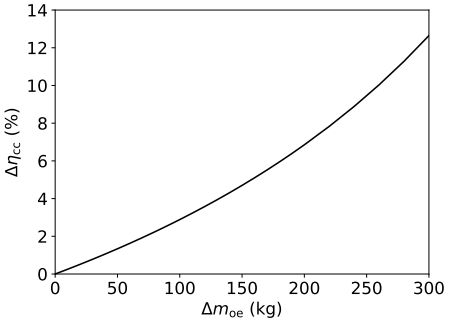

Figure 2.2: Required CC-APU efficiency improvement over baseline APU ($\Delta\eta_{cc}$) to break even with increased mission fuel consumption due to added operating empty mass (Δm_{oe})

Table 2.2: CC-APU combined-cycle efficiency (η_{cc}) and ORC power fraction $\dot{W}_{orc}/\dot{W}_{cc}$ for different values of ORC heat recovery factor (χ), and corresponding values of fuel mass flow rate ($\dot{m}_{fuel}$) for the provision of 250 kW of shaft power ($\dot{W}_{cc}$), and values of required minimum ORC mass-specific power ($e_{orc,min}$). The results are based on η_{orc} = 20% and η_{gt} = 18%.

χ (-)	0.2	0.4	0.6
η_{cc} (-)	21%	25%	28%
$\dot{W}_{orc}/\dot{W}_{cc}$ (-)	15%	27%	35%
$\dot{m}_{fuel}$ (kg/s)	0.027	0.024	0.021
$e_{orc,min}$ (kW/kg)	0.35	0.35	0.35

2.3.4. CASE 3: CC-TS FOR TURBOELECTRIC AIRCRAFT

Case 3 considers a combined-cycle turboshaft (CC-TS) engine replacing the turboshaft engines of a medium-range turboelectric aircraft. The ONERA Dragon turboelectric aircraft concept is selected as the reference aircraft from which masses and the lift-do-drag ratio are taken [13]. This aircraft utilizes two turboshaft engines providing electrical power to a distributed propulsion system of under-the-wing mounted electrically driven ducted-fans. The question is whether mission fuel consumption can be reduced by replacing the simple-cycle turboshaft engines with CC-TS engines.

Mission fuel consumption is estimated using the method presented in Section 2.2.2. The aircraft has a m_{oe} of 42 700 kg, a $\frac{L}{D}_{cr}$ of 17.2, and transports a payload of 13 600 kg at a cruise Mach number of 0.78 over a range of 2750 NM. Each turboshaft engine has a power capacity of 5.25 MW, and a η_{gt} of 61%. The CC-TS's gas turbine engine is assumed to have the same efficiency as the baseline turboshaft engines. $TSFC_{cr}$ is calculated with

the following relation

$$\mathrm{TSFC}_{\mathrm{cr}} = \frac{V_\infty}{\eta_{\mathrm{gt}}\eta_{\mathrm{pt}}\eta_{\mathrm{prop}}\mathrm{LHV}}, \tag{2.10}$$

where η_{pt} is the electrical powertrain efficiency and η_{prop} the propulsive efficiency of the ducted fans. η_{pt} is defined as the electric motor shaft power driving the ducted fan divided by the turboshaft or CC-TS shaft power output. η_{prop} is defined by the thrust power of the ducted-fan divided by the electric motor shaft power.The value of $\eta_{\mathrm{pt}} = 0.89$ is selected according to the technology assumptions of Ref. [13], and the value of η_{prop} is set to 86% [14].

Figure 2.3 shows the required improvement of η_{cc} over the baseline turboshaft efficiency ($\Delta\eta_{\mathrm{cc}}$) to compensate for the extra fuel consumption due to an increase in operating empty mass (Δm_{oe}). In the considered range of Δm_{oe} an almost linear improvement of $\Delta\eta_{\mathrm{cc}}$ is required. For an increase in m_{oe} of 1000 kg the CC-TS efficiency needs to be roughly one absolute percent point higher than the baseline turboshaft efficiency of 61%. Table 2.3 gives the values of η_{cc} determined using Eq. 2.5, and the values of $\dot{m}_{\mathrm{fuel}}$ for the provision of $\dot{W}_{\mathrm{cc}} = 5.25$ MW for values of χ ranging between 0.2 and 0.6. Furthermore, the table presents the required minimum ORC mass-specific power ($e_{\mathrm{orc,min}}$) to break even with the additional fuel consumption due to the increased operating empty mass. This value is determined assuming that the mass of the CC-TS's gas turbine stays constant and equal to the mass of the baseline turboshaft engine and that Δm_{oe} is entirely due to the added ORC components. The value of $e_{\mathrm{orc,min}}$ stays constant at 0.11 kW/kg for different values of χ due to the almost linear nature of the curve presented in Fig. 2.3. This value is lower than the value identified for the ORC WHR system for a 2 MW turboprop engine designed by Zarati et al. [2]. Therefore, this application is considered worth a more detailed investigation.

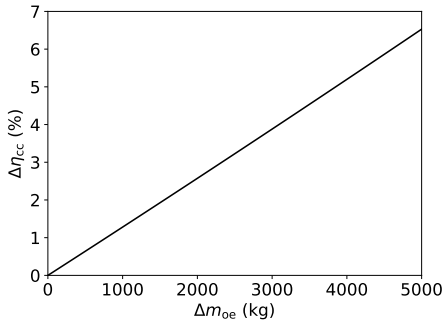

Figure 2.3: Required CC-TS efficiency improvement over baseline turboshaft engine ($\Delta\eta_{\mathrm{cc}}$) to break even with increased mission fuel consumption due to added operating empty mass (Δm_{oe})

Table 2.3: CC-TS combined-cycle efficiency (η_{cc}) and ORC power fraction $\dot{W}_{\mathrm{orc}}/\dot{W}_{\mathrm{cc}}$ for different values of ORC heat recovery factor (χ), and corresponding values of fuel mass flow rate ($\dot{m}_{\mathrm{fuel}}$) for the provision of 5.25 MW of shaft power ($\dot{W}_{\mathrm{cc}}$), and values of required minimum ORC mass-specific power ($e_{\mathrm{orc,min}}$). The results are based on $\eta_{\mathrm{orc}} = 20\%$ and $\eta_{\mathrm{gt}} = 61\%$.

χ (-)	0.2	0.4	0.6
η_{cc} (-)	63%	64%	66%
$\dot{W}_{\mathrm{orc}}/\dot{W}_{\mathrm{cc}}$ (-)	3%	5%	8%
$\dot{m}_{\mathrm{fuel}}$ (kg/s)	0.194	0.191	0.185
$e_{\mathrm{orc,min}}$ (kW/kg)	0.11	0.11	0.11

2.4. CONCLUSIONS

A "back-of-the-envelope"–style method for calculating the performance of a combined-cycle engine consisting of a gas turbine engine and an ORC bottoming unit is developed. This method is based on several simplifying assumptions regarding component efficiencies and the impact of the WHR system on gas turbine performance. Nevertheless, it can capture the sensitivity of combined-cycle efficiency to gas turbine efficiency, ORC efficiency, and the waste-heat recovery factor.

This method is applied to three cases with different combined-cycle configurations and mission scenarios. It is concluded, that using an ORC WHR system to improve the efficiency of propulsive power production during cruise can reduce mission fuel consumption. Based on the favorable results obtained for Cases 2 and 3, a detailed analysis will be conducted in the following chapters.

BIBLIOGRAPHY

[1] J. Roskam, *Airplane Design, Part 1: Preliminary Sizing of Airplanes*. DARcorporation, 1997.

[2] K. Zarati, S. Maalouf, and A. T. Isikveren, "Potential of the bottom organic Rankine cycle to recover energy on turboprop engine architecture," in *23rd ISABE Conference*, 2017.

[3] G. Whyatt and L. Chick, "Electrical generation for more-electric aircraft using solid oxide fuel cells," US Department of Energy, Tech. Rep., 2012.

[4] D. Scholz, R. Seresinhe, I. Staack, and C. P. Lawson, "Fuel consumption due to shaft power off-takes from the engine," in *Workshop on Aircraft System Technologies AST 2013*, 2013, doi: 10.15488/4462.

[5] Jane's Information Group, "Jane's aero-engines," 2022. [Online]. Available: https://shop.janes.com/products/air-space/janes-aero-engines

[6] C. Snyder and M. T. Tong, "Modeling turboshaft engines for the revolutionary vertical lift technology project," in *Proceedings of the Vertical Flight Society 75th Annual Forum*, 2019.

[7] L. M. Stohlgren and L. D. Werner, "The GTCP36-300, a gas turbine auxiliary power unit for advanced technology transport aircraft," *American Society of Mechanical Engineers*, 4 1986, doi: 10.1115/86-GT-285.

[8] E. Torenbeek, "The initial calculation of range and mission fuel during conceptual design," Delft University of Technology, Faculty of Aerospace Engineering, Tech. Rep., 1987, report LR-525.

[9] A. Padhra, "Emissions from Auxiliary Power Units and Ground Power Units during Intraday Aircraft Turnarounds at European Airports," *Transportation Research Part D: Transport and Environment*, vol. 63, pp. 433–444, 8 2018, doi: 10.1016/J.TRD.2018.06.015.

[10] Eurocontrol, "Taxi times - winter 2018-2019," 2019, accessed on 29 November 2022. [Online]. Available: https://www.eurocontrol.int/publication/taxi-times-winter-2018-2019

[11] ——, "Taxi times - summer 2019," 2019, accessed on 29 November 2022. [Online]. Available: https://www.eurocontrol.int/publication/taxi-times-summer-2019

[12] Eurostat, "Air passenger transport by main airports in each reporting country," 2022, accessed on 29 November 2022. [Online]. Available: https://ec.europa.eu/eurostat/databrowser/view/AVIA_PAOA__custom_3991485/default/table?lang=en

[13] P. Schmollgruber, D. Donjat, M. Ridel, I. Cafarelli, O. Atinault, C. François, and B. Paluch, "Multidisciplinary design and performance of the ONERA hybrid electric distributed propulsion concept (Dragon)," in *AIAA SciTech Forum*, 2020, doi: 10.2514/6.2020-0501.

[14] S. Defoort, E. Nguyen, and P. Schmollgruber, “Personal communication with onera,” 2023.

3

ORC WHR System for Stationary Gas Turbines

Parts of this chapter have been published in:

D. Krempus, S. Bahamonde, T. P. van der Stelt, W. Klink, P. Colonna, C. M. De Servi, "On mixtures as working fluids of air-cooled ORC bottoming power plants of gas turbines," *Applied Thermal Engineering*, Volume 236, Part D, 2024, 121730, doi: j.applthermaleng.2023.121730.

ABSTRACT

The use of mixtures as working fluids of organic Rankine cycle (ORC) waste heat recovery (WHR) power plants has been proposed in the past to improve the matching between the temperature profile of the hot and the cold streams of condensers and evaporators, thus to possibly increase the energy conversion efficiency of the system. The goal of this study is to assess the benefits in terms of efficiency, environmental (GWP), and operational safety (flammability) that can be obtained by selecting optimal binary mixtures as working fluids of air-cooled ORC bottoming power plants of medium-capacity industrial gas turbines. Furthermore, two thermodynamic cycle configurations are analyzed, namely the simple recuperated cycle and the so-called split-cycle configurations. The benchmark case is a combined-cycle power plant formed by an industrial gas turbine and an air-cooled recuperated ORC power unit with cyclopentane as the working fluid. The results of this study indicate that binary mixtures provide the designer with a wider choice of optimal working fluids, however, in the case of the recuperated-cycle configuration, no improvement in terms of combined-cycle efficiency over the benchmark case can be achieved. The split-cycle configuration leads to an increase of combined-cycle efficiency of the order of 1.5%, both in the case of pure and blended working fluids. Furthermore, for this cycle configuration, using Novec 649 as the working fluid is advantageous because it is environmentally and operationally safe, and it does not involve any penalty in terms of combined-cycle efficiency if compared to the benchmark case. Additionally, using this fluid would lead to a more compact turbine, as the corresponding thermodynamic cycle would determine a turbine volume flow ratio that is half of the value of the benchmark case and a specific enthalpy difference over the expansion that is one-fifth.

3.1. INTRODUCTION

In the European Union alone, the amount of wasted thermal energy that could be recovered for further use is estimated to be about 300 TWh/year [1, 2]. Bianchi et al. [1] report that 55% of this recoverable energy is due to heat sources with temperatures above 300 °C while the rest is available at lower temperatures. Papapetrou et al. [2] indicate similar values.

A more recent report documents in more detail the availability of industrial waste heat in EU countries per industrial sector, temperature level, and geographical location, further highlighting the large potential of this renewable-equivalent energy source [3].

High-temperature industrial heat sources provide a substantial potential for waste heat recovery (WHR) and for waste-heat-to-power (WH2P) in particular. WH2P from high-temperature thermal energy and for large power capacities is traditionally realized by means of steam-cycle power plants, but the number of large high-temperature heat sources is very limited. For lower power capacities the resulting steam mass flow rate would be too small and the specific enthalpy over the expansion too large for the realization of efficient steam turbines [4]. The use of an organic compound as a working fluid allows for realizing simple and efficient turbines and in general a simpler and more cost-effective power plant configuration. For example, the fluid can be chosen to keep the working fluid in the condenser at super-atmospheric pressure.

Recovering waste heat from stationary and mobile gas turbines, internal combustion, and, in the future, fuel cell engines with ORC systems provides an enormous opportunity for efficiency increase and emission reduction. The most prominent limitation of using organic compounds as working fluids of high-temperature ORC power plants is their relatively low thermal stability if compared, for instance, to that of water. The use of organic fluids featuring high thermal stability (some hydrocarbons, siloxanes, some phased-out refrigerants) is often restricted by regulations regarding operational safety (flammability) [5] and environmental sustainability (GWP, ODP) [6].
In this regard, the use of mixtures as working fluids may result in cycle configurations providing higher energy conversion efficiency [7] and, at the same time, compliance with regulatory requirements. Especially in the case of mobile applications and of power plants employing air-cooled condensers either because regulation forbids the use of water cooling or because they are located in remote and arid areas, the use of mixtures as working fluids may be advantageous. The efficiency of air-cooled ORC power plants might benefit from non-isothermal condensation because the power absorbed by fans, which may be rather large, can be reduced in comparison with the amount needed for the isothermal condensation of a pure working fluid. However, more heat transfer surface is usually required. In their work on mixtures as working fluids for air-cooled ORC WH2P systems for fuel cells, Angelino and Colonna [8, 9] showed that the improved temperature profile matching in the condenser due to the working fluid temperature glide over condensation leads to a substantial reduction of air-cooler fan power at the cost of larger heat transfer surface, and may contribute to an increase of the combined-cycle net power output. Moreover, the additional cost due to a larger condenser could be recovered in a very short time.

After the seminal works of Angelino and Colonna [8, 9], researchers have investigated the use of mixtures as working fluids for various ORC applications such as waste heat recovery and conversion of solar and geothermal energy, see the literature reviews presented by Braimakis et al. [10] and Abadi and Kim [11]. While for low-temperature ORC power plants, numerous studies indicate that the use of mixtures as working fluids allows for an increase of conversion efficiency, in the case of high-temperature systems, contrasting results have been reported in the literature. Most of these works focus on water-cooled ORC systems as bottoming units of internal combustion engines (ICE). For instance, Fang et al. [12] considered as working fluids of a simple ORC system zeotropic mixtures composed by combining two high critical temperature hydrocarbons, namely decane and toluene, and two low critical temperature refrigerants, i.e., R245fa and R123. They found that the power output of the ORC bottoming unit operating with mixtures is always lower than that estimated in case toluene is the working fluid. However, the adoption of a 0.9 toluene / 0.1 decane mixture may allow for a lower levelized cost of electricity for the plant thanks to a reduction in the size of the heat exchangers that is achieved at the cost of a marginal decrease in power output with respect to the ORC operating with pure toluene. Conversely, in the case of heat recuperation from large Diesel engines for power generation on offshore platforms, Kolahi et al. [13] estimated significant gains in the efficiency of the ORC unit if mixtures of hexane and cyclohexane with the refrigerants R236ea and R245fa are adopted as working fluid. The improvement with respect to the efficiency achieved with the same pure fluids is up to 20%, while the cor-

responding reduction in the specific investment costs and payback time of the ORC unit is lower than 10%. Scaccabarozzi et al. [14] optimized the conceptual design of an ORC bottoming unit considering two ICEs as topping units, featuring different exhaust gas temperatures, and two operating scenarios: in the first one, the output of the combined system consists only of electricity, while in the second one, the plant is operated in co-generation mode. The authors analyzed for each scenario more than twenty fluids and the binary mixtures resulting from their combination if these mixtures feature a temperature glide over condensation of at least 5 °C. Their results show that mixtures allow for an ORC power output increase of the order of about 3% in all the considered scenarios. The authors attributed the limited efficiency improvement to the supercritical configuration of the optimal cycles: the temperature glide is exploited only over condensation and, as a result, the thermodynamic benefit of adopting mixtures in place of pure fluids is reduced. As an alternative to a supercritical cycle configuration, researchers have explored the adoption of mixtures in two cascaded ORC loops, see, e.g, [15, 16]. These studies indicate that zeotropic mixtures allow for a higher ORC power output, though the extent of the increase varies significantly, from a few percentage points, as in Ref. [14], to up to 20%.

In the case of solar power conversion, supercritical CO_2 power plants are one of the most promising solutions, because of their high conversion efficiency and the expected compactness of the equipment. Researchers have investigated the blending of CO_2 with other organic compounds featuring high thermal stability to improve further plant efficiency as well as to mitigate some of the technical challenges that supercritical CO_2 technology entails, e.g., the high-pressure of the cycle [17, 18, 19]. Contrary to what was observed for waste heat recovery from ICE, the researchers calculated substantial efficiency gains. With respect to the supercritical CO_2 power cycle, the relative increase in efficiency ranges from 5% to 15% depending on the considered minimum and maximum cycle temperature.

Regarding high-temperature WH2P systems (thermal source temperature above 300 °C), only Ren et al. [20] assessed the use of mixtures as working fluid of an ORC bottoming unit. The authors studied a gas turbine and water-cooled organic Rankine cycle combined system and included among the assessed working fluids mixtures of siloxanes, alkanes, and aromatic hydrocarbons. Moreover, four commercial gas turbines with different exhaust temperatures ($280 - 500\,^{\circ}C$) and power capacity ($600\,kW - 53\,MW$) were considered as topping unit of the plant. Their results show that the mixtures may allow for marginal improvements of the ORC unit efficiency, except for small power capacity gas turbines, where they are outperformed by bottoming cycles using cyclopentane as the working fluid.

Note that only a limited amount of fluids were considered in the majority of the cited literature, thus preventing the generalization of those results: better performance may be achieved with pure compounds or mixtures that were not considered. To address this limitation, Papadopoulos et al. [21] were the first to propose a Computer-Aided Molecular Design (CAMD) framework for the synthesis of binary mixtures suitable as working fluids of ORC power plants. Their methodology integrates an ORC system model with a group contribution method and a cubic equation of state to calculate the thermodynamic properties of the mixtures. Thanks to the group contribution method, it is

possible to calculate with acceptable accuracy the thermodynamic properties of a fluid made by a generic molecule and then assess the corresponding performance through the ORC system model. This in turn enables the optimization of the molecular structure of the two working fluids based on the chosen objective functions. It follows that the ORC design is not limited by the chosen set of candidate fluids, provided that the group contribution method enables the modeling of a broad spectrum of fluids. In Ref. [21] the demonstrative academic case is a geothermal plant exploiting a brine at 95 °C. The objective functions are the maximization of the thermal and exergy efficiency as well as the minimization of the flammability characteristics of the two fluids. The resulting optimal working fluid is a blend of two fluorinated derivatives of propane. However, the authors did not compare the ORC power plant performance estimated in the case of the optimal mixture of working fluids with that of pure working fluids. This comparison is instead performed by Schilling et al. [22], who implemented a CAMD framework based on a group-contribution method applied to the physically-based perturbed-chain statistically associating fluid theory (PC-SAFT) equation of state, and capable of optimizing the thermo-economic performance of ORC processes operating with mixtures. The authors discovered that the potential of mixtures strongly depends on the temperature rise of the cooling water in the condenser and the temperature of the thermal source and that the optimal mixture varies considerably with the considered process specifications. With regard to the effect of the thermal source temperature, the results of Schilling et al. [22] show that using binary mixtures as working fluids is very advantageous for low-temperature heat sources in the range of $100 - 125$ °C. The relative efficiency increase can be higher than 50%, while the reduction in the specific costs of the plant is much lower and of the order of $2 - 3$%. For higher heat source temperatures, namely between $150 - 200$ °C, the results of calculations do not provide any clear trend about the effect of using binary mixtures as working fluids on thermodynamic cycle efficiency. The net power output achieved with the optimal mixture is always $5 - 10$% higher than the net power output obtained with the optimal pure component, confirming the potential of mixtures. At the same time, the economic benefit of adopting mixtures remains approximately independent from the thermal source inlet temperature.

It is therefore possible to conclude that the potential of mixtures as working fluids of ORC systems converting thermal sources at temperatures in excess of 300 °C has not been properly characterized yet. If, on the one hand, clear benefits have been demonstrated for supercritical CO_2 power cycles in solar applications, on the other, contradictory results are reported for other ORC systems, especially in the case of waste heat recovery from ICEs. The reason may be the limited number of working fluids and mixtures considered by the researchers. Moreover, the studies investigating WH2P applications involving gas turbines or fuel cells are too few to draw a general conclusion. Another important limitation is that the majority of the literature about the use of zeotropic mixtures focuses on water-cooled ORC power plants despite the earlier works of Angelino and Colonna [8, 9] already demonstrated that the main advantage offered by fluid blends is the lower air-cooler fan power consumption enabled by the temperature glide over condensation. Moreover, water cooling is most often impossible either because of the typical geographical location of these power plants or because of the current regulatory framework.

This work contributes to the filling of the knowledge gap regarding the use of working fluid mixtures in high-temperature air-cooled ORC power plants for WH2P applications. The impact of using mixtures on combined-cycle efficiency, especially considering its influence on fan power demand, the potential of selecting environmentally and operationally safe fluids, as well as the impact of the working fluid on turbine design were analyzed. A combined-cycle power plant formed by an industrial gas turbine and an air-cooled recuperated ORC power unit with cyclopentane as the working fluid, a power plant that is similar to a product offered on the market, was chosen as the benchmark. Two different cycle configurations were analyzed and a very wide range of pure fluids (26) and binary mixtures (325) as the working fluid were considered. Optimal cycle parameters and working fluid combinations are subsequently identified using an evolutionary optimization algorithm targeting the net power output as the optimization objective. Given that there is no experimental database that could have supported the modeling of such an extensive set of blends, with compositions optimized for the considered application, the estimation of their thermodynamic properties requires a predictive equation of state (EoS) model. The chosen thermodynamic model is the PCP-SAFT EoS [23], thanks to its capability to provide reasonably accurate values of mixture thermodynamic properties given a few pure component parameters.

3.2. METHODOLOGY

3.2.1. THERMODYNAMIC CYCLE CONFIGURATIONS

Two cycle configurations are considered in this study. With reference to Fig. 3.1, these are the recuperated cycle, and the novel *split-cycle* [24]. Both configurations assume the use of an air-cooled condenser (Cond). The main difference with respect to the common recuperated cycle is that, in the split-cycle, the flow is divided into two downstream of the pump. One stream passes through the recuperator (Rec) while the other one exchanges thermal energy with the heat source in the preheater (Pre). Both streams are merged before entering the heat recovery vapor generator (HRVG). The degree of mass flow that is split from the mainstream (m_{frac}) is defined as the fraction of mass flow rate through the recuperator cold side over that through the hot side.

The benchmark case is a combined-cycle power plant formed by a Siemens SGT-750 gas turbine and an ORC bottoming unit. This ORC system implements the recuperated-cycle configuration and uses cyclopentane as the working fluid. The gas turbine has a net power output ($\dot{W}_{\text{net,gt}}$) of 34.6 MW and a thermal efficiency ($\eta_{\text{net,gt}}$) of 38.5% at an ambient temperature (T_{amb}) of 30 °C. The net power output of the ORC system ($\dot{W}_{\text{net,orc}}$) is 9.9 MW. This results in a combined-cycle power output of 44.5 MW and a combined-cycle thermal efficiency ($\eta_{net,cc}$) of 49.5%, with $\eta_{\text{net,cc}} = (\dot{W}_{\text{net,gt}} + \dot{W}_{\text{net,orc}})/(\dot{W}_{\text{net,gt}}/\eta_{\text{th,gt}})$.

3.2.2. WORKING FLUIDS

The fluids selected for this analysis comprehend compounds featuring high thermal stability (HCs, PFCs, Siloxanes), low GWP, and low flammability (HFC, HFOs, HCFOs). These are listed in Tab. 3.3 together with their main characteristics. The ozone depletion potential of all fluids except for HCFO-1244yd-Z and HCFO-1233zd-E is zero. For these two fluids, Arpagaus et al. [29] state ODP values of 1.2E-4 and 3.4E-4, respectively.

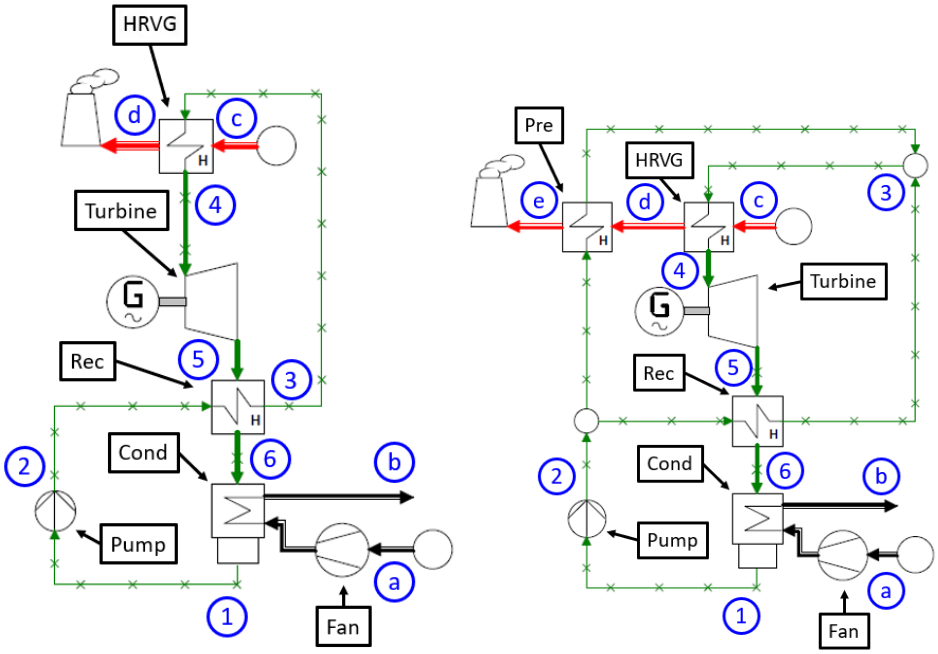

Figure 3.1: Process flow diagrams of the recuperated-cycle (a) and split-cycle (b) configurations.

3.2.3. THERMODYNAMIC MODELS

Cycle calculations are performed by means of an in-house tool that relies on a widely adopted fluid property library [45] implementing a variety of models. Among these models, the PCP-SAFT equation of state is adopted in this study, see Ref. [23] for more details. Thanks to its predictive capabilities, the PCP-SAFT EoS is reasonably accurate also for the prediction of thermodynamic properties of mixtures, as showcased in the original papers documenting this thermodynamic model [46, 23]. The accuracy of the PCP-SAFT model is confirmed by a recent study [47] aimed at developing a group contribution method for the prediction of its binary interaction parameters. The thermodynamic properties of binary mixtures formed by either two polar fluids or two nonpolar fluids are generally predicted with high accuracy also if the binary interaction parameters (k_{ij}) are set equal to zero. However, a certain degree of uncertainty in the results can be expected for mixtures resulting from the combination of a polar and a nonpolar compound. The largest inaccuracy can be expected for mixtures formed by a polar and an associating fluid. None of the substances in Tab. 3.3 is formed by associating molecules. In light of these considerations and the fact that predictive methods for the binary interaction parameters of PCP-SAFT are still under development and are limited to hydrocarbons, all mixture binary interaction parameters are set to zero. This is common engineering practice in studies involving chemical processes if experimental data are unavailable for EoS calibration.

Table 3.1: Thermodynamic cycle specifications

Parameter	Value	Parameter	Value
$T_{\mathrm{h,hrvg,in}}$ *	760.25 K	$\Delta T_{\mathrm{pp,rec}}$	10 K
$\dot{m}_{\mathrm{hrvg}}$ *	105.6 kg/s	$\Delta p_{\mathrm{h,rec}}$	2500 Pa
$\Delta p_{\mathrm{h,hrvg}}$ *	2500 Pa	$\Delta p_{\mathrm{c,rec}}$	2.5% of p_{max}
$\Delta p_{\mathrm{c,hrvg}}$	2.5% of p_{max}	Δp_{pre} **	0 Pa
$\Delta T_{\mathrm{pp,hrvg}}$	10 K	η_{pump}	70%
$\Delta T_{\mathrm{pp,cond}}$ *	7 K	η_{turb}	80%
$\Delta p_{\mathrm{h,cond}}$	5000 Pa	η_{fan}	75%
$\Delta p_{\mathrm{c,cond}}$	200 Pa	T_{amb} *	303.15 K

* Values provided by Klink [25]. The remaining values are estimates.
** Entire pressure drop assumed in HRVG.

Table 3.2: Simulation cases and settings

Simulation Case*	Design variables
pure/recuperated	T_{min}, T_{max}, p_{max}
pure/split	T_{min}, T_{max}, p_{max}, m_{frac}
binary/recuperated	T_{min}, T_{max}, p_{max}, z_{i}
binary/split	T_{min}, T_{max}, p_{max}, z_{i}, m_{frac}

* Working fluid composition/cycle configuration.

The air-cooler fan power consumption ($\dot{W}_{\mathrm{fan}}$) is calculated as the product of the cooling air mass flow rate ($\dot{m}_{\mathrm{c,cond}}$) times the condenser cold-side pressure drop ($\Delta p_{\mathrm{c,cond}}$) divided by air density and fan isentropic efficiency. For the same amount of rejected thermal power, a temperature glide over condensation allows for increased heating of the cooling air and thus a reduction in $\dot{m}_{\mathrm{c,cond}}$. As $\Delta p_{\mathrm{c,cond}}$ is fixed (see in Tab. 3.1), only the impact of the $\dot{m}_{\mathrm{c,cond}}$ variation on $\dot{W}_{\mathrm{fan}}$ is accounted for in this analysis. The gas turbine exhaust gas is modeled as an ideal gas mixture with a molar composition of 73.9% N_2, 13.8% O_2, 3.1% CO_2, 8.1% H_2O and 0.9% Ar [25]. Table 3.1 lists the overall cycle specifications.

3.2.4. OPTIMIZATION PROBLEM

Numerical optimization is used to identify a cycle design that maximizes $\dot{W}_{\mathrm{net,orc}}$. Therefore, the following constrained single-objective optimization problem is solved:

$$\begin{aligned} \text{maximize} \quad & F(\boldsymbol{x}) = \dot{W}_{\mathrm{net,orc}}, \\ \text{subject to} \quad & p_{\mathrm{min}} \geq 1.013\,\mathrm{bar}, \\ & x_i^{\mathrm{L}} \leq x_i \leq x_i^{\mathrm{U}}. \end{aligned} \tag{3.1}$$

Table 3.3: List of candidate fluids

	Synonym	Chemical Formula	CAS-Nr.	$p_{crit}(10^5 Pa)$	$T_{crit}(K)$	Molecular Weight (kg/kmol)	$T_{limit}(K)$	$T_{nbp}(K)$	GWP	Flammability
Old Refrig.	R125	C2HF5	354-33-6	36.2[a]	339.2[a]	120.0[a]	669[b]	225[a]	3500[c]	No[c]
	R134a	C2H2F4	811-97-2	40.6[a]	374.2[a]	102.0[a]	641[b]	247[a]	1300[d]	No[d]
	R32	CH2F2	75-10-5	57.8[a]	351.3[a]	52.0[a]	843[c]	221[a]	675[c]	Mild[c]
	R245fa	C3H3F5	460-73-1	36.4[a]	427.2[a]	134.0[a]	573[s]	288[a]	858[f]	No[d]
Modern Refrig.	HFO-1336mzz-Z	C4H2F6	692-49-9	30.5[d]	444.30[d]	164.1[d]	523[e]	306[d]	2[d]	No[d]
	HFO-1336mzz-E	C4H2F6	66711-86-2	32.9[d]	412.5[d]	164.1[d]	523[g]	281[d]	18[d]	No[d]
	HCFO-1224yd-Z	C3HClF4	111512-60-8	33.8[d]	429.2[d]	148.5[d]	448[f,*]	287[d]	1[d]	No[d]
	HCFO-1233zd-E	C3H2ClF3	102687-65-0	36.2[d]	439.7[d]	130.5[d]	450[k,*]	291[d]	7[k]	No[d]
	HFO-1234yf	C3H2F4	754-12-1	33.8[a]	367.9[a]	114.0[a]	N/A*	244[a]	4[h]	Mild[j]
	HFO-1243zf	C3H3F3	677-21-4	36.1[a]	378.6[a]	96.1[a]	N/A*	248[a]	0.8[h]	Mild[j]
	Novec 649	C6F12O	756-13-8	18.7[n]	441.8[n]	316.0[i]	573[i]	322[i]	1[i]	No[i]
HCs	cyclopentane	C5H10	287-92-3	45.1[a]	511.7[a]	70.1[a]	573[c]	322[a]	6[c]	Yes[c]
	toluene	C7H8	108-88-3	41.1[a]	591.8[a]	92.1[a]	673[c]	384[a]	3.3[o]	Yes[c]
	isobutane	C4H10	75-28-5	36.4[a]	407.8[a]	58.1[a]	593[q]	261[a]	3[d]	Yes[d]
	propane	C3H8	74-98-6	42.5[a]	369.8[a]	44.1[a]	633[r]	231[a]	3[d,o]	Yes[d]
	ethane	C2H6	74-84-0	48.7[a]	305.3[a]	30.1[a]	633[r]	185[a]	2.9[o]	Yes
Siloxanes	D4	C8H24O4Si4	556-67-2	13.2[a]	586.5[a]	296.6[a]	623[c]	448[a]	0[c]	Mild[c]
	D5	C10H30O5Si5	541-02-6	10.4[a]	617.4[a]	370.8[a]	623[c]	484[a]	0[c]	Mild[c]
	D6	C12H36O6Si6	540-97-6	9.01[a]	645.8[a]	444.9[a]	623[c]	518[a]	0[c]	Mild[c]
	MM	C6H18OSi2	107-46-0	19.2[a]	519.0[a]	162.4[a]	573[c]	374[a]	0[c]	Yes[c]
	MDM	C8H24O2Si3	107-51-7	14.6[a]	564.4[a]	236.5[a]	573[c]	426[a]	0[c]	Mild[c]
	MD2M	C10H30O3Si4	141-62-8	11.9[a]	599.4[a]	310.7[a]	573[c]	477[a]	0[c]	Mild[c]
	MD3M	C12H36O4Si5	141-63-9	9.45[a]	628.4[a]	384.8[a]	573[c]	503[a]	0[c]	Mild[c]
	MD4M	C14H42O5Si6	107-52-8	8.04[a]	653.2[a]	459.0[a]	573[c]	533[a]	0[c]	Mild[c]
PFCs	PP2	C7F14	355-02-2	20.2[m]	486.4[m]	350.1[m]	673[l]	349[m]	N/A[$]	No[l]
	PP5	C10F18	306-94-5	17.8[m]	565.1[m]	462.1[m]	673[l]	415[m]	7190[p]	No[l]

[a] Rowley et al. [26], using 2019 Database
[b] Calderazzi and Colonna [27]
[c] Astolfi and Macchi [28]
[d] Arpagaus et al. [29]
[e] Kontomaris [30]
[f] Mateu-Royo et al. [31]
[g] Juhasz [32]
[h] McLinden et al. [33]
[i] 3M Corporation [34]
[j] Takizawa et al. [35]
[k] Perkins et al. [36]
[l] F2 Chemicals Ltd. [37]
[m] Marsh et al. [38]
[n] McLinden et al. [39]
[o] Collins et al. [40]
[p] IPCC [41]
[q] Dai et al. [42]
[r] Acc. to Preißinger and Brüggemann [43] the compound is present as decomposition product of MM at T > 633.15 K
[s] Angelino and Invernizzi [44]
* For this analysis 523 K was assumed
$ Assumed to be same as for PP5

The optimization problem comprises one constraint that ensures a super-atmospheric condensing pressure. This constraint is adopted in agreement with the usual conservatism that informs design choices related to real-world power plants so as to ensure technical and economic feasibility. If the pressure in the condenser is greater than the atmospheric pressure, ambient air cannot leak into the system. Avoiding inward air leakage provides two operational advantages: first, in case the working fluid is flammable, leaked air can lead to the formation of an ignitable mixture inside the system which poses a safety issue; second, oxygen is a catalyst for thermal decomposition of the working fluid which reduces fluid lifetime and decreases the plant performance. In the case of a configuration with a sub-atmospheric condenser, it is, therefore, necessary to adopt a vacuum system, which introduces additional cost and may affect the reliability of the plant.

Depending on the simulation case, the design vector ($\boldsymbol{x}$) consists of up to five variables. Table 3.4 lists the single design variables (x_i) considered in the optimization together with their lower bounds (x^{L}) and upper bounds (x^{U}). In the case of mixtures of

working fluids, there are no predictive methods to determine the thermal stability limit given the characteristics of the molecules in the blend or the thermal stability limit of the pure constituents. In addition, experimental studies are very limited and show contradictory results. Liu et al. [48] investigated the thermal stability of a mixture of two refrigerants, R32 and R1234ze(E). The experimental data show that the thermal stability limit of the mixture is equal to that of the fluid that decomposes at the lowest temperature, R1234ze(E). The mixing of the two refrigerants promotes also the pyrolysis of R32 at a temperature that is lower than the decomposition temperature of the fluid if unmixed. A more complex interaction was instead observed by Gallarini et al. [49] for the mixture of two siloxanes, MM and MDM, whereby recombination of the two molecules seems to enhance the thermal stability of MDM, the less thermally stable compound in the mixture. Due to the lack of experimental information and a general theory of thermal degradation of mixtures, in this study the upper bound of T_{max} is conservatively set equal to the lowest thermal stability limit of the involved compounds $T_{limit,A}$ and $T_{limit,B}$, respectively. In the case of pure fluids, T_{max} is set equal to the thermal stability limit reported in Table 3.3. The upper bound of the maximum reduced pressure $p_{max,r} = p_{max}/p_{crit}$ is set to 1.2. Higher cycle pressures offer limited benefits in terms of cycle efficiency due to the increased pump power demand. High pump power demand also leads to an increased sensitivity of cycle efficiency to pump isentropic efficiency. Consequently, higher cycle pressure leads to increased component complexity and cost. For example, as opposed to the off-the-shelf pumps commonly used for subcritical ORC systems, a multi-stage pump may be required for supercritical-cycle power plants. Furthermore, the primary heat exchanger walls need to be thicker to sustain higher pressure [28]. The optimization problem is solved using the genetic algorithm eaMuPlusLambda implemented in the DEAP Python library [50].

Table 3.4: Design variables and their respective bounds

Variables (x_i)	**Description (Unit)**	**Bounds** (x^L/x^U)
T_{min}	Minimum temperature ORC working fluid (K)	281/303
T_{max}	Maximum temperature ORC working fluid (K)	473/min($T_{limit,A}$, $T_{limit,B}$)
$p_{max,r}$	Maximum reduced pressure ORC working fluid (-)	0.8/1.2
m_{frac}	Split cycle mass flow fraction (-)	0.1/0.9
z_i	Mixture molar composition (-)	0.0/1.0

3.3. RESULTS

325 binary mixtures resulting from the combination of the fluids in Tab. 3.3 are considered as the working fluid of the bottoming ORC unit. Not all the combinations of working fluids could be assessed because in some cases the thermodynamic property calculations fail and in other cases, no condensation occurs for the considered range of minimum cycle pressures. The performance of cycles employing binary mixtures is compared against that achievable with cycles employing pure working fluids. All simulations are run based on the cycle specifications listed in Table 3.1 and the optimization settings given in Tab. 3.2 and Tab. 3.4. Only cases that fulfill the constraint of super-atmospheric condensing pressure are presented hereafter. Figure 3.2 shows a comparison between the processes of the recuperated-cycle and of the split-cycle configurations in the temperature entropy diagram of R245fa as an example. Both cycles are supercritical and feature a similar minimum and maximum temperature. The maximum temperatures are close to the estimated thermal stability limit of the working fluid, which is 573 K. The split-cycle allows the recovery of substantially more thermal energy from the exhaust gases due to the preheater. The relative increase in combined-cycle efficiency is about 3%. However, such a performance increase is not obtained for all fluids and depends on the fluid critical temperature T_{crit} as discussed in Section 3.4.

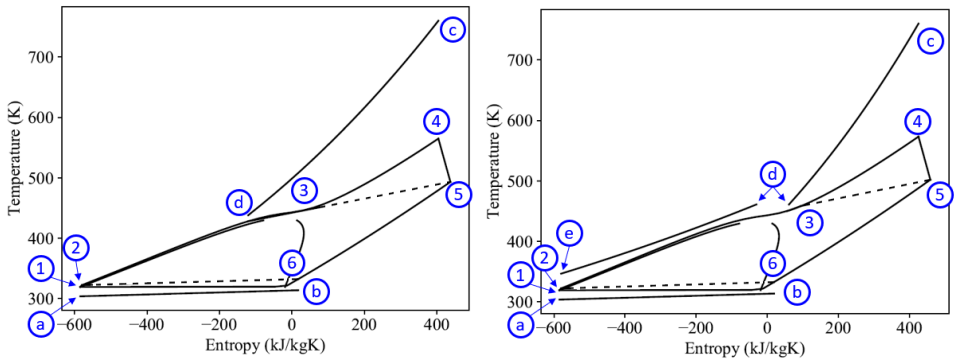

Figure 3.2: Ts-diagram representation of the processes forming the recuperated-cycle (a) and split-cycle (b) configurations in case R245fa is the working fluid; The thermodynamic state numbering is consistent with that of Fig. 3.1; Note 1: dashed lines indicate heat transfer between hot and cold recuperator streams; Note 2: the gap in saturation curve close to the critical point is due to convergence problems of the vapor-liquid equilibrium calculation very close to the critical point.

Figure 3.3 presents $\dot{W}_{net,orc}$ as a function of T_{crit} and molecular complexity (σ) for the recuperated-cycle and split-cycle configurations. According to Angelino et al. [51] the molecular complexity of the working fluid is "a function of the number and mass of the atoms forming the molecule and controls the shape of the saturation curve in the T–S (sic) plane." A positive value of σ is therefore associated with a larger value of the isobaric specific heat, a smaller value of the latent heat of vaporization, and a positive slope of the vapor saturation curve in the temperature-entropy diagram. Likewise, negative values of the molecular complexity are associated with a lower complexity of the molecules, larger

values of the latent heat of vaporization, and a negative slope of the vapor saturation curve in the temperature-entropy diagram. Note that the T_{crit} values are calculated as prescribed by the PCP-SAFT model and therefore might differ from experimental values. Higher power output can be achieved with the split-cycle configuration as compared to the recuperated-cycle configuration. Furthermore, with the split-cycle configuration, the best performance is obtained with fluids with lower T_{crit}.

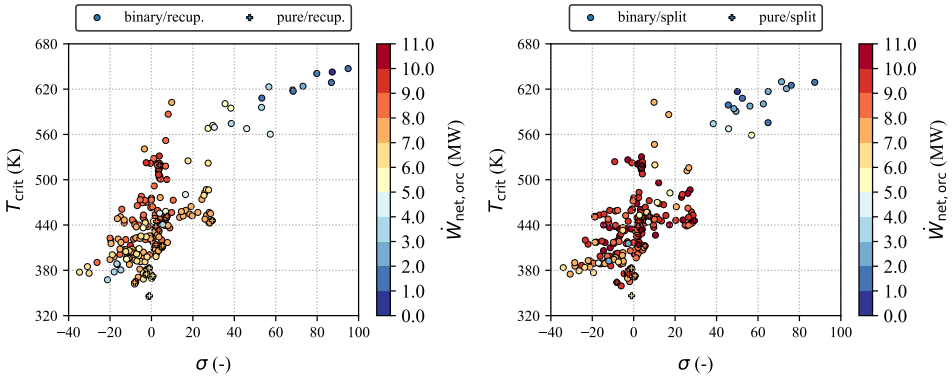

Figure 3.3: $\dot{W}_{net,orc}$ as a function of T_{crit} and molecular complexity for both the recuperated-cycle (a) and the split-cycle (b) configurations.

Figure 3.4 presents values of $\eta_{net,cc}$ in relation to a representative selection of fluids. The corresponding working fluid composition is indicated in Tab. 3.5. Non-flammable fluids with a GWP ≤ 150 are highlighted in blue in Fig. 3.4. The results show that the split-cycle configuration leads to a better performance with all the considered working fluids and can also outperform the benchmark cycle. Furthermore, some low GWP/non-flammable fluids allow to achieve a performance comparable to that of the benchmark, if the split-cycle configuration is adopted. In the case of the recuperated-cycle configuration with a pure working fluid, cyclopentane is the optimal working fluid, while, in the case of the split-cycle configuration, R245fa is the optimal working fluid, followed by isobutane and cyclopentane. Mixtures provide a wider range of fluids whose use offers good combined-cycle performance, but, as is the case for the recuperated-cycle configuration, the benchmark provides the best performance. Only in the case of the split-cycle configuration, the use of a mixture working fluid is beneficial if compared to a pure fluid, including cyclopentane. Despite the large variety of considered mixtures, in the case of the recuperated-cycle configuration, 19 of the 20 mixtures providing the best $\eta_{net,cc}$ contain cyclopentane with a mole fraction above 90%. Furthermore, among the 100 mixtures providing the best $\eta_{net,cc}$, 10 feature a low GWP and are non-flammable in the case of the recuperated-cycle configuration and 13 in the case of the split-cycle configuration.

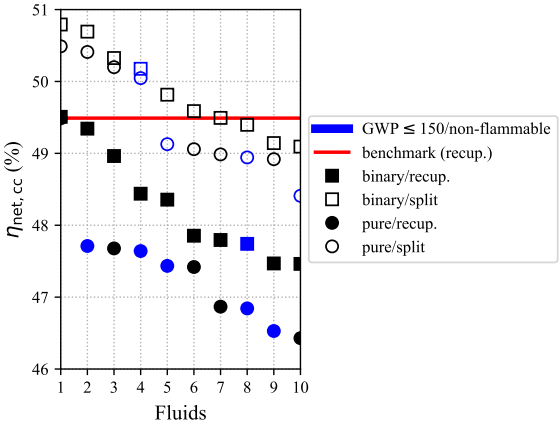

Figure 3.4: $\eta_{net,cc}$ corresponding to a selection of working fluids. Table 3.5 lists the fluid number identifier.

Table 3.5: Table of selected fluids

Fluid	pure/recuperated	pure/split	binary/recuperated	binary/split
1	cyclopentane	R245fa	cyclopentane[0.92]& R134a[0.08]	R245fa[0.72]& PP2[0.28]
2	HFO-1233zd-Z*	isobutane	cyclopentane[0.79]& R245fa[0.21]	R245fa[0.68]& cyclopentane[0.32]
3	R245fa	cyclopentane	cyclopentane[0.80]& HFO-1336mzz-Z[0.20]	cyclopentane[0.93]& isobutane[0.07]
4	HFO-1336mzz-Z*	Novec 649*	R245fa[0.94]& D5[0.06]	Novec 649[0.95]& R134a[0.05]*
5	HCFO-1224yd-Z*	HFO-1336mzz-Z*	HCFO-1233zd-E[0.83]& toluene[0.17]	R32[0.83]& toluene[0.17]
6	isobutane	R134a	HCFO-1224yd-Z[0.90]& MM[0.10]	HFO-1336mzz-Z[0.92]& HFO-1243zf[0.08]
7	R32	HCFO-1224yd-Z*	isobutane[0.73]& R32[0.27]	propane[0.89]& D4[0.11]
8	Novec 649*	R32	HCFO-1233zd-E[0.61]& HFO-1336mzz-Z[0.39]*	Novec 649[0.85]& MM[0.15]
9	HFO-1336mzz-E*	HCFO-1233zd-Z*	isobutane[0.80]&Novec 649[0.20]	HCFO-1233zd-E[0.78]& R134a[0.22]
10	R134a	HFO-1336mzz-E*	HCFO-1224yd-Z[0.94]& HFO-1243zf[0.06]	HCFO-1224yd-Z[0.76]& isobutane[0.24]

* Fluids with GWP ≤ 150 and zero flammability.
Note: numbers in brackets indicate molar composition z_i.

3.4. DISCUSSION

3.4.1. RELATION BETWEEN CYCLE CONFIGURATION AND FLUID CRITICAL TEMPERATURE

Figure 3.5 shows $\eta_{net,cc}$ with respect to T_{crit} for both the recuperated-cycle and split-cycle configurations. In the case of the split-cycle configuration, $\eta_{net,cc}$ reaches the highest values for values of T_{crit} that are approximately 100 K lower than the T_{crit} of the fluids providing the best performance in case of the recuperated-cycle configuration. The reason is that the amount of thermal energy recovery associated with the split-cycle configuration does not decrease with the adoption of a high degree of recuperation that fluids with lower critical temperatures require to achieve high conversion efficiency.

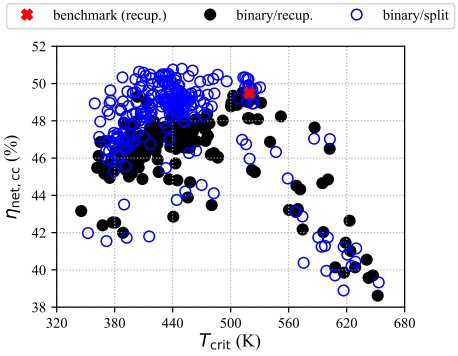

Figure 3.5: Comparison of $\eta_{net,cc}$ over T_{crit}

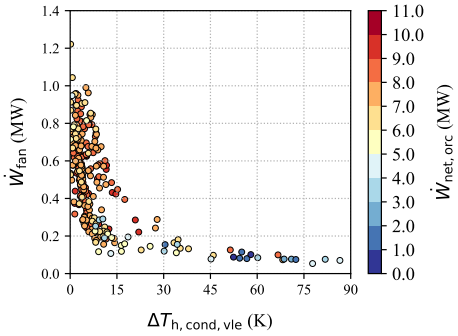

Figure 3.6: $\dot{W}_{net,orc}$ as a function of $\dot{W}_{fan}$ and $\Delta T_{h,cond,vle}$ for the binary/recuperated case.

3.4.2. EFFECT OF TEMPERATURE GLIDE

The isobaric phase change of a zeotropic mixture is non-isothermal, therefore it occurs with a temperature glide. This physical behavior is beneficial for the matching of the temperature profiles of the working fluid and air in the condenser and of the working fluid and exhaust gas in the evaporator. Since most optimum cycle configurations considered in this analysis are of the supercritical type, evaporation is not affected by the temperature glide. However, the temperature glide in the condenser can decrease the fan power demand $\dot{W}_{fan}$ of air-cooled ORC systems, which in turn can yield an increase of $\dot{W}_{net,orc}$.

Figure 3.6 shows $\dot{W}_{net,orc}$ as a function of $\dot{W}_{fan}$ and condenser temperature glide occurring across the vapor-liquid equilibrium (VLE) region ($\Delta T_{h,cond,vle}$) for the recuperated cycle configuration. $\dot{W}_{fan}$ reduces for increasing values of the $\Delta T_{h,cond,vle}$. High values of $\dot{W}_{net,orc}$ are however only obtained for a narrow range of low $\Delta T_{h,cond,vle}$ values. Outside this range the beneficial $\dot{W}_{fan}$ reduction is offset by the decrease in thermodynamic efficiency. Figure 3.7 shows $\Delta T_{h,cond,vle}$ for the selected fluids listed in Tab. 3.5.

The question remains, why $\dot{W}_{net,orc}$ does not benefit from the reduction of $\dot{W}_{fan}$ with increasing temperature glide. To answer this question an exergy analysis was performed. For the recuperated-cycle configuration, Fig. 3.8 provides a comparison between exergy

losses in case cyclopentane is the working fluid with the losses in case binary mixtures are the working fluid, according to Tab. 3.5. While a slight trend towards reduced condenser losses can be observed for the mixtures, the use of mixtures leads to an overall increase in exergy losses associated with the heat transfer in the HRVG or, in a few cases, in the recuperator. Furthermore, $\dot{W}_{\text{fan}}$ contributes little to the losses. Therefore, for the specific application investigated in this study, a reduction of $\dot{W}_{\text{fan}}$, e.g., due to the temperature glide, only has a small impact on the plant overall performance.

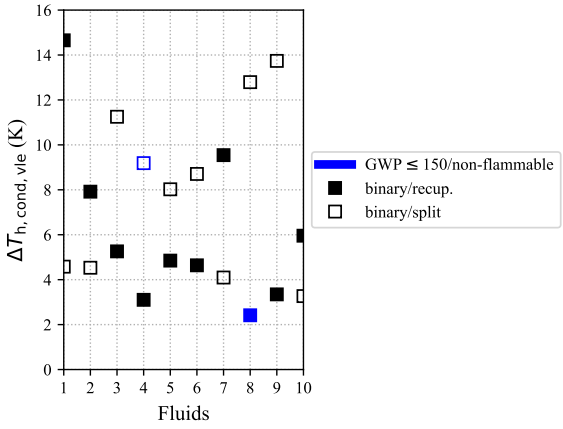

Figure 3.7: $\Delta T_{\text{h,cond,vle}}$ for selected fluids. Fluid number identifier in Tab. 3.5.

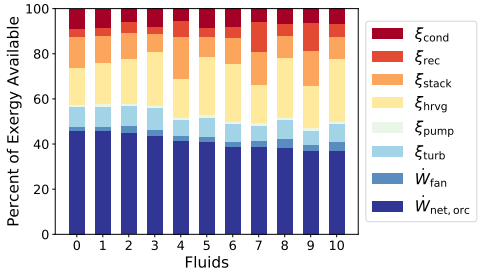

Figure 3.8: Exergy analysis comparing the recuperated-cycle configuration using the benchmark working fluid cyclopentane (Fluid 0) with the binary/recuperated cases according to Tab. 3.5 indicated with their respective fluid number; Note: Exergy available assumes cooling of the heat source to ambient conditions, therefore, ξ_{stack} represents the lost energy at the HRVG exit.

3.4.3. IMPACT OF CONDENSATION PRESSURE ON CYCLE PERFORMANCE

Based on the following reasoning, it is hypothesized that lifting the super-atmospheric condensation pressure constraint might lead to a better performance of cycle configurations using mixtures as working fluids. A relaxation of this constraint would allow lower condensation temperatures. Lower condensation temperatures in turn would result in a

lower condenser cold-side temperature difference and consequently to a higher $\dot{m}_{\text{fan}}$ demand for a given condenser heat load. In the assumption that the condenser is designed for similar airspeed, an increase in $\dot{m}_{\text{fan}}$ would increase $\dot{W}_{\text{fan}}$. In this case, a temperature glide of the working fluid may therefore be more beneficial, in that it increases the temperature difference of the cooling air across the condenser.

To verify this hypothesis, all pure/recuperated and binary/recuperated simulations are re-run without imposing the super-atmospheric condensation pressure constraint. From the analysis of the results, the following observations can be made. First of all, lifting the pressure constraint results in an increased range of feasible solutions including cycles using pure toluene and siloxanes as working fluids and cycles using mixtures containing toluene and siloxanes with large mole fractions. Secondly, for the cycles employing pure working fluids, it is observed that the condenser cold-side temperature difference is smaller, which results in larger $\dot{W}_{\text{fan}}$. If toluene is the working fluid, the cycle efficiency is the maximum among all considered cases. However, the calculated efficiency is very similar to that calculated in case cyclopentane is the working fluid. In both cases, the computed $\dot{W}_{\text{net,orc}}$ is slightly above 10 MW. Thirdly, the cycles employing binary mixtures as working fluid do not result in improved $\eta_{\text{net,cc}}$. Again, the efficiency of cycles with mixtures based on toluene as the working fluid is slightly better than that of cycles with cyclopentane-based mixtures. However, the specific enthalpy difference over the turbine (Δh_{turb}) and the turbine volume flow ratio (VR) (around 500) associated with toluene are larger if compared to those associated with cyclopentane. The impact of these parameters on turbine design is discussed in Section 3.4.4. Therefore, the hypotheses put forward that cycle performance may benefit from the adoption of working fluid mixtures in case of lower condensation pressures is invalid for the considered application.

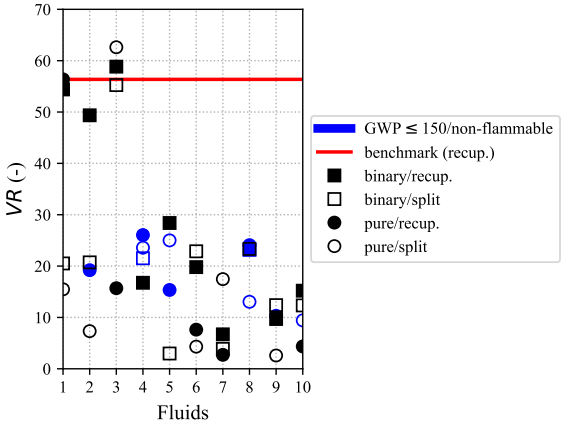

Figure 3.9: VR for selected fluids. Table 3.5 lists the fluid number identifier.

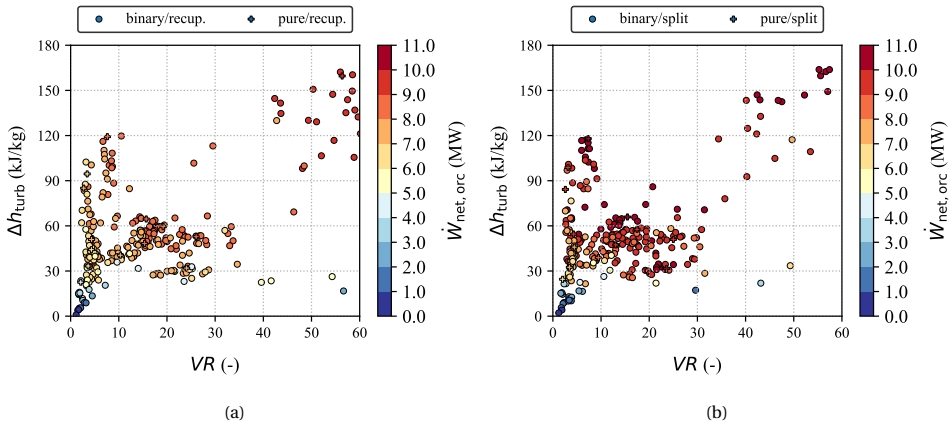

Figure 3.10: $\dot{W}_{net,orc}$ as a function of Δh_{turb} and VR for the recuperated-cycle (a) and split-cycle (b).

3.4.4. WORKING FLUID AND TURBINE DESIGN

Turbine design complexity, size, efficiency, and therefore cost, are driven by Δh_{turb} and VR of the working fluid vapor over the expansion [28]. Figure 3.10 displays the variation of these parameters for pure fluids and binary mixtures. On the one hand, with the recuperated-cycle configuration, the highest $\eta_{net,cc}$ is achieved with fluids featuring high Δh_{turb} and VR. These fluids contain a large mole fraction of cyclopentane. On the other hand, with the split-cycle, high $\eta_{net,cc}$ is obtained with fluids also featuring lower Δh_{turb} and VR. For example, Figure 3.10 (b) indicates that high performance can be attained with fluids leading to a VR range from 10 to 25 and a Δh_{turb} between 30 and 60 kJ/kg. Comparing this VR range with the data given in Fig. 3.9 and Tab. 3.5 reveals that the working fluids in this region include R245fa and modern refrigerants and their mixtures. Modern refrigerants are characterized by very low GWP and zero flammability. For example, Novec 649 is therefore an interesting working fluid because of its low GWP and non-flammability. A power plant adopting the split-cycle configuration and Novec 649 as the working fluid entails a calculated $\eta_{net,cc}$ higher than that of the benchmark, a VR of 23.6 and Δh_{turb} of 32.7 kJ/kg. Such a fluid would fulfill regulations concerning environmental and operational safety and would allow the design of a compact and cost-effective turbine.

3.5. CONCLUSIONS

The use of mixtures as working fluids for air-cooled ORC systems as the bottoming cycle of medium-capacity gas turbines is investigated by means of steady-state simulations. Zeotropic mixtures undergo isobaric phase change with a temperature glide, and this effect can in principle be exploited to reduce condenser fan power consumption at the cost of additional heat transfer surface. As a result, overall combined-cycle efficiency may increase. Low GWP and non-flammable fluids suitable for high-temperature waste heat recovery were considered. Furthermore, a new cycle configuration especially suitable for waste heat recovery was tested as a part of this study. The main findings are:

- In comparison to pure fluids, a larger number of mixtures can be used as working fluids of high-performance air-cooled ORC systems. However, in the case of the recuperated cycle configuration, even if the benefit of air-cooler fan power reduction is verified, under the given assumptions the performance of the benchmark case employing cyclopentane as the working fluid cannot be overcome, due to the higher exergy losses associated with heat transfer.
- The split-cycle configuration allows to increase the combined-cycle efficiency if compared to the recuperated cycle configuration and the performance estimated with a wide range of working fluids is better than the performance calculated for the benchmark. The optimum combined-cycle performance is achieved with pure fluids and mixtures featuring lower critical temperatures as compared with the working fluids of the recuperated cycle configuration.
- A range of pure fluids and mixtures with lower critical temperatures may allow obtaining a conversion efficiency similar to that of the benchmark case but the resulting turbine is more compact and thus more cost-effective.
- The combined-cycle efficiency of a system adopting the split-cycle configuration for the bottoming unit and Novec 649 as the working fluid, a low GWP and non-flammable fluid, is higher than the efficiency computed for the benchmark case.
- The adoption of mixtures as working fluid does not lead to a relevant performance increase with respect to the benchmark also if the condensation pressure is sub-atmospheric.

The performance improvement achieved with the split-cycle configuration comes at the cost of larger heat exchanger surfaces. To quantify the advantage of this configuration, the economic aspects related to the need for more heat transfer surface and the turbine design need to be taken into account. The effect of employing mixtures of working fluids on the size of the heat exchangers is of specific interest for airborne applications due to the volume limitation onboard the aircraft. Furthermore, in the case of ram-air-cooled airborne ORC unit configurations, the non-isothermal isobaric condensation of mixtures of working fluids may allow a reduction of the required air mass flow rate and therefore pressure drop for the rejection of a given heat load. As a result, aircraft drag due to the addition of the condenser may be reduced. As a last remark, it must be noted that, while the PCP-SAFT equation of state employed in this study to calculate the thermodynamic properties of fluids belongs to the class of physics-based models, its application to highly non-ideal mixtures without a proper estimation of binary interaction parameters introduces some uncertainty.

BIBLIOGRAPHY

[1] G. Bianchi, G. P. Panayiotou, L. Aresti, S. A. Kalogirou, G. A. Florides, K. Tsamos, S. A. Tassou, and P. Christodoulides, "Estimating the waste heat recovery in the European Union industry," *Energy, Ecology and Environment*, vol. 4, pp. 211–221, 2019, doi: 10.1007/s40974-019-00132-7.

[2] M. Papapetrou, G. Kosmadakis, A. Cipollina, U. L. Commare, and G. Micale, "Industrial waste heat: Estimation of the technically available resource in the EU per industrial sector, temperature level and country," *Applied Thermal Engineering*, vol. 138, pp. 207–216, 6 2018, doi: 10.1016/j.applthermaleng.2018.04.043.

[3] P. Colonna, M. Astolfi, J. van Buijtenen, C. Wieland, G. David, F. Garofalo, M. Baresi, H. Öhman, and W. Klink, "Thermal energy harvesting: The path to tapping into a large CO_2-free european power source," Knowledge Center on Organic Rankine Cycle technology, techreport, 2021, accessed, 23 August 2024. [Online]. Available: https://kcorc.org/wp-content/uploads/2022/06/Thermal_Energy_Harvesting_-_the_Path_to_Tapping_into_a_Large_CO2-free_European_Power_Source.pdf

[4] P. Colonna, E. Casati, C. Trapp, T. Mathijssen, J. Larjola, T. Turunen-Saaresti, and A. Uusitalo, "Organic Rankine cycle power systems: From the concept to current technology, applications, and an outlook to the future," *Journal of Engineering for Gas Turbines and Power*, vol. 137, 10 2015, doi: 10.1115/1.4029884.

[5] European Parliament, "Directive 2014/34/EU of the European Parliament and of the Council of 26 February 2014 on the harmonisation of the laws of the member states relating to equipment and protective systems intended for use in potentially explosive atmospheres," 2014.

[6] ——, "Regulation (EU) no 517/2014 of the European Parliament and of the Council of 16 April 2014 on fluorinated greenhouse gases and repealing regulation (EC) no 842/2006."

[7] G. Angelino and P. Colonna, "Multicomponent working fluids for organic Rankine cycles (ORCs)," *Energy*, vol. 23, no. 6, pp. 449–463, 1998, doi: 10.1016/S0360-5442(98)00009-7.

[8] ——, "Air cooled siloxane bottoming cycle for molten carbonate fuel cells," in *Fuel Cell Seminar*, 2000, pp. 667–670.

[9] ——, "Organic Rankine cycles for energy recovery from molten carbonate fuel cells," in *35th Intersociety Energy Conversion Engineering Conference (IECEC)*, no. 2000-3052. AIAA, 2000, pp. 1–11, doi: 10.1109/IECEC.2000.870957.

[10] K. Braimakis, A. Mikelis, A. Charalampidis, and S. Karellas, "Exergetic performance of CO_2 and ultra-low GWP refrigerant mixtures as working fluids in ORC for waste heat recovery," *Energy*, vol. 203, p. 117801, 7 2020, doi: 10.1016/j.energy.2020.117801.

[11] G. B. Abadi and K. C. Kim, "Investigation of organic Rankine cycles with zeotropic mixtures as a working fluid: Advantages and issues," *Renewable and Sustainable Energy Reviews*, vol. 73, pp. 1000–1013, 2017.

[12] Y. Fang, F. Yang, and H. Zhang, "Comparative analysis and multi-objective optimization of organic Rankine cycle (ORC) using pure working fluids and their zeotropic mixtures for diesel engine waste heat recovery," *Applied Thermal Engineering*, vol. 157, p. 113704, 2019, doi: 10.1016/j.applthermaleng.2019.04.114.

[13] M. Kolahi, M. Yari, S. Mahmoudi, and F. Mohammadkhani, "Thermodynamic and economic performance improvement of ORCs through using zeotropic mixtures: Case of waste heat recovery in an offshore platform," *Case Studies in Thermal Engineering*, vol. 8, pp. 51–70, 2016, doi: 10.1016/j.csite.2016.05.001.

[14] R. Scaccabarozzi, M. Tavano, C. M. Invernizzi, and E. Martelli, "Comparison of working fluids and cycle optimization for heat recovery ORCs from large internal combustion engines," *Energy*, vol. 158, pp. 396–416, 2018, doi: 10.1016/j.energy.2018.06.017.

[15] Z. Ge, J. Li, Q. Liu, Y. Duan, and Z. Yang, "Thermodynamic analysis of dual-loop organic Rankine cycle using zeotropic mixtures for internal combustion engine waste heat recovery," *Energy Conversion and Management*, vol. 166, pp. 201–214, 2018, doi: 10.1016/j.enconman.2018.04.027.

[16] L.-H. Zhi, P. Hu, L.-X. Chen, and G. Zhao, "Parametric analysis and optimization of transcritical-subcritical dual-loop organic Rankine cycle using zeotropic mixtures for engine waste heat recovery," *Energy Conversion and Management*, vol. 195, pp. 770–787, 2019, doi: 10.1016/j.enconman.2019.05.062.

[17] G. Di Marcoberardino, C. Invernizzi, P. Iora, A. Ayub, D. Di Bona, P. Chiesa, M. Binotti, and G. Manzolini, "Experimental and analytical procedure for the characterization of innovative working fluids for power plants applications," *Applied Thermal Engineering*, vol. 178, p. 115513, 2020, doi: 10.1016/j.applthermaleng.2020.115513.

[18] Y. Yang, T. Xue, Z. Rao, and S. Liao, "Potential of transcritical recompression Rankine cycle operating with CO_2-based binary mixtures," *Energy Conversion and Management*, vol. 252, p. 115040, 2022, doi: 10.1016/j.enconman.2021.115040.

[19] F. Crespi, P. Rodríguez de Arriba, D. Sánchez, A. Ayub, G. Di Marcoberardino, C. Invernizzi, G. Martínez, P. Iora, D. Di Bona, M. Binotti, and G. Manzolini, "Thermal efficiency gains enabled by using CO_2 mixtures in supercritical power cycles," *Energy*, vol. 238, p. 121899, 2022, doi: 10.1016/j.energy.2021.121899.

[20] J. Ren, Y. Cao, Y. Long, X. Qiang, and Y. Dai, "Thermodynamic comparison of gas turbine and ORC combined cycle with pure and mixture working fluids," *Journal of Energy Engineering*, vol. 145, no. 1, p. 05018002, 2019, doi: 10.1061/(ASCE)EY.1943-7897.0000580.

[21] A. I. Papadopoulos, M. Stijepovic, P. Linke, P. Seferlis, and S. Voutetakis, "Molecular design of working fluid mixtures for organic Rankine cycles," *Computer Aided Chemical Engineering*, vol. 32, pp. 289–294, 2013, doi: 10.1016/B978-0-444-63234-0.50049-X.

[22] J. Schilling, M. Entrup, M. Hopp, J. Gross, and A. Bardow, "Towards optimal mixtures of working fluids: Integrated design of processes and mixtures for organic Rankine cycles," *Renewable and Sustainable Energy Reviews*, vol. 135, p. 110179, 1 2021, doi: 10.1016/j.rser.2020.110179.

[23] J. Gross and J. Vrabec, "An equation-of-state contribution for polar components: Dipolar molecules," *AIChE Journal*, vol. 52, no. 3, pp. 1194–1204, 2006, doi: 10.1002/aic.10683.

[24] M. Gaia, R. Bini, R. Vescovo, and E. Spagnoli, "Cogenerative organic Rankine cycle system," 11 Patent WO2017199170A1, 2017.

[25] W. Klink, "Personal communication with wolfgang klink of Siemens Energy AG," 2018.

[26] R. Rowley, W. Widling, J. Oscarson, Y. Yang, N. Zundel, T. Daubert, and R. Danner, "DIPPR® data compilation of pure chemical properties, design institute for physical properties," 2006, software.

[27] L. Calderazzi and P. Colonna, "Thermal stability of R-134a, R-141b, R-13I1, R-7146, R-125 associated with stainless steel as a containing material," *International Journal of Refrigeration*, vol. 20, pp. 381–389, 1 1997, doi: 10.1016/S0140-7007(97)00043-1.

[28] M. Astolfi and E. Macchi, *Organic Rankine Cycle (ORC) Power Systems*. Elsevier, 2017, doi: 10.1016/C2014-0-04239-6.

[29] C. Arpagaus, F. Bless, M. Uhlmann, J. Schiffmann, and S. S. Bertsch, "High temperature heat pumps: Market overview, state of the art, research status, refrigerants, and application potentials," *Energy*, vol. 152, pp. 985–1010, 6 2018, doi: 10.1016/j.energy.2018.03.166.

[30] K. Kontomaris, "HFO-1336mzz-Z: High temperature chemical stability and use as a working fluid in organic Rankine cycles," *Purdue University*, 2014.

[31] C. Mateu-Royo, J. Navarro-Esbrí, A. Mota-Babiloni, M. Amat-Albuixech, and F. Molés, "Thermodynamic analysis of low GWP alternatives to HFC-245fa in high-temperature heat pumps: HCFO-1224yd(Z), HCFO-1233zd(E) and HFO-1336mzz(Z)," *Applied Thermal Engineering*, vol. 152, pp. 762–777, 4 2019, doi: 10.1016/j.applthermaleng.2019.02.047.

[32] J. R. Juhasz, "Novel working fluid, HFO-1336mzz(E), for use in waste heat recovery application," in *12th IEA Heat Pump Conference*, 2017.

[33] M. O. McLinden, A. F. Kazakov, J. S. Brown, and P. A. Domanski, "A thermodynamic analysis of refrigerants: Possibilities and tradeoffs for low-GWP refrigerants," *International Journal of Refrigeration*, vol. 38, pp. 80–92, 2 2014.

[34] 3M Corporation, "Novec™ 649 product datasheet," 2009. [Online]. Available: https://multimedia.3m.com/mws/media/569865O/3m-novec-engineered-fluid-649.pdf

[35] K. Takizawa, K. Tokuhashi, and S. Kondo, "Flammability assessment of CH2CFCF3: Comparison with fluoroalkenes and fluoroalkanes," *Journal of Hazardous Materials*, vol. 172, pp. 1329–1338, 12 2009, doi: 10.1016/j.jhazmat.2009.08.001.

[36] R. A. Perkins, M. L. Huber, and M. J. Assael, "Measurement and correlation of the thermal conductivity of trans-1-Chloro-3,3,3-trifluoropropene (R1233zd(E)," *Journal of Chemical and Engineering Data*, vol. 62, pp. 2659–2665, 9 2017, doi: 10.1021/acs.jced.7b00106.

[37] F2 Chemicals Ltd., "FLUTEC® product datasheet," 2012, accessed 23 August 2024. [Online]. Available: https://f2chemicals.com/pdf/technical/Compatability.pdf

[38] K. N. Marsh, A. Abramson, D. Ambrose, D. W. Morton, E. Nikitin, C. Tsonopoulos, and C. L. Young, "Vapor-liquid critical properties of elements and compounds. 10. organic compounds containing halogens," *Journal of Chemical and Engineering Data*, vol. 52, pp. 1509–1538, 9 2007, doi: 10.1021/je700336g.

[39] M. O. McLinden, R. A. Perkins, E. W. Lemmon, and T. J. Fortin, "Thermodynamic properties of 1,1,1,2,2,4,5,5,5-nonafluoro-4-(trifluoromethyl)-3-pentanone: Vapor pressure, (p, ρ, t) behavior, and speed of sound measurements, and an equation of state," *Journal of Chemical and Engineering Data*, vol. 60, pp. 3646–3659, 12 2015, doi: 10.1021/acs.jced.5b00623.

[40] W. J. Collins, R. G. Derwent, C. E. Johnson, and D. S. Stevenson, "The oxidation of organic compounds in the troposphere and their global warming potentials," *Climatic Change 2002 52:4*, vol. 52, pp. 453–479, 2002, doi: 10.1023/A:1014221225434.

[41] IPCC, "Climate change 2013: The physical science basis. contribution of working group I to the fifth assessment report of the Intergovernmental Panel on Climate Change," 2013.

[42] X. Dai, L. Shi, Q. An, and W. Qian, "Screening of hydrocarbons as supercritical ORCs working fluids by thermal stability," *Energy Conversion and Management*, vol. 126, pp. 632–637, 10 2016, doi: 10.1016/j.enconman.2016.08.024.

[43] M. Preißinger and D. Brüggemann, "Thermal stability of hexamethyldisiloxane (MM) for high-temperature organic Rankine cycle (ORC)," *Energies*, vol. 9, p. 183, 3 2016, doi: 10.3390/en9030183.

[44] G. Angelino and C. Invernizzi, "Experimental investigation on the thermal stability of some new zero ODP refrigerants," *International Journal of Refrigeration*, vol. 26, pp. 51–58, 1 2003, doi: 10.1016/S0140-7007(02)00023-3.

[45] P. Colonna and T. van der Stelt, "FluidProp (version 3.1): A program for the estimation of thermophysical properties of fluids," 2019, software.

[46] J. Gross and G. Sadowski, "Perturbed-chain SAFT: An equation of state based on a perturbation theory for chain molecules," *Industrial & engineering chemistry research*, vol. 40, no. 4, pp. 1244–1260, 2001, doi: 10.1021/ie0003887.

[47] P. Rehner, A. Bardow, and J. Gross, "Modeling mixtures with PC-SAFT: Insights from large-scale parametrization and group-contribution method for binary interaction parameters," *Journal of Thermophysics*, 08 2023, doi: 10.1007/s10765-023-03290-3.

[48] J. Liu, Y. Liu, C. Liu, L. Xin, and W. Yu, "Experimental and theoretical study on thermal stability of mixture R1234ze (E)/R32 in organic Rankine cycle," *Journal of Thermal Science*, pp. 1–19, 2023, doi: 10.1007/s11630-023-1790-2.

[49] S. Gallarini, A. Spinelli, L. Lietti, and A. Guardone, "Thermal stability of linear siloxanes and their mixtures," *Energy*, vol. 278, p. 127687, 2023, doi: 10.1016/j.energy.2023.127687.

[50] F. Fortin, U. M. Gardner, M. Parizeau, and C. Gagné, "DEAP: Evolutionary algorithms made easy," *Journal of Machine Learning Research*, vol. 13, pp. 2171–2175, 2012.

[51] G. Angelino, C. Invernizzi, and E. Macchi, "Organic working fluid optimization for space power cycles," *Modern Research Topics in Aerospace Propulsion*, pp. 297–326, 1991, doi: 10.1007/978-1-4612-0945-4$_1$6.

4

CC-APU FOR THE PROVISION OF GROUND POWER

Parts of this chapter have been submitted to the Journal of the Global Power and Propulsion Society.

ABSTRACT

The prime mover of current-day auxiliary power units (APUs) onboard passenger aircraft is a small single-shaft gas turbine. Given the low overall pressure ratio and turbine inlet temperature of these engines, their thermal efficiency is low and typically in the range of $15-20\%$. For a short-range flight, the fuel consumption of the APU amounts to approximately 1.0–1.5% of the mission fuel mass. Therefore, an improvement in APU efficiency is desirable. This paper documents an investigation of the feasibility of adding an organic Rankine cycle (ORC) waste heat recovery (WHR) system to the APU. Furthermore, the simulations and resulting analysis of this simple configuration provide a test case to verify a newly developed multidisciplinary design method based on reduced-order models of the aircraft, the gas turbine, and the ORC system in preparation for more complex studies on so-called combined-cycle power units and engines. The simulation infrastructure is implemented in Python and allows for the analysis of the thermodynamic performance and the estimation of the system size and mass. This method is coupled with an optimizer to identify the combined-cycle APU (CC-APU) design leading to the lowest mission fuel mass, under the assumption that the CC-APU is only used to provide power during ground operation. The case study considers the replacement of the 250 kW APU of an Airbus A320neo with the envisaged CC-APU and investigates its impact on mission fuel burn for a 600 NM mission. Results indicate that the fuel consumption of the CC-APU associated with the provision of ground power can be 50% lower than the fuel consumption of the currently installed APU. This corresponds to a reduction of overall mission fuel mass of 0.6%. The thermal efficiency of the optimal CC-APU design is 34% and the dry mass is 148 kg. The ORC WHR unit features an estimated mass-specific power of 1.7 kW/kg. The design of the ORC WHR unit is driven by system size and mass constraints rather than achieving optimal thermodynamic performance. This is in contrast to conventional applications of such systems for stationary applications. In the future, the developed simulation infrastructure will be extended to assess the feasibility of ORC WHR systems for larger power-capacity aircraft engines.

4.1. INTRODUCTION

Efforts to make aviation environmentally more sustainable mostly focus on fuel burn reduction during flight. While the main engines cause the majority of ground-based emissions, extended operating times of auxiliary power units (APUs) combined with their poor thermal efficiency of around 18% [1, 2] contribute a non-negligible share to overall pollution. The purpose of APUs is to provide secondary power in the form of compressed air to the environmental control system (ECS) or the main engine starter, and electrical power to other auxiliary systems. Normally, APUs are operated only on the ground. However, in emergency situations, they can also provide a limited amount of power during flight. The availability of ground power often determines whether the APU has to be used for extended times, and some airports impose restrictions on their use. Such restrictions, for example, dictate maximum APU running times in case both electrical power and compressed air can be provided at the parking stand. According to the database of the Boeing Company [3], 137 out of 651 airports enforce regulations on the use of APUs.

To better quantify the impact of APU-induced emissions, Padhra [4] conducted a field study tracking the APU usage of 200 Airbus A320 aircraft in service in Europe on short-range routes between 125 airports. Data related to more than 25,000 turnarounds were obtained from the flight data recorders of these aircraft. The analysis of these data specifically addressed APU-induced emissions during aircraft turnaround operations while in the parking position. The study concludes that the use of electric grid power can lead to ground emission reductions of about 50%. Furthermore, time stamps of APU usage after arrival at the stand and before departing from the stand show that only in 6% of the cases the time restrictions imposed by airport regulations are complied with. It is highlighted that especially unforeseen delays in leaving the parking position cause unnecessarily long APU running times.

APU-related emissions can be lowered by increasing the availability of ground power at airports and by improving APU thermal efficiency. The thermal efficiency of gas turbines can be enhanced by increasing the overall pressure ratio (OPR) and turbine inlet temperature (TIT) and/or by further optimizing turbomachinery aerodynamics. However, some of these improvements are difficult to achieve if the power capacity is low. Small-scale effects penalize turbomachinery efficiencies and make turbine blade cooling unfeasible, which, in turn, limits the maximum TIT [5]. One way of circumventing these inherent limitations on the thermal efficiency of small gas turbine engines may be the addition of an organic Rankine cycle (ORC) system to convert the thermal energy of the gas turbine exhaust into additional power. However, the knowledge base on the design of such systems and their impact on aircraft emissions is still very limited and inconclusive regarding the concept of waste heat recovery (WHR) onboard of aircraft.

To provide more detailed information about the feasibility of combined-cycle engines onboard aircraft, a multidisciplinary simulation framework is developed and documented here. This framework, named ARENA (airborne thermal energy harvesting for aircraft), is implemented in Python and includes modules for gas turbine and ORC system performance simulation as well as for the concurrent preliminary design of the ORC turbine and heat exchangers (HEX). The system mass is estimated based on component sizing and empirical correlations. The impact of system mass on fuel consumption for a given flight mission is estimated using the Breguet range equation. An optimizer is used to identify combined-cycle design variables that result in minimum mission fuel mass. As a first demonstrative case, the ARENA framework is used to investigate the possible benefit of employing an ORC WHR unit to recover thermal energy from the APU's exhaust gas of an Airbus A320neo, which is used to provide secondary power on ground only. The overall fuel mass for a 600 NM mission is calculated and compared with that of the aircraft employing the conventional APU, namely the Garrett GTCP36-300 APU [2].

This chapter is structured as follows. In Section 4.2, the methodology to design the CC-APU is presented. Based on this methodology an optimization problem is formulated whereby the objective is the minimization of mission fuel mass. In Section 4.3 this method is applied to the design of an optimized CC-APU, and the change in fuel consumption with respect to a nominal APU is computed together with other figures of merit. Conclusions are drawn in Section 4.4, and recommendations for further research are presented.

4.2. METHODOLOGY

Given the typical operational pattern of APUs, the ARENA framework is used to assess the performance of the system at one operating condition, namely ground operation. The ARENA framework consists of four main modules implementing models to determine 1) the APU on-design performance, 2) the ORC system on-design performance, 3) the preliminary design of the ORC turbogenerator and its performance, and 4) the preliminary design of the heat exchangers (HEX). Figure 4.1 provides a sketch of the aft of the aircraft housing the APU, indicating major dimensions, and a possible placement of the ORC components. Figures 4.2 and 4.3 show the process flow diagram (PFD) and the extended design structure matrix (XDSM) of the CC-APU system. The XDSM indicates dependencies between components with the thick gray lines, and the thin black line indicates the computational flow. The exchange of dependent variables between disciplines is indicated with the gray boxes. The white boxes at the top row of the diagram indicate the required user input data.

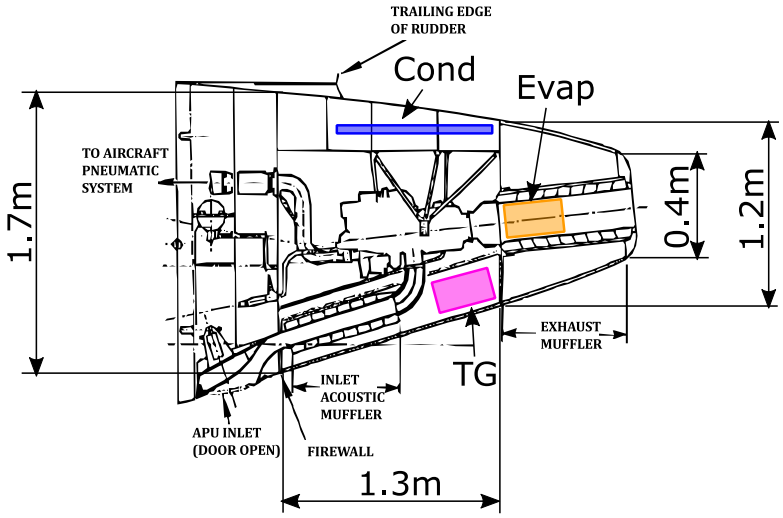

Figure 4.1: Sketch of the APU compartment adapted from Ref. [2] indicating major dimensions as taken from Ref. [6]. The shaded boxes, which are not to scale, indicate possible locations of the condenser (Cond), evaporator (Evap), and ORC turbogenerator (TG).

4.2.1. OPTIMIZATION PROBLEM

Numerical optimization is used to determine the CC-APU design, which minimizes the mission fuel mass (m_{fuel}). Therefore, the constrained single-objective optimization prob-

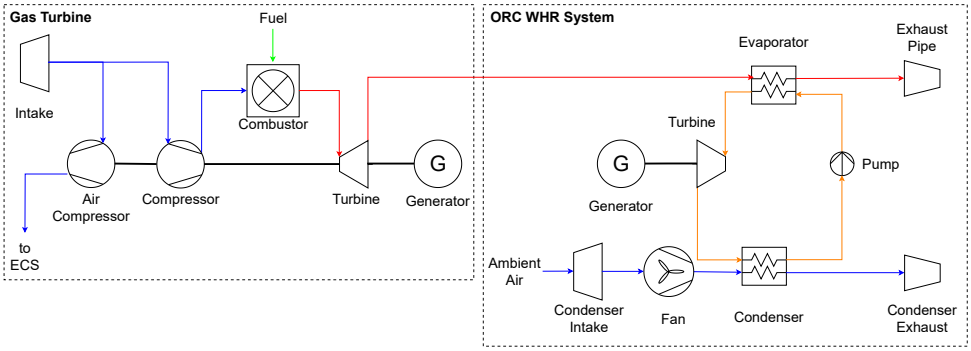

Figure 4.2: Process flow diagram of the CC-APU system configuration.

lem that is solved can be written as

$$\begin{aligned} \text{minimize} \quad & F(\boldsymbol{x}) = m_{\text{fuel}}(\boldsymbol{x}), \\ \text{subject to} \quad & \Delta p_{\text{c,cond}} \leq 600\,\text{Pa}, \\ & X_{\text{cond}} \leq 1.0\,\text{m}, \\ & Z_{\text{evap}} \leq 0.8\,\text{m}, \\ & x_i^{\text{L}} \leq x_i \leq x_i^{\text{U}}. \end{aligned} \tag{4.1}$$

This optimization problem comprises three constraints. The pressure drop between the inlet and the outlet of the cold side of the condenser ($\Delta p_{\text{c,cond}}$) is constrained to a realistic value, which is set according to common practice. Similarly, the width of the condenser core (X_{cond}) and the depth of the evaporator core (Z_{evap}) are also constrained to maximum values, which would allow them to fit within the available space. It is assumed that all heat exchangers are placed within the tail cone of the aircraft, which also houses the APU. The values of the maximum dimensions of the heat exchangers are determined by estimating lengths using the drawings of the APU compartment provided by Stohlgren and Werner [2] and by Airbus [6] (see Fig. 4.1). The design vector ($\boldsymbol{x}$) is composed of 15 variables characterizing either the thermodynamic cycle or the components of the CC-APU system, namely the gas turbine, the ORC unit, the ORC turbogenerator, and the heat exchangers. Table 4.1 lists the design variables (x_i) together with their lower bounds (x_i^{L}) and upper bounds (x_i^{U}). The optimization problem is solved using a genetic algorithm implemented in the Python library *pymoo* [7]. A population size of ten times the number of design variables is adopted. The convergence criterion is as follows: the relative change between the last and the 5^{th}-to-last generation should be lower than 10^{-6}.

4.2.2. AIRCRAFT AND MISSION SETTINGS

The Airbus A320neo has an operating empty mass (m_{oe}) of 43 520 kg, a lift-to-drag ratio (L/D) of 17.9, estimated using a method proposed by Torenbeek [8], and a thrust-specific fuel consumption (TSFC) at cruise of 14.4 mg/Ns. The TSFC is calculated for the CFM LEAP-1A engine based on information reported in the database of Ref. [9]. The

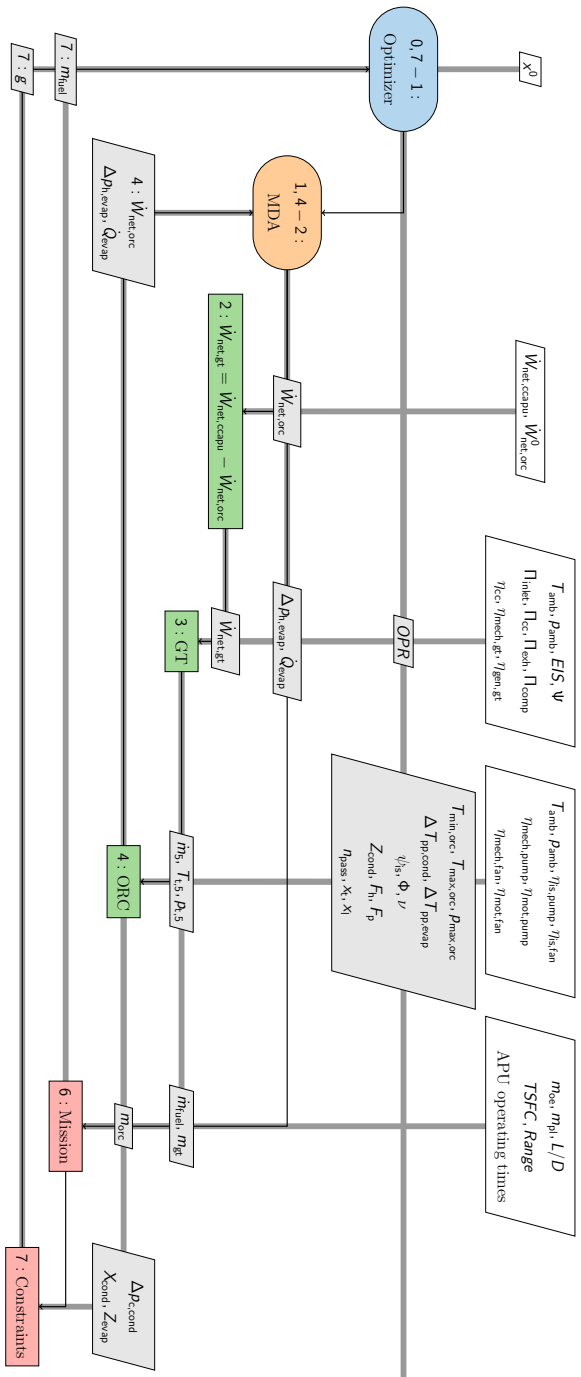

Figure 4.3: Extended design structure matrix of the CC-APU system model.

Table 4.1: CC-APU: design variables and their bounds.

Model	Variables (x_i)	Description (Unit)	Bounds ($x_i^{\mathrm{L}}/x_i^{\mathrm{U}}$)
APU	OPR	Overall pressure ratio (-)	4/10
ORC	$T_{\mathrm{min,orc}}$	Minimum cycle temperature (K)	323/423
	$T_{\mathrm{max,orc}}$	Maximum cycle temperature (K)	$1.01\,T_{\mathrm{crit}}/1.07\,T_{\mathrm{crit}}$
	$p_{\mathrm{max,orc}}$	Maximum cycle pressure (Pa)	$1.05\,p_{\mathrm{crit}}/1.50\,p_{\mathrm{crit}}$
	$\Delta T_{\mathrm{pp,cond}}$	Condenser pinch point temperature difference (K)	10/50
	$\Delta T_{\mathrm{pp,evap}}$	Evaporator pinch point temperature difference (K)	10/50
ORC Turbo-generator	ψ_{is}	Isentropic stage loading (-)	0.4/1.3
	ϕ	Flow coefficient (-)	0.10/0.40
	ν	Hub-to-tip ratio (-)	0.40/0.65
ORC HEX	Z_{cond}	Condenser core depth (mm)	30/70
	F_{h}	Condenser fin height (mm)	7.0/12.0
	F_{p}	Condenser fin pitch (mm)	1.0/2.0
	x_{t}	Evaporator non-dimensional transversal pitch (-)	1.25/3.00
	x_{l}	Evaporator non-dimensional longitudinal pitch (-)	1.25/3.0
	n_{pass}	Evaporator number of passes (-)	8/20

m_{oe} of the aircraft equipped with the CC-APU is computed considering that the operating empty mass of the reference aircraft includes the dry mass of the conventional APU amounting to 117 kg [2]. The analyzed mission is over a range of 600 NM[1] at a cruise Mach number of 0.78 and a payload mass (m_{pl}) of 19 280 kg. The mission is split up into a ground phase (parking, taxing) and a flight phase (take-off, climb, cruise, descend, landing). The fuel consumption of the flight phase is estimated using the Breguet range equation for a cruise at constant altitude and Mach number [8]. The TSFC at cruise conditions and the fuel fractions for the non-fuel intensive flight phases (take-off, climb, descend, and landing) used for the computation are those reported by Roskam [10]. The product of the fuel fractions is 0.96. The fuel consumption of the ground phase is calculated by multiplying the fuel flow rate of the APU and of the main engine with the corresponding operating times for short-range routes as listed in Tab. 4.2. Single-engine taxiing is assumed with an engine fuel flow rate of 5.8 kg/min [11]. During single-engine taxiing, only one main engine is used to provide thrust for taxiing, while the APU provides secondary power. A report of Airbus [11] highlights the economic benefits of this procedure with respect to fuel burn and maintenance cost if compared to the main engines. The summation of the fuel consumption of the ground phase and the flight phase gives the overall mission fuel mass (m_{fuel}).

Furthermore, it is assumed that the APU covers the full secondary power demand during the ground phase. Based on data provided by Stohlgren and Werner [2], the secondary power demand under hot-day (ISA+25) sea-level conditions is approximately 250 kW. This includes the power to drive the air compressor and the gas turbine mounted

[1] This range corresponds to the average distance flown in Europe in the year 2022 according to data of Eurocontrol, https://ansperformance.eu/economics/cba/standard-inputs/chapters/ifr_average_flight_distance_and_flight_duration.html, accessed on 24 July 2024.

generator. In case of the CC-APU, the power demand is supplied by the gas turbine which drives the air compressor ($\dot{W}_{\text{shaft,gt}}$), the electrical generator connected to the gas turbine ($\dot{W}_{\text{gen,gt}}$) and the net power output of the ORC unit ($\dot{W}_{\text{net,orc}}$). The net power output of the CC-APU ($\dot{W}_{\text{net,ccapu}}$) is therefore

$$\dot{W}_{\text{net,ccapu}} = \dot{W}_{\text{net,gt}} + \dot{W}_{\text{net,orc}} \quad \text{with} \quad \dot{W}_{\text{net,gt}} = \dot{W}_{\text{shaft,gt}} + \dot{W}_{\text{gen,gt}}. \tag{4.2}$$

The combined-cycle efficiency ($\eta_{\text{net,ccapu}}$) is thus

$$\eta_{\text{net,ccapu}} = \frac{\dot{W}_{\text{net,ccapu}}}{\dot{m}_{\text{fuel}} \cdot \text{LHV}}, \tag{4.3}$$

where $\dot{m}_{\text{fuel}}$ is the gas turbine fuel flow rate and LHV is the lower heating value of the fuel, which is assumed to be 43 MJ/kg.

The performance of the aircraft utilizing the CC-APU system is compared with a reference case utilizing the GTCP36-300 APU [2] on board the Airbus A320neo. The reference fuel mass $m_{\text{fuel,ref}}$ obtained for the given mission is 6815 kg and the APU fuel mass for the provision of secondary power on the ground $m_{\text{fuel,apu}}$ amounts to 78 kg. Notice that the Airbus A320neo adopts the Honeywell 131-9 APU [12] and not the GTCP36-300 APU, which often equips the Airbus A320 [2, 4]. However, data presented by Padhra [4] suggest that the fuel consumption of these gas turbines is similar. As more information is available for the GTCP36-300, this type of gas turbine is considered in this study.

Table 4.2: Averaged APU operating times based on 1) APU operation after arrival and before departure of parking position, assuming the availability of ground power [4] and 2) taxi times averaged over the data related to the 100 busiest European airports [13, 14, 15].

Arrival	Departure	Taxi-in	Taxi-out	Sum
6.1 min	17.3 min	5.4 min	12.0 min	40.8 min

4.2.3. GAS TURBINE MODEL

The gas turbine considered in this work is a single-spool turboshaft engine without a free power turbine. It provides shaft power to a generator and to an air compressor. The PFD of the APU is shown in Fig. 4.2, on the left-hand side. The gas turbine model provides as output the performance of the turboshaft engine at the design point as well as its mass. The thermodynamic cycle calculations are complemented with a turbine blade cooling model to predict the required cooling air, and with a procedure to estimate the efficiency of the turbomachines, as detailed in the following sections.

THERMODYNAMIC CYCLE CALCULATION

The thermodynamic properties of the exhaust gas and of the air are modeled using the entropy function as defined by Kurzke and Halliwell [16, Part D] in combination with polynomials for the specific heat at constant pressure given by Walsh and Fletcher [17, Ch. 3]. The fuel is assumed to be Jet-A. Turbomachinery efficiencies are determined using correlations presented by Samuelsson et al. [18], which are derived from the method

described in Ref. [19, Ch. 5]. Based on statistical data, this method provides an estimate of the efficiency of turbomachinery as a function of the entry into service (EIS) date, stage loading, and scale effects based on reduced mass flow rate. Furthermore, the method accounts for different turbomachinery types (axial/radial) and distinguishes between the turbomachinery of the low and high-pressure sections of the engine. In general, the efficiency of a combined-cycle engine increases with TIT [17, Ch. 6]. Therefore, the TIT of the CC-APU is set equal to the maximum allowable TIT (TIT_{max}). The procedure to determine TIT_{max} is presented in Section 4.2.3. A comparison of results obtained with the developed gas turbine performance code and with the commercial software GSP Visser [20] gives an error of 0.5% in the estimated values of air and fuel mass flow rate.

TURBINE COOLING

Due to the small turbine blade size (height < 15 mm) resulting from the low power capacity of the turboshaft engine, blade cooling cannot be implemented except for the nozzle guide vanes (NGVs) of the first stage. For the NGVs, convective air cooling is assumed [21]. The turbine cooling model of Gauntner [22] is adopted to estimate cooling air demand in the NGVs and turbine efficiency degradation due to cooling. The required coolant mass flow rate of the NGVs is based on the maximum allowable blade bulk metal temperature ($\overline{T}_{b,max}$). According to Gauntner [22], $\overline{T}_{b,max}$ of the stator blades can be set to a temperature that is 55 K higher than that of the rotor blades.

MAXIMUM TURBINE INLET TEMPERATURE

$\overline{T}_{b,max}$ of the uncooled first stage rotor blades sets a limit to the stator outlet temperature (SOT) and TIT. SOT refers to the absolute gas temperature at the exit of the NGVs. $\overline{T}_{b,max}$ is estimated assuming creep as the dominant failure mechanism of the rotor blades, and it, therefore, depends on material characteristics, blade stress, and desired minimum lifetime for a certain amount of creep strain. For a given material, the relation between these variables can be captured using the Larson-Miller Parameter (LMP). The LMP is a function of blade temperature (T_b) at a given spanwise section of the blade and lifetime ($t_{b,life}$) in hours for a given amount of creep strain: $LMP = T_b[20 + log(t_{b,life})]$. Creep strain is determined by the combination of blade stress and temperature. Both vary along the blade span. While the highest stress is experienced at the blade root, the highest blade temperatures are around mid-span. As a result, the location of the highest creep strain is located around a quarter or one-third of the blade span [23, Ch. 9]. In this work, creep stress is limited to 90% of the creep rupture stress [23, Ch. 9], which corresponds to a creep strain of approximately 1% for single-crystal alloys according to Grieb [19, Ch. 5]. First-stage rotor blades experience the highest creep due to high centrifugal stress combined with very high temperatures.

In the following, a procedure to determine $\overline{T}_{b,max}$ for uncooled first stage rotor blades and the resulting SOT_{max} is presented. SOT_{max} in combination with the turbine cooling model allows us to determine the value of TIT_{max}. The main assumptions and steps of the procedure are:

1. The stress acting on the turbine rotor blade is determined. To simplify the blade stress calculation, it is assumed that the blade root represents the most critical

section of the blade with respect to creep life, according to Sawyer [23]. Centrifugal blade root stress (σ_r) for a blade with a linear taper ratio (K) is calculated according to Ref. [24, Ch. 8] with

$$\sigma_r = 1.75 \cdot 10^{-9} K \rho_b A N^2 \quad \text{with} \quad K = \frac{1+d_t}{3} + \frac{\nu + d_t}{3(1+\nu^*)}, \tag{4.4}$$

and the mechanical design parameter AN^2 is calculated according to Ref. [19, Ch. 5] with

$$AN^2 = 60^2 \frac{\Delta h_{t,st}}{\Psi} \frac{1}{\pi} \frac{1-\nu^{*2}}{1+\nu^{*2}}. \tag{4.5}$$

Here, ρ_b is the turbine blade material density, d_t is the turbine blade tip-to-hub area ratio, ν^* is the hub-to-tip ratio of the first stage turbine rotor, Ψ is the turbine stage loading and $\Delta h_{t,st}$ is the total enthalpy drop per stage, which is determined assuming equal work per stage. Gas bending stress is neglected. A safety factor of 1.15 is applied to σ_r to take account for cyclic loads (i.e., low and high cycle fatigue) [19, Ch. 5].

2. The maximum allowable temperature at the blade root ($T_{b,root,max}$) is determined. Once σ_r is known, the LMP value can be estimated based on charts derived from experiments for the selected blade material. Figure 4.4 shows such a chart for the single-crystal alloy CMSX-10 and the directionally solidified (DS) nickel-base alloy Rene 150. In combination with the specified blade lifetime, this results in $T_{b,root,max}$ from the definition of LMP. In the presented work, a blade lifetime of $15 \cdot 10^3$ hours is applied, which according to Walsh and Fletcher [17, Ch. 6] equals a typical value for the time between overhaul of civil aircraft engines.

3. $\overline{T}_{b,max}$ is determined. Equation 4.6 provided by Kurzke and Halliwell [16, Ch. 4] makes use of the radial temperature distribution factor (RTDF) to relate exhaust gas temperature at the blade root ($T_{t,rel,root}$) to the averaged exhaust gas temperature at the rotor inlet plane ($\overline{T}_{t,rel}$). The averaged exhaust gas temperature at the rotor inlet plane ($\overline{T}_{t,rel}$) is calculated according to the empirical relation provided by Kurzke and Halliwell [16, Ch. 4] as

$$\overline{T}_{t,rel} = \frac{T_{t,rel,root}}{1 - \text{RTDF}} \tag{4.6}$$

with the exhaust gas temperature at the blade root $T_{t,rel,root}$. The subscript "rel" indicates that these temperatures are in the relative reference frame of the rotor blades. Based on the simplifying assumption of a recovery factor of unity, gas and metal temperatures are equal. Therefore, in Eq. 4.6 $\overline{T}_{t,rel}$ can be substituted with $\overline{T}_{b,max}$ and $T_{t,rel,root}$ with $T_{b,root,max}$. Furthermore, an RTDF of 0.08 [19, Ch. 5] is applied.

4. The application of a thermal barrier coating (TBC) to the stator blades allows to increase SOT_{max}. In this case, a temperature difference across the TBC (ΔT_{tbc}) is added to $\overline{T}_{b,max}$. Based on data provided by Grieb [19, Ch. 5] a ΔT_{tbc} of 100 K is applied to the stator blades.

5. The value of $\overline{T}_{t,rel}$ that allows an uncooled rotor blade is determined. Turbine cooling design is based on a hotspot temperature ($T_{t,rel,hotspot}$). This temperature is defined as

$$T_{t,rel,hotspot} = \overline{T}_{t,rel} + \mathrm{RTDF}(\mathrm{TIT} - T_{t,3}), \tag{4.7}$$

where the term $\mathrm{TIT} - T_{t,3}$ indicates the combustor temperature rise. For an uncooled rotor blade, the following relation must hold: $T_{t,rel,hotspot} = \overline{T}_{b,max}$. Substituting this relation into Eq. 4.7 and rearranging the equation allows to identify the value of $\overline{T}_{t,rel}$ that fulfills the requirement of having no rotor blade cooling.

6. Finally, SOT_{max} is determined by converting the average temperatures from the relative to the absolute reference frame according to

$$\overline{T}_{t,abs} = \overline{T}_{t,rel} + \Delta T_{t,abs,st}\left(0.5 - \frac{r-1}{\Psi}\right), \tag{4.8}$$

with a degree of reaction (r) of 0.5 [19, Ch. 5], and $\overline{T}_{t,abs}$ and $\Delta T_{t,abs,st}$ are the averaged total temperature in the absolute reference frame entering the rotor row and the total temperature change over the turbine stage, respectively. In this equation $\overline{T}_{t,abs}$ can be substituted with SOT_{max} and $\overline{T}_{t,rel}$ results from Eq. 4.7. The following equation gives the final expression to determine SOT_{max}.

$$\mathrm{SOT}_{max} = \frac{T_{b,root,max}}{1-\mathrm{RTDF}} - \mathrm{RTDF}(\mathrm{TIT} - T_{t,3}) + \Delta T_{t,abs,st}\left(0.5 - \frac{r-1}{\Psi}\right) \tag{4.9}$$

In the case of an uncooled stator, the value of TIT_{max} is directly evaluated by setting it equal to SOT_{max}. However, in the case of a cooled stator, the procedure above is iterative. First, based on an initial value for TIT and the value obtained for $\overline{T}_{b,max}$ the needed coolant mass fraction is calculated as explained in Section 4.2.3. For this purpose, the stator cooling air temperature is taken equal to the compressor discharge temperature ($T_{t,3}$). Second, the value of TIT_{max} is updated based on SOT_{max} resulting from Eq. 4.9 assuming isentropic mixing of the main exhaust gas stream with stator cooling air. Third, the updated value of TIT_{max} is used to re-evaluate the thermodynamic cycle and SOT_{max} until convergence of the entire system model is achieved.

The applicability of this method in estimating $\overline{T}_{b,max}$ is verified by comparison with computations of Halila et al. [25] for the turbine of a gas generator test rig. The two-stage high-pressure turbine design of Halila et al. [25] is characterized by film-cooled rotor blades made of directionally solidified Rene 150 superalloy. The life ($t_{b,life}$) of the first stage rotor blades is 250 h under hot-day take-off conditions. The first stage features a Ψ of 1.48 and a ν of 0.88. The value of d_t of the rotor blades is not specified. Under hot-day take-off conditions $\overline{T}_b$ of these rotor blades is 1230 K. This data is used as input for steps 1) to 3) and yields $\overline{T}_{b,max}$ = 1190 K for d_t = 1.0 and $\overline{T}_{b,max}$ = 1200 K for d_t = 0.8. These results are based on a limitation of creep stress to 90% of the rupture stress (see Fig. 4.4). The resulting error is below 4%, which is acceptable at the conceptual design level of the present work.

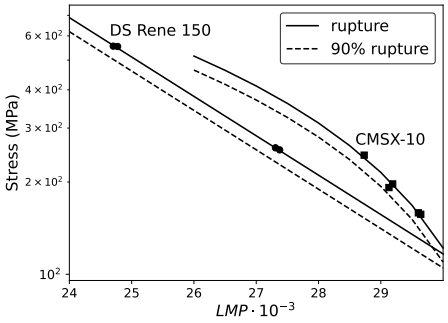

Figure 4.4: Creep rupture stress and 90% creep rupture stress over LMP for 3rd generation single crystal alloy CMSX-10 and the directionally solidified (DS) nickel-base alloy Rene 150. The markers indicate experimental data points taken from Refs. [26, 27]. A logarithmic curve fit is applied to the experimental data points of CMSX-10, which compares well with data provided in Ref. [24] and an exponential fit to the data of DS Rene 150.

4

GAS TURBINE MASS

The mass of the gas turbine including the generator (m_{gt}) is estimated, to a first approximation, with an empirical correlation whose sole input is the compressor entry mass flow rate ($\dot{m}_0$). Data available in the database of Ref. [9] for 12 turboshaft engines in the power range of 300-3000 kW are used to derive the following relation

$$m_{gt} = 21.56\dot{m}_0 + 85. \tag{4.10}$$

with an R^2 value of 0.9. It must be acknowledged that such a correlation based on historical data can only give a rough estimate of the engine mass. This is especially true for combined-cycle applications, where OPR and TIT might vary with respect to conventional turboshaft engine configurations. Furthermore, the turboshaft engines used to produce this correlation do not employ a dedicated air compressor such as APUs usually do. For this reason, air compressor mass is neglected in the presented work. Despite this fact, inserting the mass flow rate of the GTCP36-300 APU [1] into Eq. 4.10 yields a mass that is only 2% off of the actual mass.

GAS TURBINE DESIGN ASSUMPTIONS

The gas turbine is sized for hot-day (ISA+25) sea level static (SLS) conditions. The upper part of Fig. 4.5 depicts the power transmission architecture of the gas turbine. A mechanical efficiency of the gas turbine shaft ($\eta_{mech,gt}$) of 99% [17, Ch. 5], a gearbox efficiency (η_{gbx}) of 99% [17, Ch. 5], and a gas turbine generator efficiency ($\eta_{gt,gen}$) of 95% [28] are assumed. Gas turbine efficiency is defined as

$$\eta_{net,gt} = \frac{\dot{W}_{net,gt}}{\dot{m}_{fuel} LHV}. \tag{4.11}$$

In the present work, an axial-radial compressor is employed with a varying number of stages depending on OPR. For an OPR below or equal to 4, a single radial stage is as-

sumed. For OPR above 4, a stage pressure ratio of 3.2 is assumed for the radial component and a stage pressure ratio (Π_{comp}) of at most 1.5 for each axial stage needed to reach the selected OPR value. The polytropic efficiency of the axial and radial compressors are determined independently based on the method of Grieb [19, Ch. 5]. The turbine is a two-stage axial turbine with a stage loading (Ψ) 3.0. An EIS of 2035 is assumed for turbomachinery efficiency estimation. The maximum value of OPR is limited by the requirement of a feasible blade height at the exit of the compressor. The upper bound of OPR is determined based on geometrical relations for axial-radial compressors provided by Grieb [19, Ch. 5], knowledge of the expected air mass flow rate of the gas turbine, and a minimum blade height at the exit of the radial compressor of 5 mm, which is similar to the value reported by Ripolles [21]. A relative nozzle pressure ratio of 0.08% is applied, which is defined as $\Pi_{exh} = \frac{p_{t,9} - p_{amb}}{p_{t,9}}$, where $p_{t,9}$ refers to the total pressure at the exit of the exhaust pipe. Note that the value of Π_{exh} is outside the range of typical values applied for turboshaft and turboprop engine design which is 2-10% according to Grieb [19, Ch. 6]. Lowering Π_{exh} results in a larger exhaust pipe diameter and lower exhaust gas velocities for the same mass flow rate. While potentially increasing the cross-sectional area of the engine, this allows a reduction of evaporator hot side pressure loss ($\Delta p_{h,evap}$) and, therefore, an improvement of engine performance. An increase of $\Delta p_{h,evap}$ by 1% results in a reduction of APU efficiency of 0.2%. The single-crystal alloy CMSX-10 [26] is considered as the turbine blade material. The hub-to-tip ratio (ν^*) of the first stage turbine rotor is set to 0.825, which represents an averaged value for multi-stage high-pressure turbines [19, Ch. 5] and the turbine blade tip-to-hub area ratio (d_t) is set to 0.8 [23, Ch. 9]. Values for air intake pressure ratio (Π_{inlet}) of 0.985 and combustor pressure ratio (Π_{cc}) of 0.965 for the GTCP36-300 APU are taken from Ref. [2]. Furthermore, a combustion efficiency (η_{cc}) of 99.5% [29, Ch. 4] is assumed.

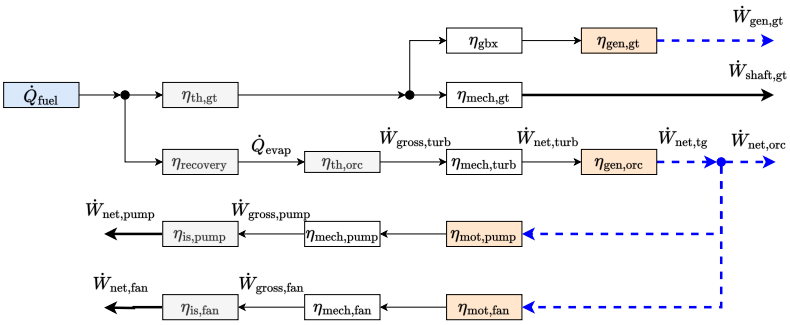

Figure 4.5: Flow chart of the CC-APU power transmission architecture indicating main components that are incurring losses; black lines indicate mechanical power, dashed lines indicate electrical power.

4.2.4. ORC WASTE HEAT RECOVERY SYSTEM MODEL

The simulation of the organic Rankine cycle system is conducted using an in-house tool for on-design point thermodynamic cycle calculations *pycle*. This program was verified by comparison with a commercial program for thermodynamic modeling and optimiza-

tion of energy conversion systems [30]. The Helmholtz equation of state implemented in CoolProp [31] is used for thermodynamic fluid property modeling of the ORC working fluid, while the ideal gas model of Ref. [32] is used for the APU exhaust gas through the evaporator. For simplicity, a fixed mass-specific composition of the exhaust gases is assumed, containing 74% N_2, 15.9% O_2, 6.4% CO_2, 2.5% H_2O, 1.2% Ar. This composition is representative of an engine burning Jet-A/A1 at a fuel-to-air ratio of 0.02. Figure 4.2, on the right-hand side, shows the PFD of the ORC, which is of the non-recuperated type. Table 4.3 gives the ORC thermodynamic cycle specifications and indicates the input derived from other sub-models. The ORC unit is designed for the same environmental conditions as the APU, i.e., SLS ISA+25. In the present study, the hydrocarbon cyclopentane is considered as the working fluid. Cyclopentane has a critical temperature (T_{crit}) of 512 K, a critical pressure p_{crit} of 45.1×10^5 Pa and a normal boiling point temperature of 322 K [33]. As identified in Chapter 3, due to its high thermal stability ($T_{max,fluid}$) of 573 K [34] and high T_{crit} cyclopentane is especially suited for WHR applications of medium power-capacity gas turbines. However, it is possible that cyclopentane is not the optimal working fluid for the low power-capacity application studied in this work. Future investigations will focus on selecting the optimum working fluid for airborne ORC WHR systems. With the upper optimization bound applied to $T_{max,orc}$ (see Tab. 4.1), it is ensured that a safety margin is maintained with respect to $T_{max,fluid}$. A supercritical cycle is adopted in this study to maximize thermodynamic efficiency resulting from high $T_{max,orc}$. No benefits in terms of system weight and HEX performance are expected for subcritical cycles for the following three reasons:

- Evaporator mass highly depends on tube thickness which in turn is a function of the pressure difference between the cold and hot sides of the tube. The design routine selects a tube thickness close to the minimum value from a manufacturability standpoint for the chosen working fluid, supercritical operating conditions, and HEX materials. Therefore, no significant mass savings are expected for the subcritical cycle.

- For a subcritical cycle, the majority of evaporator heat duty is exchanged during phase change at a constant temperature. Therefore, the evaporator adopts the effectiveness of a counterflow heat exchanger. This is also true for any multipass counter-crossflow HEX with a large number of passes [35]. Since this is the chosen layout for the evaporator, the benefit of the effectiveness gain due to phase change in a subcritical cycle is diminished.

- The thermal resistance of the evaporator is dominated by the low heat transfer coefficient that is encountered on the hot gas side. Therefore, no advantage is gained from the increased heat transfer coefficient on the working fluid side during isothermal phase change.

The ORC turbine gross power ($\dot{W}_{gross,turb}$) is converted into electrical power via a dedicated generator (see Fig. 4.5). The turbine mechanical efficiency ($\eta_{mech,turb}$) and ORC generator efficiency ($\eta_{gen,orc}$) are an output of the ORC turbogenerator preliminary design procedure explained in Section 4.2.6. An electrically driven fan provides the necessary air mass flow rate through the condenser during ground operations. The fan power

Table 4.3: Main parameters and variables of the ORC waste heat recovery unit model.

Parameter	Input	Parameter	Input	Parameter	Input
$T_{max,orc}$	Design variable	$\Delta p_{h,evap}$	HEX model	$\eta_{is,pump}$	65%
$T_{min,orc}$	Design variable	$\Delta p_{c,evap}$	HEX model	$\eta_{is,turb}$	Turbogenerator model
$p_{max,orc}$	Design variable	$\Delta T_{pp,evap}$	Design variable	$\eta_{is,fan}$	60%
T_{amb}	313.15 K	$\Delta p_{h,cond}$	HEX model	$\eta_{mot,pump}$, $\eta_{mot,fan}$	98%
$\dot{m}_{h,evap}$	APU model	$\Delta p_{c,cond}$	HEX model	$\eta_{mech,pump}$, $\eta_{mech,fan}$	99%
$T_{h,evap,in}$	APU model	$\Delta T_{pp,cond}$	Design variable		

Note: Subscripts h and c indicate heat exchanger (HEX) hot and cold sides.

consumption ($\dot{W}_{net,fan}$) is calculated with

$$\dot{W}_{net,fan} = \frac{\dot{m}_{air}\Delta p_{c,cond}}{\rho_{air}\eta_{is,fan}}, \tag{4.12}$$

where $\dot{m}_{air}$ is the air mass flow rate, ρ_{air} the air density and $\eta_{is,fan}$ the fan isentropic efficiency. As depicted in Fig. 4.2 the fan is placed in front of the condenser. Placement of the fan behind the condenser results in higher $\dot{W}_{net,fan}$ due to the reduced air density, and exposing the fan to a higher air temperature could complicate its design. A $\eta_{is,fan}$ of 60% is selected based on experience with similar systems designed for stationary use. Note that $\Delta p_{c,cond}$ only includes the pressure losses originating from the condenser and does not account for losses induced by the ducting, which are not modeled. Preliminary design of the electrically driven pump is not performed. Based on the pump selection guide provided in Ref. [36, Ch. 1] the expected pump head and volumetric flow rate suggest the use of a positive displacement pump or centrifugal pump. Positive displacement pumps are more suited for fluids with higher viscosity that can also provide lubrication. Due to the low viscosity of the considered working fluid a centrifugal pump is adopted. Research on electrically driven centrifugal pumps for small space launch vehicles conducted by Kwak et al. [37] suggests a mass-specific power of around 4 kW/kg and an isentropic pump efficiency $\eta_{is,pump}$ of around 65%. The efficiency of the pump motor ($\eta_{mot,pump}$) and fan motor ($\eta_{mot,fan}$) are assumed to be 98% as suggested by Schmollgruber et al. [28] for an EIS year of 2035. Furthermore, a pump ($\eta_{mech,pump}$) and fan mechanical efficiency ($\eta_{mech,fan}$) of 99% are assumed. ORC efficiency based on $\dot{W}_{net,orc}$ is defined as

$$\eta_{net,orc} = \frac{\dot{W}_{net,orc}}{\dot{Q}_{evap}}, \tag{4.13}$$

where $\dot{Q}_{evap}$ is the thermal power recovered by the evaporator. According to Fig. 4.5 $\dot{W}_{net,orc}$ is defined as

$$\dot{W}_{net,orc} = \dot{W}_{gross,turb}\eta_{mech,turb}\eta_{gen,orc} - \frac{\dot{W}_{net,pump}}{\eta_{mech,pump}\eta_{mot,pump}} - \frac{\dot{W}_{net,fan}}{\eta_{mech,fan}\eta_{mot,fan}}. \tag{4.14}$$

Furthermore, the recovery factor (χ) describes how much of the available thermal power ($\dot{Q}_{exh,avail}$) is recovered by the WHR system and it is defined as

$$\chi = \frac{\dot{Q}_{evap}}{\dot{Q}_{exh,avail}}. \tag{4.15}$$

$\dot{Q}_{exh,avail}$ is defined as the product of the exhaust gas mass flow rate and the specific enthalpy difference between the turbine exit and ambient conditions.

The ORC system mass is the sum of pump (m_{pump}), turbogenerator (m_{tg}), condenser (m_{cond}), evaporator (m_{evap}), working fluid (m_{fluid}), fan, and balance-of-plant masses. m_{tg} is the sum of the ORC turbine mass (m_{turb}) and the ORC generator mass ($m_{gen,orc}$). The heat exchanger and turbogenerator masses are an outcome of the respective sub-models. The working fluid mass is estimated as the product of 1.2 times the evaporator cold side volume and the density of the working fluid at one atmosphere and 25 °C. The mass of the fan, including its motor and balance-of-plant, is assumed to contribute 10% to the overall system mass. This value is similar to the assumption made by Zarati et al. [38]. However, as the knowledge base on flying ORC systems is small a large amount of uncertainty is related to this value.

4.2.5. HEAT EXCHANGER PRELIMINARY DESIGN

The preliminary design of the heat exchangers for the CC-APU is carried out by means of a dedicated in-house software developed in Python named *HeXacode*, which is integrated with the ARENA framework. The program was verified by comparison with a commercial code for heat exchanger design and rating [39]. The two heat exchangers of the ORC system under consideration are the supercritical evaporator and the condenser. The sizing tools aim at finding the heat transfer area that satisfies the required heat duty given the inlet temperatures, inlet pressures, and mass flow rates of the hot and cold streams. The core materials and geometric parameters are also an input to the model. The preliminary design routine then returns the size, mass, and pressure drops on both fluid sides of the heat exchanger. In the following, an overview of each heat exchanger model is presented.

EVAPORATOR

Figure 4.6 shows the chosen layout and topology for the evaporator, which is a multi-pass bare-tube-bundle HEX placed right after the turbine diffuser in a counter-crossflow arrangement. This configuration, as shown by Sabau et al. [40] yields smaller exergy losses in a supercritical cycle because of a better thermal match between the heat source and the working fluid. The Nickel-base alloy Hastelloy® X is chosen as the material for the evaporator as suggested by Grieb [19, Ch. 5] based on mechanical considerations. Preliminary system design runs showed that reducing the pressure drop on the hot side of the evaporator yields significant improvements in the overall combined-cycle efficiency. Although in-line tube bundles are usually heavier than their staggered counterpart for a given frontal area, the cycle efficiency improvement that can be achieved with a lower hot side pressure drop outweighs the effect of the increased mass of the HEX. For this reason, the in-line tube arrangement is chosen instead of the staggered one.

As fluid properties can change significantly for fluids in supercritical conditions, the sizing routine divides the HEX into several subsections or cells in which fluid property variations are small. The total heat duty of the HEX is then distributed over each cell following a logarithmic distribution. In the present study, the number of cells is conveniently set equal to the number of passes, which is an input to the design problem.

Initially, a uniform pressure distribution across the cells in the two streams is assumed. This pressure distribution is updated in a convergence loop with the pressure drop estimate until both the fluid properties and the calculated pressure drop in each cell do not change. As a result, the preliminary design problem can be split into a series of interconnected individual HEX sizing problems, for which the heat transfer area A^i is unknown. The core height (Y_{evap}) and width (X_{evap}) of the evaporator, which determine the hot side frontal area, are input to the problem and are estimated given the cross-sectional area of the gas turbine exhaust pipe, assuming a smooth transition to a square-shaped frontal area. The core depth (Z_{evap}) is, instead, calculated to meet the design specifications as

$$Z_{\text{evap}} = d_{\text{o}} + \frac{x_{\text{t}}\, x_{\text{l}}\, d_{\text{o}}^2}{Y_{\text{evap}}} \left(\sum_{i=0}^{N_{\text{cells}}} \text{round}\left(\frac{A_{\text{c}}^i}{\pi\, d_{\text{i}}\, X_{\text{evap}}} \right) - 1 \right). \tag{4.16}$$

where A_{c}^i is the cold side heat transfer area of the cell i, x_{t} and x_{l} are the transversal and longitudinal pitch, respectively. d_{o} and d_{i} are the tube outer and inner diameters, respectively. The cell cold side heat transfer area is calculated as

$$A_{\text{c}}^i = \frac{\dot{Q}^i (U_{\text{c}}^i)^{-1}}{F^i \Delta T_{\text{ml}}^i}, \tag{4.17}$$

where U_{c}^i is the cold side heat transfer coefficient of cell i that depends on the fluid velocity and properties, ${\Delta T_{\text{ml}}}^i$ is the local mean logarithmic temperature difference and F^i is its correction factor. In the case of heat transfer at non-constant temperature, F^i is lower than unity for any flow arrangement different from the pure counterflow and depends on the local number of transfer units, effectiveness, and heat capacity ratio. The pressure drop across the tube bundle is calculated by combining the laminar ($C_{\text{f,lam}}$) and turbulent ($C_{\text{f,turb}}$) friction coefficients through a switch function (F_{f}) to estimate the non-dimensional pressure drop per tube row [41, Part L], while the heat transfer coefficient on the hot gas side is calculated from the dimensionless pressure drop as shown by Martin [42]. For the working fluid side, the pressure drop inside the tubes is estimated using the friction factor formulation of Brkić and Praks [43] while the Nusselt number of the supercritical fluid is calculated using correlations developed by Pioro and Mokry [44]. The output of each sizing iteration is thus the heat transfer area required in each cell. The sizing routine then stops when the calculated required number of tubes does not change across consecutive iterations. The model then returns the core mass and pressure drops of the heat exchanger, together with the volume occupied by the working fluid and its corresponding mass during nominal operating conditions.

CONDENSER

As depicted in Fig. 4.7, the chosen condenser topology is a flat-tube microchannel heat exchanger with louvered fins. The working fluid flows in small rectangular channels within the flat-tubes, while the air flows through fins of the multi-louvered type. These fins can achieve high levels of compactness (over $1100\,\text{m}^2/\text{m}^3$ [45]) and heat transfer coefficient at the expense of larger pressure drop due to the continuous mixing of the flow passing through the louvers [35]. This HEX topology promotes small and light designs

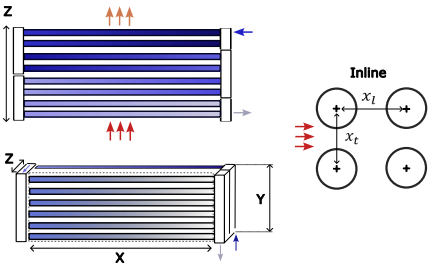

Figure 4.6: Multi-pass bare-tube-bundle heat exchanger.

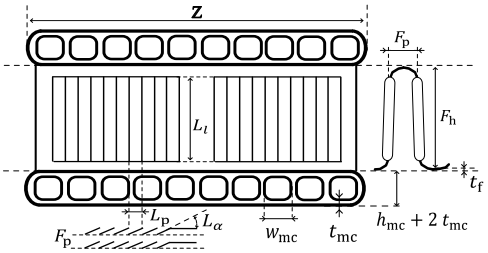

Figure 4.7: Flat-tube microchannel louvered fin heat exchanger.

4

and is often used in the automotive and aerospace sectors. The pitch between two microchannels w_{mc} is fixed equal to the flat-tube height (h_{mc}), which is 2 mm. The louver fin angle (L_α) is set to 27°. The flat-tube length is set equal to the condenser core depth (Z_{cond}), which is used as an optimization variable. The louver pitch (L_p) is taken equal to the fin pitch (F_p), which is an optimization variable. The louver length (L_l) is set to 80% of the fin height (F_h), which is an optimization variable. The fin thickness (t_f) is set to 0.11 mm while the flat-tube wall thickness (t_{mc}) is 0.2 mm. These fixed geometry-specific parameters are chosen based on engineering judgment and manufacturability considerations. The height of the condenser Y_{cond} is fixed to 1.0 m. This value is selected based on the available space in the APU compartment, which is approximated using drawings provided in Refs. [2] and [6]. The chosen aluminum alloy for the condenser is the 3000 series, as suggested in the document of the Kaltra GmbH [46].

The condenser sizing tool implements a moving boundary method to capture the variation of the fluid phase along the HEX. Notably, the model subdivides the condenser into three control volumes depending on the working fluid phase, namely the superheated vapor, a condensing two-phase flow, and the subcooled liquid. The heat transfer area associated with each control volume varies in size depending on the specific enthalpy drop, which is initially estimated assuming a uniform pressure distribution. The enthalpy drops are updated at each iteration with the calculated local pressure drop, till the routine converges to the required heat transfer area of each control volume (A_c^i). As Z_{cond} is fixed, the heat transfer area of each control volume is adjusted by changing its width X_{cond}^i. The total core width then reads

$$X_{cond} = \sum_{i=1}^{3} X_{cond}^i = \sum_{i=1}^{3} \frac{A_c^i}{N_y\, n_{mc}\, (w_{mc} + h_{mc} - 2\,t_{mc})}, \tag{4.18}$$

where N_y is the number of flat-tubes, n_{mc} is the number of microchannels within a flat-tube. The sizing procedure keeps updating the HEX core width until the relative difference of X_{cond} between two consecutive iterations is less than or equal to 1%. Once convergence is reached, the model returns the total core width and calculates the overall pressure drops on both sides. Finally, the total dry core weight of the HEX is added to the casing weight. The casing is comprised of two flat plates positioned at the top and

bottom of the HEX core, providing structural stability. The manifold weight, on the other hand, is not accounted for.

The adopted heat transfer and pressure drop correlations vary depending on the fluid phase. In particular, for the de-superheating and subcooling zones inside the microchannels, the heat transfer coefficient is estimated using the Whitaker [47] correlation for turbulent flow with the correction for temperature dependant effects by Sieder and Tate [48]. The pressure drop is calculated using laminar or turbulent flow friction factors as shown in Ref. [41, Ch. L1]. For the condensing region, the local heat transfer coefficient is estimated using correlations for internal condensation in horizontal tubes for annular film flow [35, Tab. C.2], while the Müller-Steinhagen & Heck (MSH) model [49] is used to estimate the pressure drop per unit length. On the cold air side, the heat transfer and friction factor coefficients are estimated using correlations of Chang and Wang [50] and Chang et al. [51] for multi-louver fin geometries, respectively.

4.2.6. ORC TURBOGENERATOR PRELIMINARY DESIGN

The turbogenerator consists of a radial-inflow turbine (RIT) driving a permanent-magnet (PM) generator. The choice of using a RIT as the expander of the ORC system is based on the high efficiency and mass-specific power obtainable, resulting in a compact single-stage design Bahamonde et al. [52]. Furthermore, PM generators are attractive due to a power factor that is close to unity and therefore requires little or null excitation currents to operate them, high mass-specific power, and high efficiency, which is usually in excess of 95% [53]. Figure 4.8 depicts the components of the turbogenerator consisting of 1) a single-stage RIT (section 1 to 4) comprising a prismatic radial stator (section 1 to 2) and a radial-axial impeller (section 3 to 4), 2) a circular cross-section volute (section 0 to 1) to distribute the flow tangentially at the stator inlet, 3) an annular diffuser (section 4 to 5) to recover the turbine exit kinetic energy, and 4) a PM generator. In the following, the modeling methodology for each of the above components is briefly described.

RADIAL-INFLOW TURBINE MODELING

The thermodynamic performance and mechanical design of the RIT is modeled using the numerical framework described in Ref. [54]. This model takes the design variables ψ_{is}, ϕ, ν, ORC working fluid mass flow rate and the problem boundary conditions $p_{max,orc}$, $T_{max,orc}$, $T_{min,orc}$ as inputs and computes the thermodynamic conditions and geometrical characteristics in sections 1, 2, 3 and 4 (see Fig. 4.8).

The volute sizing and loss prediction is performed by solving the following system of equations consisting of the angular momentum conservation equation, the mass conservation equation, the thermodynamic equation of state (EoS), and the energy conservation equation across the volute

$$\begin{aligned} V_0 \cdot R_{c,0} &= V_{\theta 1} \cdot R_1, \\ \rho_0 V_0 A_0 &= \rho_1 V_{m1} 2\pi R_1 b_1, \\ s_0 &= EoS\left(h_{t1}, p_{t1} + \Delta p_{t,0-1}\right), \\ h_{t0} - \frac{V_0^2}{2} &= h_0(\rho_0, s_0). \end{aligned} \tag{4.19}$$

This system of equations is solved iteratively in the 4 unknowns: absolute velocity (V_0), density (ρ_0), entropy (s_0), and enthalpy (h_0) at the inlet of the turbine volute as a function of the volute centerline radius at the inlet section ($R_{c,0}$). The total pressure loss occurring between section 0 and 1 ($\Delta p_{t,0-1}$) is computed using the empirical model for centrifugal compressors proposed by Japikse [55] and adapted to turbine volutes.

At the turbine exit (section 4 in Fig. 4.8) an annular diffuser is used to recover part of the exit kinetic energy and increase the overall turbine total-static efficiency. A one-dimensional physics-based model proposed and validated by Agromayor et al. [56] is implemented to design the diffuser and estimate its performance. The diffuser model requires the turbine outlet geometry and flow state as input, as well as the diffuser cant angle (ϕ_{diff}), the wall semi-aperture angle (ε), and the diffuser area ratio (AR_{diff}) and solves the continuity, energy, axial and tangential momentum equations in the diffuser. Viscous losses are computed according to the model documented in Ref. [56], and applying a friction factor coefficient equal to 0.1.

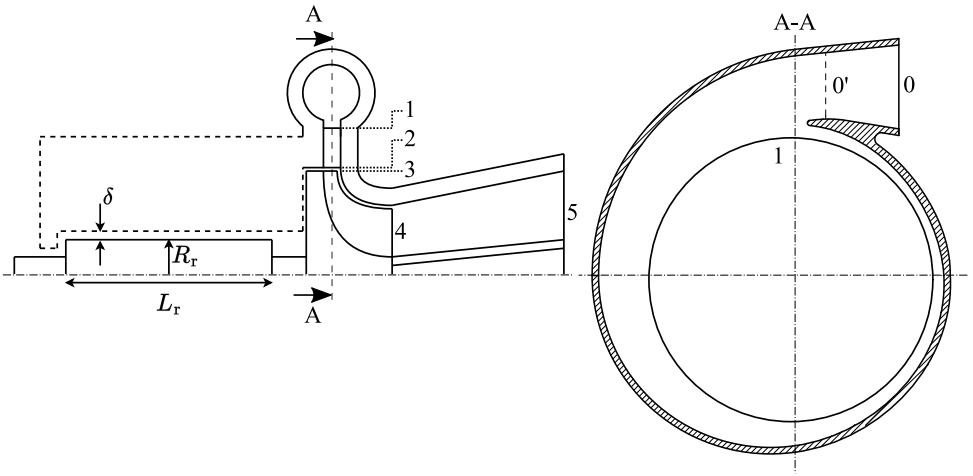

Figure 4.8: ORC turbogenerator schematic (left) and volute cross-section plane A-A (right). The part of the turbogenerator assembly represented using dashed lines corresponds to the main casing containing the stator windings of the PM generator and the power electronics, whose geometry has not been modeled in this work.

Once the size of the flow path is determined, the total mass of the radial-inflow turbine can be computed. A number of approximations are made when evaluating the turbine mass. Due to the relatively small mass of the impeller blades compared to the disk mass, its contribution is neglected. Similarly, the stator mass is assumed equal to that of the base plate of the ring, neglecting the mass of the blades. The volute geometry is treated as a simple hollow torus, whilst the inlet cone (section 0 – 0') is modeled as a hollow cylinder. The annular diffuser mass is determined as the sum of the outer and inner wall mass, whereas the mass of the struts required to align the two diffuser walls is neglected. The wall thickness of the volute, stator base plate, diffuser, and impeller shroud is set to 5 mm, based on manufacturing considerations. The open-source Python package *CadQuery* [57] is used to perform the geometrical modeling of the turbine impeller,

stator, volute, and diffuser. Based on this three-dimensional model, the turbine mass (m_{turb}) is calculated, considering a typical steel grade as material for the turbine components.

The main output parameters of the RIT model that are utilized in the present work are the turbine total-total isentropic efficiency defined as

$$\eta_{\text{is,turb}} = \frac{h_{\text{t0}} - h_{\text{t3}}}{h_{\text{t0}} - h_{\text{t3,is}}} \tag{4.20}$$

the turbine mechanical efficiency ($\eta_{\text{mech,turb}}$) and m_{turb}.

GENERATOR MODELING

The PM generator technology considered in this work is that of an iron-cobalt *FeCo* cylindrical permanent magnet electric machine to maximize the magnetic flux saturation and minimize the losses [58]. The left side of Fig. 4.8 shows a schematic of the PM generator. In this figure the stator windings of the generator are enclosed in the generator casing, represented with the dashed line. The geometrical details of the stator were not part of this investigation and are therefore not shown in the picture. The rotor is geometrically defined by the outer radius (R_{r}), the axial length (L_{r}), and the clearance between the stator and the rotor (δ). A forced-air flow is injected into the gap between the stator and rotor, providing the necessary cooling to keep the stator winding temperature below 150 °C and the rotor retaining sleeve temperature below 80 °C [58].

R_{r} is found by iteratively solving the power balance across the generator defined as

$$\frac{\dot{W}_{\text{net,tg}}}{\eta_{\text{el}}} + \Delta\dot{W}_{\text{w}} = \dot{W}_{\text{turb,net}}, \tag{4.21}$$

where the electromagnetic power output of the turbogenerator ($\dot{W}_{\text{net,tg}}$) and windage loss ($\Delta\dot{W}_{\text{w}}$) are calculated according to James and Zahawi [59] as

$$\dot{W}_{\text{net,tg}} = \pi B_{\text{s}} J_{\text{s}} \left(R_{\text{r}} + \delta\right)^2 L_{\text{r}} \Omega \cos\phi, \tag{4.22}$$

and

$$\Delta\dot{W}_{\text{w}} = 0.5\pi\rho_{\text{gap}}\Omega^3 R_{\text{r}}^4 L_{\text{r}} C_{\text{f}}\left(Re_{\delta}\right) \tag{4.23}$$

respectively.

The values of δ, the magnetic flux density (B_{s}), the linear current density (J_{s}), and the electrical efficiency (η_{el}) are assumed according to data of optimized electric machines as a function of R_{r} [58]. C_{f} is the friction factor, herein calculated for a rotating cylinder within a coaxial sleeve, expressed as a function of the air gap Reynolds number (Re_{δ}) [60]. L_{r} is calculated assuming a typical value of the rotor aspect ratio $L_{\text{r}}/R_{\text{r}}$ of 3, whereas a conservative value of the generator power factor ($\cos\phi$) of 0.8 is chosen. The mass-specific power is selected according to data of optimized electric machines [58] based on the resulting value of R_{r}. Furthermore, state-of-art mass-specific power values for the power electronics and AC-DC converter of 14.3 kW/kg and 62.0 kW/kg, respectively, are taken according to Gesell et al. [61]. Estimates based on historical data presented in Ref. [62] of AC-DC converter technology show that similar mass-specific

power values can realistically be obtained by 2030. Additionally, Granger et al. [63] show that AC-DC converters for aerospace power systems featuring mass-specific power values around 10 kW/kg can already be achieved with current technologies. The total mass of the PM assembly ($m_{\text{gen,orc}}$) is the sum of the electric machine, AC-DC converter, and power electronic masses. The individual component masses are calculated as the product of their inverse mass-specific power values and $\dot{W}_{\text{net,tg}}$. The main output parameters of the generator model that are utilized in the present work are $m_{\text{gen,orc}}$ and generator overall efficiency ($\eta_{\text{gen,orc}}$), which is defined as

$$\eta_{\text{gen,orc}} = \frac{\dot{W}_{\text{gen}}}{\dot{W}_{\text{net,turb}}}. \tag{4.24}$$

4

4.3. RESULTS AND DISCUSSION

In this section, first results for the optimized CC-APU design are presented. Secondly, the performance of the CC-APU in terms of mission fuel consumption is compared to the reference case which is a GTCP36-300 APU [2] on-board an Airbus A320neo. Thirdly, design variables and constraints most critical for CC-APU performance are discussed. Lastly, the sensitivity of the final design to design variable perturbations is analyzed.

4.3.1. OPTIMIZED CC-APU DESIGN

Table 4.4 gives the design vector for the optimized CC-APU design. The design is only constrained by the condenser size constraint. Figure 4.10 gives the temperature-entropy diagram of the CC-APU. The temperature-entropy diagram shows a large temperature difference between the evaporator's hot-side inlet and the cold-side exit. This large temperature difference is due to the low thermal efficiency of the prime mover. As a result, the optimal ORC for the studied configuration is the one with the highest $T_{\text{max,orc}}$, thus the highest thermal efficiency. This is in contrast to stationary combined-cycle power units that aim at maximum power output that results from a trade-off between bottoming cycle efficiency and the recovered thermal power.

Table 4.4: Design vector for the optimized CC-APU configuration

Parameter	OPR	$T_{\text{min,orc}}$	$T_{\text{max,orc}}$	$p_{\text{max,orc}}$	$\Delta T_{\text{pp,cond}}$	$\Delta T_{\text{pp,evap}}$	ψ_{is}	ϕ
Value	9.5	374 K	548 K	59.5 bar	32 K	47 K	0.843	0.400
Parameter	ν	Z_{cond}	F_{h}	F_{p}	x_{t}	x_{l}	n_{pass}	
Value	0.457	41 mm	11 mm	1.5 mm	2.9	1.25	13	

The identified CC-APU design has a total mass m_{ccapu} of 148 kg and a combined-cycle efficiency $\eta_{\text{net,ccapu}}$ (Eq. 4.3) of 33.9%. The gas turbine mass m_{gt} is 104 kg and its efficiency $\eta_{\text{net,gt}}$ (Eq. 4.11) is 25.3%. The ORC mass m_{orc} is 44 kg and its efficiency $\eta_{\text{net,orc}}$ (Eq. 4.13) is 14.9%. Notably, the ORC turbogenerator has a mass of 15 kg constituting about a third of the overall ORC unit mass. In this regard, notice that the generator represents by far the heaviest component of the ORC assembly, with a mass of 12 kg. Figure 4.9 gives the mass breakdown of the CC-APU. The CC-APU provides 250 kW of net

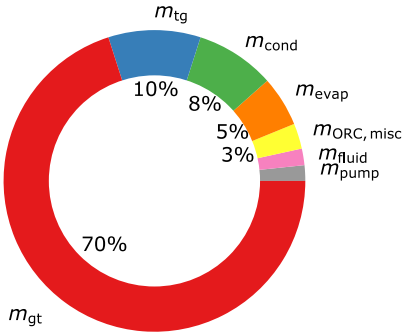

Figure 4.9: CC-APU mass breakdown

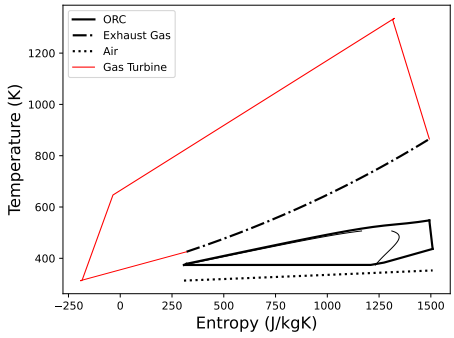

Figure 4.10: Temperature-entropy diagram of the CC-APU using a non-recuperated ORC

power output $\dot{W}_{\text{net,ccapu}}$ which is split up into 187 kW provided by the gas turbine and 63 kW provided by the ORC system ($\dot{W}_{\text{net,orc}}$). Therefore, the ORC turbogenerator provides 25% of the required power. This results in mass-specific power values of the gas turbine, the ORC, and the CC-APU of 1.8 kW/kg, 1.4 kW/kg and 1.7 kW/kg, respectively. The ORC turbine has a gross power output $\dot{W}_{\text{gross,turb}}$ of 84 kW which results in a mass-specific power of 5.6 kW/kg. Notably, the ORC turbine mass-specific power is one order larger than the value assumed by Zarati et al. [38]. The optimized ORC turbine design features a $\eta_{\text{is,turb}}$ of 94% and speed of 160 krpm. The turbogenerator features $\eta_{\text{mech,turb}}$ of 99% and a $\eta_{\text{gen,orc}}$ of 97%. The evaporator and condenser designs feature an effectiveness (ϵ) of 90% and 54%, respectively. In the case of the evaporator, the high effectiveness suggests that system performance profits from a maximization of heat transfer rate over a minimization of heat exchanger mass. In the case of the condenser, the moderate effectiveness indicates that a minimization of air-side pressure drop is favored over a maximization of heat transfer area. The exhaust duct diameter required to house the evaporator with a square-shaped frontal area is 0.39 m. This is smaller than the dimension of the tail cone where the exhaust exits which is 0.4 m (see Fig. 4.1). Table 4.5 lists additional data on the design of the ORC unit.

4.3.2. PERFORMANCE COMPARISON

Table 4.6 shows a comparison of the GTCP36-300 APU with the optimized CC-APU as well as a simple-cycle APU using advanced technology. The latter case is based on the same design assumptions as the gas turbine of the CC-APU and is presented to allow a fair comparison of the benefits an ORC WHR system can give for the investigated application. The estimated fuel consumption of the CC-APU for the provision of secondary power on the ground is 42 kg as opposed to 78 kg when using the GTCP36-300 APU. Therefore, fuel consumption for the provision of secondary power on the ground is halved when using the CC-APU. Taking into account the increase in flight phase fuel consumption of 2 kg due to the addition of 31 kg to m_{oe}, an overall fuel saving of 34 kg,

Table 4.5: Results of the optimized ORC WHR system

Parameter	Value	Parameter	Value	Parameter	Value
$\eta_{\text{net,orc}}$	14.9%	$\dot{Q}_{\text{evap}}$	426 kW	$\dot{Q}_{\text{cond}}$	352 kW
χ	81.0%	$X/Y/Z_{\text{evap}}$	0.28/0.28/0.23 m	$X/Y/Z_{\text{cond}}$	1.00/1.00/0.041 m
$\dot{W}_{\text{net,orc}}$	63 kW	m_{evap}	8.0 kg	m_{cond}	12.6 kg
$\dot{W}_{\text{net,fan}}$	6.7 kW	$T_{\text{h,in,evap}}$	865 K	$T_{\text{c,in,cond}}$	313 K
m_{orc}	44 kg	$T_{\text{h,out,evap}}$	425 K	$T_{\text{c,out,cond}}$	353 K
$\dot{m}_{\text{fluid}}$	0.8 kg/s	$\Delta p_{\text{h,evap}}$	2010 Pa	$\Delta p_{\text{c,cond}}$	513 Pa
T_{min}	374 K	$\dot{m}_{\text{h,evap}}$	0.9 kg/s	$\dot{m}_{\text{c,cond}}$	8.8 kg/s
T_{max}	548 K	$\Delta T_{\text{pp,evap}}$	47 K	$\Delta T_{\text{pp,cond}}$	32 K
p_{max}	59.5 bar	ϵ_{evap}	89.0%	ϵ_{cond}	51.0%
$\dot{W}_{\text{net,pump}}$	9.9 kW	N_{tg}	160 krpm	$\eta_{\text{is,turb}}$	94.0%

Table 4.6: Comparison of the GTCP36-300 APU [2] with an advanced APU design and the optimized CC-APU

Parameter	GTCP36-300	Advanced APU	CC-APU
η_{net} (-)	18.3%	27.2%	33.9%
$\dot{m}_{\text{fuel}}$ (kg/s)	0.0317	0.0214	0.0172
$\dot{W}_{\text{gross}}$ (kW)	258	258	274
$\dot{W}_{\text{net}}$ (kW)	250	250	250
$\dot{m}_{\text{air}}$ (kg/s)	1.60	1.10	0.88
TIT (K)	1310	1340	1340
OPR (-)	6.1	10.0	9.5
$\eta_{\text{is,comp}}$	73.4%*	82.5%	82.7%
$\eta_{\text{is,turb}}$	83.2%*	86.5%	85.6%
m (kg)	117	109	148
$m_{\text{fuel,apu/ccapu}}$ (kg)	78	52	42
m_{fuel} (kg)	5505	5479	5471

* Value estimated based on data provided in Ref. [2].

i.e., a reduction of mission fuel mass by 0.6%, is possible using the CC-APU system. The application of the advanced APU design reduces ground fuel consumption for providing secondary power by one-third and reduces mission fuel mass by 0.5%.

4.3.3. SENSITIVITY OF DESIGN VARIABLES: DESIGN GUIDELINES

To better understand the CC-APU design a discussion of the obtained design vector is presented. This represents a first step towards developing design guidelines for airborne ORC WHR systems. Figure 4.11 indicates the relation of the optimized design variable values with their respective lower and upper bounds specified in Tab. 4.1. Especially those design variables that adopt their respective upper or lower bounds are of interest. In the following, the values obtained for the individual design variables are discussed based on the underlying physical phenomena.

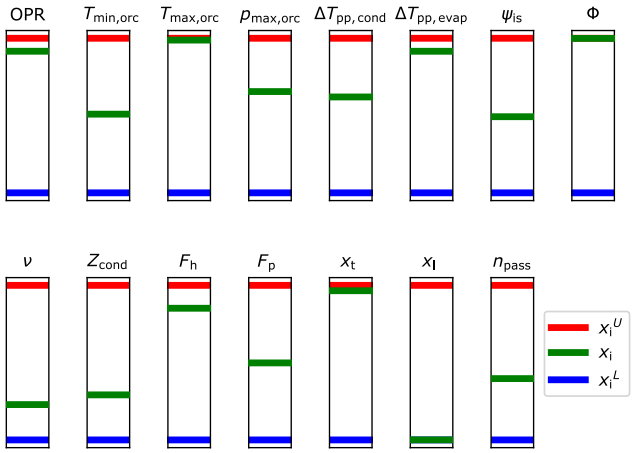

Figure 4.11: Bar charts showing the relation of the optimized design variables x_i with respect to lower bound x_i^{L} and upper bound x_i^{U}.

OPR and TIT have the largest impact on gas turbine efficiency. The value of $\mathrm{TIT}_{\mathrm{max}}$ obtained for the CC-APU is only 30 K higher than the TIT of the GTCP36-300 APU which is 1310 K [2]. The GTCP36-300 uses convectively cooled NGVs made of the material Mar-M-247, which is an early nickel-base alloy, and an uncooled radial inflow turbine whose construction material is not specified by Stohlgren and Werner [2]. The method described in Section 4.2.3 does not apply to radial inflow turbines and, therefore, cannot be verified with data of Stohlgren and Werner [2]. The applicability of the method to determine $\overline{T}_{\mathrm{b,max}}$ is verified at the end of Section 4.2.3. Figure 4.13 shows the sensitivity of $\mathrm{TIT}_{\mathrm{max}}$ to a variation of the input parameters used for the advanced APU design and provided in Section 4.2.3. $\mathrm{TIT}_{\mathrm{max}}$ shows high sensitivity to the value of ν and low sensitivity to all other input parameters. Together with the thermodynamic conditions ν determines the blade height, which affects the centrifugal stress along the blade span. Therefore, knowledge of the engine geometry is important to obtain an optimum ther-

modynamic design. Using statistical data based on engines with higher power capacity such as presented by Grieb [19, Ch. 5] may result in errors in the predicted thermodynamic performance of small gas turbine engines. Incorporating engine gas path and mechanical design methods can improve the accuracy of such analysis.

Nevertheless, further improvements in gas turbine efficiency by increasing TIT are limited as shown in Fig. 4.12, which gives the engine thermal efficiency as a function of TIT and OPR. The discontinuity of the presented curves results from a change in the required compressor stage number as OPR varies. The number of stages affects the stage loading which is an input for determining stage polytropic efficiency with the method explained in Section 4.2.3. Under the assumption of no limitations regarding blade cooling and OPR, a further increase of $\eta_{\text{net,apu}}$ of less than 2% is possible when designing the engine with a TIT of 1500 K and an OPR of 18.

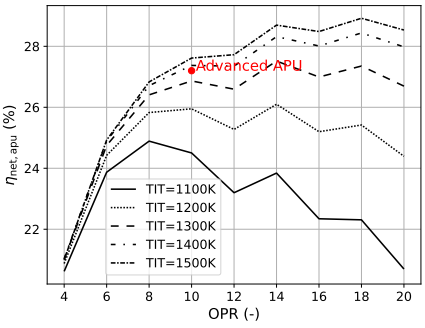

Figure 4.12: Variation of gas turbine net efficiency with turbine inlet temperature (TIT) and overall pressure ratio (OPR).

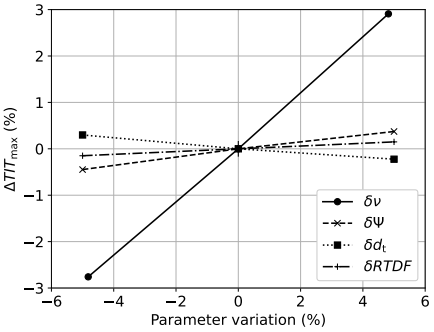

Figure 4.13: Variation of maximum turbine inlet temperature (TIT_{max}) to a +/- 5% change in turbine rotor hub-to-tip ratio (ν), turbine stage loading (Ψ), turbine rotor blade tip-to-hub area ratio (d_t), and radial temperature distribution factor (RTDF) with respect to the values of the optimized advanced APU design.

From a thermodynamic standpoint, ORC efficiency is maximized by maximizing $T_{\text{max,orc}}$ and $p_{\text{max,orc}}$ and minimizing $T_{\text{min,orc}}$. $T_{\text{max,orc}}$ has a very dominant impact on $\eta_{\text{net,ccapu}}$, and many system parameters have a large sensitivity to its value. The optimized solution adopts a value for $T_{\text{max,orc}}$ that is at the upper bound. This indicates that despite its large influence on system design the value of $T_{\text{max,orc}}$ can be selected based on thermodynamic reasoning. Similarly high sensitivity of system performance with respect to the value of $T_{\text{min,orc}}$ is observed. Contrary to $T_{\text{max,orc}}$ the optimized value of $T_{\text{min,orc}}$ is located in the mid-ranges. This indicates that the selection of $T_{\text{min,orc}}$ cannot be based solely on thermodynamic reasoning but its optimal value is highly dependent on the system architecture. For example a reduction of $T_{\text{min,orc}}$ by 1% from its optimized value increases $\dot{m}_{\text{c,cond}}$ by 20% which causes a 30% higher $\Delta p_{\text{c,cond}}$. The combined effect leads to an increase of $\dot{W}_{\text{net,fan}}$ by 60% (Equation 4.12). For this reason, $\dot{W}_{\text{net,fan}}$ is identified as the most limiting factor of CC-APU performance. To maximize system performance it is therefore crucial to adopt an aerodynamically optimized fan. The maximum value of

$p_{max,orc}$ is limited by the increasing pump power consumption which at one point counters the thermodynamic advantages of a further increase. Therefore, for the selection of $p_{max,orc}$ pump power demand should be considered. At the same time for the analyzed supercritical cycle, the sensitivity of $\eta_{net,ccapu}$ to variations in $p_{max,orc}$ is low which makes the selection of $p_{max,orc}$ less critical.

Size and pressure drop constraints limit the amount of heat that can be rejected by the condenser. In the present study, only the size is imposed as an active constraint, while the pressure drop is effectively limited by the penalizing effect of $\dot{W}_{net,fan}$. The optimization algorithm tends to drive the condenser design towards the maximum available frontal area to reduce flow velocity and therefore pressure drop. As expected, it is more beneficial to add heat transfer area by increasing the core width (X_{cond}) and varying the core parameters instead of increasing the core depth Z_{cond} which linearly increases the pressure drop. Similarly, the free flow to frontal area ratio of the condenser is also minimized to reduce the channel flow acceleration and maximum velocities. This is done by reducing the number of flat-tubes, effectively driving the variable F_h towards the imposed upper bound. The fin pitch (F_p) adopts a value that seems to fall right in the middle of the imposed bounds. This is the result of a non-trivial trade-off between more heat transfer area, higher heat transfer coefficient, and less pressure drop. The pinch point temperature difference in the condenser $\Delta T_{pp,cond}$ impacts the required heat transfer area as well as the cold side pressure drop. On one hand, larger values of $\Delta T_{pp,cond}$ imply larger temperature differences between the hot and cold side, which effectively reduces the required heat transfer area and thus the size of the heat exchanger. On the other hand, larger values of $\Delta T_{pp,cond}$ correspond to higher air mass flow rates. This results in higher flow velocities, thus negatively affecting $\Delta p_{c,cond}$. As a result, the optimizer adopts a value of $\Delta T_{pp,cond}$ that provides a good trade-off between these opposing trends.

As stated in Section 4.2.3 gas turbine efficiency is very sensitive to the pressure loss in the exhaust duct. Therefore, the combination of evaporator design variables tends towards the lowest possible hot side pressure drop that still satisfies the size constraint on the core depth (Z_{evap}). This is achieved by minimizing the intensity, size, and position of the detached flow vortices behind each tube. The intensity of the recirculation zones is mainly affected by the local flow velocity, which is then minimized as much as possible by driving the transversal pitch (x_t) toward the upper bound. On the other hand, the reduced vortex intensity lowers the heat transfer coefficient and increases the required heat transfer area. Contrary to x_t, larger values of longitudinal pitch (x_l) slightly increase both the heat transfer coefficient and pressure drop due to the re-attachment of the separation before the next tube [64]. Since the heat transfer improvement is weaker than the pressure drop increase, and the designs are not close to the size constraint, x_l is minimized. The number of passes (n_{pass}) settles to a value that tends to limit the total number of streamwise tubes, which linearly affects the pressure drop. On the one hand, increasing the number of passes tends to reduce the number of streamwise tubes per pass, thus increasing the working fluid velocity in the tubes and slightly increasing the overall heat transfer coefficient. On the other hand, this results in an increased pressure drop on the working fluid side. As a result, the optimal number of passes is a trade-off value between these opposing trends. Finally, the evaporator pinch point temperature

difference $\Delta T_{pp,evap}$ adopts the upper bound value in order to reduce evaporator heat load which in turn leads to lower required evaporator heat transfer area and therefore pressure drop.

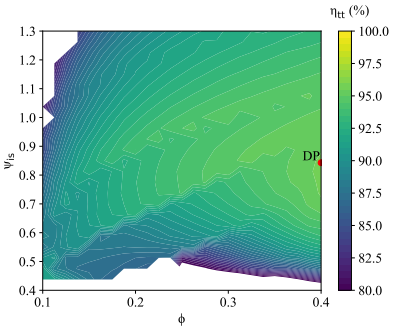

Figure 4.14: ORC turbine total-total efficiency map as a function of duty coefficients ψ_{is} and ϕ for fixed inflow conditions, pressure ratio and hub-to-tip ratio ν.

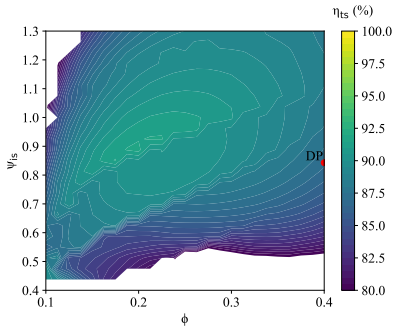

Figure 4.15: ORC turbine total-static efficiency map as a function of duty coefficients ψ_{is} and ϕ for fixed inflow conditions, pressure ratio, and hub-to-tip ratio ν.

To understand the selection of the optimum ORC turbine design the impact of varying the design variables ψ_{is} and ϕ on turbine total-total efficiency $\eta_{is,turb}$ is investigated through a parametric study. Figure 4.14 shows a contour plot of $\eta_{is,turb}$ with respect to ψ_{is} and ϕ, where ν, the turbine inflow conditions as well as the pressure ratio are kept at their respective values identified for the optimized CC-APU design. The point DP in Fig. 4.14 indicates the optimized design point. This point also coincides with the highest mass-specific power of the turbogenerator. Furthermore, the value of the stage efficiency around point DP has rather low sensitivity to small variations in the design variables ψ_{is} and ϕ. The analysis also shows that best turbine performance is achieved with values of ν in the lower ranges, leading to lower blade deflection in the impeller for a given set of ψ_{is} and ϕ, and thus lower blade loading losses. In this work, the flow kinetic energy at the exit of the turbine impeller is considered as being completely recovered. This is a reasonable assumption for a closed loop cycle if one neglects the friction losses in the piping system to convert this kinetic energy into total pressure. Common design guidelines for radial inflow turbines [65] relate optimum total–static efficiency to the duty coefficients ψ_{is} and ϕ. The plot of total–static efficiency in Fig. 4.15 shows that the point DP from the present optimization is shifted away from the locus of maximum total–static efficiency. A comparison of Fig. 4.14 and Fig. 4.15 shows that ψ_{is} takes on very similar values for turbines optimized for total–static and total–total efficiency. Furthermore, if the turbine is optimized for total–total efficiency, then the optimum value of ϕ will be larger than for a turbine optimized for total–static efficiency. This suggests that the assumption of whether the turbine exit kinetic energy can, or can not, be recovered is a driver for the optimal turbine design. Thus, it is important to be aware of the differences in the turbine efficiency definitions and choose the most appropriate one for the system studied.

In general, it is observed that pressure drops on the ORC working fluid sides of the heat exchangers have little impact on overall system performance. Furthermore, due to

the imposed HEX size and pressure drop constraints the encountered pinch point temperature differences are higher than commonly applied for ORC WHR systems of stationary applications. For stationary applications, depending on the component, pinch point temperature differences in the range of $5-10\,^{\circ}\mathrm{C}$ are adopted, as reported in Chapter 3.

A summary of design aspects derived from the optimized CC-APU design, that can inform future work on combined-cycle gas turbine engines employing ORC WHR systems, is given in the following list:

- System performance benefits from selecting the highest possible value of $T_{\mathrm{max,orc}}$.
- System performance is less critical to $p_{\mathrm{max,orc}}$, its value can be selected based on engineering judgement.
- ORC turbine maximum total-total efficiency coincides with maximum mass-specific power and design variables should be selected accordingly.
- To limit condenser cold side pressure drop, the condenser design should employ the largest possible frontal area in combination with a minimized number of flat-tubes.
- To limit evaporator hot side pressure drop, an in-line bare-tube-bundle evaporator design should employ a large transversal pitch and a low longitudinal pitch. The magnitude of the pitches may be dictated by the validity range of the applied heat transfer and pressure drop correlations.
- Employing an aerodynamically optimized fan is crucial to achieve maximum performance.

4.3.4. METHODOLOGY LIMITATIONS

Steps 1) to 3) of the method to estimate $\overline{T}_{\mathrm{b,max}}$ (Section 4.2.3) is based on the assumption that the turbine operates at a single operating point over its lifetime. In the case of an aircraft APU, this assumption is reasonable. However, in the case of gas turbine engines with a wider operating range, blade creep strain varies between operating points. An analysis considering the thermal conditions and operating times encountered during the entire mission is required to determine blade lifetime for an allowable total strain. However, the presented method can still be used if the equivalent blade life resulting in the allowable strain at a given operating point is known. For example, Halila et al. [25] state that the strain accumulated over the entire mission life of $18\cdot10^{3}$ hours is equivalent to operating the turbine for 250 hours at hot-day take-off conditions. In this case, 250 hours can be used as input to determine $\overline{T}_{\mathrm{b,max}}$.

The estimation of system mass presents the largest factor of uncertainty. The current methodology is limited to using an empirical correlation for gas turbine mass estimation. This aspect will be improved in a future version of the ARENA framework by integrating a component-based engine mass estimation tool currently under development (see Chapter 7). The mass of the ducting related to the ORC system and the APU and condenser air intakes is currently not modeled. Estimating the mass of the structural elements required to integrate the system with the aircraft is difficult to model at the conceptual level.

The impact of the CC-APU assembly on aircraft aerodynamics is not modeled in the present analysis. Considering the large size of the condenser its air intake must be closed off during flight using a hatch to prevent additional drag during cruise. Similarly, the air intake of conventional APUs is closed during flight.

4.4. CONCLUSIONS

In this work the application of an organic Rankine cycle (ORC) waste heat recovery (WHR) system to an aircraft auxiliary power unit (APU) is investigated using a multidisciplinary simulation framework. An optimal design for the combined-cycle APU (CC-APU) system for the provision of secondary power during ground operations is identified using a genetic algorithm. The objective is the minimization of mission fuel mass based on the variation of 15 design variables. It is shown that the CC-APU can attain an overall efficiency of 34%, 7% more than an advanced simple-cycle APU design with an efficiency of 27%. However, this comes at the expense of a relative increase in system mass of the CC-APU of 35% when compared to the advanced simple-cycle APU. Compared to using a current-day APU, the use of the CC-APU system consumes half the fuel mass required to provide secondary power on the ground. For a short-range aircraft, the optimal CC-APU leads to a mission fuel mass reduction of 0.6% compared to a current-day APU and 0.1% compared to an advanced simple-cycle APU. Fan power consumption in combination with condenser air-side pressure drop is identified as the main limiter of CC-APU performance. In this regard, the minimum ORC working fluid temperature $T_{\text{min,orc}}$ is the most critical design variable of the system. Additionally, size constraints imposed on the condenser further constrain the achievable thermodynamic efficiency. The large size of the condenser indicates that the integration of a CC-APU would require substantial modifications to the airframe. The identified ORC WHR unit design is in contrast to conventional designs used for stationary applications. Stationary combined-cycle power units aim at a maximization of power output, while for the airborne ORC WHR unit of a low power-capacity gas turbine, a maximization of ORC thermodynamic efficiency is optimal. This is achieved with a supercritical ORC. Additionally, as a result of size and mass constraints, the minimum ORC operating temperature and heat exchanger pinch point temperature differences for airborne ORC WHR applications differ from conventional design guidelines for stationary systems. Based on the analysis of the obtained optimized design vector a first set of design guidelines for airborne ORC WHR systems is presented. These findings will allow a refined selection of design variables for future optimization studies.

While this work only considered the operation of the CC-APU to provide the secondary power demand of a current-day aircraft, other use scenarios of such a system can be envisaged. For example, advantages could be derived from operating a CC-APU during flight to provide secondary power. This way the main engines of the aircraft can be relieved from the task of providing secondary power during some flight conditions. This could result in a simplification of their design or operational advantages. Another ground-based application may be the provision of electrical power for electric taxiing concepts that are in active development. A secondary advantage not investigated in this work could be the reduction of jet noise resulting from decreased exhaust velocity and temperatures.

Future investigations will include the application of ORC WHR systems to large turboshaft engines of turboelectric and hybrid-electric powertrains. Furthermore, a more detailed analysis of the chosen ORC working fluid is required. It is also worth investigating different alternatives for ORC turbine power utilization, such as mechanically coupling the ORC turbine shaft with the shaft of the gas turbine. This could potentially result in system simplification and weight reduction.

BIBLIOGRAPHY

[1] L. M. Stohlgren, "The GTCP331, a 600 hp auxiliary power unit program," *American Society of Mechanical Engineers*, 4 1983, doi: 10.1115/83-GT-188.

[2] L. M. Stohlgren and L. D. Werner, "The GTCP36-300, a gas turbine auxiliary power unit for advanced technology transport aircraft," *American Society of Mechanical Engineers*, 4 1986, doi: 10.1115/86-GT-285.

[3] Boeing Company, "Airport compatibility - airport planning and engineering services," 2022, accessed on 1 September 2022. [Online]. Available: https://www.boeing.com/commercial/noise/list.page

[4] A. Padhra, "Emissions from Auxiliary Power Units and Ground Power Units during Intraday Aircraft Turnarounds at European Airports," *Transportation Research Part D: Transport and Environment*, vol. 63, pp. 433–444, 8 2018, doi: 10.1016/J.TRD.2018.06.015.

[5] M. Bentele and J. J. Laborde, "Evolution of small turboshaft engines," *SAE Technical Papers*, 2 1972, doi: 10.4271/720830.

[6] Airbus, "Airbus A320 aircraft characteristics: Airport and maintenance planning," Airbus, Tech. Rep., 2020, accessed on 10 August 2022. [Online]. Available: https://www.airbus.com/sites/g/files/jlcbta136/files/2021-11/Airbus-Commercial-Aircraft-AC-A320.pdf

[7] J. Blank and K. Deb, "Pymoo: Multi-objective optimization in Python," *IEEE Access*, vol. 8, pp. 89 497–89 509, 2020, doi: 10.1109/ACCESS.2020.2990567.

[8] E. Torenbeek, "The initial calculation of range and mission fuel during conceptual design," Delft University of Technology, Faculty of Aerospace Engineering, Tech. Rep., 1987, report LR-525.

[9] Jane's Information Group, "Jane's aero-engines," 2022. [Online]. Available: https://shop.janes.com/products/air-space/janes-aero-engines

[10] J. Roskam, *Airplane Design, Part 1: Preliminary Sizing of Airplanes*. DARcorporation, 1997.

[11] Airbus, "Getting to grips with fuel economy," 2004, accessed on 5 September 2022.

[12] aerospace-technology.com, "Airbus selects honeywell auxiliary power units for A320 aircraft model," 2017, accessed on 1 September 2022. [Online]. Available: https://www.aerospace-technology.com/news/newsairbus-selects-honeywell-auxiliary-power-units-for-a320-aircraft-model-5769803

[13] Eurocontrol, "Taxi times - winter 2018-2019," 2019, accessed on 29 November 2022. [Online]. Available: https://www.eurocontrol.int/publication/taxi-times-winter-2018-2019

[14] ——, "Taxi times - summer 2019," 2019, accessed on 29 November 2022. [Online]. Available: https://www.eurocontrol.int/publication/taxi-times-summer-2019

[15] Eurostat, "Air passenger transport by main airports in each reporting country," 2022, accessed on 29 November 2022. [Online]. Available: https://ec.europa.eu/eurostat/databrowser/view/AVIA_PAOA__custom_3991485/default/table?lang=en

[16] J. Kurzke and I. Halliwell, *Propulsion and Power: An Exploration of Gas Turbine Performance Modeling*. Springer International Publishing, 2018, ISBN: 978-3-319-75979-1, doi: 10.1007/978-3-319-75979-1.

[17] P. P. Walsh and P. Fletcher, *Gas Turbine Performance*, 2nd ed. Blackwell Science, 2004, ISBN: 978-0-632-06434-2.

[18] S. Samuelsson, T. Gronstedt, and K. G. Kyprianidis, "Consistent conceptual design and performance modeling of aero engines," in *Proceedings of the ASME Turbo Expo*, 2015, doi: 10.1115/GT2015-43331.

[19] H. Grieb, *Projektierung von Turboflugtriebwerken*. Birkhäuser Basel, 2004, ISBN: 978-3-0348-7938-5, doi: 10.1007/978-3-0348-7938-5.

[20] W. Visser, "Generic analysis methods for gas turbine engine performance: The development of the gas turbine simulation program GSP," Ph.D. dissertation, Delft University of Technology, 2015.

[21] F. Ripolles, "Helicopter turboshaft engine: the specificities to meet airframe requirements and customer needs," in *European Rotorcraft Forum*, 2017.

[22] J. W. Gauntner, "Algorithm for calculating turbine cooling flow and the resulting decrease in turbine efficiency," NASA Lewis Research Centre, Tech. Rep., 1980, NASA-TM-81453.

[23] J. W. Sawyer, *Sawyer's Gas Turbine Engineering Handbook, Volume 1: Theory & Design*, 3rd ed. Turbomachinery International Publications, 1985, ISBN: 0-937506-14-1.

[24] H. I. H. Saravanamuttoo, G. F. C. Rogers, H. Cohen, P. V. Straznicky, and A. C. Nix, *Gas Turbine Theory*, 7th ed. Pearson Education, 2017, ISBN: 0132224372.

[25] E. E. Halila, D. T. Lenahan, T. T. Thomas, D. T. Lenahan, and T. T. Thomas, "Energy efficient engine: High pressure turbine test hardware detailed design report," NASA Lewis Research Center, Tech. Rep., 1982, NASA-CR-167955.

[26] G. L. Erickson, "The development and application of CMSX®-10," *Superalloys*, 1996.

[27] G. J. DeBoer, "Materials for advanced turbine engines project completion report 2: Rene 150 directionally solidified superalloy turbine blades, volume 1," General Electric, Tech. Rep., 1981, nASA-CR-167992.

[28] P. Schmollgruber, D. Donjat, M. Ridel, I. Cafarelli, O. Atinault, C. François, and B. Paluch, "Multidisciplinary design and performance of the ONERA hybrid electric distributed propulsion concept (Dragon)," in *AIAA SciTech Forum*, 2020, doi: 10.2514/6.2020-0501.

[29] J. D. Mattingly, W. H. Heiser, K. M. Boyer, B. A. Haven, and D. T. Pratt, *Aircraft Engine Design*, 3rd ed. AIAA, 2018, ISBN: 978-1-62410-650-7.

[30] T. Van der Stelt, N. Woudstra, P. Colonna *et al.*, "Cycle-tempo: a program for thermodynamic modeling and optimization of energy conversion systems," 1980, software.

[31] I. H. Bell, J. Wronski, S. Quoilin, and V. Lemort, "Pure and pseudo-pure fluid thermophysical property evaluation and the open-source thermophysical property library CoolProp," *Industrial & Engineering Chemistry Research*, vol. 53, no. 6, pp. 2498–2508, 2014, doi: 10.1021/ie4033999.

[32] P. Colonna and T. van der Stelt, "FluidProp (version 3.1): A program for the estimation of thermophysical properties of fluids," 2019, software.

[33] E. W. Lemmon, I. H. Bell, M. L. Huber, and M. O. McLinden, "Nist standard reference database 23: Reference fluid thermodynamic and transport properties-REFPROP, Version 10.0, national institute of standards and technology," 2018, software.

[34] M. Astolfi and E. Macchi, *Organic Rankine Cycle (ORC) Power Systems*. Elsevier, 2017, doi: 10.1016/C2014-0-04239-6.

[35] D. Shah, R. Sekulic, *Fundamentals of heat exchanger design*. John Wiley and Sons, 2003.

[36] I. J. Karrasik, J. P. Messina, P. Cooper, and C. C. Heald, *Pump Handbook*, 4th ed. McGraw Hill, 2008.

[37] H. D. Kwak, S. Kwon, and C. H. Choi, "Performance assessment of electrically driven pump-fed LOX/kerosene cycle rocket engine: Comparison with gas generator cycle," *Aerospace Science and Technology*, vol. 77, pp. 67–82, 6 2018, doi: 10.1016/J.AST.2018.02.033.

[38] K. Zarati, S. Maalouf, and A. T. Isikveren, "Potential of the bottom organic Rankine cycle to recover energy on turboprop engine architecture," in *23rd ISABE Conference*, 2017.

[39] GREThh, "Echtherm version 3.2," 2023, software.

[40] A. S. Sabau, A. H. Nejad, J. W. Klett, A. Bejan, and K. Ekici, "Novel evaporator architecture with entrance-length crossflow-paths for supercritical organic Rankine cycles," *International Journal of Heat and Mass Transfer*, vol. 119, pp. 208–222, 2018, doi: 10.1016/j.ijheatmasstransfer.2017.11.042.

[41] VDI e. V., *VDI Heat Atlas*, 2nd ed. Springer, 2010, ISBN: 978-3-540-77877-6.

[42] H. Martin, "The generalized Lévêque equation and its practical use for the prediction of heat and mass transfer rates from pressure drop," *Chemical Engineering Science*, vol. 57, no. 16, pp. 3217–3223, 2002, doi: 10.1016/S0009-2509(02)00194-X.

[43] D. Brkić and P. Praks, "Unified friction formulation from laminar to fully rough turbulent flow," *Applied Sciences*, vol. 8, no. 11, 2018, doi: 10.3390/app8112036.

[44] I. Pioro and S. Mokry, "Heat transfer to supercritical fluids," in *Heat Transfer*, A. Belmiloudi, Ed. Rijeka: IntechOpen, 2011, ch. 19, doi: 10.5772/13792.

[45] B. Zohuri, *Compact Heat Exchangers*. Springer International Publishing, 2017, ISBN: 978-3-319-29835-1.

[46] Kaltra GmbH, "Microchannel condensers: Heat exchangers for condenser applications," 2020, accessed on 16 June 2023. [Online]. Available: https://www.kaltra.com/wp-content/uploads/2020/04/TM_Microchannel-Condensers_Ver.3.0_EN.pdf

[47] S. Whitaker, "Forced convection heat transfer correlations for flow in pipes, past flat plates, single cylinders, single spheres, and for flow in packed beds and tube bundles," *AIChE Journal*, vol. 18, no. 2, pp. 361–371, 1972, doi: 10.1002/aic.690180219.

[48] E. N. Sieder and G. E. Tate, "Heat transfer and pressure drop of liquids in tubes," *Industrial & Engineering Chemistry*, vol. 28, no. 12, pp. 1429–1435, 1936, doi: 10.1021/ie50324a027.

[49] H. Müller-Steinhagen and K. Heck, "A simple friction pressure drop correlation for two-phase flow in pipes," *Chemical Engineering and Processing: Process Intensification*, vol. 20, no. 6, pp. 297–308, 1986, doi: https://doi.org/10.1016/0255-2701(86)80008-3.

[50] Y. Chang and C. Wang, "A generalized heat transfer correlation for iouver fin geometry," *International Journal of Heat and Mass Transfer*, vol. 40, no. 3, pp. 533–544, 1997, doi: 10.1016/0017-9310(96)00116-0.

[51] Y. Chang, K. Hsu, Y. Lin, and C. Wang, "A generalized friction correlation for louver fin geometry," *International Journal of Heat and Mass Transfer*, vol. 43, no. 12, pp. 2237–2243, 2000, doi: 10.1016/S0017-9310(99)00289-6.

[52] S. Bahamonde, M. Pini, C. De Servi, A. Rubino, and P. Colonna, "Method for the preliminary fluid dynamic design of high-temperature mini-organic Rankine cycle turbines," *Journal of Engineering for Gas Turbines and Power*, vol. 139, 2017, doi: 10.1115/1.4035841.

[53] A. Binder and T. Schneider, "Permanent magnet synchronous generators for regenerative energy conversion - a survey," in *2005 European Conference on Power Electronics and Applications*. IEEE, 2005, doi: 10.1109/EPE.2005.219668.

[54] M. Majer and M. Pini, "Design guidelines for high-pressure ratio supersonic radial-inflow turbines of organic Rankine cycle systems," *Journal of the Global Power and Propulsion Society*, 2024, submitted for publication.

[55] D. Japikse, *Centrifugal Compressor Design and Performance*. Concepts ETI, 1996.

[56] R. Agromayor, B. Müller, and L. O. Nord, "One-dimensional annular diffuser model for preliminary turbomachinery design," *International Journal of Turbomachinery, Propulsion and Power*, vol. 4, p. 31, 9 2019, doi: 10.3390/IJTPP4030031.

[57] CadQuery, version 2.X. [Online]. Available: https://github.com/CadQuery/cadquery

[58] M. van der Geest, H. Polinder, J. A. Ferreira, and M. Christmann, "Power density limits and design trends of high-speed permanent magnet synchronous machines," *IEEE Transactions on Transportation Electrification*, vol. 1, no. 3, pp. 266–276, 2015, doi: 10.1109/TTE.2015.2475751.

[59] B. P. James and B. Zahawi, "High speed generator for turbocharger based domestic combined heat and power unit employing the inverted brayton cycle," *Energy Procedia*, vol. 42, pp. 249–260, 2013, doi: 10.1016/j.egypro.2013.11.025.

[60] J. Saari, "Friction losses and heat transfer in high-speed electrical machines," TKK, Working Paper Report 50, 1996.

[61] H. Gesell, F. Wolters, and M. Plohr, "System analysis of turbo-electric and hybrid-electric propulsion systems on a regional aircraft," *The Aeronautical Journal*, vol. 123, no. 1268, p. 1602–1617, 2019, doi: 10.1017/aer.2019.61.

[62] C. Hall, C. L. Pastra, A. Burrell, J. Gladin, and D. N. Mavris, "Projecting power converter specific power through 2050 for aerospace applications," in *2022 IEEE Transportation Electrification Conference & Expo (ITEC)*, 2022, pp. 760–765, doi: 10.1109/ITEC53557.2022.9813991.

[63] M. G. Granger, D. Avanesian, R. Jansen, S. R. Kowalewski, A. Leary, R. Bowman, A. Dimston, E. Stalcup, and W. A. Miller, "Design of a high power density, high efficiency, low THD 250kW converter for electric aircraft," in *AIAA Propulsion and Energy 2021 Forum*, 2021, doi: 10.2514/6.2021-3332.

[64] A. M. F. El-Shaboury and S. J. Ormiston, "Analysis of laminar forced convection of air crossflow in in-line tube banks with nonsquare arrangements," *Numerical Heat Transfer, Part A: Applications*, vol. 48, no. 2, pp. 99–126, 2005.

[65] H. Chen and N. Baines, "The aerodynamic loading of radial and mixed-flow turbines," *International Journal of Mechanical Sciences*, vol. 36, no. 1, pp. 63–79, 1994, doi: 10.1016/0020-7403(94)90007-8.

5

CC-TS FOR TURBOELECTRIC AIRCRAFT

Parts of this chapter have been published in:

D. Krempus, F. Beltrame, R. Vos, C. M. De Servi, P. Colonna, "OORC waste heat recovery system for the turboshaft engines of turboelectric aircraft," *Aerospace Europe Conference 2023* - 10^{TH} *EUCASS* - 9^{TH} *CEAS.*, 2023, doi:10.13009/EUCASS2023-658

and

D. Krempus, F. Beltrame, R. Vos, C. M. De Servi, P. Colonna, "ORC waste heat recovery system for the turboshaft engines of turboelectric aircraft: Correction," *TU Delft Technical Report*, 2024, url: https://research.tudelft.nl/en/publications/orc-waste-heat-recovery-system-for-the-turboshaft-engines-of-turb, accessed on 10 June 2024.

ABSTRACT

This chapter presents a preliminary study about a combined-cycle engine based on a turboshaft engine and an organic Rankine cycle (ORC) bottoming unit to be used onboard an aircraft with a turboelectric propulsion system. The aim is to analyze whether benefits with respect to mission fuel consumption can be derived by employing such a combined-cycle engine when compared to a simple-cycle turboshaft engine. For this purpose, a multidisciplinary optimization framework is developed, incorporating models for the engine, ORC system, ORC turbine, heat exchangers, and mission analysis. This framework is coupled with an optimizer to identify the optimal combined-cycle engine design for minimum mission fuel consumption. The results suggest that fuel savings of around 1.5% are possible with the optimized system if compared to the aircraft employing turboshaft engines. Heat exchanger volume is identified as the most constraining parameter when it comes to combined-cycle performance. The analysis of the results suggests as aspects that might lead to further improvements the evaluation of other ORC architectures, working fluids, and heat exchanger topologies.

5.1. INTRODUCTION

The combined-cycle auxiliary power unit (CC-APU) concept presented in Chapter 4 showed that adopting an ORC bottoming unit to a small turboshaft engine providing ground power can reduce mission fuel consumption by 0.6%. The present chapter investigates whether a similar benefit on mission fuel consumption can be obtained for a larger power capacity turboshaft engine equipped with an ORC bottoming unit. Such an engine could be employed as the prime mover of a turboelectric drivetrain. Turboelectric aircraft configurations employ gas turbine engines that provide power to electric propulsors. The required thrust may be provided in full by the electric propulsors or, in the case of a partial-turboelectric configuration, partially by the gas turbine engines and the electric propulsors. As outlined in Chapter 1 advantages on propulsive efficiency and aircraft aerodynamics can be derived from such configurations. In the following, examples of turboelectric aircraft configurations are presented.

The ONERA Dragon turboelectric aircraft concept studied by Schmollgruber et al. [1] employs two turboshaft engines housed in pods in the aft of the aircraft to provide electrical power to an under-the-wing distributed propulsion system consisting of electrically-driven ducted fans. The aircraft has similar top-level aircraft requirements (TLARs) as an Airbus A320 and modeling is conducted based on technology assumptions for an entry into service in the year 2035. Their results indicate that fuel consumption can be reduced by 7% compared to a traditional tube-and-wing aircraft employing turbofan engines with the same technology level. A similar concept was studied by Schiltgen and Freeman [2]. Their ECO-150 concept features a powertrain consisting of two turboshaft engines and an electrically driven distributed propulsion system integrated into the wing's leading edge. The modeling also included the preliminary design of the thermal management system required to cool the electrical powertrain. Overall, mission analysis shows that the aircraft has a similar fuel efficiency as an Airbus A320. A turboelectric concept based on a blended wing body airframe was studied by Felder et al. [3]. Their N3-X aircraft has TLARs similar to a Boeing B777-200LR. The powertrain consists

of two podded turboshaft engines mounted to the wing tips that provide electrical power to a distributed propulsion system integrated with the airframe close to the trailing edge on the top side. NASA's N+3 technology assumptions for an entry into service in the year 2025 were applied. Their results suggest a reduction in fuel burn of approximately 70% over a B777. These savings are attributed to 1) overall improved aerodynamic performance and 2) benefits derived from the distributed propulsion system such as reduced nacelle drag and benefits derived from boundary layer ingestion. The latter is estimated to contribute about 20% to the fuel-saving potential.

The research presented in this chapter investigates the adoption of a combined-cycle turboshaft engine (CC-TS) consisting of a turboshaft engine and an ORC bottoming unit onboard a single-aisle turboelectric aircraft. The main research question of this work is: What is the impact on mission fuel consumption of adopting an ORC bottoming unit for turboshaft engines of a turboelectric aircraft? For this purpose, the ARENA simulation framework presented in Chapter 3 is further developed to capture the impact adopting a CC-TS engine has on aircraft design and performance. The reference aircraft selected for this study is the ONERA Dragon [1]. Figure 5.1 gives a rendering of this aircraft and Tab. 5.1 its TLARs. The work at hand analyzes the performance of this aircraft architecture when replacing the simple-cycle turboshaft engines with CC-TS engines. This new aircraft concept is referred to as Dragon CC-TS.

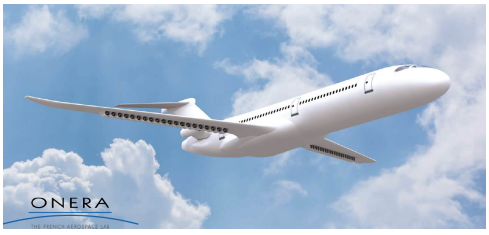

Figure 5.1: Rendering of the ONERA Dragon aircraft concept as presented in Ref. [1].

Table 5.1: Top-level aircraft requirements (TLARs) of the ONERA Dragon [1]

Parameter	Input
Range (NM/km)	2750/5100
Number of passengers (-)	150
Mach number (-)	0.78
Design payload (kg)	13600

5.2. METHODOLOGY

The numerical framework developed for the preliminary design and evaluation of the CC-TS system is modular and all modules are integrated into a system model using the Python library *openMDAO* [4]. The framework is hereafter referred to as the ARENA framework and the acronym ARENA stands for airborne energy harvesting for aircraft. Figure 5.2 shows the extended design structure matrix (XDSM) of the system model containing all its major modules. Figure 5.3 shows the process flow diagram (PFD) of the CC-TS.

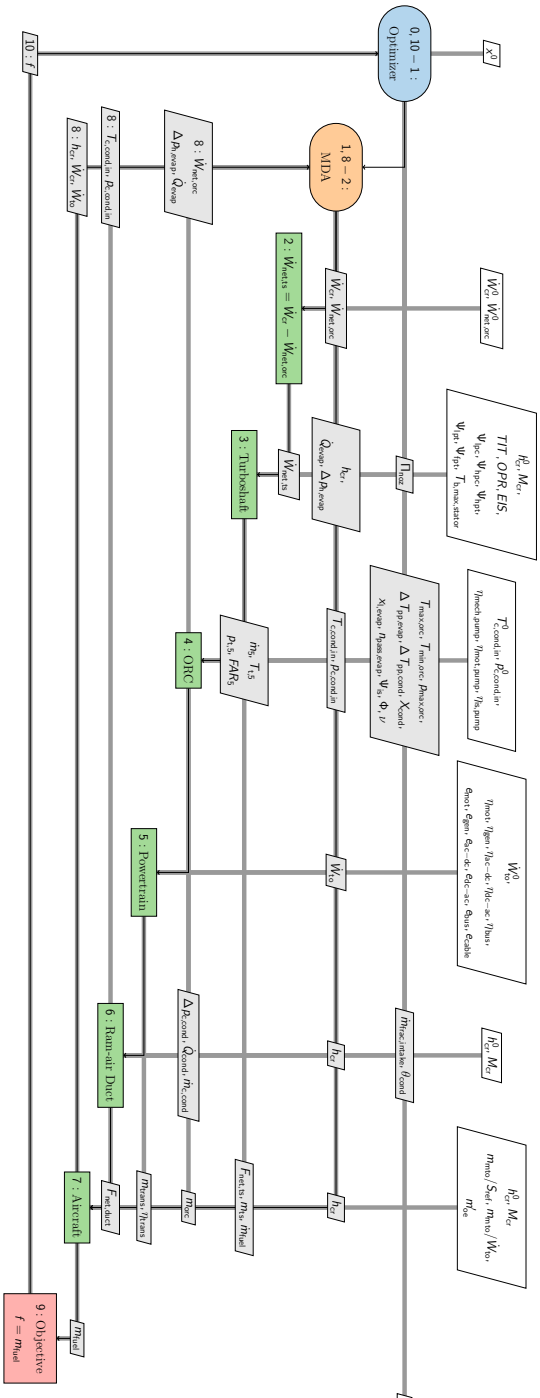

Figure 5.2: XDSM of the Dragon CC-TS system model.

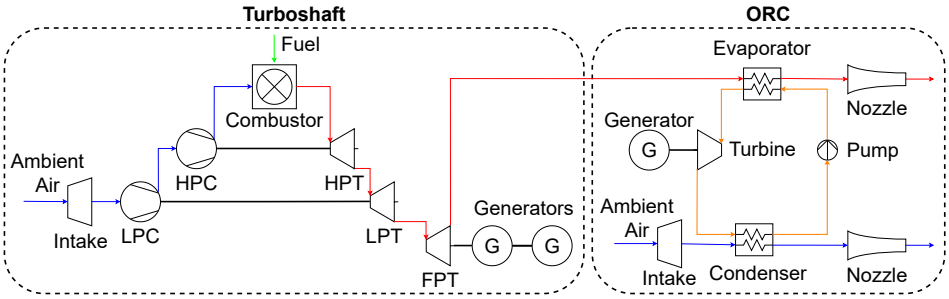

Figure 5.3: Process flow diagram of the CC-TS configuration.

5.2.1. OPTIMIZATION PROBLEM

Numerical optimization is used to identify a CC-TS design that minimizes mission fuel mass (m_{fuel}). Therefore, the following single-objective optimization problem is solved

$$\begin{aligned} &\text{minimize} && F(\boldsymbol{x}) = m_{\text{fuel}}(\boldsymbol{x}) \\ &\text{subject to:} && x_i^{\text{L}} \leq x_i \leq x_i^{\text{U}}. \end{aligned} \tag{5.1}$$

The design vector ($\boldsymbol{x}$) is composed of 18 variables which relate to the thermodynamic cycle and the preliminary design of the components of the CC-TS system, namely the turboshaft engine, the ORC, the heat exchangers, the ORC turbogenerator and the ram-air duct. Table 5.2 lists the design variables (x_i) considered in the optimization together with their lower bounds (x_i^{L}) and upper bounds (x_i^{U}). The optimization problem is solved using a genetic algorithm implemented in the Python library *pymoo* [5]. A population size of approximately ten times the number of design variables is used for the genetic algorithm. The convergence criterion is that the relative change between the last and the 5^{th} to last generation is below 10^{-6}.

5.2.2. AIRCRAFT AERODYNAMICS, MASS AND PERFORMANCE

This module of the ARENA framework performs aircraft mass and mission analysis. This process includes the evaluation of: 1) lift coefficient (C_{L}) and drag coefficient (C_{D}), 2) maximum take-off mass (m_{mto}), 3) mission fuel mass (m_{fuel}), 4) required generator output power during take-off ($\dot{W}_{\text{to}}$) and wing area (S_{ref}), 5) cruise altitude (h_{cr}) and 6) required generator output power during cruise ($\dot{W}_{\text{cr}}$).

The aircraft's drag polar is expressed using the three-term equation $C_{\text{D}} = C_{\text{D,min}} + K_{\text{L}}(C_{\text{L}} - C_{\text{L,min}})^2$, as detailed in Ref. [6]. The parameter $C_{\text{D,min}}$ is estimated to be equal to the zero-lift drag coefficient of the two-term drag polar, approximated through the methodology outlined in Ref. [7]. The values of the parameters K_{L} and $C_{\text{L,min}}$ are determined with two additional equations: 1) $\left.\frac{dL/D}{dC_{\text{L}}}\right|_{\text{cr}} = 0$, assuming cruise at the maximum lift-to-drag ratio (L/D), and 2) $C_{\text{D}}^* = f(C_{\text{L}}^*)$, where $C_{\text{L}}^* = 0.47$ and $C_{\text{D}}^* = 0.0273$ are estimated for the ONERA Dragon at mid-cruise conditions based data provided in Ref. [1]. The values of the derived parameters are $C_{\text{D,min}} = 0.0183$, $K_{\text{L}} = 0.0937$ and

Table 5.2: CC-TS design variables and their corresponding bounds.

Model	Variables (x_i)	Description (Unit)	Bounds ($x_i^{\mathrm{L}}/x_i^{\mathrm{U}}$)
Turboshaft	Π_{noz}	Nozzle pressure ratio (-)	1.05/1.4
ORC	$T_{\mathrm{min,orc}}$	Minimum cycle temperature (K)	323/423
	$T_{\mathrm{max,orc}}$	Maximum cycle temperature (K)	520/570
	$p_{\mathrm{max,orc}}$	Maximum cycle pressure (Pa)	$1.1p_{\mathrm{crit}}/1.5p_{\mathrm{crit}}$
	$\Delta T_{\mathrm{pp,cond}}$	Condenser pinch point temperature difference (K)	20/100
	$\Delta T_{\mathrm{pp,evap}}$	Evaporator pinch point temperature difference (K)	20/100
ORC HEX	X_{cond}	Condenser flat-tube length (m)	0.5/1.0
	$\phi_{\mathrm{l,cond}}$	Condenser louver angle (deg)	10/30
	$b_{\mathrm{f,cond}}$	Condenser fin height (mm)	7.0/12.0
	$p_{\mathrm{f,cond}}$	Condenser fin pitch (mm)	1.0/4.0
	$x_{\mathrm{t,evap}}$	Evaporator non-dimensional transversal pitch (-)	1.25/3.00
	$x_{\mathrm{l,evap}}$	Evaporator non-dimensional longitudinal pitch (-)	1.25/3.0
	$n_{\mathrm{pass,evap}}$	Evaporator number of passes (-)	8/19
Ram-air Duct	$\dot{m}_{\mathrm{frac,intake}}$	Intake design mass flow rate ratio (-)	0.4/1.0
	θ_{cond}	Condenser tilt angle ($^\circ$)	45/75
ORC Turbo Generator	ψ_{is}	Isentropic stage loading (-)	0.4/1.3
	ϕ	Flow coefficient (-)	0.10/0.40
	ν	Hub-to-tip ratio (-)	0.40/0.65

$C_{\mathrm{L,min}} = 0.160$. In the case of the Dragon CC-TS, the net force arising from the ram-air duct is interpreted as a change in zero-lift drag and results in a parallel shift of the drag polar.

Estimating the mass of turboelectric and hybrid-electric aircraft configurations proves challenging in conceptual aircraft design, as conventional empirical laws linking m_{mto} to m_{oe} do not encompass these novel configurations. Hence, there is a need to employ a more detailed component-based mass estimation approach. In this work, a method proposed by De Vries et al. [8] is used. This method assumes that m_{oe} minus wing mass (m_{wing}) and powertrain mass (m_{pt}), denoted as m'_{oe}, remains independent of the powertrain architecture. m_{oe} can subsequently be determined as

$$m_{\mathrm{oe}} = m'_{\mathrm{oe}} + m_{\mathrm{pt}} + m_{\mathrm{wing}}. \tag{5.2}$$

The value of m'_{oe} can be determined either by further subdividing the airframe into its major components and applying empirical relations to establish the corresponding masses. Alternatively, in retro-fitting scenarios, it may be possible to derive its value for the reference aircraft. For the ONERA Dragon, m'_{oe} is approximated to be 24 900 kg. This value is determined with a m_{oe} of 42.7 t and a m_{pt} of 9.4 t [1]. According to Ref. [1] the wing of the ONERA Dragon is 5% lighter than that of an Airbus A320 which has a mass of 8.8 t as reported in Ref. [7]. Notably, there are no existing empirical methods for estimating m_{wing} of aircraft employing a distributed wing-mounted propulsion system. In this study, the methodology of Torenbeek [9, App. C] is employed, which demonstrates

good sensitivity of m_{wing} to major design parameters, including the option to consider 0, 2, or 4 wing-mounted engines. The m_{wing} estimated with this method assuming 4 wing-mounted engines shows good agreement with the m_{wing} estimated for the ONERA Dragon (see Tab. 5.5) if geometrical details of the wing such as sweep, aspect ratio, thickness-to-chord ratio, and inclination angles are set to the values provided by Ref. [1].

Mission fuel mass is estimated based on the Breguet range equation for cruise-climb in combination with a definition of an equivalent cruise range according to Torenbeek [10]. This equivalent cruise range includes the nominal cruise range according to the top-level aircraft requirements (TLARs), a lost range representing the amount of fuel required for climbing, and the range required for divergence, holding, and contingency. A divergence range of 400 km, a holding time of 30 min, and a contingency fraction of 5% are assumed as suggested by Ref. [10]. Cruise is performed at constant Mach number and at maximum L/D resulting in a continuous cruise-climb trajectory.

To ensure that the Dragon CC-TS fulfills the design requirements of the ONERA Dragon aircraft, the same wing loading, and power loading at maximum take-off mass is adopted. Using these values together with the evaluated m_{mto}, the values of $\dot{W}_{\text{to}}$ and S_{ref} are determined. Note that $\dot{W}_{\text{cr}}$ and $\dot{W}_{\text{to}}$ refer to generator output power.

In the second to last step, the h_{cr} is determined based on the given Mach number, C_{L}, and mid-cruise aircraft mass. In the last step, the required generator output power during cruise is evaluated taking into account the residual jet thrust ($F_{\text{net,ts}}$) produced by the CC-TS engines according to the power balance

$$\dot{W}_{\text{cr}} = \frac{(D - 2F_{\text{net,ts}})\, v_{\infty}}{\eta_{\text{trans}}\eta_{\text{prop}}}, \tag{5.3}$$

where D is the aircraft drag, v_{∞} the cruise velocity, η_{trans} the electrical powertrain efficiency (see Section 5.2.3) and η_{prop} the propulsive efficiency. All cruise-related parameters are evaluated based on the mid-cruise aircraft mass (m_{cr}) approximated according to [10] as $m_{\text{cr}} = \sqrt{m_{\text{mto}}(m_{\text{mto}} - m_{\text{fuel,cr}})}$, where $m_{\text{fuel,cr}}$ is the fuel mass required for the cruise range according to the TLARs.

5.2.3. POWERTRAIN

The powertrain architecture of the Dragon CC-TS is the same as that of the ONERA Dragon with the exception of the added ORC unit. The main components of the powertrain are the CC-TS, electrical power transmission components, and ducted-fans. The distributed propulsion system consists of 26 ducted fans. Figure 5.4 shows half of the cross-redundant architecture. Note that fault current limiters and circuit breakers are omitted in this figure for simplicity. Table 5.3 gives mass-specific power and efficiency values of the electrical components, which are sized for maximum power demand, thus during take-off. Note that the indicated values for generator mass-specific power and efficiency do not apply to the ORC turbogenerator, and are determined by a separate preliminary design tool explained in Section 5.2.6.

The powertrain mass (m_{pt}) is the sum of two times the CC-TS mass (m_{ccts}) and the mass of the electrical power transmission components (m_{trans}). m_{ccts} is the sum of the turboshaft mass (m_{ts}), the mass of the two turboshaft mounted generators (m_{gen}), and the mass of the ORC unit assembly (m_{orc}). m_{trans} is the sum of the individual electrical

component masses. These masses are determined by dividing the rated power of each component by its mass-specific power value listed in Tab. 5.3. The variation of ducted-fan size and mass with input power and the variation of cooling system mass with rated power of the electrical components are not modeled. The masses of these components are considered fixed and included in the mass m'_{oe} (see Section 5.2.2).

The powertrain efficiency (η_{pt}) is defined as the product of the net CC-TS efficiency ($\eta_{\text{net,ccts}}$), the electrical component transmission efficiency (η_{trans}) and the ducted-fan propulsive efficiency (η_{prop}). The net efficiencies of the turboshaft, ORC system and CC-TS are defined as

$$\eta_{\text{net,ts}} = \frac{\dot{W}_{\text{net,ts}}}{\dot{m}_{\text{fuel}} \cdot \text{LHV}}, \eta_{\text{net,orc}} = \frac{\dot{W}_{\text{net,orc}}}{\dot{Q}_{\text{evap}}}, \eta_{\text{net,ccts}} = \frac{\dot{W}_{\text{net,ccts}}}{\dot{m}_{\text{fuel}} \cdot \text{LHV}}, \tag{5.4}$$

where $\dot{m}_{\text{fuel}}$ is the fuel mass flow rate, $\dot{Q}_{\text{evap}}$ the thermal power recovered by the evaporator and LHV the lower heating value of the fuel which is 43 MJ/kg for kerosene. The CC-TS net power output ($\dot{W}_{\text{net,ccts}}$) is the sum of turboshaft net power output ($\dot{W}_{\text{net,ts}}$) and ORC net power output ($\dot{W}_{\text{net,orc}}$). $\dot{W}_{\text{net,ccts}}$ of a single CC-TS unit is half the required power demand during cruise $\dot{W}_{\text{cr}}$ (Eq. 5.3) and take-off $\dot{W}_{\text{to}}$, respectively. Note that net power output refers to generator power output of the turboshaft and ORC unit, also see Fig. 5.4. η_{trans} accounts for losses occurring in the electrical components between the CC-TS and the ducted-fans and is calculated as $\eta_{\text{trans}} = \eta_{\text{acdc}}\eta_{\text{pmu}}\eta_{\text{dcac}}\eta_{\text{mot}}$, where η_{acdc} is the inverter efficiency, η_{pmu} the combined efficiency of the DC busses, η_{dcac} is the converter efficiency and η_{mot} the electrical motor efficiency. η_{prop} is set to 86%, which is the value applied for the ONERA Dragon [11].

The power-specific fuel consumption (PSFC) is defined as the fuel mass flow rate divided by the total generator power output. The use of the generator power output instead of the engine shaft power output allows a direct comparison between aircraft configurations using simple-cycle turboshaft engines and CC-TS engines. The PSFC of CC-TS is calculated as

$$\text{PSFC}_{\text{ccts}} = \frac{\dot{m}_{\text{fuel}}}{\dot{W}_{\text{net,ccts}}}. \tag{5.5}$$

5.2.4. ENGINE

The turboshaft engine considered in this work is a two-spool engine with a free power turbine (FPT). The FPT powers two electric generators. The use of two generators instead of one provides redundancy and their diameter is smaller than that of a single generator which is important for the integration with the turboshaft engine. The PFD of this engine is depicted on the left-hand side of Fig. 5.3. As shown in the XDSM in Fig. 5.2 the turboshaft sub-model provides as output the performance of the turboshaft engine at the design point.

THERMODYNAMIC MODELING AND MASS ESTIMATION

The thermodynamic performance of the engine is calculated with the Python library *pycycle* [13]. Jet-A/A1 is used as the fuel. Turbomachinery polytropic efficiencies are determined using correlations presented by Samuelsson et al. [14], which are derived from the

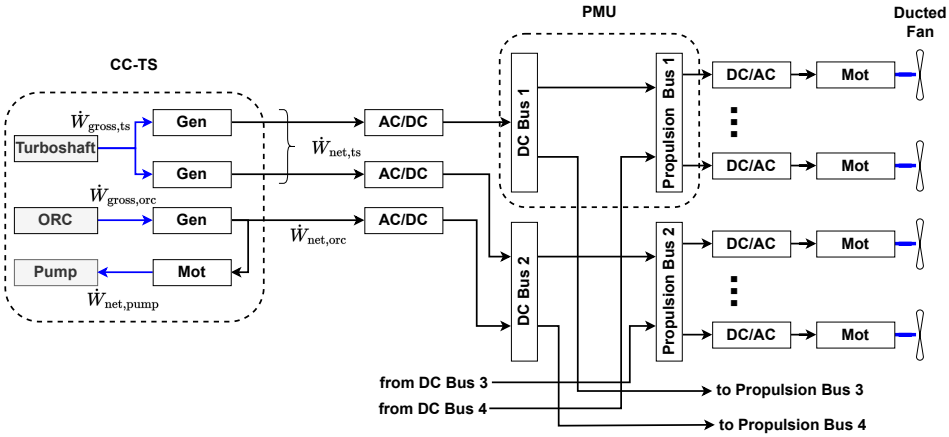

Figure 5.4: Dragon CC-TS powertrain architecture (adapted from Schmollgruber et al. [1]). Thick blue lines indicate mechanical power transmission, thick black lines electrical power transmission.

Table 5.3: Assumptions regarding the technology level of electric components. A moderate technology level is selected in accordance with the values provided in Ref. [1]

Component	**Mass specific power (kW/kg)**	**Efficiency (η)**
Generator (Gen)	13.5	0.95
Motor (Mot)	19.0	0.98
Inverter (AC/DC)	19.0	0.98
Converter (DC/AC)	19.0	0.98
Power management unit (PMU)	20.0	0.99
Cables	16.0*	1.00**

* The value is estimated by dividing the take-off power by the overall cable mass as given for the ONERA Dragon aircraft in Ref. [12] and is therefore not a generally applicable value.

** Cable losses are omitted for simplicity.

method described in Ref. [15, Ch. 5]. Based on statistical data, this method provides an estimate of turbomachinery efficiency as a function of the entry into service (EIS) year, and of the stage loading. It also takes into account scale effects based on the reduced mass flow rate ($\dot{m}_{\text{red}}$). Furthermore, the method accounts for different turbomachinery types (axial/radial) and distinguishes between the turbomachinery of the low and high-pressure sections of the engine. In this work, all engine-related turbomachinery is considered to be of the axial type.

The turbine cooling model of Gauntner [16] is adopted to estimate cooling air demand as a function of the maximum allowable turbine blade temperature and technology level.

The maximum allowable rotor blade temperature is estimated assuming creep as the

dominant failure mechanism of the rotor blades and it therefore depends on material characteristics, blade stress, and desired minimum lifetime for a certain amount of creep strain. For a given material, the relation between these variables can be modeled with the Larson-Miller Parameter LMP. The LMP is a function of blade temperature (T_b) at a given spanwise section of the blade and lifetime ($t_{b,life}$) in hours for a given amount of creep strain: LMP = $T_b[20 + log(t_{b,life})]$. Creep strain is determined by the combination of blade stress and temperature. Both vary along the blade span. While the highest stress is experienced at the blade root, the highest blade temperatures are around mid-span. As a result, the highest creep strain is located around a quarter or one-third of the blade span [17, Ch. 9]. In this work creep stress is limited to 90% of creep rupture stress [17, Ch. 9] which corresponds to a creep strain of approximately 1% for single-crystal alloys according to Grieb [15, Ch. 5]. First-stage rotor blades experience the highest creep due to high centrifugal stress combined with very high temperatures. A simplified method is applied to determine rotor blade stress due to the centrifugal load at the root of the blade as outlined in Ref. [18]. Differently from the rotor blades, the implemented method assumes a constant value of maximum allowable temperature for the stator blades.

The dry mass of the engine excluding generators (m_{ts}) is estimated, to a first approximation, with an empirical correlation whose sole input is the corrected air mass flow rate at the compressor inlet ($\dot{m}_{0,red}$). Data available in the database of Ref. [19] for 12 turboshaft engines in the 300-3000 kW power range are used to derive the following relation

$$m_{ts} = 21.56 \cdot \dot{m}_{0,red} + 85. \tag{5.6}$$

The mass resulting from this equation in combination with the considered engine power capacity results in mass-specific power values that are in good agreement with the technology assumptions cited by Schmollgruber et al. [1]. The mass of the generators is calculated by dividing the required take-off power with the mass-specific power value given in Tab. 5.3.

DESIGN ASSUMPTIONS

The thermodynamic design point of the engine is cruise (CR) at ISA+15 conditions. The overall pressure ratio (OPR) and turbine inlet temperature (TIT) that yield the highest efficiency at the design point are 45 and 1600 K, respectively. These values result from the requirement of keeping the high-pressure compressor (HPC) exit temperature during take-off below the allowable limit of 950 K [15]. The compression process is performed by a HPC with a pressure ratio of 20 and a low-pressure compressor (LPC) with a pressure ratio of 2.25.

The design point condition of the turbine cooling system is take-off (TO) where the highest value of TIT occurs. However, presently the framework is only capable of simulating a single design point of the CC-TS, which is cruise. To prevent an underestimation of the cooling air demand based on lower turbine temperatures during cruise, the temperature provided to the cooling model is multiplied by a correction factor. The value of this correction factor is approximated as $\theta_{0,to}/\theta_{0,cr} \approx TIT_{to}/TIT_{cr}$ [20], where θ_0 is the ratio of total free-stream temperature to static mean-sea-level temperature, assuming International Standard Atmosphere (ISA) conditions. The validity of this approach is verified by means of on/off-design simulations of the turboshaft engine. The cooling

flow rate is also a function of the maximum allowable turbine blade temperature. A maximum allowable stator blade temperature of 1755 K is selected, assuming that the construction material is a ceramic matrix composite [21]. The single-crystal alloy TMS-238 is selected as the turbine blade metal and its characteristics are documented in Ref. [22]. Furthermore, a thermal barrier coating (TBC) is assumed to be applied to all blades, and the temperature difference across the TBC is assumed to be 100 K [15].

The polytropic efficiencies are determined with the method of Grieb [15]. The values of average stage loading ($\bar{\Psi}$) are $\bar{\Psi}_{\text{lpc}} = 0.8$, $\bar{\Psi}_{\text{hpc}} = 1.0$, $\bar{\Psi}_{\text{hpt}} = 3.5$, $\bar{\Psi}_{\text{lpt}} = 3.5$, $\bar{\Psi}_{\text{fpt}} = 3.5$. Note that $\bar{\Psi} = \frac{2\Delta H}{U_{\text{m}}^2}$, where ΔH is the polytropic enthalpy change per stage and U_{m} the meridional velocity. Furthermore, 2035 is assumed as the entry into service (EIS) year of the investigated engine concept.

The cross-section of the exhaust duct of the engine is assumed to be of squared shape to accommodate the ORC evaporator. For each percent of pressure drop caused by the presence of the evaporator, the turboshaft thermal efficiency is reduced by approx. 0.2%. Therefore, a large evaporator frontal area is desirable as it reduces flow velocity and therefore pressure drop. However, the size of the evaporator needs to be limited to a reasonable level in order to be integrated into the nacelle of the engine. For this reason, the side length of the exhaust duct is fixed to be approximately 20% larger than the power turbine exit diameter (see Fig. 5.7). The nozzle pressure ratio (Π_{noz}), which is defined as the ratio of the nozzle throat total pressure to ambient static pressure, is adopted as a design variable. Its value sets the amount of residual thrust ($F_{\text{net,ts}}$) that the engine generates. Producing thrust with the engines could be beneficial to counter the drag induced by the ram-air ducts housing the ORC condensers. Other design assumptions are made based on data provided by Mattingly et al. [20, Ch. 4] for an engine with EIS 2035, namely, that the air intake pressure loss is 0.2%, the combustor pressure loss is 4%, the high pressure and low-pressure shaft mechanical efficiency is 99.6%, the FPT shaft mechanical efficiency is 98% and the nozzle pressure loss is 0.3%.

5.2.5. ORGANIC RANKINE CYCLE UNIT

The right side of Fig. 5.3 shows the PFD of the ORC system, based on an air-cooled non-recuperated configuration. To maximize thermodynamic efficiency a supercritical cycle is adopted. An in-house tool written in Python for on-design point thermodynamic cycle calculations, named *pycle*, is used to analyze the organic Rankine cycle. This program was verified by comparison with a commercial program for thermodynamic modeling and optimization of energy conversion systems [23]. Thermodynamic properties of the working fluid, cyclopentane, are calculated with a state-of-the-art Helmholtz equation of state (HEOS) model implemented in the open-source library *CoolProp* [24], while the ideal gas model [25] is used for the turboshaft exhaust gas. Cyclopentane has a critical temperature (T_{crit}) of 512 K, a critical pressure (p_{crit}) of $45.1 \times 10^5 Pa$ and a normal boiling point temperature of 322 K [26]. According to results presented in Chapter 3, cyclopentane is a suitable working fluid for an ORC system recuperating thermal energy from a gas turbine due to its high thermal stability ($T_{\text{max,fluid}}$) of 573 K and high T_{crit}. It is, however, possible that cyclopentane is not the optimal working fluid, both in terms of the performance of the resulting system and other technical and safety considerations. Alternative working fluids will be assessed in future works.

The ORC turbine gross power output ($\dot{W}_{\text{gross,orc}}$) is converted into electrical power via a dedicated generator (see Fig. 5.4). The turbine mechanical efficiency ($\eta_{\text{mech,turb}}$) and ORC generator efficiency ($\eta_{\text{gen,ORC}}$) are an output of the turbogenerator design procedure described in Section 5.2.6. For the pump, an isentropic pump efficiency ($\eta_{\text{is,pump}}$) of 65% and a mass-specific power of 4 kW/kg are assumed. These values are taken from Kwak et al. [27] which documents research on electrically driven centrifugal pumps for small space launch vehicles, which operate under similar conditions as expected for the pump of the ORC unit. The efficiency of the pump motor ($\eta_{\text{mot,pump}}$) is taken from Tab. 5.3. Furthermore, a pump mechanical efficiency ($\eta_{\text{mech,pump}}$) of 99% is assumed. The net power output of the ORC waste-heat-recovery system ($\dot{W}_{\text{net,orc}}$) is defined as

$$\dot{W}_{\text{net,orc}} = \dot{W}_{\text{gross,orc}}\eta_{\text{mech,turb}}\eta_{\text{gen,orc}} - \frac{\dot{W}_{\text{net,pump}}}{\eta_{\text{mech,pump}}\eta_{\text{mot,pump}}}. \tag{5.7}$$

Furthermore, the recovery factor (χ) describes how much of the available thermal power ($\dot{Q}_{\text{exh,avail}}$) is recovered by the WHR system and it is defined as

$$\chi = \frac{\dot{Q}_{\text{evap}}}{\dot{Q}_{\text{exh,avail}}}. \tag{5.8}$$

$\dot{Q}_{\text{exh,avail}}$ is defined as the product of the exhaust gas mass flow rate and the specific enthalpy difference between the turbine exit and ambient conditions.

The ORC system mass (m_{orc}) is determined as the sum of pump mass (m_{pump}), turbogenerator mass (m_{tg}), condenser mass (m_{cond}), evaporator mass (m_{evap}), working fluid mass (m_{fluid}) and balance-of-plant mass ($m_{\text{bop,orc}}$). The heat exchanger and turbogenerator masses are an output of the corresponding modules performing their preliminary design. m_{fluid} is estimated as the product of 1.2 times the evaporator cold side volume and the density of the working fluid at one atmosphere and 25 °C. It is further assumed that $m_{\text{bop,orc}}$ constitutes 10% of m_{orc}. This value is similar to that taken by Zarati et al. [28]. However, the value assumed for the mass of the balance-of-plant components is affected by uncertainty given the lack of information regarding ORC systems design for airborne applications.

The ORC unit is designed for the same environmental conditions as the turboshaft engine, i.e., CR ISA+15. Table 5.4 lists the ORC thermodynamic cycle specifications and indicates the input values which are output values of other sub-models.

Table 5.4: ORC thermodynamic cycle specifications

Parameter	Input	Parameter	Input	Parameter	Input
$T_{\text{max,orc}}$	Design variable	$\Delta p_{\text{h,ecap}}$	HEX model	$\eta_{\text{is,pump}}$	65%
$T_{\text{min,orc}}$	Design variable	$\Delta p_{\text{c,evap}}$	HEX model	$\eta_{\text{is,turb}}$	Turbogenerator model
$p_{\text{max,orc}}$	Design variable	$\Delta T_{\text{pp,evap}}$	Design variable		
$T_{\text{c,cond,in}}$	Ram-duct model	$\Delta p_{\text{h,cond}}$	HEX model		
$\dot{m}_{\text{h,evap}}$	Turboshaft model	$\Delta p_{\text{c,cond}}$	HEX model		
$T_{\text{h,evap,in}}$	Turboshaft model	$\Delta T_{\text{pp,cond}}$	Design variable		

Note: Subscripts h and c indicate heat exchanger (HEX) hot and cold sides.

5.2.6. ORC TURBOGENERATOR

The ORC turbogenerator is modeled by means of an in-house Python program for the preliminary design of high-speed turbomachinery named *Turbosim* (also see Section 4.2.6). The code has been used for the preliminary design of a 10 kW laboratory high-speed ORC turbine being realized at Delft University of Technology. The turbogenerator consists of the radial-inflow turbine, the circular cross-section volute guiding the flow at the turbine inlet, and a permanent-magnet generator.

The model employed to design the single-stage radial-inflow turbine is based on an iterative routine based on the theoretical framework described by Chen and Baines [29]. All flow losses (internal and external) occurring in the stage are modeled by means of low-order physical models, equivalent to those adopted by Giuffré and Pini [30] for axial turbine stages. Volute losses are computed using the model proposed by Japikse [31] for centrifugal compressors and adapted to the case of turbine volutes. Fluid thermodynamic properties are calculated with a commercial software library [32]. The combined impeller and volute mass is determined based on an automatically generated and simplified computational-aided design model generated by the program. In this procedure, rotor and stator blade masses are neglected and the volute is treated as a hollow toroidal duct. The wall thickness of the components volute, stator base plate, and impeller shroud is set to 5 mm. This value is based on engineering practice and manufacturing considerations.

The generator is assumed to be a cylindrical FeCo-based permanent-magnet machine with a carbon fiber retaining sleeve. The electromagnetic power of the generator and its windage loss within the air gap is modeled according to the method of James and Zahawi [33] using optimized machine-specific parameters documented by van der Geest et al. [34]. The mass-specific power is computed by interpolation using data from Ref. [34] expressed as a function of the rotor surface velocity. The total mass of the generator system is obtained by summing the mass of the generator, the mass of its power electronics, and the mass of the DC-DC converter. The individual component masses are calculated by dividing the electromagnetic power by the mass-specific power. Values of state-of-the-art mass-specific power related to the power electronics and to the DC-DC converter are taken as 14.3 kW/kg and 62.0 kW/kg, respectively. These values are obtained from the work of Gesell et al. [35]. The turbogenerator mass (m_{tg}) is the sum of generator system mass, radial-inflow turbine mass, and volute mass.

The turbogenerator preliminary design tool requires as input the total inlet pressure and temperature, the total-to-total stage pressure ratio, and the design mass flow rate. The main output variables are the turbine total-to-total efficiency ($\eta_{\text{is,turb}}$), the turbine mechanical efficiency ($\eta_{\text{mech,turb}}$), the generator efficiency ($\eta_{\text{gen,orc}}$), and the m_{tg}.

5.2.7. HEAT EXCHANGERS

Figure 5.5 shows the chosen topology for the ORC evaporator, namely a multi-pass in-line bare-tube bundle heat exchanger where the working fluid flows inside the tubes in a counter-crossflow arrangement with respect to the exhaust gases. The nickle-base alloy Hastelloy X® is selected as construction material owing to its good oxidation resistance, manufacturability, and strength at high temperatures [15]. The tube outer diameter is set to 1.8 mm, while the tube thickness is calculated given the pressure difference be-

tween the working fluid and the exhaust gases. The evaporator optimization variables are the non-dimensional transversal pitch ($x_{t,evap}$), the non-dimensional longitudinal pitch ($x_{l,evap}$) and the number of passes ($n_{pass,evap}$).

The condenser is a flat-tube-microchannel heat exchanger with louvered fins (see Fig. 5.6). Based on manufacturability considerations the following values are fixed: fin thickness 0.11 mm, flat tube thickness 0.2 mm, height of the microchannels 1.6 mm. Furthermore, the louver fin length and louver pitch are set to be 90% of the fin height and fin pitch, respectively. The condenser optimization variables are the fin height ($b_{f,cond}$), the fin pitch ($p_{f,cond}$), the louver angle ($\phi_{l,cond}$) and the length of the flat-tubes (X_{cond}). Based on the estimated space demand for the turboshaft engine inside the nacelle the condenser width (Y_{cond}) is fixed to 1.5 m (see Fig. 5.7). An aluminium alloy of the 3000 series is selected as the construction material, as suggested in the technical report of Kaltra GmbH [36].

The in-house Python tool *HeXacode* is used for heat exchanger sizing. The program was verified by comparison with a commercial code for heat exchanger design and rating [37]. The sizing procedure consists of calculating the required heat transfer area for a given heat duty, given the inlet temperature, pressure, and mass flow rate of the hot and cold streams. The outputs are the heat exchanger dimensions, mass, and pressure drops of the cold and hot sides. For both the evaporator and the condenser, the frontal area is an input, while the depth is calculated to meet the design specifications. In the case of the condenser, this corresponds to determining the number of microchannels within a single flat tube and in the case of the evaporator the number of streamwise tubes per pass. For both heat exchanger types, the geometry is discretized into several control volumes in which mean values of the fluid thermodynamic properties and the corresponding heat transfer and friction coefficients are evaluated. The evaporator features a multi-pass layout and the number of cells is set equal to the number of passes. The condenser is discretized into three volumes representing the different phases the working fluid undergoes (superheated vapor, two-phase fluid, sub-cooled liquid). The heat transfer correlations are formulated in terms of the Colburn factor or the Nusselt number, and the pressure drop calculation is based on the estimate of the friction factor or the pressure gradient. The design calculation stops when the relative difference in the calculated overall heat transfer area between two consecutive iterations is smaller than 1%.

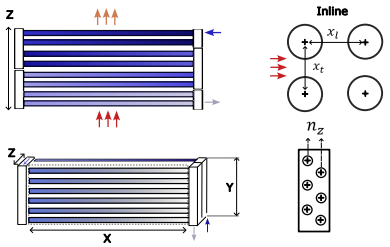

Figure 5.5: Evaporator core geometry: multi-pass inline bare tube bundle.

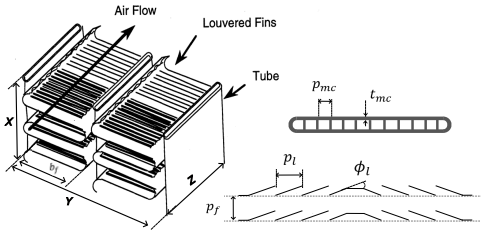

Figure 5.6: Condenser core geometry: Flat tube microchannels with louvered fins.

5.2.8. RAM-AIR DUCT

The ram-air duct houses the condenser of the ORC unit and provides it with ambient air for cooling. It consists of an intake, a diffuser, a duct accommodating the heat exchanger, and a convergent nozzle. Figure 5.7 gives an overview of the main components of the ram-air duct and how they are arranged in the CC-TS configuration. The ram-air duct model allows to compute internal losses and external losses due to friction and pressure drag, as well as thermal energy input to the airflow due to the condensing fluid in the heat exchanger. The model is based on the compressible duct model of the Python library *openConcept* [38] and is coupled with loss models for the intake, the diffuser, and pressure losses arising from heat exchanger tilt. The thermal energy input results from the simulation of the ORC system on-design operation and the condenser cold side pressure loss is computed according to the procedure described in Section 5.2.7. The expansion through the nozzle of the duct is considered isentropic.

A subsonic scoop intake is assumed and its pressure recovery and drag are estimated using the method reported in Ref. [39]. This method considers drag contributions due to skin friction, spillage drag, and diverter drag. With reference to Fig. 5.7, due to the location of the ram-air duct on the nacelle, the boundary layer thickness along the short part of the nacelle in front of the intake is neglected, as well as the possible presence of a diverter. The drag of the intake as well as the pressure recovery is a function of the intake design mass flow fraction ($\dot{m}_{\text{frac,intake}}$), which is defined as the geometrical intake area A_1 divided by the stream tube area (A_0) ahead of the intake (see Fig. 5.7). A value of $\dot{m}_{\text{fraction}} < 1$ results in an isentropic compression of the incoming airflow ahead of the intake. This reduces the Mach number at the entry to the intake and therefore increases the internal pressure recovery. However, spillage drag occurs. A value of $\dot{m}_{\text{fraction}} = 1$ results in zero spillage drag but no isentropic compression ahead of the intake and an increased intake Mach number which results in lower internal pressure recovery. Therefore, the selection of $\dot{m}_{\text{frac,intake}}$ depends on a trade-off between internal and external losses and, for this reason, its optimal value is selected by the optimizer (see Tab. 5.2).

The intake is followed by a rectangular diffuser. The total pressure losses are calculated based on the ratio of the actual pressure over the ideal pressure recovery coefficient and depend on the diffuser area ratio $AR_{\text{diff}} = A_2 / A_1$ [40]. While the diffuser entrance area (A_1) is calculated from the intake specifications and the required mass flow rate, the diffuser exit area (A_2) depends on both the heat exchanger frontal area (A_3) and its tilt angle (θ_{cond}). θ_{cond} is defined as the angle between the normal of the heat exchanger frontal area plane and the core duct velocity direction (see Fig. 5.7). A higher value of θ_{cond} is beneficial for the frontal area of the heat exchanger if the duct cross-sectional area is limited. This also reduces the required AR_{diff} and therefore results in less diffuser pressure loss. However, a larger tilt angle requires more deflection of the air stream, therefore it implies additional drag. The additional pressure loss arising due to the heat exchanger tilt is modeled based on a fit of experimental results reported by Nichols [41]. The heat exchanger inlet conditions are calculated assuming an isentropic expansion from the diffuser exit (A_2 in Fig. 5.7) to the heat exchanger inlet (A_3 in Fig. 5.7).

5.2.9. CC-TS INTEGRATION

The addition of an ORC WHR system to a turboshaft engine not only involves a mass addition but also demands additional space, which is limited onboard an aircraft. Volume limitations mainly affect the integration of the ORC heat exchangers, posing a strong limitation on their performance, as the optimal heat transfer surface is bound to be smaller than the optimal value if unconstrained by the volume limitation. Therefore, the integration of the ORC unit within the aircraft is of key importance. Figure 5.7 depicts a preliminary concept regarding the integration of the ORC heat exchangers into the nacelle containing the turboshaft engine and generators. A single evaporator is located right after the free power turbine in a square-shaped duct extending to approximately 1.2 times the diameter of the engine. Two condensers are integrated into the nacelle of the turboshaft engine. Tilting the condensers allows to keep the frontal area of the assembly as small as possible. The maximal width of the condenser (Y_{cond}) is given by the engine and generator size requirements. Note that no information is available on how the generators are integrated into the nacelle of the ONERA Dragon.

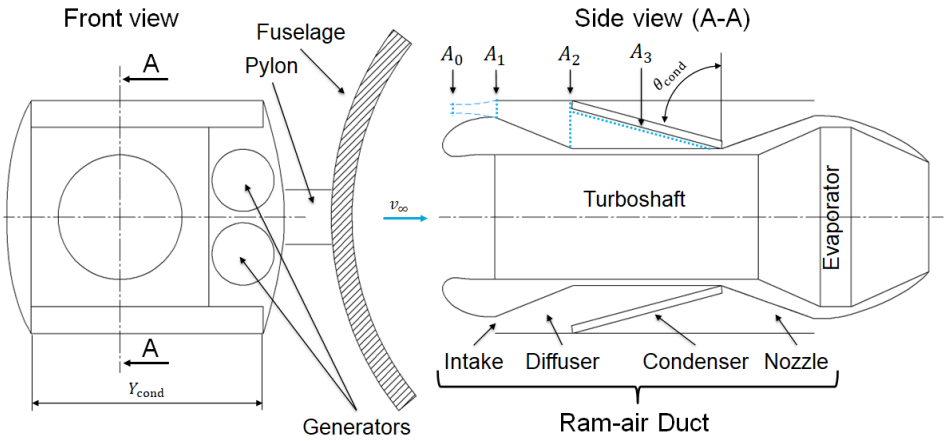

Figure 5.7: Preliminary concept of the integration of the ORC WHR unit and the turboshaft engine within the nacelle in the aft of the aircraft. Variables A_0, A_1, A_2 and A_3 indicate the cross-sectional areas along ram-air duct flow path.

5.3. RESULTS AND DISCUSSION

The ARENA framework is first verified by simulating the ONERA Dragon aircraft and comparing the results with published data related to this aircraft concept [1]. Secondly, the verified framework is used to compute the performance of a Dragon-type aircraft equipped with the optimized CC-TS engines and the result is compared with a reference aircraft. The TLARs of all considered aircraft are the same as those of the ONERA Dragon and are listed in Tab. 5.1.

5.3.1. VERIFICATION CASE

Two verification cases are simulated. They differ in the value of power-specific fuel consumption during cruise ($PSFC_{net,cr}$), while the TLARs remain the same as listed in Tab. 5.1. For verification case nr. 1 $PSFC_{net,cr}$ is fixed to a value of 0.145 kg/(kWh) and m_{pt} to 9.40 t, which are values derived from data regarding the ONERA Dragon provided by Schmollgruber et al. [1]. Schmollgruber et al. [1] assume a 10% improvement in PSFC over an engine designed in the year 2020. However, no details on the technological advancements necessary to achieve this reduction in PSFC are given. Therefore, a different value of PSFC has to be expected when using the engine model described in Section 5.2.4. For verification case nr. 2 $PSFC_{net,cr}$ is calculated using the engine model and the modeling assumptions stated in Section 5.2.4. The value of Π_{noz} is set to 1.17, to obtain an almost zero net thrust production by the turboshaft engine. Table 5.5 compares the results of the verification cases with the data of the ONERA Dragon provided by Schmollgruber et al. [1].

The comparison shows that verification case nr. 1 is in good agreement with the data reported for the ONERA Dragon. This verifies that the ARENA framework is able to compute the main characteristics of the aircraft with a sufficient degree of accuracy. Based on the modeling assumptions of verification case nr. 2, the turboshaft engine has a $PSFC_{net,cr}$ that is approximately 10% larger than the value reported for the ONERA Dragon. This leads to an increase in fuel consumption of 13% and an overall heavier and larger aircraft. The reference aircraft simulated and compared with the optimized Dragon CC-TS concept in Section 5.3.2 differs in a similar way from the ONERA Dragon.

Table 5.5: Comparison of the results obtained with the developed simulation framework with the data published for the ONERA Dragon [1].

Parameter	ONERA Dragon	Verification Case 1	Delta	Verification Case 2	Delta
m_{mto} (t)	67.9	68.2	0.4%	69.5	2.4%
m_{oe} (t)	42.7	42.8	0.2%	42.8	0.2%
m_{pt} (t)	9.40*	9.40	0.0%	9.29	-1.2%
m_{wing} (t)	8.40*	8.51	1.3%	8.64	2.9%
m_{fuel} (t)	11.5	11.8	2.6%	13.1	13.9%
L/D (-)	17.2	17.2	0.0%	17.2	0.0%
S_{ref} (m^2)	121	122	0.8%	124	2.5%
b (m)	36.0	36.1	0.3%	36.5	1.4%
$PSFC_{net,cr}$ (kg/kWh)	0.145	0.145	0.0%	0.159	9.7%
$\dot{W}_{cr}$ (MW)	10.5**	10.8	-2.9%	10.9	3.8%
$\dot{W}_{to}$ (MW)	23.2	23.3	0.4%	23.7	2.2%

* Approximated based on data given in Ref. [1]
** Approximated based on data given in Ref. [1] and propulsive efficiency given by Defoort et al. [11]

5.3.2. OPTIMIZED DRAGON CC-TS

The optimized Dragon CC-TS and the reference aircraft adopt the same powertrain architecture (Fig. 5.4) and only differ in the used engine type. Both the CC-TS and the

simple-cycle turboshaft engines of the reference aircraft are based on the design assumptions given in Section 5.2.4. Table 5.6 lists the optimized design vector calculated for the Dragon CC-TS. In the case of the reference aircraft, Π_{noz} is selected as the only design variable, and its optimum value for minimum fuel consumption is determined to be 1.35.

Table 5.6: Design vector of the optimized Dragon CC-TS

Parameter	Π_{noz}	$T_{min,orc}$	$T_{max,orc}$	$p_{max,orc}$	$\Delta T_{pp,cond}$	$\Delta T_{pp,evap}$	X_{cond}	$\phi_{l,cond}$	$b_{f,cond}$
Value	1.27	398 K	549 K	54.4 bar	41.8 K	97.8 K	1.00 m	29.7°	10.1 mm
Parameter	$p_{f,cond}$	$x_{t,evap}$	$x_{l,evap}$	$n_{pass,evap}$	$\dot{m}_{frac,intake}$	θ_{cond}	Ψ_{is}	Φ	ν
Value	1.41 mm	3.00	1.25	9	0.670	59.4°	0.966	0.394	0.460

Table 5.7: Comparison of the optimized Dragon CC-TS with the reference aircraft

Parameter	**Reference Aircraft**	**Dragon CC-TS**	**Delta**
m_{mto} (t)	69.4	69.7	0.4%
m_{oe} (t)	42.8	43.3	1.2%
m_{pt} (t)	9.26	9.72	5.0%
m_{wing} (t)	8.62	8.69	0.8%
m_{fuel} (t)	13.0	12.8	-1.5%
L/D (-)	17.2	17.3	0.6%
S_{ref} (m^2)	124	125	0.8%
b (m)	36.4	36.5	0.3%
$PSFC_{net,cr}$ (kg/kWh)	0.168	0.157	-6.5%
$\dot{W}_{cr}$ (MW)	10.3	10.8	4.9%
$\dot{W}_{to}$ (MW)	23.7	23.8	0.4%

Table 5.7 shows a comparison between the main performance parameters of the optimized Dragon CC-TS aircraft and those of the reference aircraft. The simulation of the aircraft powered by the optimized CC-TS results in an improvement of the estimated PSFC (Eq. 5.5) of 6.5% and a reduction of mission fuel consumption (m_{fuel}) of 1.5% if compared to the reference aircraft. m_{fuel} is a function of $\dot{m}_{fuel}$ which is computed as the product of PSFC and $\dot{W}_{cr}$. While the PSFC of the Dragon CC-TS is 6.5% lower than that calculated for the reference aircraft, its $\dot{W}_{cr}$ is 4.9% higher (see Section 5.3.3). As a result, the percentage of fuel saving is smaller than the improvement of PSFC. The powertrain mass of the Dragon CC-TS is 460 kg heavier than that of the reference aircraft, which is mainly due to the added mass of the ORC unit. Despite the resulting increase in m_{oe} wing mass (m_{wing}) does not vary appreciably. Furthermore, the increase in empty mass of the Dragon CC-TS is balanced by a fuel mass reduction of 200 kg which results in the values of m_{mto} being similar for both aircraft. The lift-to-drag ratio (L/D) of the Dragon CC-TS is slightly higher due to thrust production by the ram-air ducts which is considered as a reduction in zero-lift drag (see Section 5.2.2). The reference aircraft and the Dragon

CC-TS aircraft are both larger aircraft in terms of mass and wing size compared to the ONERA Dragon. This is due to the engine design assumptions as explained in Section 5.3.1. The larger wing area combined with a fixed wing aspect ratio (see Section 5.2.2) results in a slight violation of the wing span limit of 36 m that is taken as a constraint for the ONERA Dragon design. This limit is not a certification requirement for the aircraft, but a limit imposed by airport gate size for Airbus A320-sized aircraft. However, in order not to restrict the design space unnecessarily, it is not imposed as an optimization constraint.

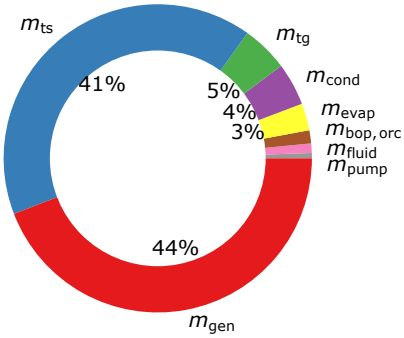

Figure 5.8: CC-TS mass breakdown; The engine generator mass m_{gen} and the condenser mass m_{cond} account for two units each.

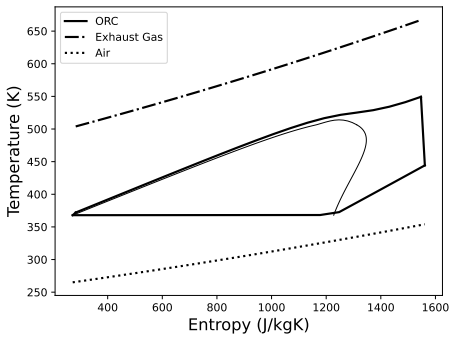

Figure 5.9: Temperature-entropy diagram of the ORC including engine exhaust gas and cooling air.

Table 5.8: Results of the optimized ORC WHR system at cruise

Parameter	Value	Parameter	Value	Parameter	Value
$\eta_{net,orc}$	17.2%	$\dot{Q}_{evap}$	1.94 MW	$\sum \dot{Q}_{cond}$ *	1.60 MW
χ	42%	$X/Y/Z_{evap}$	1.1/1.1/0.1 m	$X/Y/Z_{cond}$	1.0/1.5/0.07 m
$\dot{W}_{net,orc}$	335 kW	m_{evap}	48 kg	$\sum m_{cond}$ *	76 kg
m_{orc}	260 kg	$T_{h,in,evap}$	670 K	$T_{c,in,cond}$	265 K
N_{tg}	74.5 krpm	$T_{h,out,evap}$	500 K	$T_{c,out,cond}$	354 K
$\dot{m}_{fluid}$	3.3 kg/s	$\Delta p_{h,evap}$	2060 Pa	$\Delta p_{c,cond}$	730 Pa
T_{min}	398 K	$\dot{m}_{h,evap}$	11.2 kg/s	$\sum \dot{m}_{c,cond}$ *	17.8 kg/s
T_{max}	549 K	$\Delta T_{pp,evap}$	98 K	$\Delta T_{pp,cond}$	42 K
p_{max}	54.4 bar	ϵ_{evap}	60%	ϵ_{cond}	50%
$\dot{W}_{net,pump}$	38 kW				

* Summed up over 2 condensers.

Figure 5.8 reports the mass breakdown of the CC-TS engine and Fig. 5.9 the simplified temperature-entropy diagram of the ORC. The overall mass of the optimized CC-TS is 1710 kg, of which 1450 kg or 85% account for the mass of the turboshaft engine and of

the two engine-mounted generators, while the estimated mass of the ORC unit is 260 kg or 15% of the total mass. The ORC turbogenerator mass (m_{tg}) is 83 kg, thus it accounts for about one-third of the overall ORC system mass. $\dot{W}_{cr}$ of a single CC-TS engine is 5.42 MW, of which 5.08 MW is the electric power output of the engine-mounted generators and 335 kW is the net electric power output of the ORC unit. The resulting mass-specific power of the CC-TS, turboshaft engine including generators and ORC unit are 3.2 kW/kg, 3.5 kW/kg and 1.3 kW/kg, respectively. The thermal efficiencies of the CC-TS, turboshaft, and ORC unit are $\eta_{net,ccts}$ = 53.2%, $\eta_{net,ts}$ = 49.9% and $\eta_{net,orc}$ = 17.2%, respectively. The evaporator and the condenser designs feature moderate effectiveness (ϵ) values of 60% and 50%, respectively. Compared to the CC-APU design (see Section 4.3), the effectiveness of the evaporator is lower as its heat transfer area must be kept small to reduce the pressure drop in the exhaust duct. The evaporator hot side pressure drop ($\Delta p_{h,evap}$) is 2060 Pa which amounts to 6% of the FPT exit total pressure. The optimized ORC radial-inflow turbine design has an efficiency ($\eta_{is,turb}$) of 95%, a speed of 74 500 rpm and a gross power output ($\dot{W}_{gross,orc}$) of 390 kW. The ORC turbogenerator mechanical efficiency ($\eta_{mech,turb}$) is 99% and the generator efficiency ($\eta_{gen,orc}$) is 97%. After accounting for turbine mechanical losses and generator efficiency the net power output of the turbogenerator is 374 kW and its mass-specific power is 4.5 kW/kg. Table 5.8 lists additional data on the ORC unit design.

5.3.3. RESULTS DISCUSSION

Table 5.6 lists the optimized design vector of the Dragon CC-TS aircraft. The values of the design variables result from the complex mutual interaction of all sub-modules. For example, from a thermodynamic standpoint, ORC efficiency is maximized by maximizing $T_{max,orc}$ and $p_{max,orc}$ and minimizing $T_{min,orc}$. However, the requirements associated with the integration of the ORC unit within the nacelle result in values for these design variables that differ from their thermodynamically optimal values, and lie between the respective lower and upper bounds specified in Tab. 5.2.

The pressure loss in the exhaust duct of the turboshaft caused by the evaporator ($\Delta p_{h,evap}$) is 6% and it reduces the turboshaft thermal efficiency by approximately 1.2%. As mentioned in Section 5.2.4, the evaporator frontal area is larger than the FPT outlet area. This results in a lower bulk flow velocity and therefore pressure loss. Furthermore, the evaporator optimization variables adopt values to minimize $\Delta p_{h,evap}$. The lowest pressure drop is achieved with the maximum value of $x_{t,evap}$ and the minimum value of $x_{l,evap}$. This configuration minimizes detached flow behind each tube and therefore pressure loss. The number of passes ($n_{pass,evap}$) is the minimum value because this variable has little effect on the evaporator number of tubes, and thus on $\Delta p_{h,evap}$. A higher number of passes would only lead to a higher working fluid pressure drop. Finally, the evaporator pinch point difference ($\Delta T_{pp,evap}$) is maximum because it reduces the required evaporator heat transfer area and therefore $\Delta p_{h,evap}$.

Despite the optimized evaporator design, the resulting configuration entails several disadvantages. First, a diffuser is necessary to connect the FPT outlet to the evaporator. This not only adds length and mass to the system but also causes additional pressure loss due to diffusion. Secondly, the increase in evaporator area and therefore the potential to reduce pressure loss is limited by the additional nacelle drag as a result of an increase in

propulsion system size.

While the evaporator only influences the thermodynamic performance of the CC-TS, the condenser additionally interacts with the aircraft aerodynamics via the net force produced by the ram-air duct. The present results show that it is possible to balance internal and external ram-air duct drag with the production of thrust due to heat addition to the airflow, provided that the duct is properly designed. To achieve this benefit, optimal design variable values for the condenser are those that provide a balance between the heat transfer area, the heat transfer coefficient, and the air-side pressure drop ($\Delta p_{\mathrm{c,cond}}$). The optimizer therefore selects the condenser design with the maximum frontal area to reduce the flow velocity and therefore $\Delta p_{\mathrm{c,cond}}$. The optimization process highlights that it is more beneficial to add heat transfer area by increasing the flat-tube length (X_{cond}) and by tuning the fin parameters instead of increasing the depth, which linearly increases the pressure drop. Similarly, a maximization of the free-flow-to-frontal-area ratio of the condenser reduces the channel flow acceleration and, therefore, the maximum velocities and the pressure drop. This result is achieved by reducing the number of flat-tubes which entails that the condenser fin height $b_{\mathrm{f,cond}}$ is maximized. Conversely, the fin pitch $p_{\mathrm{f,cond}}$ is minimized in order to keep the heat transfer area to suitable values, and this causes a minimal pressure drop penalty. Additionally, the ram-air duct adopts a large diffuser area ratio ($\mathcal{AR}_{\mathrm{diff}}$) to reduce the condenser face velocity as much as possible. $\mathcal{AR}_{\mathrm{diff}}$ adopts a value that is close to 6 which is the upper limit of the used correlation.

As a consequence of the impact of the heat exchangers on turboshaft efficiency and aircraft drag, the performance of the ORC unit is limited. This results in a $\dot{W}_{\mathrm{net,orc}}$ that only accounts for approximately 5% of cruise power demand. To summarize the discussion above, the need to keep heat exchanger gas-side pressure drops as low as possible results in: 1) high pinch point temperature differences which reduce the amount of heat exchanged with the exhaust gas and the ram-air and 2) an increase in $T_{\mathrm{min,orc}}$ which reduces ORC efficiency. This highlights the impact of heat exchanger selection and integration on system performance and the mutual dependency between different parts of the system.

The working fluid is an important degree of freedom in the design of ORC systems [42], the thermodynamic cycle parameters, the conversion efficiency, the design of the components, and their techno-economic performance (turbine, heat exchangers, pump), depend on it. As briefly mentioned in Section 5.2.5, cyclopentane is selected as the working fluid because the research documented in Chapter 3 indicates that it satisfies many of the requirements for stationary WHR applications in this power range. For this reason, it was already selected as the working fluid for the CC-APU concept presented in Chapter 4. However, the exhaust gas temperature of the turboshaft engine considered in this work (670 K) is lower than the exhaust gas temperature of the stationary gas turbine (760 K) studied in Chapter 3. The difference in temperature is due to the higher thermal efficiency of the turboshaft engine. Further investigation is therefore required in the optimal selection of the ORC working fluid for highly efficient aircraft gas turbine engines.

The generator output power required during cruise ($\dot{W}_{\mathrm{cr}}$) by the reference aircraft is 4.9% lower than that required by the Dragon CC-TS, despite similar mass and L/D. This difference is caused by the different amount of residual thrust ($F_{\mathrm{net,ts}}$) produced by the

turboshaft engines of the reference aircraft with respect to the CC-TS engines. $F_{\text{net,ts}}$ affects the required $\dot{W}_{\text{cr}}$ according to Eq. 5.3. The $F_{\text{net,ts}}$ of a single engine amounts to 970 N for the reference aircraft and 170 N for the Dragon CC-TS. The engine residual thrust is set by the nozzle pressure ratio (Π_{noz}) which is an optimization parameter in both cases. The optimum value of Π_{noz} depends on the exhaust duct pressure losses ($\Delta p_{\text{h,evap}}$), on the exhaust duct heat extraction ($\dot{Q}_{\text{evap}}$), as well as on propulsive efficiency (η_{prop}). For the studied engine configuration a value of Π_{noz} in the range of approximately 1.0-1.2 results in a negative $F_{\text{net,ts}}$ and therefore an increased demand of $\dot{W}_{\text{cr}}$. A parametric study of the turboshaft model considering variations of the parameters $\Delta p_{\text{h,evap}}$, $\dot{Q}_{\text{evap}}$ and η_{prop} shows that optimal values of Π_{noz} always lead to a positive value of $F_{\text{net,ts}}$. Furthermore, with increasing η_{prop}, the optimal value of Π_{noz} reduces as the thrust is more efficiently generated by the powertrain if electric power is deliverer to the ducted-fans than if it is generated by the exhaust jet. These results highlight that it is important to consider the impact of Π_{noz} on the overall system performance.

5.3.4. METHODOLOGY LIMITATIONS

5

Possible improvements and limitations of the methodology are as follows.

- The current powertrain model does not consider the cooling requirements of electrical components. Especially the turboshaft-mounted generators, with a rated power of approximately 6 MW, require active cooling during take-off. The variation in mass and power requirement of this system is not included in the current analysis. As explained in Section 5.2.3 the cooling system mass is assumed constant and included in the aircraft mass m'_{oe}.
- The aircraft model does not consider the variation of the nacelle size and drag with respect to engine size. It can be argued that the baseline drag polar of the reference aircraft includes the contribution of the nacelle. However, in the case of the CC-TS, modifications to the nacelle are necessary. The current modeling approach only considers a change in the wetted area of the nacelle by the ram-air duct model. Furthermore, nacelle and ram-air duct mass are neglected.
- Fluid dynamic losses related to the engine exhaust duct are only partially modeled. For example, losses encountered in the diffuser connecting the FPT outlet to the evaporator are not accounted for. Furthermore, a physics-based modeling of the engine's nozzle losses is missing.
- The CC-TS system schematic of Fig. 5.7 shows that according to this conceptual arrangement the generators are connected to the FPT via a radial drive shaft similar to the ones adopted for secondary power off-takes of turbofan engines. However, the use of a high-speed generator might allow for the direct coupling of the generator with the FPT shaft. Such a direct coupling may affect the air intake or nozzle flow path if the generators are placed on the centerline of the engine. Therefore, the integration of the generators with the turboshaft engines and its impact on propulsion system size and performance requires further investigation.
- The objective of the present work is to identify a propulsion system that is environmentally friendlier than conventional gas turbine engines. Mission fuel consumption is selected as the figure of merit to assess the environmental impact. How-

ever, while uncertainty is still large, most recent research suggests that non-CO_2 emissions, such as the emission of NOx and water vapor, account for two-thirds of radiative forcing caused by aviation [43]. Therefore, to identify a CC-TS design that results in the least climate impact, it is necessary to extend the current framework to also account for non-CO_2 emissions. In this case, a suitable figure of merit can be the average temperature response suggested by Dallara et al. [44].

5.4. CONCLUSIONS

The work documented here is an initial feasibility investigation of the concept of a novel power unit for turboelectric aircraft based on the concept of a combined-cycle engine formed by a turboshaft engine and an organic Rankine cycle (ORC) waste-heat-recovery (WHR) system. This novel aircraft architecture is investigated by means of a newly developed multidisciplinary simulation framework encompassing the modeling of the complex powertrain and of the main design elements of the aircraft to estimate the merit parameters of the new aircraft over a representative mission. In particular, this framework allows to compute the thermodynamic performance of the combined-cycle engine, performs the preliminary design of the components, and considers changes to the aircraft aerodynamics and operating empty mass due to the addition of the new system. An optimal combined-cycle turboshaft engine (CC-TS) design is identified using a genetic algorithm. The optimization objective is the minimization of the mission fuel mass based on the variation of 18 design variables. The investigated aircraft configuration is similar to that of the ONERA Dragon concept. It is shown that a reduction of mission fuel mass of 1.5% is possible if the turboelectric powertrain is equipped with a CC-TS instead of a simple-cycle turboshaft engine. The increase in operating empty mass of the aircraft employing the CC-TS due to its heavier powertrain is balanced by the reduction in fuel mass, which results in both the reference aircraft and the new concept having a similar take-off mass. Furthermore, calculations demonstrate that the drag resulting from the ram-air duct which houses the condenser of the ORC unit can be balanced by thrust generated due to thermal energy addition to the air stream. Heat exchanger size limitations and the need to keep gas-side pressure drop as low as possible are identified as the most critical performance limitations of the ORC WHR unit. Based on these findings, future work will investigate:

- different condenser topologies to reduce air-side pressure drop,
- different evaporator layouts that allow reduced gas-side pressure drop while keeping engine frontal area as small as possible,
- different ORC architectures, e.g., adopting a recuperator could allow a reduction in condenser size and subsequently a potential reduction in drag due to ram-air ducts in case of an air-cooled ORC configuration,
- different ways to utilize the power provided by the ORC turbine, e.g., via mechanical coupling with the turboshaft engine,
- the identification of an optimal ORC working fluid for airborne WHR applications,
- the optimal integration of the ORC system with the gas turbine engine and airframe, and

- the identification of an optimized CC-TS design for minimized environmental impact including non-CO_2 effects.

BIBLIOGRAPHY

[1] P. Schmollgruber, D. Donjat, M. Ridel, I. Cafarelli, O. Atinault, C. François, and B. Paluch, "Multidisciplinary design and performance of the ONERA hybrid electric distributed propulsion concept (Dragon)," in *AIAA SciTech Forum*, 2020, doi: 10.2514/6.2020-0501.

[2] B. T. Schiltgen and J. Freeman, "Aeropropulsive interaction and thermal system integration within the ECO-150: A turboelectric distributed propulsion airliner with conventional electric machines," in *16th AIAA Aviation Technology, Integration, and Operations Conference*, 2016, doi: 10.2514/6.2016-4064.

[3] J. L. Felder, G. V. Brown, H. DaeKim, and J. Chu, "Turboelectric distributed propulsion in a hybrid wing body aircraft," in *20th ISABE Conference*, 2011.

[4] J. S. Gray, J. T. Hwang, J. R. R. A. Martins, K. T. Moore, and B. A. Naylor, "OpenMDAO: An open-source framework for multidisciplinary design, analysis, and optimization," *Structural and Multidisciplinary Optimization*, vol. 59, no. 4, pp. 1075–1104, April 2019, doi: 10.1007/s00158-019-02211-z.

[5] J. Blank and K. Deb, "Pymoo: Multi-objective optimization in Python," *IEEE Access*, vol. 8, pp. 89 497–89 509, 2020, doi: 10.1109/ACCESS.2020.2990567.

[6] E. Torenbeek, *Advanced Aircraft Design*. John Wiley and Sons, 2013, ISBN: 9781118568101.

[7] E. Obert, *Aerodynamic Design of Transport Aircraft*. IOS Press, 2009, ISBN: 978-1-58603-970-7.

[8] R. De Vries, M. Brown, and R. Vos, "A preliminary sizing method for hybrid-electric aircraft including aero-propulsive interaction effects," in *AIAA Aviation Forum*, Atlanta, Georgia, USA, 2018, doi: 10.2514/6.2018-4228.

[9] E. Torenbeek, *Synthesis of Subsonic Airplane Design*. Delft University Press, 1982, ISBN: 90-247-2724-3.

[10] ——, "The initial calculation of range and mission fuel during conceptual design," Delft University of Technology, Faculty of Aerospace Engineering, Tech. Rep., 1987, report LR-525.

[11] S. Defoort, E. Nguyen, and P. Schmollgruber, "Personal communication with onera," 2023.

[12] M. Ridel, E. Nguyen Van, T. Prosvirnova, D. Donjat, C. Seguin, and P. Choy, "DRAGON: hybrid electrical architecture for distributed fans propulsion," in *MEA Conference*, Bordeaux, France, 2021.

[13] E. S. Hendricks and J. S. Gray, "pyCycle: A tool for efficient optimization of gas turbine engine cycles," *Aerospace 2019*, vol. 6, p. 87, 8 2019, doi: 10.3390/AEROSPACE6080087.

[14] S. Samuelsson, T. Gronstedt, and K. G. Kyprianidis, "Consistent conceptual design and performance modeling of aero engines," in *Proceedings of the ASME Turbo Expo*, 2015, doi: 10.1115/GT2015-43331.

[15] H. Grieb, *Projektierung von Turboflugtriebwerken*. Birkhäuser Basel, 2004, ISBN: 978-3-0348-7938-5, doi: 10.1007/978-3-0348-7938-5.

[16] J. W. Gauntner, "Algorithm for calculating turbine cooling flow and the resulting decrease in turbine efficiency," NASA Lewis Research Centre, Tech. Rep., 1980, NASA-TM-81453.

[17] J. W. Sawyer, *Sawyer's Gas Turbine Engineering Handbook, Volume 1: Theory & Design*, 3rd ed. Turbomachinery International Publications, 1985, ISBN: 0-937506-14-1.

[18] H. I. H. Saravanamuttoo, G. F. C. Rogers, H. Cohen, P. V. Straznicky, and A. C. Nix, *Gas Turbine Theory*, 7th ed. Pearson Education, 2017, ISBN: 0132224372.

[19] Jane's Information Group, "Jane's aero-engines," 2022. [Online]. Available: https://shop.janes.com/products/air-space/janes-aero-engines

[20] J. D. Mattingly, W. H. Heiser, K. M. Boyer, B. A. Haven, and D. T. Pratt, *Aircraft Engine Design*, 3rd ed. AIAA, 2018, ISBN: 978-1-62410-650-7.

[21] S. M. Jones, W. J. Haller, and M. T.-H. Tong, "An N+3 technology level reference propulsion system," NASA Glenn Research Centre, Tech. Rep., 2017, NASA-TM-2017-219501.

[22] K. Kawagishi, A. C. Yeh, T. Yokokawa, T. Kobayashi, Y. Koizumi, and H. Harada, "Development of an oxidation-resistant high-strength sixth-generation single-crystal superalloy TMS-238," *Superalloys*, pp. 189–195, 10 2012, doi: 10.1002/9781118516430.CH21.

[23] T. Van der Stelt, N. Woudstra, P. Colonna *et al.*, "Cycle-tempo: a program for thermodynamic modeling and optimization of energy conversion systems," 1980, software.

[24] I. H. Bell, J. Wronski, S. Quoilin, and V. Lemort, "Pure and pseudo-pure fluid thermophysical property evaluation and the open-source thermophysical property library CoolProp," *Industrial & Engineering Chemistry Research*, vol. 53, no. 6, pp. 2498–2508, 2014, doi: 10.1021/ie4033999.

[25] P. Colonna and T. van der Stelt, "FluidProp (version 3.1): A program for the estimation of thermophysical properties of fluids," 2019, software.

[26] M. Astolfi and E. Macchi, *Organic Rankine Cycle (ORC) Power Systems*. Elsevier, 2017, doi: 10.1016/C2014-0-04239-6.

[27] H. D. Kwak, S. Kwon, and C. H. Choi, "Performance assessment of electrically driven pump-fed LOX/kerosene cycle rocket engine: Comparison with gas generator cycle," *Aerospace Science and Technology*, vol. 77, pp. 67–82, 6 2018, doi: 10.1016/J.AST.2018.02.033.

[28] K. Zarati, S. Maalouf, and A. T. Isikveren, "Potential of the bottom organic Rankine cycle to recover energy on turboprop engine architecture," in *23rd ISABE Conference*, 2017.

[29] H. Chen and N. Baines, "The aerodynamic loading of radial and mixed-flow turbines," *International Journal of Mechanical Sciences*, vol. 36, no. 1, pp. 63–79, 1994, doi: 10.1016/0020-7403(94)90007-8.

[30] A. Giuffré and M. Pini, "Design guidelines for axial turbines operating with non-ideal compressible flows," *Journal of Engineering for Gas Turbines and Power*, vol. 143, no. 1, p. 011004, 2021, doi: 10.1115/1.4049137.

[31] D. Japikse, *Centrifugal Compressor Design and Performance*. Concepts ETI, 1996.

[32] E. W. Lemmon, I. H. Bell, M. L. Huber, and M. O. McLinden, "Nist standard reference database 23: Reference fluid thermodynamic and transport properties-REFPROP, Version 10.0, national institute of standards and technology," 2018, software.

[33] B. P. James and B. Zahawi, "High speed generator for turbocharger based domestic combined heat and power unit employing the inverted brayton cycle," *Energy Procedia*, vol. 42, pp. 249–260, 2013, doi: 10.1016/j.egypro.2013.11.025.

[34] M. van der Geest, H. Polinder, J. A. Ferreira, and M. Christmann, "Power density limits and design trends of high-speed permanent magnet synchronous machines," *IEEE Transactions on Transportation Electrification*, vol. 1, no. 3, pp. 266–276, 2015, doi: 10.1109/TTE.2015.2475751.

[35] H. Gesell, F. Wolters, and M. Plohr, "System analysis of turbo-electric and hybrid-electric propulsion systems on a regional aircraft," *The Aeronautical Journal*, vol. 123, no. 1268, p. 1602–1617, 2019, doi: 10.1017/aer.2019.61.

[36] Kaltra GmbH, "Microchannel condensers: Heat exchangers for condenser applications," 2020, accessed on 16 June 2023. [Online]. Available: https://www.kaltra.com/wp-content/uploads/2020/04/TM_Microchannel-Condensers_Ver.3.0_EN.pdf

[37] GREThe, "Echtherm version 3.2," 2023, software.

[38] E. J. Adler and J. R. R. A. Martins, "Efficient aerostructural wing optimization considering mission analysis," *Journal of Aircraft*, vol. 60, no. 3, pp. 800–816, 2023, doi: 10.2514/1.C037096.

[39] H. C. Garner, "ESDU86002: Drag and pressure recovery characteristics of auxiliary air inlets at subsonic speeds," ESDU, Tech. Rep., 2004, ISBN: 978 0 85679 554 1.

[40] G. Sovran and E. D.Klomp, "Experimentally determined optimum geometries for rectilinear diffusers with rectangular, conical or annular cross-section," General Motors Research Laboratories, Tech. Rep., 1968.

[41] M. R. Nichols, "Investigation of flow through an intercooler set at various angles to the supply duct," NASA Langley Research Center, Tech. Rep., 1942.

[42] P. Colonna, E. Casati, C. Trapp, T. Mathijssen, J. Larjola, T. Turunen-Saaresti, and A. Uusitalo, "Organic Rankine cycle power systems: From the concept to current technology, applications, and an outlook to the future," *Journal of Engineering for Gas Turbines and Power*, vol. 137, 10 2015, doi: 10.1115/1.4029884.

[43] D. Lee, D. Fahey, A. Skowron, M. Allen, U. Burkhardt, Q. Chen, S. Doherty, S. Freeman, P. Forster, J. Fuglestvedt, A. Gettelman, R. De León, L. Lim, M. Lund, R. Millar, B. Owen, J. Penner, G. Pitari, M. Prather, R. Sausen, and L. Wilcox, "The contribution of global aviation to anthropogenic climate forcing for 2000 to 2018," *Atmospheric Environment*, vol. 244, p. 117834, 2021, doi: 10.1016/j.atmosenv.2020.117834.

[44] E. S. Dallara, I. M. Kroo, and I. A. Waitz, "Metric for comparing lifetime average climate impact of aircraft," *AIAA Journal*, vol. 49, no. 8, pp. 1600–1613, 2011, doi: 10.2514/1.J050763.

6

CC-TF Engine for Partial-Turboelectric Aircraft

Parts of this chapter have been submitted to the Journal of Propulsion and Power

ABSTRACT

This chapter presents a study on a novel combined-cycle turbofan (CC-TF) engine concept consisting of a turbofan engine and an organic Rankine cycle (ORC) bottoming unit. The performance of this engine is investigated as part of the propulsion system of a partial-turboelectric aircraft. This work aims to identify if benefits in terms of mission fuel consumption can be derived from the CC-TF engine if compared to a simple-cycle turbofan engine with entry into service in the year 2035. For this purpose, a multidisciplinary optimization framework is employed, incorporating models of the engine, the distributed propulsion system, the ORC unit, the heat exchangers, the aircraft, and mission analysis. A propulsion system design for minimum fuel consumption is obtained by coupling the simulation framework with an optimizer. The results suggest that fuel savings of around 4% are possible with the optimized system if compared to the benchmark, therefore a partial-turboelectric aircraft adopting simple-cycle turbofan engines. The ORC turbogenerator contributes approximately one-fifth of the required electrical power demand and the ORC system has a mass-specific power of approximately 1 kW/kg. The estimated thrust-specific fuel consumption of the partial-turboelectric propulsion system adopting the CC-TF engine is 13.5 mg/Ns, which is approximately 6% lower than that of the benchmark. The CC-TF engine benefits from the ORC system in two ways. Firstly, the contribution of the ORC system to shaft power production reduces the required fuel mass flow rate. Secondly, the thermal energy transfer to the engine bypass stream from the condensers of the ORC system increases both the engine propulsive efficiency and the specific thrust if compared to a simple-cycle turbofan engine with a similar bypass ratio. As a consequence, the power capacity of the prime mover is lower at the cruise design point. However, to satisfy the take-off thrust demand the smaller engine operates at a higher turbine inlet temperature than a simple-cycle turbofan engine. This requires more turbine cooling air which penalizes cruise performance. The CC-TF engine could therefore benefit from a turbine cooling system with adaptive cooling flow rates. As aspects for further investigation, an analysis of the effect of ORC working fluids on system design and of mechanical coupling of the ORC turbine with the engine shaft are proposed. Furthermore, an extension of the simulation framework with the full capability to perform aircraft conceptual design is desirable.

6.1. INTRODUCTION

The analysis of the combined-cycle turboshaft (CC-TS) engine concept presented in Chapter 5 shows that adopting an ORC bottoming unit to recover thermal energy from the turboshaft engines of a turboelectric aircraft may reduce mission fuel consumption by 1.5%. Building upon these results, the research documented in this chapter is about an improved combined-cycle propulsion system for turboelectric aircraft.

The major limitation of ORC WHR system performance concerns the rejection of thermal energy associated with the condensation of the working fluid. In the case of the CC-TS concept, the condensers are placed inside ram-air ducts. According to the results presented in Chapter 5, the thrust produced by heat addition to the ram air balances the additional drag due to the heat exchanger, the ducting, and the intakes, resulting in a net zero force acting on the aircraft. However, the enthalpy available for thrust

production caused by the expansion of the air through the duct increases if thermal energy is transferred to a compressed gaseous stream. Simple calculations show, that at a typical fan pressure ratio of 1.5, transferring 80 kW of thermal power per kg/s to the air stream (an amount similar to the value obtained for the ram-air ducts of the CC-TS concept) increases propulsive efficiency by 30% in absolute terms, assuming that the heat exchanger causes no pressure loss. Propulsive efficiency is defined as the net thrust power divided by the power required to compress the air. This observation is the basis of the research regarding the combined-cycle turbofan (CC-TF) engine concept, whereby the condensers are integrated into the engine bypass duct downstream of the fan.

Adopting this engine configuration affects the overall propulsion system architecture of the aircraft. Contrary to the fully-turboelectric architecture (see Fig. 6.1) treated in Chapter 5, the work documented here is about the analysis of a partial-turboelectric architecture where the thrust is provided both by the CC-TF engines and by an under-the-wing distributed propulsion system composed of electrically-driven ducted-fans (see Fig. 6.1). In this chapter, to clearly distinguish between the two turboelectric architectures, the term fully-turboelectric is used instead of turboelectric.

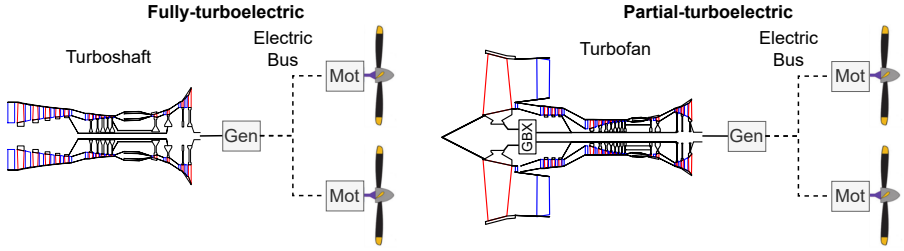

Figure 6.1: Schematics of the fully-turboelectric and partial-turboelectric powertrain architectures.

Examples of partial-turboelectric aircraft concepts are those studied by NASA, namely the STARC-ABL [1] (Fig. 6.2) and the SUSAN [2] (Fig. 6.3) concepts. The top-level aircraft requirements (TLAR) of both concepts are similar to those of the Airbus A320 and employ turbofan engines to generate both thrust and electrical power which is delivered to electric propulsors. In the case of the STARC-ABL concept, two under-the-wing mounted turbofan engines provide electrical power to a fan located in the aftbody of the aircraft. It is reported that a fuel saving of 7 to 12% with respect to a conventional aircraft of the same technology level is achievable with simple-cycle turbofan engines. Furthermore, while the aircraft maximum take-off mass increases due to larger wing and empennage surfaces, the propulsion system mass is reduced due to a lack of electric motor power lapse with altitude and speed, allowing for the downsizing of the turbofan engines. The aft-fan provides approximately one-third of the required cruise thrust. The SUSAN concept employs one single tail-mounted turbofan engine which provides 20 MW of electrical power to a distributed propulsion system located under the wings. The turbofan engine supplies 35% of the total thrust during cruise. The aircraft achieves a fuel consumption reduction of 27% if compared to the Boeing B737-800.

The aircraft studied in this work are derived from the ONERA Dragon fully-turboelectric aircraft concept (see Fig. 6.4) [3]. This aircraft employs two turboshaft engines housed in

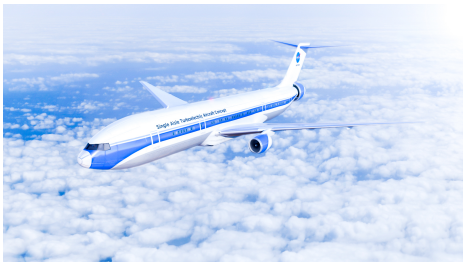

Figure 6.2: Rendering of the NASA STARC-ABL concept [1].

Figure 6.3: Rendering of the NASA SUSAN concept [2].

pods in the aft of the aircraft to provide electric power to a distributed propulsion system mounted under the wings and consisting of electrically-driven ducted-fans. The objective of this research is to analyze the performance of two partial-turboelectric aircraft configurations where the turboshaft engines of the ONERA Dragon are replaced with simple-cycle turbofan engines in the case of the reference aircraft and CC-TF engines in the case of the CC-TF aircraft. The ARENA framework is used to identify preliminary fuel-optimized designs of both propulsion system concepts.

Figure 6.4: Rendering of the ONERA Dragon aircraft concept as presented in Ref. [3].

Table 6.1: Top-level aircraft requirements (TLARs) of the ONERA Dragon [3]

Parameter	Input
Range (NM/km)	2750/5100
Number of passengers (-)	150
Mach number (-)	0.78
Design payload (kg)	13600

6.2. METHODOLOGY

The ARENA framework is developed for the preliminary design and performance evaluation of aircraft using simple-cycle as well as combined-cycle engines. The framework is modular and all modules are integrated into a system model using the Python library *openMDAO* [4].

6.2.1. ENGINE ARCHITECTURE

A geared two-spool turbofan engine serves as the prime mover of the reference and the CC-TF aircraft. In the case of the CC-TF engine, an ORC WHR unit recovers thermal energy from the gas turbine. Figure 6.5 depicts the integration of the CC-TF engine into the nacelle which is attached with a pylon to the tail cone of the fuselage. In the case of the simple-cycle turbofan engine, the same integration and mounting architecture is assumed, except for the missing heat exchangers. The process flow diagram of the

CC-TF is depicted in Fig. 6.6 and the extended design structure matrix (XDSM) of the CC-TF aircraft system model containing all major modules is shown in Fig. 6.7. The XDSM indicates dependencies between components with the thick gray lines, and the thin black line indicates the computational flow. The exchange of dependent variables between disciplines is indicated with the gray boxes. The white boxes at the top row of the diagram indicate the required user input data.

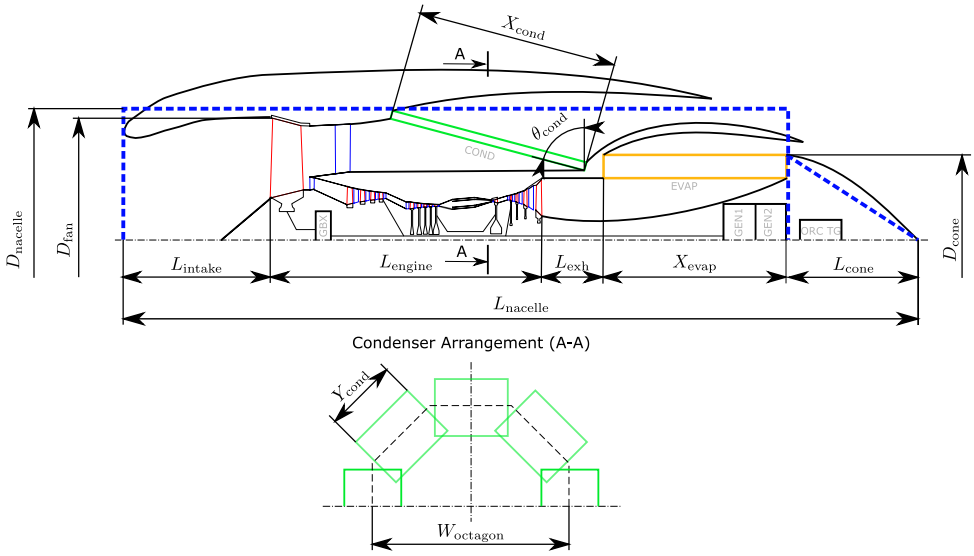

Figure 6.5: Schematic of the CC-TF engine concept including major dimensions and a cutplane (A-A) showing the condenser arrangement. The thick dashed blue line indicates the simplified geometry used for nacelle sizing. GBX: gearbox. COND: condenser of the ORC system. EVAP: evaporator of the ORC system. GEN: electrical generator. ORC TG: turbogenerator of the ORC system. The piping and feed pump of the ORC system are omitted.

The CC-TF concept features three generators that provide electrical power to the distributed propulsion system. Two of these generators are connected to the low-pressure spool of the gas turbine engine as shown in Fig. 6.5. Two generators instead of one provide redundancy and their diameter is smaller than that of a single generator. The third generator is connected to the ORC turbine, thus forming the ORC turbogenerator assembly. A single annular evaporator is located in the S-shaped annular exhaust duct of the core flow. After exiting the low-pressure turbine (LPT), the exhaust air is diverted outward, passes through the evaporator, and turns back towards the exit forming a ring-shaped axial nozzle. This arrangement increases the evaporator heat transfer area while keeping the engine frontal area small. Additionally, it allows for an efficient integration of the electric generators. Turboprop/turboshaft engines of the Pratt & Whitney PT6 and General Electric H-series families adopt a similar configuration of the exhaust duct, which has also been proposed as the basis for the development of recuperated engines with annular-shaped recuperators [5] and, in a more recent study, of a water-enhanced turbofan engine [6]. The aerodynamic design of the exhaust duct presents a challenge with respect to the minimization of aerodynamic losses due to the sharp flow turning.

Nevertheless, according to Badger et al. [7] "pressure loss levels equivalent to, or better than straight-out exhausts" are possible if the ducting is carefully designed. In this work, a relative pressure loss of 1.5% is taken and this assumption is based on the preliminary design of a recuperated engine with similar ducting presented by Heldenbrand and Miller [5]. Eight condensers are arranged according to an octagonal pattern inside the bypass duct of the engine, see Fig. 6.5. To reduce engine frontal area the condensers are tilted with respect to the radial direction by an angle θ_{cond}. Each condenser has the same size and exchanges the same amount of energy with the airflow.

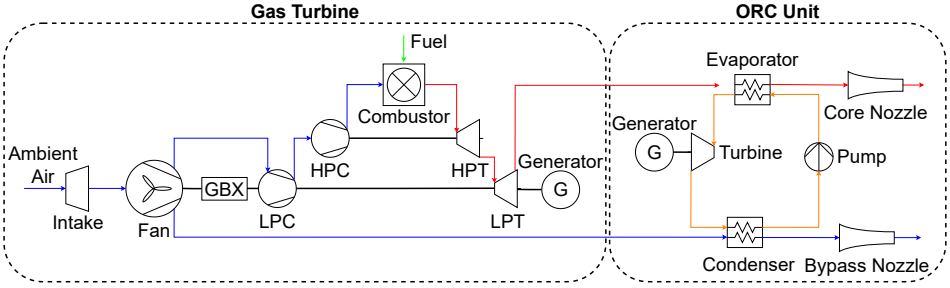

Figure 6.6: Process flow diagram of the CC-TF configuration.

6.2.2. AIRCRAFT AERODYNAMICS, MASS AND PERFORMANCE

This module of the ARENA framework performs aircraft mass and mission analysis. This numerical procedure includes the evaluation of 1) lift coefficient (C_{L}) and drag coefficient (C_{D}), 2) maximum take-off mass (m_{mto}), 3) mission fuel mass (m_{fuel}), 4) required equivalent output power of the electrical generator at the rolling-take-off (RTO) operating point ($\dot{W}_{\text{rto,eq}}$) and required wing area (S_{ref}), 5) required power output of the electrical generator and required turbofan thrust during cruise (CR), RTO and sea-level-static (SLS) conditions, and 6) cruise altitude (h_{cr}).

The drag polar of the aircraft is determined with the method outlined in Section 5.2.2. The calculation of the drag polar takes into account both the nacelle and the pylon drag. The drag coefficient associated with both the nacelle and the pylon of the ONERA Dragon turboshaft engines estimated with the method described in Section 6.2.6 is approximately 5 drag counts. In the case of the CC-TF aircraft, the variation of the nacelle drag coefficient with engine size with respect to the value calculated for the ONERA Dragon baseline is considered and accounted for as a change in zero-lift drag.

The estimation of the mass of turboelectric and hybrid-electric aircraft is challenging during the conceptual design phase because commonly used empirical laws relating m_{mto} to operating empty mass (m_{oe}) are not suitable for these novel configurations. The method to estimate m_{oe} is outlined in Section 5.2.2.

The estimation of m_{fuel} is obtained by using the Breguet range equation for a cruise-climb scenario, coupled with the definition of an equivalent cruise range according to the guidelines provided by Torenbeek [8], see Section 5.2.2 for further details on the adopted assumptions.

To ensure that the partial-turboelectric aircraft meets the design requirements set

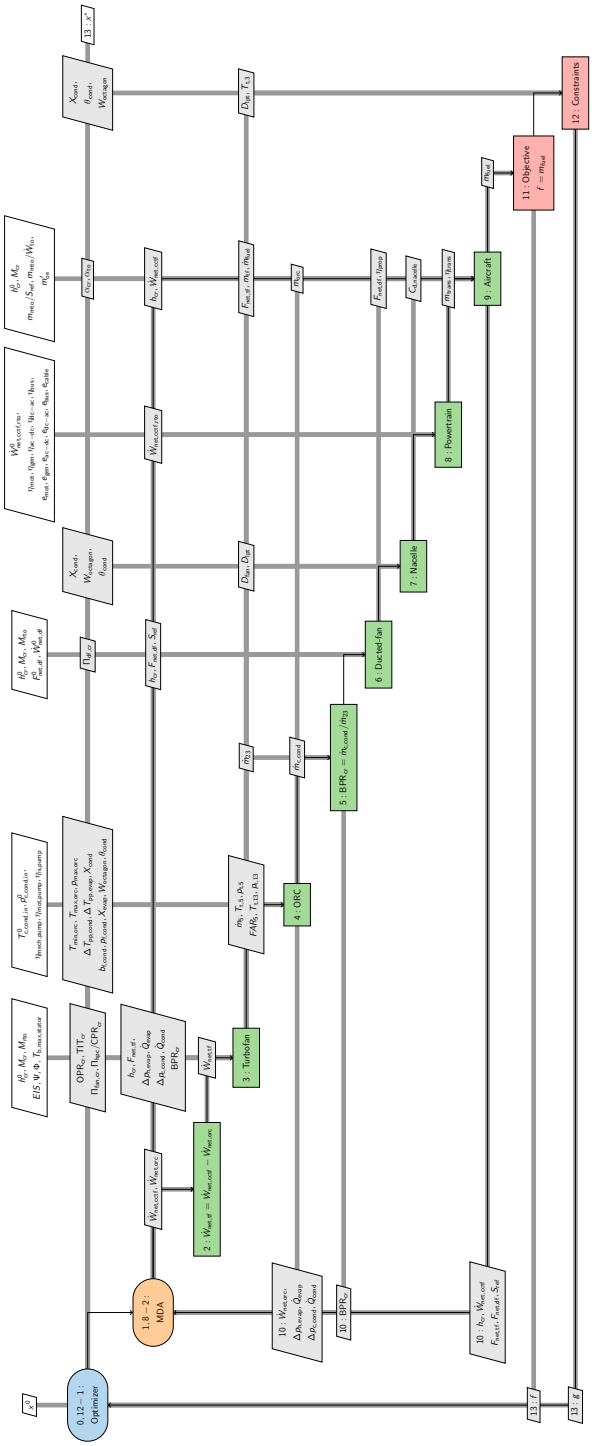

Figure 6.7: XDSM of CC-TF aircraft system model.

for the ONERA Dragon aircraft, identical wing-loading and power-loading values based on the maximum take-off mass are employed. The wing-loading is 559 kg/m^2 and the power-loading based on the output power of the electric generators is 2930 kg/MW. Using these values together with the evaluated m_{mto}, the values of S_{ref} and the equivalent generator output power during rolling-take-off ($\dot{W}_{\text{net,eq,rto}}$) are determined. $\dot{W}_{\text{net,eq,rto}}$ is the generator output power required if the ducted-fans produce the full thrust, i.e., for an aircraft equivalent to the ONERA Dragon architecture. Subsequently, the equivalent net thrust generated by the ducted-fans is calculated according to

$$F_{\text{net,eq,rto}} = \frac{\eta_{\text{prop,df,rto}}\eta_{\text{trans}}\dot{W}_{\text{net,eq,rto}}}{V_{\infty,\text{rto}}}, \tag{6.1}$$

where $\eta_{\text{prop,df,rto}}$ is the ducted-fan propulsive efficiency at RTO, and η_{trans} is the powertrain transmission efficiency defined in Eq. 6.4.

Assuming that this hypothetical fully-turboelectric aircraft and the partial-turboelectric aircraft share the same design except for the propulsion system architecture, the value of $F_{\text{net,eq,rto}}$ is taken as the required thrust at RTO ($F_{\text{req,rto}}$) of the considered partial-turboelectric aircraft. Subsequently, the required thrust at the sea-level-static (SLS) operating point ($F_{\text{req,sls}}$) is determined based on a thrust lapse rate of $\frac{F_{\text{req,rto}}}{F_{\text{req,sls}}} = 0.8$, which according to the relations presented by Mattingly et al. [9] is a suitable value for turbofan engines with a bypass ratio in the range of 5 to 8 at RTO conditions.

Once these values are computed, the thrust requirements of the engine and the ducted-fans are calculated separately, using relations that are valid for all the the considered operating points, namely CR, RTO, and SLS. The net thrust required by a single engine ($F_{\text{net,eng}}$) and a single ducted-fan ($F_{\text{net,df}}$) are calculated with

$$F_{\text{net,eng}} = \frac{F_{\text{req}}\alpha}{N_{\text{eng}}} \quad \text{and} \quad F_{\text{net,df}} = \frac{F_{\text{req}} - N_{\text{eng}}F_{\text{net,eng}}}{N_{\text{df}}}, \tag{6.2}$$

where N_{eng} and N_{df} are the number of engines and ducted-fans, respectively. Furthermore, the word engine and subscript eng are used to refer to both the simple-cycle turbofan and the CC-TF engine. The thrust ratio (α), the ratio between the net thrust provided by the engines and the total required thrust (F_{req}), is an input for all three operating points. The same value of α is set for both the RTO and SLS operating points.

With $F_{\text{net,df}}$, the required generator output power of a single engine ($\dot{W}_{\text{net,eng}}$) can be evaluated as

$$\dot{W}_{\text{net,eng}} = \frac{N_{\text{df}}F_{\text{net,df}}V_{\infty}}{\eta_{\text{trans}}\eta_{\text{prop,df}}N_{\text{eng}}}, \tag{6.3}$$

where V_{∞} is the free stream velocity, η_{trans} is the powertrain transmission efficiency (Eq. 6.4), and $\eta_{\text{prop,df}}$ is the ducted-fan propulsive efficiency at the given operating point. In the case of the simple-cycle turbofan engine, $\dot{W}_{\text{net,eng}}$ equals the net output power of the generators ($\dot{W}_{\text{net,gen}}$). In the case of the CC-TF engine, $\dot{W}_{\text{net,eng}}$ is the sum of $\dot{W}_{\text{net,gen}}$ and the net power output of the ORC unit ($\dot{W}_{\text{net,orc}}$) (see Fig. 6.8).

The cruise altitude h_{cr} is determined based on the cruise Mach number, C_{L}, and the mid-cruise aircraft mass (m_{cr}). All cruise-related parameters are evaluated based on m_{cr}, which is approximated according to Ref. [8] as $m_{\text{cr}} = \sqrt{m_{\text{mto}}(m_{\text{mto}} - m_{\text{fuel,cr}})}$, where

$m_{\text{fuel,cr}}$ is the fuel mass required for the cruise range according to the top-level aircraft requirements (TLARs).

6.2.3. POWERTRAIN ARCHITECTURE

The powertrain architecture of the partial-turboelectric aircraft is similar to the one of the ONERA Dragon, differing only in the configuration of the prime mover. However, as only part of the thrust is produced by the distributed propulsion system, the powertrain of the partial-turboelectric aircraft is expected to be lighter as the powertrain can be sized for a lower electrical load. In the following, the word engine and subscript eng are used to refer to both the simple-cycle turbofan and the CC-TF engine.

The main components of the powertrain are the engines, the electrical power transmission components, and the distributed propulsion system consisting of electric motors and ducted-fans mounted under the wings. The powertrain consists of two engines ($N_{\text{eng}} = 2$) and the distributed electric propulsion system consisting of 26 ducted-fans ($N_{\text{df}} = 26$). Figure 6.8 shows half of the cross-redundant architecture of the partial-turboelectric aircraft. Note that fault current limiters and circuit breakers are omitted in this flowchart for simplicity.

The powertrain mass (m_{pt}) is the sum of twice the engine mass (m_{eng}) and the mass of the electrical power transmission components (m_{trans}). m_{eng} comprises the gas turbine mass (m_{gt}), the mass of the two gas-turbine-mounted generators (m_{gen}), and, in the case of the CC-TF engine, the mass of the ORC unit assembly (m_{orc}). m_{trans} is the sum of the masses of each electrical component, which are determined by dividing the rated power of each component by its mass-specific power. The powertrain transmission efficiency (η_{trans}) accounts for losses occurring in the electrical components between the engine electric generator and the ducted-fan and it is calculated as

$$\eta_{\text{trans}} = \eta_{\text{acdc}}\eta_{\text{pmu}}\eta_{\text{dcac}}\eta_{\text{mot}}, \tag{6.4}$$

where η_{acdc} is the rectifier efficiency, η_{pmu} is the combined efficiency of the DC busses, η_{dcac} is the inverter efficiency and η_{mot} is the electrical motor efficiency. In the case of the CC-TF engine, the combined power output of the generators of the gas turbine ($\dot{W}_{\text{net,eng}}$) and of the ORC unit ($\dot{W}_{\text{net,orc}}$) equals the required power, which is determined with Eq. 6.3. The gross shaft power demand of the gas turbine engine ($\dot{W}_{\text{gross,gt}}$) is calculated by dividing $\dot{W}_{\text{net,gt}}$ by the generator efficiency (η_{gen}). The combined efficiency of the partial-turboelectric propulsion system is defined as

$$\eta_{\text{tot,sys}} = \frac{(N_{\text{eng}}F_{\text{net,eng}} + N_{\text{df}}F_{\text{net,df}})V_{\infty}}{N_{\text{eng}}\dot{m}_{\text{fuel}}\text{LHV}}, \tag{6.5}$$

where $\dot{m}_{\text{fuel}}$ is the fuel mass flow rate of a single engine and LHV is the lower heating value of the fuel, which is 43 MJ/kg for kerosene.

POWERTRAIN DESIGN ASSUMPTIONS

Table 6.2 lists mass-specific power and efficiency values for all the electrical components, which are designed for maximum power demand, thus typically for RTO. Values for generator efficiency and mass-specific power are set equal to those of an experimental 4 MW aerospace-grade generator developed by Golovanov et al. [10]. However, values

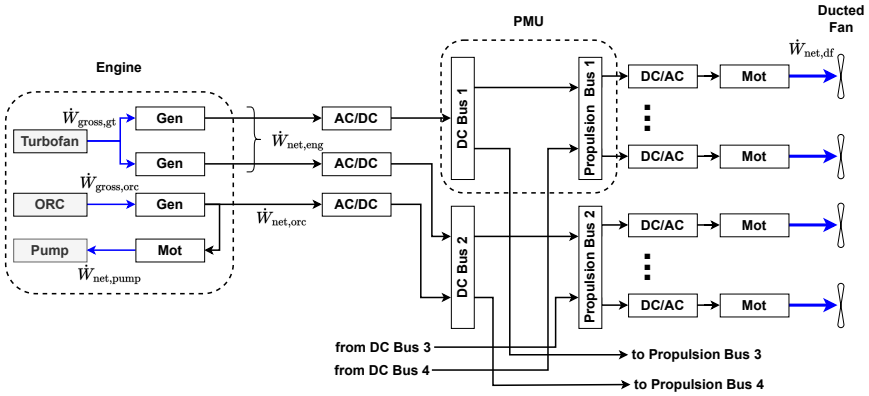

Figure 6.8: Flowchart of the powertrain architecture of the partial-turboelectric CC-TF aircraft (adapted from Ref. [3]). Thick blue lines indicate mechanical power transmission, and thick black lines electric power transmission.

of mass-specific power and efficiency for the ORC turbogenerator are determined differently, i.e., with the dedicated tool described in Section 4.2.6. These values are given in Tab. 6.6. The variation of the size and mass of ducted-fan turbomachinery and nacelle with input power is not modeled and the variation of the number of ducted fans (N_{df}) with respect to the reference aircraft is not considered. However, the variation of the mass of ducted-fan motors is considered as described in this section. Furthermore, the mass of the thermal management system of the electrical drivetrain is not modeled and it is considered to be part of m'_{oe} (see Section 6.2.2).

Table 6.2: Assumptions regarding the technology level of electric components. Values for the generator are taken from Ref. [10]. Values for all other components are taken or estimated from Ref. [3] assuming a moderate technology level.

Component	**Mass-specific power** (e)	**Efficiency** (η)
Generator (Gen)	17.3 kW/kg	98%
Motor (Mot)	19.0 kW/kg	98%
Inverter (AC/DC)	19.0 kW/kg	98%
Converter (DC/AC)	19.0 kW/kg	98%
Power management unit (PMU)	20.0 kW/kg	99%
Cables	16.0 kW/kg*	100%**

* The value is estimated by dividing the take-off power by the overall cable mass as given for the ONERA Dragon aircraft in Ref. [11] and is therefore not a generally applicable value.

** Losses due to ohmic resistance are neglected for simplicity.

6.2.4. ENGINE

The thermodynamic performance of the engine in design and off-design conditions is calculated with the Python library *pycycle* [12]. Jet-A is considered as the fuel. Turbomachinery polytropic efficiencies are determined using correlations presented by Samuelsson et al. [13], which are derived from the method described in Ref. [14, Ch. 5]. Based on statistical data, this method estimates turbomachinery efficiency as a function of the entry into service (EIS) year and the stage loading. It also considers scale effects based on the reduced mass flow rate at the entrance of the component. Furthermore, the method accounts for different turbomachinery types (axial/radial) and distinguishes between the turbomachinery of the low and high-pressure sections of the engine. In this work, all engine-related turbomachinery is considered to be of the axial type.

The turbine cooling model of Gauntner [15] is adopted to estimate the cooling air demand as a function of the maximum allowable turbine blade temperature and technology level. Additionally, this model estimates the degradation of turbine efficiency as a function of the cooling flow rate. The maximum allowable rotor blade temperature is estimated assuming creep as the dominant failure mechanism. A method to determine this temperature as a function of blade material, blade stress, and desired minimum lifetime for a certain amount of creep strain is explained in Section 4.2.3. The maximum allowable stator blade temperature is set to a constant value. The virtual rotor inlet temperature method of Kurzke and Halliwell [16, Part D, Ch.5] is applied to split the stator and rotor cooling air fractions into *non-chargeable* and *chargeable* cooling flows. The non-chargeable cooling flows are injected before the first turbine rotor and contribute to the work extraction, the chargeable cooling flows are injected at the exit of the turbine and do not contribute to work extraction.

The mass of the gas turbine engine excluding the mass of the electric generators (m_{gt}) is estimated using a correlation valid for geared turbofan engines provided by Greitzer et al. [17]. This correlation requires as input the values of the bypass ratio, OPR, and the core mass flow rate at SLS conditions. The mass of the electrical generators is calculated by dividing the take-off shaft power by the value of the mass-specific power given in Tab. 6.2.

An in-house tool for the mechanical design of gas turbine engines coded in Python and named *WEST*, see Chapter 7, is used to design the engine gas path. For this purpose, WEST requires as input the thermodynamic conditions, shaft speeds, and turbomachinery duty coefficients at the engine design point, as well as geometrical features such as blade aspect ratios, taper ratios, and connecting duct lengths. Gas path dimensions such as fan diameter (D_{fan}) and engine length (L_{engine}) are used for the sizing of the nacelle and of the air-intake. The air-intake length (L_{intake}) is calculated with a fixed ratio of fan diameter to air-intake length of 0.65 suggested by Ref. [9].

The gas generator efficiency is defined as

$$\eta_{\text{gg}} = \frac{0.5\dot{m}_{45}(V_{45,\text{id}}^2 - V_{\infty}^2)}{\dot{m}_{\text{fuel}} \cdot \text{LHV}}, \tag{6.6}$$

where the numerator defines the enthalpy available at the exit of the high-pressure turbine (HPT) (engine station 45) if the exhaust gas was isentropically expanded to ambient conditions reaching the speed $V_{45,\text{id}}$. The following definition of propulsive efficiency of

the turbofan bypass stream is adopted

$$\eta_{\text{prop,byp}} = \frac{F_{\text{net,byp}} V_\infty}{\dot{W}_{\text{fan}} \dfrac{\text{BPR}}{1+\text{BPR}}}, \tag{6.7}$$

$F_{\text{net,byp}}$ is the net thrust of the bypass stream, and the denominator relates to the fraction of the shaft power transferred to the fan ($\dot{W}_{\text{fan}}$) required to compress the bypass air stream. The propulsive efficiency in Eq. 6.7 is defined in the same way as the propulsive efficiency of the ducted-fans (Eq. 6.19), which allows a direct performance comparison of both propulsors. For the simple-cycle turbofan engine of the reference aircraft, the bypass ratio during cruise (BPR_{cr}) is given as a design variable. For the CC-TF engine BPR_{cr} is calculated as

$$\text{BPR}_{\text{cr}} = \frac{\sum \dot{m}_{\text{c,cond}}}{\dot{m}_{23}}, \tag{6.8}$$

where the numerator is the condenser cold side air mass flow rate ($\dot{m}_{\text{c,cond}}$) summed over all condensers and the denominator is the core air mass flow rate at cruise ($\dot{m}_{23}$). The nozzle gross thrust coefficient (C_{fg}) is a measure of the nozzle efficiency and it takes into account all the losses due to viscous effects and flow angularity [9]. It is defined as

$$C_{\text{fg}} = \frac{F_{\text{g}}}{F_{\text{g,i}}}, \tag{6.9}$$

which is the ratio of the actual gross thrust (F_{g}) to the ideal gross thrust ($F_{\text{g,i}}$).

ENGINE DESIGN ASSUMPTIONS

Table 6.3 gives the design assumptions for an EIS year of 2035. The thermodynamic design point of the engine is CR at ISA+15 conditions. The considered off-design points are RTO and SLS. Sea level conditions and a Mach number of 0.25 are set for the RTO operating point. The same turbomachinery maps as those assumed for the NASA N+3 engine concept [18] are used. The cooling system is designed at the RTO operating point and an advanced film cooling technique is assumed (cooling configuration 6 according to Ref. [15, Tab. 1]). The cooling air mass fractions determined at RTO are set equal at all other operating points. This is common practice for gas turbine performance simulations [19]. For the determination of the turbine cooling flow rate, a maximum allowable stator blade temperature of 1755 K is selected, assuming ceramic matrix composite as the construction material [18]. The single-crystal alloy TMS-238 is chosen as the turbine blade metal and its characteristics are documented in Ref. [20]. Furthermore, a thermal barrier coating (TBC) is assumed to be applied to the stator and rotor blades, and the temperature difference across the TBC is considered to be 100 K [14]. A radial temperature distribution factor of 0.13 and an overall temperature distribution factor of 0.3 are assumed based on data provided in Ref. [14]. The values adopted for the gross thrust coefficient of the core and bypass nozzles are based on experimental data of 1970s-era turbofan engines presented in Ref. [21]. The values of the relative pressure drop in the exhaust and bypass ducts ($dPqP$, the variable acronym is taken from Ref. [18]) are fixed and the same for all operating points. In the case of the CC-TF engine, these values serve

as the baseline, and the pressure drop due to the heat exchangers is added to the baseline value.

The high-pressure spool speed at the design point is set to 25 000 rpm, which is determined based on mechanical considerations. The rotational speed of the low-pressure spool at the design point is set to the design speed of the electric generators mounted to that shaft, which is 15 000 rpm [10]. The fan speed at the design point is calculated assuming an axial inflow Mach number of 0.6, a fan rotor hub-to-tip ratio of 0.3, and a relative rotor tip Mach number of 1.3. Table 6.4 reports the turbomachinery work coefficients (Ψ) and flow coefficients (Φ) used for engine sizing and turbomachinery efficiency estimation. The degree of reaction is set to 0.5 for all turbomachines. The values of these coefficients, except for those of the fan, are approximated following the method outlined in Section 7.3.1 assuming the CFM56-7B engine as the baseline. The reason for selecting this engine as the baseline is that data about its performance and component masses are available in the literature. It is acknowledged that the choice of this engine as the baseline is not optimal considering that the CC-TF is a geared turbofan configuration that adopts a low-speed fan and a high-speed LPT. For this reason, the duty coefficients of the fan are modified to result in a fan rotor hub-to-tip ratio of approximately 0.3.

Table 6.3: Engine Design Assumptions

Parameter	Value	Parameter	Value
$dPqP_{\text{intake}}$	0.002 [9, Ch. 4]	$C_{\text{fg,cr}}{}^{*}$	97% [21, Ch. 8]
$dPqP_{\text{duct,byp}}$	0.01 [14, Ch. 5]	$C_{\text{fg,rto}}{}^{*}$	99% [21, Ch. 8]
$dPqP_{\text{duct,exh}}$	0.015 [5]	$C_{\text{fg,sls}}{}^{*}$	99% [21, Ch. 8]
$dPqP_{\text{noz}}{}^{*}$	0.003 [9, Ch. 4]	RTDF	0.13
$dPqP_{\text{cc}}$	0.04 [9, Ch. 4]	OTDF	0.3
$\eta_{\text{mech,hp}}$	99.6% [9, Ch. 4]	ΔT_{tbc}	100 K
$\eta_{\text{mech,lp}}$	99.6% [9, Ch. 4]	$T_{\text{max,stator}}$	1755 K
$\eta_{\text{mech,gbx}}$	99% [18]		

* Same for core and bypass nozzle

Table 6.4: Values of duty coefficient assumed for the design of turbomachinery.

Parameter	Value	Parameter	Value
Ψ_{fan}	1.0	Φ_{fan}	1.2
Ψ_{lpc}	0.3	Φ_{lpc}	0.7
Ψ_{hpc}	0.3	Φ_{hpc}	0.6
Ψ_{hpt}	1.7	Φ_{hpt}	0.5
Ψ_{lpt}	1.9	Φ_{lpt}	1.0

6.2.5. ORGANIC RANKINE CYCLE UNIT

The thermodynamic cycle calculation related to the on-design operating condition and the mass estimation of the ORC unit follows the methodology outlined in Section 5.2.5. The ORC turbine gross power output ($\dot{W}_{\text{gross,orc}}$) is converted into electrical power via a dedicated electrical generator (see Figure 6.8). An electrical motor drives the ORC pump whose net power input ($\dot{W}_{\text{net,pump}}$) is assumed to be provided by the ORC turbogenerator (see Fig. 6.6). Therefore, the ORC net power output is calculated as

$$\dot{W}_{\text{net,orc}} = \dot{W}_{\text{gross,orc}} \eta_{\text{mech,turb}} \eta_{\text{gen,orc}} - \frac{\dot{W}_{\text{net,pump}}}{\eta_{\text{mech,pump}} \eta_{\text{mot,pump}}}, \tag{6.10}$$

taking into account the mechanical efficiency of the ORC turbine ($\eta_{\text{mech,turb}}$), the ORC generator efficiency ($\eta_{\text{gen,orc}}$), the mechanical efficiency of the pump ($\eta_{\text{mech,pump}}$), and the efficiency of the electric motor of the pump ($\eta_{\text{mot,pump}}$). The net efficiency of the ORC system is defined as

$$\eta_{\text{net,orc}} = \frac{\dot{W}_{\text{net,orc}}}{\dot{Q}_{\text{evap}}}, \tag{6.11}$$

where $\dot{Q}_{\text{evap}}$ is the thermal power recovered by the evaporator of the ORC system[1]. Furthermore, the recovery factor (χ) describes how much of the available thermal power ($\dot{Q}_{\text{exh,avail}}$) is recovered by the WHR system and it is defined as

$$\chi = \frac{\dot{Q}_{\text{evap}}}{\dot{Q}_{\text{exh,avail}}}. \tag{6.12}$$

$\dot{Q}_{\text{exh,avail}}$ is defined as the product of the exhaust gas mass flow rate and the specific enthalpy difference between the state of the exhaust gas at the turbine exit and that at ambient conditions.

ORC UNIT DESIGN ASSUMPIONS

Figure 6.6 shows the process flow diagram of the CC-TF engine, with it, that of the ORC unit, which is of an air-cooled non-recuperated configuration. A supercritical thermodynamic cycle is adopted to maximize the thermal efficiency of the ORC system. As explained in Section 4.2.4 and Section 4.3, in the particular case of an airborne system, aircraft fuel efficiency benefits more from maximizing the ORC unit thermal efficiency than the amount of recovered thermal energy. Moreover, an improvement in fuel efficiency over the cruise phase has the largest impact on the overall mission fuel consumption. Therefore, the thermodynamic design point of the ORC WHR unit is the same as that of the prime mover, i.e., CR at ISA+15 conditions. It is assumed that the ORC unit is not operational in operating conditions other than CR. The reason is that the current implementation of the design tool pycle is limited to on-design simulations only. Therefore, the effect of the pressure drop caused by heat exchangers and the variation of heat transfer rate on gas turbine performance, and the contribution of the ORC system to

[1] This heat exchanger is called evaporator even if, being the fluid supercritical, no phase change takes place. However, the fluid at the exit is in a vapor-like state, and the term evaporator is often used also in the case of supercritical power plants. Alternatively, this heat exchanger is also called primary heat exchanger.

power production are not evaluated at these operating points. However, the influence of neglecting the contribution of the ORC system to the overall performance at operating points other than cruise is minimal because:

1. The relatively high ambient temperature at sea level implies that the condensation temperature of the working fluid is much higher than during cruise operation, thus the value of $\eta_{\text{net,orc}}$ is considerably lower.

2. At take-off, the heat capacity (mass flow rate times specific heat capacity) in the core and bypass streams of the gas turbine is appreciably larger than during cruise. However, the heat exchangers of the ORC system are designed for thermal loads during cruise. Therefore, the evaporator cannot exploit the large amount of thermal power discharged by the gas turbine at take-off. In addition, the bypass air temperature increase due to the thermal power discharged by the ORC condenser is small due to the large air mass flow rate at take-off, therefore its positive effect on propulsive efficiency is small.

However, while not modeled, it is hypothesized that the ORC condenser heats the bypass stream just enough to balance the negative effect of aerodynamic drag due to the presence of the heat exchanger in the bypass. The validity of this hypothesis is confirmed by the results of engine off-design simulations in which it is assumed that the pressure drop and heat transfer to the bypass stream caused by the condenser are the same as in cruise conditions.

Cyclopentane is assumed as the working fluid of the ORC unit. Cyclopentane has a critical temperature (T_{crit}) of 512 K, a critical pressure (p_{crit}) of 4.51 MPa, and a normal boiling point temperature of 322 K [22]. As discussed in Chapter 3, cyclopentane is a suitable working fluid for ORC systems recovering thermal energy from gas turbine engines of stationary power plants and is adopted for power plants in operation[2]. Favorable characteristics are its high thermal stability in contact with stainless steel ($T_{\text{max,fluid}}$) of 573 K [23] and high T_{crit}. However, for reasons of thermodynamic performance of the resulting system and other technical and safety-related considerations, it is possible that cyclopentane is not the optimal fluid for the type of aircraft engines considered in this study. Other working fluids will be assessed as part of the continuation of this research program. In this study, the Turbosim computer program (see Section 4.2.6) is not used to design the ORC turbogenerator. Instead, values of ORC turbine efficiency ($\eta_{\text{is,turb}}$) and mass-specific power (e_{tg}) for the optimized turbogenerator design obtained for the configuration reported in Section 5.3.2 are used (see Tab. 6.6). The mass of the turbogenerator is calculated by dividing the turbogenerator net power output by the turbogenerator mass-specific power. The values of the pump isentropic efficiency and the mass-specific power are taken from the work of Kwak et al. [24], who document research on electrically driven centrifugal pumps for small space launch vehicles, which operate under similar conditions as expected for the pump of the ORC unit. Table 6.5 summarizes the input variables for the specification of the thermodynamic cycle of the ORC unit and whether they are a design variable or taken from other sub-modules. Table 6.6 lists assumed values of efficiencies and mass-specific power of the pump and the turbogenerator.

[2] To the author's knowledge, the combined-cycle power plant being built at the Dahshour gas compression station in Egypt, see https://www.turboden.com/solutions/2603/combined-cycles, is an example.

Table 6.5: Input variables for the specification of the thermodynamic cycle of the ORC system.

Parameter	Input	Variable	Input
$T_{\text{max,orc}}$	Design variable	$\Delta p_{\text{h,ecap}}$	HEX model
$T_{\text{min,orc}}$	Design variable	$\Delta p_{\text{c,evap}}$	HEX model
$p_{\text{max,orc}}$	Design variable	$\Delta T_{\text{pp,evap}}$	Design variable
$T_{\text{c,cond,in}}$	Ram-duct model	$\Delta p_{\text{h,cond}}$	HEX model
$\dot{m}_{\text{h,evap}}$	Gas turbine model	$\Delta p_{\text{c,cond}}$	HEX model
$T_{\text{h,evap,in}}$	Gas turbine model	$\Delta T_{\text{pp,cond}}$	Design variable

Note: Subscripts h and c indicate heat exchanger (HEX) hot and cold sides.

Table 6.6: Values of assumed efficiencies and mass-specific power of components of the ORC system.

Parameter	Value	Parameter	Value
$\eta_{\text{is,pump}}$	65% [24]	$\eta_{\text{mech,turb}}$	99% [Ch. 5]
$\eta_{\text{mot,pump}}$	98% [3]	$\eta_{\text{gen,orc}}$	97% [Ch. 5]
$\eta_{\text{mech,pump}}$	99%	e_{pump}	4 kW/kg [24]
$\eta_{\text{is,turb}}$	95% [Ch. 5]	e_{tg}	4.5 kW/kg [Ch. 5]

6.2.6. NACELLE MODEL

The nacelle houses all the components of the engine and is connected to the tail cone of the fuselage via a pylon. The drag of the nacelle is estimated based on a simplified geometry that consists of a cylindrical part and a tail cone as indicated with a dashed blue line in Fig. 6.5. The diameter of the nacelle (D_{nacelle}) is determined as

$$D_{\text{nacelle}} = \max(D_{\text{fan}}, W_{\text{octagon}} + X_{\text{cond}} \cos\theta_{\text{cond}}), \tag{6.13}$$

where D_{fan} is the engine fan diameter, W_{octagon} is the width of the octagon along which the condensers are arranged, X_{cond} is the condenser length, and θ_{cond} is the condenser tilt angle. With reference to Fig. 6.5, the length of the nacelle (L_{nacelle}) is the sum of L_{intake}, L_{engine}, the core exhaust duct length (L_{exh}), the evaporator length (X_{evap}), and the length of the tail cone (L_{cone}). The value of L_{exh} is set to 0.3 m. The simple-cycle turbofan engine does not incorporate an evaporator but for the sake of obtaining an approximation of the nacelle size it is assumed that $X_{\text{evap}} = 0.7$ m. This value results from measured values of a cutaway drawing of the Pratt & Whitney PT6 turboshaft engine [7] which adopts a similar exhaust configuration and features an exhaust duct that is approximately 1.1 times longer than the turbine outer diameter. Test calculations related to the design of the CC-TF engine showed that the LPT exit diameter is in the range of 0.6 m. L_{cone} is fixed to 0.75 m and its diameter (D_{cone}) is set to the outer diameter of the evaporator. The value of L_{cone} is determined to ensure that there is enough space to place the engine-mounted generators and the ORC turbogenerator. The nacelle drag

coefficient ($C_{d,nacelle}$) is estimated based on the flat plate analogy as

$$C_{d,nacelle} S_{ref} = C_{f,turb}(1+\phi) S_{wet,nacelle}, \tag{6.14}$$

where $C_{f,turb}$ is the turbulent flat plate skin friction coefficient and ϕ a factor considering the lift-independent pressure drag contribution. $C_{f,turb}$ is determined with the correlation

$$C_{f,turb} = 0.044 / Re_{co}^{1/6} \quad [25], \tag{6.15}$$

together with the cut-off Reynolds number (Re_{co}) that is evaluated as

$$Re_{co} = 36.82 \cdot (L_{nacelle} / h_{eq,sand})^{1.072} \quad [21], \tag{6.16}$$

using an equivalent sand grain roughness ($h_{eq,sand}$) value of 0.001 in. The width of the pylon is taken to be 25% of $D_{nacelle}$, a value which lies in the range suggested by Torenbeek [26], and its length is set equal to $L_{nacelle}$. The drag caused by the pylon is estimated using Eq. 6.14, with the same values of $C_{f,turb}$ and ϕ adopted for the calculation of the nacelle drag. Additionally, an interference drag amounting to 10% of the combined nacelle and pylon drag is assumed, as suggested by [26]. The mass of the nacelle is considered part of m'_{oe} (see Section 6.2.2) and its variation with nacelle size is not accounted for.

6.2.7. DUCTED-FAN MODEL

The on-design and off-design thermodynamic performance of ducted-fans mounted under the wings is calculated with the Python library *pycycle* [12]. A ducted-fan assembly consists of an air-intake, a fan driven by an electric motor, a duct, and a variable-area nozzle. A variable-area nozzle is employed to improve propulsive efficiency during take-off and to prevent the surge of the fan. For simplicity, a conical nozzle is assumed and the corresponding performance parameters are used for the calculations. However, it is acknowledged that a square-shaped nozzle would be more practical to vary its throat area. The surge margin at a constant reduced mass flow rate (SM_m) is defined as

$$SM_m = \frac{\Pi_{surge} - \Pi_{df}}{\Pi_{df}}, \tag{6.17}$$

where Π_{surge} is the surge pressure ratio at a given reduced mass flow rate and Π_{df} is the ducted-fan fan pressure ratio. The polytropic efficiency of the fan is estimated as a function of Π_{df} using the relation proposed by Sgueglia et al. [27] as

$$\eta_{poly,df} = 0.98 - 0.08(\Pi_{df} - 1). \tag{6.18}$$

The propulsive efficiency of the ducted-fan is defined as

$$\eta_{prop,df} = \frac{F_{net,df} V_\infty}{\dot{W}_{net,df}}. \tag{6.19}$$

DUCTED-FAN DESIGN ASSUMPTIONS

The thermodynamic design point of the ducted-fan is CR at ISA+15 conditions. The considered off-design points are RTO and SLS. Sea level conditions and a Mach number of

0.25 are set for the RTO operating point. The same fan map as that assumed for the NASA N+3 engine concept [18] is used, as no better alternative was found in the literature. However, the map of an optimized fan for the studied cases is likely to be different. The variable area nozzle is controlled to ensure a surge margin of 30% at the SLS and RTO operating points. The fan speed at the design point is set to 10 000 rpm, which, for the expected flow conditions during cruise and an assumed hub-to-tip ratio of 0.3, ensures a subsonic tip Mach number. In accordance with data provided in Ref. [9] for component efficiencies of engines with EIS year 2035, for all operating points, relative total pressure losses amounting to 1% for the air-intake, 0.5% for the duct, and 0.3% for the nozzle are assumed. The same values of C_{fg} as for the engine nozzles are applied at the CR, RTO, and SLS operating points (see Tab. 6.3). A discussion of the sensitivity of system performance to the value of C_{fg} is presented in Section 6.3.3. The mass of the ducted-fans is considered part of m'_{oe} and the variation of ducted-fan size, nacelle drag, and mass with thrust is not accounted for. Furthermore, the number of ducted-fans is kept constant. The variation of electric motor mass with power is considered as part of the powertrain sizing as explained in Section 6.2.3.

6.2.8. HEAT EXCHANGERS

The in-house software *HeXacode*, coded in Python, is used for heat exchanger sizing [28]. The validity of this software was confirmed through a comprehensive comparison of results with those of a commercial heat exchanger design and rating code [29]. The sizing process involves determining the necessary heat transfer area for a specified heat duty, considering the inlet temperature, pressure, and mass flow rate of both the hot and cold streams. The program outputs key parameters such as heat exchanger dimensions, mass, and hot and cold side pressure drops. For both the evaporator and condenser, the frontal area is specified, while the depth is computed to satisfy the design requirements. The additional pressure loss associated with the heat exchanger tilt is modeled based on a fit of experimental results reported by Nichols [30].

HEAT EXCHANGER DESIGN ASSUMPTIONS

The evaporator features an annular arrangement and is designed as a multi-pass inline bare-tube bundle heat exchanger, with the working fluid flowing inside the tubes in a counter-crossflow arrangement with reference to the exhaust gases (see Fig. 6.9). The tubes of the evaporator are aligned with the engine axis (see Fig. 6.5). The nickel-base Hastelloy X® alloy is selected as the construction material, owing to its good oxidation resistance, manufacturability, and strength at high temperatures [14, Ch. 5]. The tube outer diameter is fixed to 1.8 mm, and the tube thickness is computed based on the pressure difference between the exhaust gases and the working fluid. As described in Section 4.3 and Section 5.3, the engine optimization leads to evaporator designs whereby the air-side pressure drop is minimized. Based on those results, the non-dimensional transversal pitch ($x_{t,evap}$) is set to 3.0, the non-dimensional longitudinal pitch ($x_{l,evap}$) to 1.25, and the number of passes ($n_{pass,evap}$) to 6. The suitability of these values was confirmed to be optimal by additional computational tests for the specific engine configuration considered in the work at hand. The evaporator length (X_{evap}) is an optimization variable. The inner diameter of the annular evaporator equals the LPT outer diameter and the

resulting perimeter is set as the evaporator width (Y_{evap}).

The flow distribution of the exhaust gas entering the evaporator perpendicular to the bare-tubes is assumed to be uniform for simplicity. Therefore, it can be expected that the resulting pressure drop is underestimated, while the heat transfer rate is overestimated.

The condenser is designed as a flat-tube microchannel heat exchanger with louvered fins (see Fig. 6.10). The value of the following design parameters is fixed, based on manufacturability considerations: the flat-tube thickness is 0.2 mm, the fin thickness is 0.11 mm, and the height of the microchannels is 1.6 mm. Furthermore, the length of the louver fins and the pitch are set to be 90% of the fin height and the fin pitch, respectively. The louver angle ($\phi_{\text{l,cond}}$) is fixed to 30°. The length of the flat-tubes (X_{cond}), the fin height ($b_{\text{f,cond}}$), the fin pitch ($p_{\text{f,cond}}$), and the condenser tilt angle (θ_{cond}) are optimization variables of the condenser. θ_{cond} is the angle between the flat-tubes and the radial direction (see Fig. 6.5). The width of the condenser (Y_{cond}) is determined by the length of the side of the octagon along which the condensers are arranged. As suggested in the technical report of Kaltra GmbH [31], an aluminium alloy of the 3000 series is selected as the construction material.

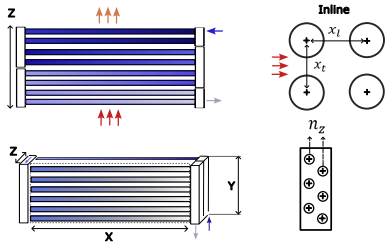

Figure 6.9: Geometry of the core of the evaporator: multi-pass inline bare tube bundle.

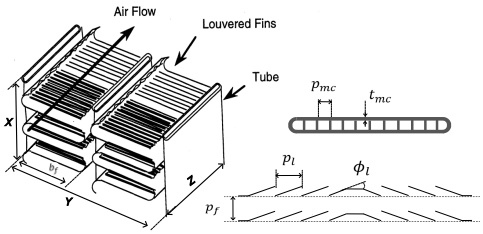

Figure 6.10: Geometry of the core of the condenser: flat-tube microchannels with louvered fins.

6.2.9. SYSTEM DESIGN OPTIMIZATION

Numerical optimization is used to identify optimized designs of both the reference aircraft and the CC-TF aircraft that minimize mission fuel mass (m_{fuel}). The constrained, single-objective optimization problem is expressed in mathematical terms as

$$\begin{aligned}
\text{minimize} \quad & F(\boldsymbol{x}) = m_{\text{fuel}}(\boldsymbol{x}), \\
\text{subject to:} \quad & x_{\text{i}}^{L} \leq x_{\text{i}} \leq x_{\text{i}}^{U}, \\
& g1 : T_{\text{t,3,rto}} \leq 950\,\text{K}, \\
& g2 : W_{\text{octagon}} \geq D_{\text{lpt}} + X_{\text{cond}} \cos(\theta_{\text{cond}}), \\
& g3 : X_{\text{cond}} \sin(\theta_{\text{cond}}) \leq 1.5\,\text{m}, \\
& g4 : \dot{W}_{\text{net,rto}} \geq \dot{W}_{\text{net,cr}} \quad \text{or} \quad \dot{W}_{\text{net,cctf,cr}}.
\end{aligned} \tag{6.20}$$

Constraint $g1$ limits the exit temperature of the high-pressure compressor (HPC) at RTO to a mechanically feasible value, which according to Ref. [14, Ch. 5] can be as-

sumed as 950 K. Constraint $g2$ ensures that the condensers are placed outside the physical boundary of the gas turbine core, which is defined by the LPT outer diameter (D_{lpt}) (see Fig. 6.5). Constraint $g3$ limits the axial extension of the condenser ($X_{\text{cond}} \sin(\theta_{\text{cond}})$) to 1.5 m so that it fits inside the bypass duct of the engine (see Fig. 6.5). Constraint $g4$ ensures that the electrical powertrain is sized for sufficient power at the RTO point to fulfill the power requirement during cruise.

The design variables x_i together with their lower bounds (x_i^{L}) and upper bounds (x_i^{U}) are listed in Tab. 6.7. For the reference aircraft, the design vector ($\boldsymbol{x}$) comprises 8 variables related to the aircraft and the thermodynamic cycle of the simple-cycle turbofan engine and the ducted-fan. The design vector of the CC-TF aircraft includes 7 of these variables, except for the engine bypass ratio at cruise (BPR_{cr}), which is calculated according to Eq. 6.8. Additionally, the design vector of the CC-TF includes 11 variables related to the thermodynamic cycle of the ORC and its heat exchangers. The optimization problem is solved using a genetic algorithm implemented in the Python library *pymoo* [32]. A population size of at least ten times the number of design variables is used. The convergence criterion is that the relative change between the last and the 5^{th} to last generation is below 10^{-6}.

Table 6.7: Design variables and corresponding bounds used to identify optimal designs of the reference aircraft and the CC-TF aircraft designs.

Model	Variables (x_{i})	Description (Unit)	Bounds (x_i^L/x_i^U)
Aircraft	α_{cr}	Turbofan to total thrust ratio at cruise (-)	0.3/0.6
	α_{to}	Turbofan to total thrust ratio at SLS/RTO (-)	0.3/0.6
Turbofan	OPR_{cr}	Overall pressure ratio (-)	35/60
	TIT_{cr}	Turbine inlet temperature (K)	1500/1800
	$\Pi_{\text{fan,cr}}$	Fan pressure ratio (-)	1.2/1.7
	$(\Pi_{\text{hpc}}/\text{CPR})_{\text{cr}}$	Ratio of HPC to core pressure ratio (-)	0.1/0.3
	BPR_{cr}	Bypass ratio during cruise (-)	4/10
Ducted-fan	$\Pi_{\text{df,cr}}$	Ducted-fan fan pressure ratio (-)	1.2/1.5
ORC	$T_{\text{min,orc}}$	Minimum cycle temperature (K)	323/423
	$T_{\text{max,orc}}$	Maximum cycle temperature (K)	520/570
	$p_{\text{max,orc}}$	Maximum cycle pressure (Pa)	$1.1p_{\text{crit}}/1.5p_{\text{crit}}$
	$\Delta T_{\text{pp,cond}}$	Condenser pinch point temperature difference (K)	20/100
	$\Delta T_{\text{pp,evap}}$	Evaporator pinch point temperature difference (K)	20/100
ORC HEX	X_{cond}	Condenser flat-tube length (m)	1.0/2.0
	$b_{\text{f,cond}}$	Condenser fin height (mm)	7.0/16.0
	$p_{\text{f,cond}}$	Condenser fin pitch (mm)	1.0/4.0
	X_{evap}	Evaporator length (m)	0.75/1.5
	W_{octagon}	Width of octagonal condenser arrangement (m)	0.8/2.3
	θ_{cond}	Condenser tilt angle (°)	50/75

6.2.10. FRAMEWORK VERIFICATION

The verification of the ARENA framework is presented in Section 5.3.1, where it is shown that this software suite can reproduce major parameters such as masses and power demand with respect to a turboelectric reference aircraft with an accuracy of +/-3%. This is considered sufficiently accurate for the preliminary analysis described here.

6.3. RESULTS AND DISCUSSION

The ARENA framework is used to optimize the preliminary design and to compute the performance of two partial-turboelectric aircraft, whose main characteristics and mission are described in Section 6.2. These two aircraft are 1) the reference aircraft propelled by simple-cycle turbofan engines and 2) the CC-TF aircraft powered by CC-TF engines. Both aircraft adopt the same powertrain architecture depicted in Fig. 6.8 and TLARs listed in Tab. 6.1.

6.3.1. OPTIMIZED REFERENCE AIRCRAFT

The design variables that are optimal in terms of minimum mission fuel consumption result from a trade-off between propulsion system efficiency and aircraft mass. The optimized design vector of the reference aircraft is given in Tab. 6.8 and a summary of the main parameters characterizing the airframe-level and engine-level results are shown in the left columns of Tab. 6.10 and Tab. 6.11, respectively. Detailed data of the reference engine thermodynamic cycle at the CR, RTO, and SLS operating points is provided in Appendix A.

The reference aircraft has a m_{mto} of 63.1 t, a m_{oe} of 36.7 t and a mission fuel consumption of 12.9 t. The propulsion system has an overall efficiency ($\eta_{\text{tot,sys,cr}}$) of 38.6% and a cruise thrust-specific fuel consumption (TSFC_{cr}) of 14.4 mg/Ns. The engine mass is determined at the SLS (see Section 6.2.4) and the electrical powertrain mass at the RTO (see Section 6.2.3) operating points. Engine and electrical powertrain mass are a function of take-off thrust and therefore directly related to the value of α_{to}. To achieve a given turbofan thrust, TIT_{rto} needs to be set accordingly, which in turn affects the required cooling air mass fraction ($m_{\text{frac,cool}}$). The cooling air mass fraction is determined based on RTO conditions and set equal at all other operating points. In this way, α_{to} influences the optimal values of the design variables defined at cruise. Propulsion system efficiency during take-off does not influence mission fuel consumption as explained in Section 6.2.2. The low mass-specific power of the electrical powertrain components is the cause of the large thrust contribution of the turbofan engines during cruise and take-off. Despite similar values of $\eta_{\text{prop,byp,cr}}$ and $\eta_{\text{prop,df,cr}}$, the turbofan engines provide 74% of the required cruise thrust. Similarly, at take-off, the turbofan engines provide 85% of the required thrust, despite $\eta_{\text{prop,df,rto}}$ being higher than $\eta_{\text{prop,byp,rto}}$. The optimization leads to an electrical powertrain whose design power capacity at take-off ($\dot{W}_{\text{net,rto}}$) is equal to the power requirement during cruise ($\dot{W}_{\text{net,cr}}$), thus reaching the limit prescribed by the optimization constraint $g4$ (see Eq. 6.20). The values of $\dot{W}_{\text{net,cr}}$ and $\dot{W}_{\text{net,rto}}$ are determined based on the values of α_{cr} and α_{to}. The optimized design selects a value of α_{cr} that results in minimum fuel consumption. Since $\dot{W}_{\text{net,cr}} = \dot{W}_{\text{net,rto}}$, the performance of the distributed propulsion system at the cruise operating point determines the value of

α_{to}.

Table 6.8: Design vector characterizing the optimized reference aircraft.

Parameter	α_{cr}	α_{to}	OPR_{cr}	TIT_{cr}	$\Pi_{fan,cr}$	BPR_{cr}	$\Pi_{df,cr}$
Value	0.74	0.85	49.1	1500 K	1.49	8.28	1.39

6.3.2. OPTIMIZED CC-TF AIRCRAFT

The optimal preliminary design of the CC-TF engine is the result of a highly complex trade-off between thermodynamic performance, mass of all the components, and its effect on aircraft aerodynamics. This trade-off is made evident by the values of the optimized design vector of the CC-TF aircraft listed in Tab. 6.9. The pie chart of Fig. 6.11 shows the mass breakdown of the components of the CC-TF engine. Furthermore, Tab. 6.10 and Tab. 6.11 list all the main parameters defining the preliminary design of the engines and the aircraft of both the reference and the CC-TF aircraft for comparison. Detailed data of the CC-TF engine thermodynamic cycle at the CR, RTO, and SLS operating points is provided in Appendix B.

Table 6.9: Design vector characterizing the optimized CC-TF engine.

Parameter	α_{cr}	α_{to}	OPR_{cr}	TIT_{cr}	$\Pi_{fan,cr}$	$\Pi_{df,cr}$	$T_{min,orc}$	$T_{max,orc}$	$p_{max,orc}$
Value	0.58	0.70	42.2	1770 K	1.64	1.37	361 K	551 K	59.5 bar
Parameter	$\Delta T_{pp,cond}$	$\Delta T_{pp,evap}$	X_{cond}	$b_{f,cond}$	$p_{f,cond}$	X_{evap}	$W_{octagon}$	θ_{cond}	
Value	29 K	86 K	1.56 m	12 mm	3 mm	0.78 m	1.11 m	74°	

The adoption of the ORC WHR system reduces the $TSFC_{cr}$ of the CC-TF aircraft during cruise by 6.3% and m_{fuel} by 3.9% if compared to the reference aircraft. The overall propulsion system efficiency at cruise conditions ($\eta_{tot,sys,cr}$) increases by 7%.

Compared to the simple-cycle turbofan engine, the optimal CC-TF engine is characterized by smaller values of BPR_{cr} and OPR_{cr}, and higher values of TIT_{cr} and $\Pi_{fan,cr}$. In general, the efficiency of combined-cycle engines benefits from higher TIT if compared to a simple-cycle engine featuring the same OPR [19]. Therefore, the optimized engine is characterized by a value of TIT_{cr} higher than that of the simple-cycle turbofan engine. The bypass ratio of the CC-TF engine is determined with Eq. 6.8 and is therefore a function of the mass flow rate of air flowing through the condenser, which is an outcome of the simulation of the ORC system operating at design conditions. The ORC system design depends on limitations constraining the size of the condenser, the effect of the size of the condenser on nacelle drag, and the impact of the pressure drop over the condenser airflow on engine thrust. This complex dependency between multiple systems and components (the ORC unit, the heat exchangers, the gas turbine engine, and the aircraft aerodynamics) highlights the need for an integrated design optimization method for the system and its subsystems.

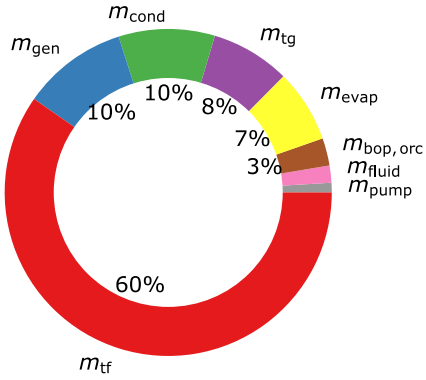

Figure 6.11: Mass breakdown of the components of the CC-TF engine. The mass of the electrical generators m_{gen} and the condensers m_{cond} are the sums of the masses of two and eight units, respectively.

Table 6.10: Main parameters characterizing the optimized design of the reference and the CC-TF aircraft.

Parameter	**Reference Aircraft**	**CC-TF Aircraft**	Δ%
m_{mto} (t)	63.1	64.2	1.7%
m_{oe} (t)	36.7	38.1	3.8%
m_{pt} (t)	4.10	5.39	31%
m_{wing} (t)	7.66	7.85	2.5%
m_{fuel} (t)	12.9	12.4	-3.9%
m_{eng} (t)	1.62	1.83	13.0%
L/D (-)	16.9	16.9	0.0%
S_{ref} (m^2)	113	115	1.8%
b (m)	34.8	35.1	0.9%
$F_{req,cr}$ (kN)	32.8	33.9	3.4%
$F_{req,rto}$ (kN)	131	130	-0.8%
$F_{req,sls}$ (kN)	163	163	0.0%
$TSFC_{cr}$ (mg/Ns)	14.4	13.5	-6.3%
$D_{nacelle}$ (m)	1.42	1.65	16.2%
$L_{nacelle}$ (m)	4.21	3.80	-9.7%
L_{engine} (m)	1.54	1.21	-21.4%
L_{intake} (m)	0.93	0.75	-19.4%
D_{fan} (m)	1.42	1.16	-18.3%

Table 6.11: Main parameters characterizing the optimized design of the propulsion system of the reference and the CC-TF aircraft.

Parameter	**Reference engine**	**CC-TF engine**	Δ%
$\dot{W}_{\text{net,cr}}$ (MW)	1.61	2.66	66%
$\dot{W}_{\text{net,rto}}$ (MW)	1.61	3.29	105%
OPR_{cr} (-)	49.1	42.2	-14%
$\Pi_{\text{fan,cr}}$ (-)	1.49	1.64	10%
BPR_{cr} (-)	8.28	7.82	-5.6%
TIT_{cr} (K)	1500	1770	18%
TIT_{rto} (K)	1610	1970	22%
$m_{\text{frac,cool}}$ (-)	3.3%	8.8%	167%
$\dot{m}_{2,\text{cr}}$ (kg/s)	119	76	-36%
ST_{cr} (N/kg/s)	100	130	30%
$\text{dPqP}_{\text{byp,cr}}$ (-)	1.0%	2.8%	180%
$\text{dPqP}_{\text{exh,cr}}$ (-)	1.5%	5.0%	233%
$\eta_{\text{prop,byp,cr}}$ (-)	70.0%	78.9%	13%
$\eta_{\text{prop,byp,rto}}$ (-)	45.6%	40.9%	-10%
$\Pi_{\text{fan,df,cr}}$ (-)	1.39	1.37	-1.4%
$\eta_{\text{prop,df,cr}}$ (-)	69.4%	69.7%	0.4%
$\eta_{\text{prop,df,rto}}$ (-)	56.8%	55.6%	-2.1%
$\eta_{\text{tot,sys,cr}}$ (-)	38.6%	41.3%	7.0%

The optimization leads to the highest possible condenser tilt angle to reduce D_{nacelle} (see Eq. 6.13). In combination with this angle and to maximize heat transfer area, the optimal condenser length is the maximum possible set by constraint $g3$ of Eq. 6.20. The value of the W_{octagon} design variable is a result of the trade-off between the increase in BPR_{cr} and nacelle drag.

Table 6.12 summarizes all the main parameters resulting from the design optimization of the ORC unit and obtained concurrently with the optimization of the turbofan engine. Figure 6.12 displays the processes of the thermodynamic cycles of the gas turbine and ORC system on the temperature-entropy diagram and Fig. 6.13 shows the temperature-heat load diagrams of the evaporator and the condenser. The calculated net thermal efficiency of the ORC system is 17.7%. The minimum cycle temperature is 361 K, and the maximum cycle temperature is 551 K, which is close to the specified temperature limit related to the thermal stability threshold of the working fluid (see Section 6.2.5). The maximum working fluid pressure in the evaporator is 59.5 bar, while the minimum working fluid pressure in the condenser is 3.1 bar, thus no inward air leaking into the working fluid loop is possible. Further analysis shows that the ORC system is optimized for maximum thermal efficiency rather than maximum thermal power input. This is in contrast to the design of stationary ORC systems recovering thermal power from industrial gas turbines, which are designed to recover the maximum amount of thermal power from the exhaust of the gas turbine, which often entails a thermal efficiency of the ORC system that is lower than the maximum attainable, as this maximizes the net ther-

mal efficiency of the combined cycle power plant [33, Ch.3]. This difference is due to all the additional constraints affecting an airborne system and the complex interaction between propulsive system efficiency, weight, and added drag.

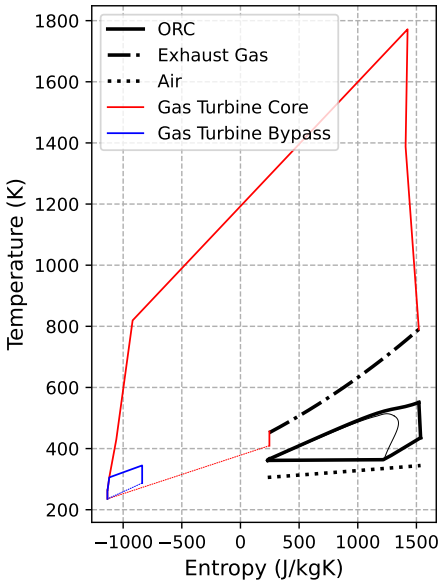

Figure 6.12: Temperature-entropy diagram of the CC-TF.

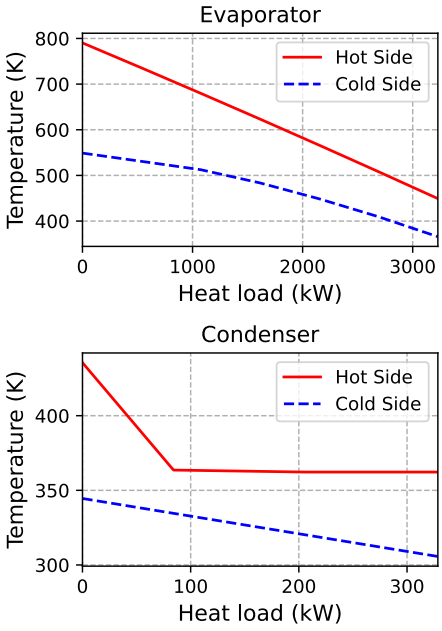

Figure 6.13: Temperature-heat load diagram of the evaporator and condenser. The heat load of the condenser is for a single unit.

The estimated effectiveness (ϵ) of the condenser and evaporator is 57% and 80%, respectively. In the case of the condenser, the moderate effectiveness indicates that the system optimization favors the minimization of the air-side pressure drop over the maximization of the heat transfer area. In addition, the optimized condenser features a high value of mean logarithmic temperature difference. In the case of the evaporator, the relatively high effectiveness indicates that maximization of the system performance favors a maximization of the heat transfer rate over a minimization of the heat exchanger mass. The evaporator recovers 71% of the available exhaust gas thermal power (see Eq. 6.12). The relative pressure drops dPqP occurring in the bypass and in the core streams of the gas turbine engine are 2.8% and 5.0%, respectively. The ORC turbine is a high-speed single-stage radial inflow turbine. The rotational speed N_{tg} is 49 krpm and the Mach number at the outlet of the stator is 1.5. This speed is calculated based on the ORC thermodynamic conditions using the design tool Turbosim (see Section 6.2.5). The net power output of the ORC system is 571 kW, which is 27% of $\dot{W}_{\text{net,eng}}$ (see Eq. 6.3).

The mass of the WHR ORC unit is 546 kg, which amounts to approximately 30% of the mass of the entire CC-TF engine, which is 1825 kg. The mass-specific power of the ORC unit is 1 kW/kg. As a result of the contribution to shaft power production of the

Table 6.12: Relevant design specifications of the optimized ORC WHR system at cruise.

Parameter	Value	Parameter	Value	Parameter	Value
$\eta_{\text{net,orc}}$	17.7%	$\dot{Q}_{\text{evap}}$	3.22 MW	$\sum \dot{Q}_{\text{cond}}{}^{*}$	2.62 MW
χ	71%	$X/Y/Z_{\text{evap}}$	0.78/1.82/0.17 m	$X/Y/Z_{\text{cond}}$	1.56/0.46/0.12 m
$\dot{W}_{\text{net,orc}}$	571 kW	m_{evap}	132 kg	$\sum m_{\text{cond}}{}^{*}$	174 kg
m_{orc}	546 kg	$T_{\text{h,in,evap}}$	790 K	$T_{\text{c,in,cond}}$	306 K
N_{tg}	49 krpm	$T_{\text{h,out,evap}}$	456 K	$T_{\text{c,out,cond}}$	345 K
$\dot{m}_{\text{fluid}}$	5.40 kg/s	$\Delta p_{\text{h,evap}}$	1340 Pa	$\Delta p_{\text{c,cond}}$	804 Pa
T_{min}	361 K	$\dot{m}_{\text{h,evap}}$	8.81 kg/s	$\sum \dot{m}_{\text{c,cond}}{}^{*}$	67.1 kg/s
T_{max}	551 K	$\Delta T_{\text{pp,evap}}$	86 K	$\Delta T_{\text{pp,cond}}$	29 K
p_{max}	59.5 bar	ϵ_{evap}	80%	ϵ_{cond}	57%
p_{min}	3.1 bar	$\dot{W}_{\text{net,pump}}$	69.3 kW		

* Summed up over 8 condensers.

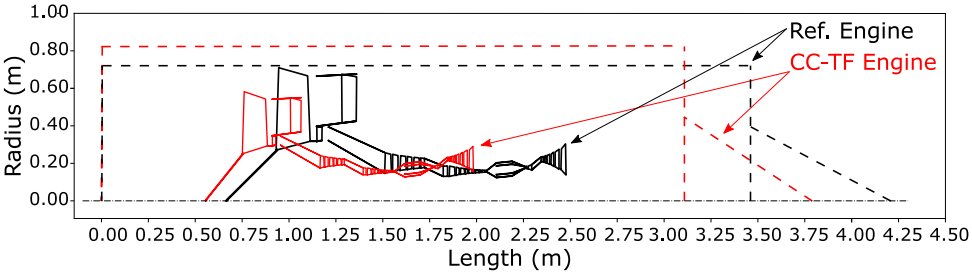

Figure 6.14: Comparison of the engine gas paths and the nacelle dimensions of the reference engine and the CC-TF engine. The dashed lines indicate the outline of the nacelle and the exhaust cone. The detailed modeling of the air intake, bypass, and exhaust duct shape is not part of the framework and therefore not depicted.

ORC WHR unit, the power capacity of the gas turbine of the CC-TF engine is reduced. The mass flow rate of the CC-TF gas turbine is 36% lower than that of the simple-cycle turbofan engine and it weighs 25% less.

Compared to the nacelle dimensions of the simple-cycle turbofan engine the CC-TF engine nacelle features a 15% larger diameter and is 12% shorter. The fan diameter of the CC-TF engine is 18% smaller due to the reduced air mass flow rate. On the one hand, the increase of nacelle diameter is determined according to Eq. 6.13 as a function of the condenser design variables. On the other hand, the reduction of nacelle length is a result of the reduced engine mass flow rate and therefore engine length. Overall, the wetted areas of both the simple-cycle turbofan and the CC-TF engine are very similar, resulting in a similar nacelle drag and values of L/D_{cr}. Figure 6.14 compares the size of the reference engine and the CC-TF engine.

The overall thermal efficiency of the CC-TF is higher than that of the simple-cycle turbofan engine. The exchange of 2.62 MW of thermal power from the eight ORC condensers to the bypass air stream increases $\eta_{\text{prop,byp,cr}}$ by 13% and the specific thrust of the engine at cruise ST_{cr} by 30%.

Despite this increase in propulsive efficiency, the thrust contribution of the CC-TF

engine during cruise is 58% and therefore smaller than for the simple-cycle turbofan engine. This can be attributed to the addition of the WHR system resulting in a lower mass flow rate of the CC-TF engine and therefore less thrust generation and a larger mass of the CC-TF engine compared to that of the simple-cycle engine.

In this study, it is assumed that during take-off the ORC unit is inoperative, thus there is no heat addition to the bypass stream and consequent increase of specific thrust. To compensate for the reduced engine size, a TIT_{rto} that is 22% larger than that of the turbofan engine of the reference aircraft is required. As a result of the higher TIT, $m_{frac,cool}$ of the CC-TF is 167% larger than that of the simple-cycle turbofan engine. This large cooling requirement strongly penalizes CC-TF engine performance during cruise in two ways: 1) by increasing the compression power demand, and 2) by resulting in a higher degradation of the HPT efficiency as estimated using the cooling model of Ref. [15]. As a result, the gas generator efficiency of the CC-TF engine during cruise is 8 absolute percent points lower than that of the simple-cycle turbofan, which is 81%. To limit the penalty that such a large cooling requirement causes to cruise performance, the design variable α_{to} is set to a value of 70%, which is lower than that of the reference turbofan engine. Under this circumstance, contrary to the reference aircraft, the electrical powertrain of the CC-TF aircraft is sized for RTO conditions, and the optimization constraint $g4$ of Eq. 6.20 is inactive.

As a result, the electrical powertrain of the CC-TF aircraft is 31% heavier than that of the reference aircraft. This translates into an overall larger aircraft, featuring a 3.8% greater m_{oe} and 1.7% greater m_{mto}. The wing span is therefore slightly larger and its mass is 2.5% larger. Despite being heavier, the CC-TF aircraft requires less thrust at RTO than the reference aircraft, see Section 6.3.7 for a discussion.

6.3.3. SENSITIVITY STUDY

As explained in Section 6.3.2, the performance of the CC-TF engine during cruise is penalized by the large cooling air demand of the HPT of the gas turbine. The performance of the CC-TF engine might benefit from a cooling system capable of modulating the cooling airflow rate depending on the operating conditions in two ways. Firstly, a large value of the cooling airflow rate is required only at take off, therefore adapting the value to the lower demand due to the lower TIT_{cr}, would considerably improve $TSFC_{cr}$. Secondly, the autonomous modulation of the cooling flow rate depending on the operating condition of the engine (cruise or take-off) would allow the gas turbine to generate more thrust at take-off because it would enable the setting of an even higher value of TIT_{rto}. If the CC-TF engine generates more thrust at take-off, the thrust demand from the electrical powertrain would be lower, resulting in a lighter electrical powertrain. This would contribute to a further reduction in fuel consumption.

A sensitivity study is therefore conducted to provide a preliminary quantification of these benefits. For this purpose, the optimized CC-TF aircraft design (see Section 6.3.2) is re-evaluated assuming cruise as the design point of the turbine cooling system and keeping cooling flow rates at take-off fixed to the values of the optimized design. This simulation is conducted for different values of α_{to}, keeping all other design variables of the CC-TF aircraft at their optimal values. Figure 6.13 shows the relative fuel-saving potential of the adaptive cooling system with respect to the optimized CC-TF aircraft. The

combination of variable cooling air and an increase of α_{to} from a value of 70% to 74% leads to approximately 1.7% fuel savings with respect to the optimized CC-TF aircraft. This translates to 5.4% savings if compared to the fuel consumption of the optimized reference aircraft. The resulting design features a $T_{t,3}$ close to the constrained value of 950 K and a TIT_{rto} of around 2100 K. For values of α_{to} larger than 74% the $T_{t,3}$ constraint is violated. Furthermore, for values of α_{to} above 76%, no feasible solution is obtained because the value of TIT_{rto} exceeds the upper bound, which is set to 2500 K in pycycle. A more appropriate comparison would be with a simple-cycle turbofan engine also benefiting from variable cooling flow rates, however, due to the lower cooling flow rates the performance gain would be smaller.

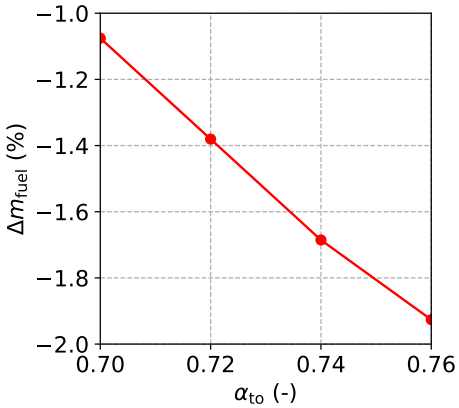

Table 6.13: Relative fuel savings with respect to the optimized CC-TF aircraft obtained with a CC-TF engine adopting a turbine cooling system designed for cruise conditions, as a function of α_{to}.

Table 6.14: Relevant aircraft parameters resulting from the simulation of three fully-turboelectric aircraft for different values of the gross thrust coefficient.

Parameter	FT-1	FT-2	FT-3
$C_{fg,cr}$ (-)	100%	99.7%	97%
$\eta_{prop,df,cr}$ (-)	79.7%	78.5%	67.9%
m_{mto} (t)	70.1	70.5	74.2
m_{oe} (t)	42.8	42.9	44.0
m_{pt} (t)	9.21	9.27	9.96
m_{fuel} (t)	13.7	14.0	16.6

Figure 6.15 shows the relative change in fuel mass with respect to the optimized CC-TF aircraft as a function of the variation of some important design parameters. These data are calculated based on the optimized CC-TF aircraft design, keeping all design variables fixed and only modifying the parameters of interest one at a time. Figure 6.15 a) shows the effect on fuel consumption of the variation of $dPqP_{byp}$ and $dPqP_{exh}$ relative to their optimized values listed in Tab. 6.11. The leftmost points of the chart refer to aircraft designs for which no pressure loss of the heat exchangers is assumed, and only the default values indicated in Tab. 6.3 are considered. System performance is more sensitive to pressure loss in the bypass duct than in the exhaust duct as most of the thrust is generated by the bypass stream. This result highlights the importance of heat exchanger designs optimized for minimum pressure drop. Furthermore, the parametric study shows that under the assumption of no pressure drop within the channels of heat exchangers, the designs corresponding to the two leftmost points in the curves of Fig. 6.15 a), fuel savings are around 1%. However, the presented parametric study only considers the effect of dPqP on gas turbine performance. A larger reduction of fuel consumption might be achieved if the CC-TF engine is optimized by considering more

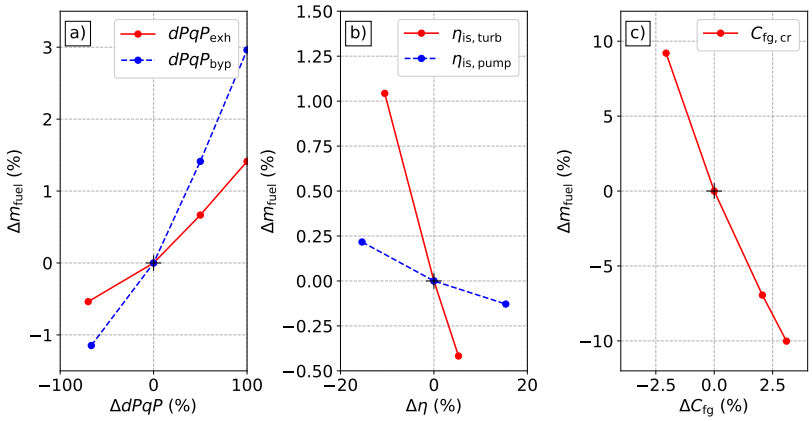

Figure 6.15: Results of a sensitivity study showing the relative change of fuel mass (Δm_{fuel}) as a function of selected parameters with respect to the optimized CC-TF aircraft. a) Δm_{fuel} as a function of the relative pressure drop in the exhaust and bypass duct. b) Δm_{fuel} as a function of the relative change in ORC turbomachinery isentropic efficiency. c) Δm_{fuel} as a function of the relative change in gas turbine and ducted-fan nozzle gross thrust coefficient during cruise.

6

advanced heat exchanger technology allowing for even lower gas-side pressure drops. In this case, the CC-TF engine could be equipped with larger heat exchangers, which would enable higher heat transfer rates, higher ORC system efficiency, and more heat addition to the bypass duct.

Figure 6.15 b) displays the effect on fuel consumption of the variation of ORC turbomachinery efficiency relative to their reference values given in Tab. 6.5. The rightmost point of the $\eta_{\text{is,turb}}$ curve refers to the fuel consumption in case the isentropic efficiency of the turbine is 100%. System performance is more sensitive to a variation of turbine efficiency than to that of the pump. This result indicates that to maximize system efficiency it is important that turbomachines are optimized.

Figure 6.15 c) reports the effect on fuel consumption of a variation of the nozzle gross thrust coefficient during cruise ($C_{\text{fg,cr}}$) with respect to the reference values given in Table 6.3 and in Section 6.2.7. The rightmost point of the curve refers to a design for which $C_{\text{fg,cr}}$ = 100%. The sensitivity of fuel consumption to this parameter is very high, therefore additional analysis is performed and a discussion on how this parameter affects aircraft performance, and possibly the feasibility of turboelectric aircraft, follows.

Table 6.14 lists simulation results obtained with the ARENA framework for three different fully-turboelectric (FT-1, FT-2, FT-3) aircraft employing different values of $C_{\text{fg,cr}}$. The powertrain architecture of these aircraft is similar to the one described in Section 6.2.3, with the exception that it is powered by simple-cycle turboshaft engines, and besides a small amount of turboshaft residual thrust, the entire thrust is generated by the distributed propulsion system. The calculations are based on the same technology assumptions and most of the modeling assumptions used to model the partial-turboelectric aircraft concept described in this work. The only difference is that the aircraft perfor-

mance is simulated only during cruise and the electrical powertrain mass and the engine mass are determined based on the methodology of Chapter 5. The turboshaft engines adopt the same thermodynamic cycle specifications, i.e., $OPR_{cr} = 45$, $TIT_{cr} = 1600\,K$. This combination of OPR_{cr} and TIT_{cr} results in maximized engine efficiency at cruise while fulfilling the constraint that $T_{t3,rto} \leq 950\,K$.

The results of aircraft FT-1 presented in Tab. 6.14 are based on $C_{fg,cr} = 100\%$, yielding $m_{fuel} = 13.7\,t$. Aircraft FT-2 adopts the value $C_{fg,cr} = 99.7\%$, which is the value used in the work of Jones et al. [18] for the simulation of the NASA N+3 turbofan engine, and by Felder et al. [34] and Schiltgen and Freeman [35] for the analysis of two fully-turboelectric aircraft concepts. Compared with the FT-1 aircraft, a $C_{fg,cr}$ reduction by 0.3% increases m_{fuel} by 2.2%. The FT-3 aircraft is characterized by $C_{fg,cr} = 97\%$, which is the same value used in this study (see Section 6.2.4 and Section 6.2.7). Compared with the FT-1 aircraft, a reduction of $C_{fg,cr}$ of 3% increases m_{fuel} by 21.2%.

The comparison of the performance calculated for these three fully-turboelectric configurations with the performance estimated for the optimized partial-turboelectric reference aircraft presented in Section 6.3.1 shows that the partial-turboelectric aircraft achieves a 22.2% fuel reduction with respect to the fuel consumption calculated for the FT-3 aircraft and its fuel consumption is even lower than that of the FT-1 aircraft. The better performance of the partial-turboelectric aircraft is mainly due to the lower mass of the electrical powertrain. Based on this analysis, the following two conclusions can be drawn. First, the feasibility of turboelectric aircraft concepts strongly depends on the value of C_{fg}. Second, there seems to be no consensus in the literature on appropriate values for C_{fg}. For example, Refs. [18, 34, 35] do not justify the assumption of the high value taken for C_{fg}, namely 99.7%, Schmollgruber et al. [3] do not provide any information on the selected value C_{fg}, and Ref. [16, Part C, Ch. 1] reports a mean value of C_{fg} of 94% without information regarding its dependency on the operating point. In this respect, the textbooks of Obert [21] and Oates [36] provide the most comprehensive information in the form of experimental data on the variation of nozzle performance with pressure ratio and altitude.

6.3.4. COMPARISON OF THE CC-TF AND CC-TS ENGINE CONCEPTS

The values of design variables characterizing the optimal design of the WHR system for both the CC-TF and the CC-TS engine are the same for the most part, and a more in-depth discussion on the most relevant design aspects is presented in Chapter 5. However, while both concepts employ the same heat exchanger topologies, their prime mover and propulsion system architectures are different.

Both CC-TS and CC-TF engines are housed in pods mounted to the tail cone of the fuselage via pylons. The CC-TS engine is integrated into the powertrain of a fully-turboelectric aircraft. The CC-TS engine features two condensers integrated into separate ram-air ducts located at the top and bottom of the engine nacelle. The evaporator of the CC-TS engine features a square frontal area and is located in the exhaust duct of the turboshaft engine and it is arranged perpendicular to the exhaust gases. Based on this architecture, the CC-TS engine achieves a reduction in fuel consumption of 1.5% with respect to a fully-turboelectric aircraft adopting simple-cycle turboshaft engines. Instead, the CC-TF engine integrated into the powertrain of a partial-turboelectric aircraft achieves a fuel

savings reduction of 4%. The combined frontal area of the optimized condenser layout of the CC-TF aircraft is 90% larger than the frontal area of the two condensers of the CC-TS engine and the combined air mass flow rate is 280% larger. Since the mass flow rate increases more than the frontal area the condensers of the CC-TF engine are subjected to higher air velocity resulting in an increase in air-side relative pressure drop by approximately 0.5 absolute percent points. At the same time, the larger heat capacity rate of the cold side of the condenser allows for a reduction of $T_{\text{min,orc}}$ and $\Delta T_{\text{pp,cond}}$. This improves the $\eta_{\text{net,orc}}$ of the ORC system equipping the CC-TF engine by 0.5 absolute percent points if compared to the ORC unit of CC-TS engine. Furthermore, the larger condenser heat transfer area and air mass flow rate, combined with the lower temperatures, increase the heat transfer rate by 60%.

The mass flow rate of the exhaust gas of the CC-TF engine is 25% lower than that of the CC-TS engine and the exhaust gas temperature of 790 K is 123 K higher than that of the CC-TS engine. The exhaust gas temperature of the CC-TF engine is higher than that of the CC-TS engine because its TIT_{cr} is 170 K higher. However, the amount of available thermal power at the outlet of the last turbine stage of both engines is similar. The lower exhaust gas mass flow rate, in combination with a 17% larger evaporator frontal area results in a dPqP_{exh} which is lower by approximately one absolute percent point if compared to the value calculated for the CC-TS engine. Furthermore, the larger heat transfer area and the larger temperature difference between the exhaust gas entering the evaporator and the ORC working fluid results in a heat transfer rate that is 66% greater if compared to that computed for the CC-TS engine. As a result of these effects, the value of $\dot{W}_{\text{net,orc}}$ estimated for the CC-TF engine is 70% larger than that computed for the CC-TS engine. Furthermore, the contribution provided by the WHR system to the total electrical power demand of a single engine during cruise is 27% for the CC-TF engine, a value much larger than the 6.6% estimated for the CC-TS engine.

6.3.5. A NOTE ON THE CC-TS CONCEPT

Before the CC-TF concept was conceived, variations to the CC-TS engine configuration were investigated. This exploration led to the octagonal condenser arrangement which was then considered for the CC-TF engine, which is depicted in Fig. 6.5. The evolution of the CC-TS configuration (Chapter 5) named the CC-TS Mark II engine adopts a ring-shaped ram-air duct integrated into the engine nacelle, encapsulating the turboshaft engine, and housing the condensers. The CC-TS Mark II engine benefits from the increased condenser area in the same way as the CC-TF engine. The same methods and modeling assumptions considered for the CC-TS aircraft are used to model the CC-TS Mark II engine onboard a fully-turboelectric aircraft. The only exception is that the nacelle is sized according to the method documented in Section 6.2.6. The fuel savings estimated in the case of the aircraft adopting optimized CC-TS Mark II engines are 2.3% compared to the reference aircraft (see Tab. 5.7). These results are affected by uncertainty regarding the applicability of the ram-air duct loss model (see Section 5.2.8) to a ring-shaped configuration. Even considering such uncertainty, this result points to the possibility of further improving the aircraft performance associated with CC-TS engines.

6.3.6. COMPARISON OF THE CC-TF ENGINE WITH THE NASA N+3 TURBOFAN ENGINE

As discussed in Section 6.3.2, the propulsive efficiency of CC-TF engines greatly benefits from the heat addition in the bypass duct. The bypass propulsive efficiency as defined by Eq. 6.7 attains similar values as the N+3 turbofan engine concept presented by Jones et al. [18], which features a bypass ratio of around 24 during cruise. However, the specific thrust of the CC-TF engine is double that of the N+3 engine, resulting in a more compact engine. Furthermore, the partial-turboelectric propulsion system relying on the CC-TF engine achieves a $TSFC_{cr}$ of 13.5 mg/Ns, which is close to the value of 13.1 mg/Ns reported for the N+3 turbofan engine. This result highlights that the partial-turboelectric powertrain whose prime movers are CC-TF engines can compete with conventional propulsion system architectures. This consideration is strengthened by the fact that the study of Jones et al. [18] is based on assumptions associated with more advanced technology, e.g., the use of $C_{fg,cr}$ = 99.7% instead of $C_{fg,cr}$ = 97%, $\eta_{poly,fan}$ = 97% instead of $\eta_{poly,fan}$ = 95%, as well as assuming ceramic matrix composite materials for both HPT stator and rotor blades, as opposed to using it for the stator only, as it is assumed in the study regarding the CC-TF engine documented here.

6.3.7. ADDITIONAL CONSIDERATIONS ON ENVIRONMENTAL IMPACT AND ON METHODOLOGY LIMITATIONS

The objective of this work is to identify a propulsion system for passenger aircraft that reduces mission fuel consumption and therefore the emission of the long-lived greenhouse gas CO_2. However, there is a clear consensus in research that a significant share of the contribution of aviation to global warming is associated with non-CO_2 effects caused by the emissions of NO_x and water vapor at high altitude, see, e.g., Lee et al. [37]. A suitable metric for the environmental impact of aviation can be the average temperature response over a timeframe of 100 years (ATR_{100}), as proposed by Dallara et al. [38]. Proesmans and Vos [39] obtained an aircraft preliminary design for minimized ATR_{100}. This aircraft flies at a lower altitude and slower speed if compared to aircraft optimized for minimum operating costs that are the standard nowadays, and its gas turbine engines feature lower OPR and TIT to reduce NO_x emissions. Therefore the fuel consumption of such aircraft is larger than that of an aircraft optimized for minimum fuel consumption. The adoption of a WHR system for this type of engine conceived to minimize NO_x emissions could reduce the relevant penalty of higher fuel consumption.

The design of aircraft for minimum environmental impact requires a multidisciplinary analysis that considers the airframe design, mission profile, and propulsion system design in a highly integrated fashion. However, currently, the capabilities of the ARENA framework concerning aircraft design are limited. The available aircraft design method relies on previously computed values of airframe masses and aerodynamic coefficients and only considers the resizing of the wing and the variation of engine nacelle drag. Aircraft constraints analysis is not performed and fixed values for wing-loading and power-loading need to be provided. The impact of the propulsion system on aircraft size and aerodynamics of the aircraft are only partially considered. For example, the variation in size, the redistribution, and/or the change in the number of the ducted-fans affects aerodynamic performance. Similarly, a variation of the position of the center-of-gravity and

the resulting requirements on empennage sizing are not considered. These limitations therefore affect the analysis documented here. Therefore, the conclusions drawn from the results of this work are limited to the design of the propulsion system and should not be taken as an integral assessment of the potential of the aircraft concept.

The limited aircraft design capabilities of the ARENA framework also affect the estimation of the value of take-off thrust ($F_{\text{net,rto}}$). The value of $F_{\text{net,rto}}$ is obtained using Eq. 6.1. This equation implies that more take-off thrust is required for a given value of power-loading and aircraft mass if the propulsive efficiency is higher. For this reason, despite the CC-TF aircraft being heavier and having a lower value of $\eta_{\text{prop,df,rto}}$ than the reference aircraft, its $F_{\text{net,rto}}$ is smaller. This result is counter-intuitive. The correct approach is to perform a constraints analysis to obtain the value of $F_{\text{net,rto}}$. Subsequently, the required shaft power can be determined based on this value and the value of $\eta_{\text{prop,df,rto}}$.

6.4. CONCLUSIONS

The research documented here concerns the fuel-saving potential of replacing the simple-cycle turbofan engines of a partial-turboelectric aircraft with combined-cycle turbofan engines (CC-TF). The CC-TF employs a waste heat recovery system based on a newly conceived aerospace-grade organic Rankine cycle (ORC) unit, which converts the thermal energy of the engine exhaust into additional electrical power via a turbogenerator. The bottoming cycle features a single evaporator placed in the exhaust duct of the gas turbine core and eight condensers arranged in the gas turbine bypass duct downstream of the fan. The effect of adopting this novel propulsion system concept on the fuel consumption of a partial-turboelectric aircraft is analyzed using a multidisciplinary simulation software suite named *ARENA framework*. These preliminary results indicate that fuel savings of approximately 4% are possible if CC-TF engines are the primary movers instead of simple-cycle turbofan engines. Based on the information presented in this chapter, the following conclusions can be drawn:

- The addition of 2.6 MW of thermal energy to the bypass stream of the CC-TF engine increases its specific thrust by 30% and the bypass propulsive efficiency by 13% at cruise if compared to a simple-cycle turbofan engine. The bypass propulsive efficiency is defined by the thrust power generated by the bypass stream divided by the power required to compress the bypass air. A comparison with the combined-cycle turboshaft (CC-TS) engine concept utilizing condensers placed in ram-air ducts shows that the integration of the condensers in the bypass duct of a turbofan engine is considerably more effective due to the air compression.

- The ORC waste heat recovery system allows for a lower power capacity of the gas turbine engine at cruise because of the additional power generated by the ORC unit. However, the performance of the CC-TF is negatively affected during off-design operations because the WHR system may contribute less power. For example, to generate the required thrust at take-off, the turbine inlet temperature of the CC-TF needs to be 20% higher than that of a simple-cycle turbofan engine because the ORC unit does not contribute any power. This increases turbine cooling air demand and reduces the achievable performance during cruise.

- The lift-to-drag ratio of the aircraft is unaffected by the adoption of the CC-TF engine configuration. The lower length of the smaller power capacity gas turbine engine in combination with the larger nacelle diameter due to the addition of the condensers results in a wetted area and drag that are similar to those of the simple-cycle turbofan engine.
- The mission fuel consumption varies by approximately 4% for an absolute change in nozzle gross thrust coefficient of 1%. Given the large sensitivity, it is therefore important that reliable values of the gross thrust coefficient of the nozzle of turbofan engines and ducted-fans are selected.

The work summarized in this chapter enlarges the rather limited knowledge base regarding the design of airborne ORC systems and their potential effect on future engine and aircraft concepts. Based on these findings, it is suggested that further research will aim at:

- investigating the effect of different ORC working fluids on system performance and other operational and safety aspects,
- estimating the potential benefit of mechanically coupling the ORC turbine with the low-speed shaft of the gas turbine engine,
- studying more advanced heat exchanger topologies and optimized channel shapes and their integration with the prime mover,
- expanding the capability of the ARENA framework regarding the aircraft design features to better evaluate and optimize the effect of the propulsion system on aircraft performance, and
- analyzing the potential of ORC systems as a means to increase the performance of aircraft optimized for minimum environmental impact.

APPENDIX A: REFERENCE ENGINE THERMODYNAMIC CYCLE DATA

PAGE INTENTIONALLY LEFT BLANK

PERFORMANCE SUMMARY

Operating Point	MN (-)	alt (km)	dTisa (K)	W0 (kg/s)	Fn (kN)	Fg (kN)	FAR (-)	TIT (K)	BPR (-)	OPR (-)	Pwr (kW)	eta_gg (-)
DESIGN	0.780	10.457	15.000	116.368	13.105	41.019	0.018	1470.252	7.500	50.828	1319.136	0.810

FLOW STATIONS

Flow Station	Pt (Pa)	Tt (K)	ht (kJ/kg)	S (kJ/(kg*K))	P_s (Pa)	W (kg/s)	MN (-)	V (m/s)	area (m**2)
ambient	36651.510	263.858	-38.761	7.032	24637.122	1.000	0.780	239.878	0.011
inlet exit	36578.207	263.858	-38.761	7.033	28713.783	116.368	0.600	188.750	1.512
fan exit	57094.754	301.022	-1.444	7.038	48000.646	116.368	0.500	169.723	1.171
splitter bypass exit	57094.754	301.022	-1.444	7.038	51067.542	13.690	0.400	136.952	0.163
splitter core exit	57094.754	301.022	-1.444	7.038	48000.646	102.677	0.500	169.723	1.034
LPC exit	171284.261	422.006	120.727	7.064	153767.583	13.690	0.400	161.874	0.065
HPC exit	1859194.874	860.077	585.890	7.132	1668112.276	13.301	0.400	227.763	0.008
burner exit	1784827.079	1470.252	544.734	7.869	1737355.383	13.540	0.200	147.372	0.022
HPT exit	413077.406	1080.138	86.870	7.908	372019.776	13.929	0.400	252.627	0.045
LPT exit	39804.132	618.488	-438.638	7.948	35659.051	13.929	0.400	194.019	0.347
exhaust duct exit	39207.070	618.488	-438.638	7.953	36810.955	13.929	0.300	146.377	0.451
core nozzle exit	39089.448	618.488	-438.638	7.953	24637.122	13.929	0.847	392.797	0.226
bypass duct exit	56523.806	301.022	-1.444	7.040	53131.199	102.677	0.300	103.415	1.581
bypass nozzle exit	56354.235	301.022	-1.444	7.041	29692.647	102.677	1.000	317.561	0.781

TURBOMACHINERY PROPERTIES

Component	Wred (kg/s)	Pr (-)	eta_a (-)	eta_p (-)	pwr (kW)	Nmech (rpm)	Nc (rpm)	SMN (-)	SMW (-)
FAN	308.463	1.561	0.959	0.961	-4342.463	4117.806	4303.189	29.211	23.194
LPC	24.833	3.000	0.908	0.923	-1672.570	15000.000	14675.783	12.234	11.941
HPC	9.801	10.854	0.878	0.910	-6368.254	26000.000	21484.408	22.598	22.468
HPT	2.691	4.321	0.902	0.885	6393.830	26000.000	505.407	N/A	N/A
LPT	10.252	10.378	0.956	0.941	7320.024	15000.000	340.185	N/A	N/A

SECONDARY FLOWS

Bleed	Wb/Win (-)	W (kg/s)	Tt (K)	Pt (Pa)
LPC blowoff	0.000	0.000	1.000	57094.754
HPT chargeable	0.000	1.000	1.000	1859194.874
HPT non-chargeable	0.028	1.000	1.000	1859194.874

NOZZLE PROPERTIES

Nozzle	PR (-)	Ath (m**2)	MNth (-)	V (m/s)	Fg (kN)	Cfg (-)
core_nozz	1.587	0.226	0.847	392.797	5.323	0.970
byp_nozz	2.287	0.781	1.000	317.561	35.696	0.970

Figure 6.16: Thermodynamic cycle data of the reference turbofan engine at the cruise operating point (thermodynamic design point).

PERFORMANCE SUMMARY

Operating Point	MN (-)	alt (km)	dTisa (K)	W0 (kg/s)	Fn (kN)	Fg (kN)	FAR (-)	TIT (K)	BPR (-)	OPR (-)	Pwr (kW)	eta_gg (-)
RTO	0.250	0.000	15.000	288.666	55.372	80.559	0.019	1571.947	7.991	40.594	1344.705	0.716

FLOW STATIONS

Flow Station	Pt (Pa)	Tt (K)	ht (kJ/kg)	S (kJ/(kg*K))	P_s (Pa)	W (kg/s)	MN (-)	V (m/s)	area (m**2)
ambient	106129.121	306.939	4.499	6.880	101324.664	1.000	0.250	87.253	0.010
inlet exit	105916.863	306.939	4.499	6.881	86510.083	288.666	0.537	183.258	1.512
fan exit	156501.146	344.485	42.288	6.885	133546.796	288.666	0.479	174.074	1.171
splitter bypass exit	156501.146	344.485	42.288	6.885	143195.374	32.107	0.360	132.157	0.163
splitter core exit	156501.146	344.485	42.288	6.885	133155.423	256.559	0.483	175.700	1.034
LPC exit	404223.297	460.559	160.029	6.907	363983.815	30.576	0.395	166.769	0.065
HPC exit	4299614.585	926.216	659.947	6.974	3864459.792	29.706	0.401	236.554	0.008
burner exit	4127630.001	1571.947	614.090	7.719	4127575.689	30.283	0.004	3.310	1.000
HPT exit	955067.384	1159.847	122.749	7.758	861868.019	31.153	0.401	262.008	0.045
LPT exit	121591.171	718.162	-390.467	7.795	114208.120	31.153	0.304	159.341	0.347
exhaust duct exit	121591.171	718.162	-390.467	7.795	117197.863	31.153	0.229	120.255	0.451
core nozzle exit	121226.397	718.162	-390.467	7.796	101324.664	31.153	0.519	267.963	0.226
bypass duct exit	156501.146	344.485	42.288	6.885	148079.577	256.559	0.289	106.513	1.581
bypass nozzle exit	156031.643	344.485	42.288	6.885	101324.664	256.559	0.810	283.446	0.781

TURBOMACHINERY PROPERTIES

Component	Wred (kg/s)	Pr (-)	eta_a (-)	eta_p (-)	pwr (kW)	Nmech (rpm)	Nc (rpm)	SMN (-)	SMW (-)
FAN	285.012	1.478	0.967	0.970	-10908.335	4097.333	3969.949	32.495	24.052
LPC	22.729	2.583	0.913	0.925	-3780.346	14925.420	13650.577	15.535	15.000
HPC	9.690	10.637	0.879	0.909	-15285.318	27080.390	21420.103	23.589	23.563
HPT	2.691	4.322	0.902	0.886	15346.705	27080.390	509.096	N/A	N/A
LPT	10.276	7.855	0.952	0.938	15988.257	14925.420	326.656	N/A	N/A

SECONDARY FLOWS

Bleed	Wb/Win (-)	W (kg/s)	Tt (K)	Pt (Pa)
LPC blowoff	0.048	0.000	1.000	156501.146
HPT chargeable	0.000	1.000	1.000	4299614.585
HPT non-chargeable	0.028	1.000	1.000	4299614.585

NOZZLE PROPERTIES

Nozzle	PR (-)	Ath (m**2)	MNth (-)	V (m/s)	Fg (kN)	Cfg (-)
core_nozz	1.196	0.226	0.519	267.963	8.330	0.990
byp_nozz	1.540	0.781	0.810	283.446	72.229	0.990

Figure 6.17: Thermodynamic cycle data of the reference turbofan engine at the rolling-take-off (RTO) operating point.

PERFORMANCE SUMMARY

Operating Point	MN (-)	alt (km)	dTisa (K)	W0 (kg/s)	Fn (kN)	Fg (kN)	FAR (-)	TIT (K)	BPR (-)	OPR (-)	Pwr (kW)	eta_gg (-)
SLS	0.000	0.000	15.000	267.672	69.215	69.216	0.019	1533.363	7.904	38.913	894.022	0.704

FLOW STATIONS

Flow Station	Pt (Pa)	Tt (K)	ht (kJ/kg)	S (kJ/(kg*K))	P_s (Pa)	W (kg/s)	MN (-)	V (m/s)	area (m**2)
ambient	101324.664	303.150	0.693	6.880	101324.664	1.000	0.000	0.003	245.801
inlet exit	101122.014	303.150	0.693	6.881	84601.232	267.672	0.507	172.620	1.512
fan exit	148099.607	339.478	37.240	6.886	127366.581	267.672	0.462	167.214	1.171
splitter bypass exit	148099.607	339.478	37.240	6.886	135121.725	30.062	0.354	129.205	0.163
splitter core exit	148099.607	339.478	37.240	6.886	127067.529	237.609	0.466	168.508	1.034
LPC exit	373618.546	451.035	150.291	6.908	335735.662	28.352	0.392	164.163	0.065
HPC exit	3934967.476	905.975	637.204	6.975	3527387.049	27.545	0.403	234.989	0.008
burner exit	3777568.777	1533.363	593.387	7.710	3777522.054	28.061	0.004	3.269	1.000
HPT exit	873125.954	1129.373	114.484	7.750	785134.395	28.868	0.402	259.405	0.045
LPT exit	118281.868	708.930	-371.644	7.786	112241.881	28.868	0.285	148.586	0.347
exhaust duct exit	118281.868	708.930	-371.644	7.786	114827.624	28.868	0.215	112.367	0.451
core nozzle exit	117927.022	708.930	-371.644	7.787	101324.664	28.868	0.479	246.726	0.226
bypass duct exit	148099.607	339.478	37.240	6.886	139623.434	237.609	0.281	103.060	1.581
bypass nozzle exit	147655.308	339.478	37.240	6.887	101324.664	237.609	0.751	263.022	0.781

TURBOMACHINERY PROPERTIES

Component	Wred (kg/s)	Pr (-)	eta_a (-)	eta_p (-)	pwr (kW)	Nmech (rpm)	Nc (rpm)	SMN (-)	SMW (-)
FAN	275.101	1.465	0.953	0.954	-9782.677	4012.761	3912.225	30.438	21.911
LPC	22.324	2.523	0.913	0.925	-3398.558	14617.348	13467.029	15.612	15.000
HPC	9.620	10.532	0.879	0.910	-13804.911	26749.279	21380.427	23.825	23.904
HPT	2.691	4.326	0.902	0.886	13860.352	26749.279	509.159	N/A	N/A
LPT	10.278	7.382	0.950	0.937	14033.565	14617.348	324.201	N/A	N/A

SECONDARY FLOWS

Bleed	Wb/Win (-)	W (kg/s)	Tt (K)	Pt (Pa)
LPC blowoff	0.057	0.000	1.000	148099.607
HPT chargeable	0.000	1.000	1.000	3934967.476
HPT non-chargeable	0.028	1.000	1.000	3934967.476

NOZZLE PROPERTIES

Nozzle	PR (-)	Ath (m**2)	MNth (-)	V (m/s)	Fg (kN)	Cfg (-)
core_nozz	1.164	0.226	0.479	246.726	7.122	0.990
byp_nozz	1.457	0.781	0.751	263.022	62.094	0.990

Figure 6.18: Thermodynamic cycle data of the reference turbofan engine at the sea-level-static (SLS) operating point.

APPENDIX B: CC-TF ENGINE THERMODYNAMIC CYCLE DATA

PAGE INTENTIONALLY LEFT BLANK

PERFORMANCE SUMMARY

Operating Point	MN (-)	alt (km)	dTisa (K)	W0 (kg/s)	Fn (kN)	Fg (kN)	FAR (-)	TIT (K)	BPR (-)	OPR (-)	Pwr (kW)	eta_gg (-)
DESIGN	0.780	10.418	15.000	75.768	9.833	28.018	0.029	1771.867	7.820	42.187	2135.579	0.734

FLOW STATIONS

Flow Station	Pt (Pa)	Tt (K)	ht (kJ/kg)	S (kJ/(kg*K))	P_s (Pa)	W (kg/s)	MN (-)	V (m/s)	area (m**2)
ambient	36880.010	264.142	-38.475	7.031	24786.789	1.000	0.780	240.008	0.011
inlet exit	36806.250	264.142	-38.475	7.032	28875.795	75.768	0.600	188.851	0.979
fan exit	60358.938	305.698	3.252	7.039	50553.659	75.768	0.500	171.030	0.730
splitter bypass exit	60358.938	305.698	3.252	7.039	53791.052	8.591	0.400	138.007	0.098
splitter core exit	60358.938	305.698	3.252	7.039	50553.659	67.177	0.500	171.030	0.647
LPC exit	181076.813	429.766	128.619	7.066	162370.460	8.591	0.400	163.323	0.039
HPC exit	1552735.075	819.382	540.793	7.130	1394380.740	7.836	0.400	222.600	0.006
burner exit	1490625.672	1771.867	475.564	8.208	1452249.627	8.066	0.200	160.436	0.018
HPT exit	489601.964	1387.723	78.115	8.200	441259.950	8.821	0.400	283.891	0.027
LPT exit	38629.842	790.223	-643.802	8.252	34720.676	8.821	0.400	217.489	0.258
exhaust duct exit	36713.752	456.037	-1009.807	7.665	34620.894	8.821	0.300	126.221	0.260
core nozzle exit	36603.611	456.037	-1009.807	7.666	24786.789	8.821	0.777	312.770	0.134
bypass duct exit	58649.868	344.567	42.372	7.167	55121.125	67.177	0.300	110.591	1.070
bypass nozzle exit	58473.918	344.567	42.372	7.168	30731.266	67.177	1.000	339.743	0.529

TURBOMACHINERY PROPERTIES

Component	Wred (kg/s)	Pr (-)	eta_a (-)	eta_p (-)	pwr (kW)	Nmech (rpm)	Nc (rpm)	SMN (-)	SMW (-)
FAN	199.707	1.640	0.954	0.955	-3161.615	5119.082	5346.657	29.211	23.194
LPC	14.854	3.000	0.906	0.920	-1077.010	15000.000	14563.107	12.234	11.941
HPC	5.871	8.575	0.877	0.906	-3540.930	25000.000	20470.734	22.598	22.468
HPT	2.107	3.045	0.867	0.851	3555.150	25000.000	442.678	N/A	N/A
LPT	6.208	12.674	0.947	0.929	6368.061	15000.000	300.126	N/A	N/A

SECONDARY FLOWS

Bleed	Wb/Win (-)	W (kg/s)	Tt (K)	Pt (Pa)
LPC blowoff	0.000	0.000	1.000	60358.938
HPT chargeable	0.021	1.000	1.000	1552735.075
HPT non-chargeable	0.066	1.000	1.000	1552735.075

NOZZLE PROPERTIES

Nozzle	PR (-)	Ath (m**2)	MNth (-)	V (m/s)	Fg (kN)	Cfg (-)
core_nozz	1.477	0.134	0.777	312.770	2.686	0.970
byp_nozz	2.359	0.529	1.000	339.743	25.332	0.970

Figure 6.19: Thermodynamic cycle data of the CC-TF engine at the cruise operating point (thermodynamic design point).

PERFORMANCE SUMMARY

Operating Point	MN (-)	alt (km)	dTisa (K)	W0 (kg/s)	Fn (kN)	Fg (kN)	FAR (-)	TIT (K)	BPR (-)	OPR (-)	Pwr (kW)	eta_gg (-)
RTO	0.250	0.000	15.000	205.004	45.554	63.441	0.034	1964.760	8.249	37.860	3357.468	0.665

FLOW STATIONS

Flow Station	Pt (Pa)	Tt (K)	ht (kJ/kg)	S (kJ/(kg*K))	P_s (Pa)	W (kg/s)	MN (-)	V (m/s)	area (m**2)
ambient	106129.121	306.939	4.499	6.880	101324.664	1.000	0.250	87.253	0.010
inlet exit	105916.863	306.939	4.499	6.881	81332.130	205.004	0.620	209.900	0.979
fan exit	165325.967	351.702	49.570	6.889	135393.679	205.004	0.541	197.525	0.730
splitter bypass exit	165325.967	351.702	49.570	6.889	148516.987	22.165	0.402	148.762	0.098
splitter core exit	165325.967	351.702	49.570	6.889	134950.823	182.839	0.545	199.147	0.647
LPC exit	484492.572	489.793	189.993	6.918	436966.534	20.982	0.389	169.411	0.039
HPC exit	4010022.469	915.058	647.403	6.981	3603478.595	19.138	0.401	235.160	0.006
burner exit	3849621.570	1964.760	569.469	8.092	3849593.168	19.783	0.003	2.898	1.000
HPT exit	1273353.880	1551.821	130.549	8.082	1153465.522	21.626	0.399	298.050	0.027
LPT exit	141646.230	972.273	-594.495	8.129	134301.594	21.626	0.285	172.047	0.258
exhaust duct exit	139521.537	972.273	-594.495	8.134	132370.438	21.626	0.288	173.299	0.260
core nozzle exit	139102.972	972.273	-594.495	8.134	101324.664	21.626	0.705	412.417	0.134
bypass duct exit	163672.707	351.702	49.570	6.892	154371.822	182.839	0.295	109.706	1.070
bypass nozzle exit	163181.689	351.702	49.570	6.893	101324.664	182.839	0.856	300.611	0.529

TURBOMACHINERY PROPERTIES

Component	Wred (kg/s)	Pr (-)	eta_a (-)	eta_p (-)	pwr (kW)	Nmech (rpm)	Nc (rpm)	SMN (-)	SMW (-)
FAN	202.409	1.561	0.934	0.939	-9239.624	5530.633	5358.688	38.221	31.465
LPC	15.008	2.931	0.900	0.915	-3112.478	16205.931	14668.839	15.314	15.000
HPC	5.721	8.277	0.879	0.907	-9597.254	26512.162	20335.189	23.621	23.803
HPT	2.107	3.023	0.868	0.854	9635.798	26512.162	445.814	N/A	N/A
LPT	6.189	8.990	0.941	0.924	15679.896	16205.931	306.632	N/A	N/A

SECONDARY FLOWS

Bleed	Wb/Win (-)	W (kg/s)	Tt (K)	Pt (Pa)
LPC blowoff	0.053	0.000	1.000	165325.967
HPT chargeable	0.021	1.000	1.000	4010022.469
HPT non-chargeable	0.066	1.000	1.000	4010022.469

NOZZLE PROPERTIES

Nozzle	PR (-)	Ath (m**2)	MNth (-)	V (m/s)	Fg (kN)	Cfg (-)
core_nozz	1.373	0.134	0.705	412.417	8.868	0.990
byp_nozz	1.610	0.529	0.856	300.611	54.573	0.990

Figure 6.20: Thermodynamic cycle data of the CC-TF engine at the rolling-take-off (RTO) operating point.

PERFORMANCE SUMMARY

Operating Point	MN (-)	alt (km)	dTisa (K)	W0 (kg/s)	Fn (kN)	Fg (kN)	FAR (-)	TIT (K)	BPR (-)	OPR (-)	Pwr (kW)	eta_gg (-)
SLS	0.000	0.000	15.000	267.672	69.215	69.216	0.019	1533.363	7.904	38.913	894.022	0.704

FLOW STATIONS

Flow Station	Pt (Pa)	Tt (K)	ht (kJ/kg)	S (kJ/(kg*K))	P_s (Pa)	W (kg/s)	MN (-)	V (m/s)	area (m**2)
ambient	101324.664	303.150	0.693	6.880	101324.664	1.000	0.000	0.003	245.801
inlet exit	101122.014	303.150	0.693	6.881	84601.232	267.672	0.507	172.620	1.512
fan exit	148099.607	339.478	37.240	6.886	127366.581	267.672	0.462	167.214	1.171
splitter bypass exit	148099.607	339.478	37.240	6.886	135121.725	30.062	0.354	129.205	0.163
splitter core exit	148099.607	339.478	37.240	6.886	127067.529	237.609	0.466	168.508	1.034
LPC exit	373618.546	451.035	150.291	6.908	335735.662	28.352	0.392	164.163	0.065
HPC exit	3934967.476	905.975	637.204	6.975	3527387.049	27.545	0.403	234.989	0.008
burner exit	3777568.777	1533.363	593.387	7.710	3777522.054	28.061	0.004	3.269	1.000
HPT exit	873125.954	1129.373	114.484	7.750	785134.395	28.868	0.402	259.405	0.045
LPT exit	118281.868	708.930	-371.644	7.786	112241.881	28.868	0.285	148.586	0.347
exhaust duct exit	118281.868	708.930	-371.644	7.786	114827.624	28.868	0.215	112.367	0.451
core nozzle exit	117927.022	708.930	-371.644	7.787	101324.664	28.868	0.479	246.726	0.226
bypass duct exit	148099.607	339.478	37.240	6.886	139623.434	237.609	0.281	103.060	1.581
bypass nozzle exit	147655.308	339.478	37.240	6.887	101324.664	237.609	0.751	263.022	0.781

TURBOMACHINERY PROPERTIES

Component	Wred (kg/s)	Pr (-)	eta_a (-)	eta_p (-)	pwr (kW)	Nmech (rpm)	Nc (rpm)	SMN (-)	SMW (-)
FAN	275.101	1.465	0.953	0.954	-9782.677	4012.761	3912.225	30.438	21.911
LPC	22.324	2.523	0.913	0.925	-3398.558	14617.348	13467.029	15.612	15.000
HPC	9.620	10.532	0.879	0.910	-13804.911	26749.279	21380.427	23.825	23.904
HPT	2.691	4.326	0.902	0.886	13860.352	26749.279	509.159	N/A	N/A
LPT	10.278	7.382	0.950	0.937	14033.565	14617.348	324.201	N/A	N/A

SECONDARY FLOWS

Bleed	Wb/Win (-)	W (kg/s)	Tt (K)	Pt (Pa)
LPC blowoff	0.057	0.000	1.000	148099.607
HPT chargeable	0.000	1.000	1.000	3934967.476
HPT non-chargeable	0.028	1.000	1.000	3934967.476

NOZZLE PROPERTIES

Nozzle	PR (-)	Ath (m**2)	MNth (-)	V (m/s)	Fg (kN)	Cfg (-)
core_nozz	1.164	0.226	0.479	246.726	7.122	0.990
byp_nozz	1.457	0.781	0.751	263.022	62.094	0.990

Figure 6.21: Thermodynamic cycle data of the CC-TF engine at the sea-level-static (SLS) operating point.

BIBLIOGRAPHY

[1] J. Welstead and J. L. Felder, "Conceptual design of a single-aisle turboelectric commercial transport with fuselage boundary layer ingestion," in *54th AIAA Aerospace Sciences Meeting*, 2016, doi: 10.2514/6.2016-1027.

[2] T. Chau, G. Kenway, and C. C. Kiris, "Conceptual exploration of aircraft configurations for the SUSAN electrofan," in *AIAA SciTech Forum*, 2022, doi: 10.2514/6.2022-2181.

[3] P. Schmollgruber, D. Donjat, M. Ridel, I. Cafarelli, O. Atinault, C. François, and B. Paluch, "Multidisciplinary design and performance of the ONERA hybrid electric distributed propulsion concept (Dragon)," in *AIAA SciTech Forum*, 2020, doi: 10.2514/6.2020-0501.

[4] J. S. Gray, J. T. Hwang, J. R. R. A. Martins, K. T. Moore, and B. A. Naylor, "OpenMDAO: An open-source framework for multidisciplinary design, analysis, and optimization," *Structural and Multidisciplinary Optimization*, vol. 59, no. 4, pp. 1075–1104, April 2019, doi: 10.1007/s00158-019-02211-z.

[5] R. W. Heldenbrand and W. S. Miller, "Regenerative engine analysis program (REAP)," USAAVRADCOM, Tech. Rep., 1981.

[6] S. Kaiser, O. Schmitz, P. Ziegler, and H. Klingels, "The water-enhanced turbofan as enabler for climate-neutral aviation," *Applied Sciences*, vol. 12, no. 23, 2022, doi: 10.3390/app122312431.

[7] M. Badger, A. Julien, A. D. LeBlanc, S. H. Moustapha, A. Prabhu, and A. A. Smailys, "The PT6 engine: 30 years of gas turbine technology evolution," in *Proceedings of the ASME Turbo Expo*, 1993, doi: 10.1115/93-GT-006.

[8] E. Torenbeek, "The initial calculation of range and mission fuel during conceptual design," Delft University of Technology, Faculty of Aerospace Engineering, Tech. Rep., 1987, report LR-525.

[9] J. D. Mattingly, W. H. Heiser, K. M. Boyer, B. A. Haven, and D. T. Pratt, *Aircraft Engine Design*, 3rd ed. AIAA, 2018, ISBN: 978-1-62410-650-7.

[10] D. Golovanov, D. Gerada, G. Sala, M. Degano, A. Trentin, P. H. Connor, Z. Xu, A. L. Rocca, A. Galassini, L. Tarisciotti, C. N. Eastwick, S. J. Pickering, P. Wheeler, J. Clare, M. Filipenko, and C. Gerada, "4-MW class high-power-density generator for future hybrid-electric aircraft," *IEEE Transactions on Transportation Electrification*, vol. 7, no. 4, pp. 2952–2964, 2021, doi: 10.1109/TTE.2021.3068928.

[11] M. Ridel, E. Nguyen Van, T. Prosvirnova, D. Donjat, C. Seguin, and P. Choy, "DRAGON: hybrid electrical architecture for distributed fans propulsion," in *MEA Conference*, Bordeaux, France, 2021.

[12] E. S. Hendricks and J. S. Gray, "pyCycle: A tool for efficient optimization of gas turbine engine cycles," *Aerospace 2019*, vol. 6, p. 87, 8 2019, doi: 10.3390/AEROSPACE6080087.

[13] S. Samuelsson, T. Gronstedt, and K. G. Kyprianidis, "Consistent conceptual design and performance modeling of aero engines," in *Proceedings of the ASME Turbo Expo*, 2015, doi: 10.1115/GT2015-43331.

[14] H. Grieb, *Projektierung von Turboflugtriebwerken*. Birkhäuser Basel, 2004, ISBN: 978-3-0348-7938-5, doi: 10.1007/978-3-0348-7938-5.

[15] J. W. Gauntner, "Algorithm for calculating turbine cooling flow and the resulting decrease in turbine efficiency," NASA Lewis Research Centre, Tech. Rep., 1980, NASA-TM-81453.

[16] J. Kurzke and I. Halliwell, *Propulsion and Power: An Exploration of Gas Turbine Performance Modeling*. Springer International Publishing, 2018, ISBN: 978-3-319-75979-1, doi: 10.1007/978-3-319-75979-1.

[17] E. M. Greitzer, P. Bonnefoy, E. De la Rosa Blanco, C. Dorbian, M. Drela, D. Hall, R. Hansman, J. Hileman, R. Liebeck, J. Lovegren *et al.*, "N+3 aircraft concept designs and trade studies, final report," NASA Glenn Research Center, Tech. Rep., 2010, NASA-CR-2010-216794/vol2.

[18] S. M. Jones, W. J. Haller, and M. T.-H. Tong, "An N+3 technology level reference propulsion system," NASA Glenn Research Centre, Tech. Rep., 2017, NASA-TM-2017-219501.

[19] P. P. Walsh and P. Fletcher, *Gas Turbine Performance*, 2nd ed. Blackwell Science, 2004, ISBN: 978-0-632-06434-2.

[20] K. Kawagishi, A. C. Yeh, T. Yokokawa, T. Kobayashi, Y. Koizumi, and H. Harada, "Development of an oxidation-resistant high-strength sixth-generation single-crystal superalloy TMS-238," *Superalloys*, pp. 189–195, 10 2012, doi: 10.1002/9781118516430.CH21.

[21] E. Obert, *Aerodynamic Design of Transport Aircraft*. IOS Press, 2009, ISBN: 978-1-58603-970-7.

[22] E. W. Lemmon, I. H. Bell, M. L. Huber, and M. O. McLinden, "Nist standard reference database 23: Reference fluid thermodynamic and transport properties-REFPROP, Version 10.0, national institute of standards and technology," 2018, software.

[23] M. Astolfi and E. Macchi, *Organic Rankine Cycle (ORC) Power Systems*. Elsevier, 2017, doi: 10.1016/C2014-0-04239-6.

[24] H. D. Kwak, S. Kwon, and C. H. Choi, "Performance assessment of electrically driven pump-fed LOX/kerosene cycle rocket engine: Comparison with gas generator cycle," *Aerospace Science and Technology*, vol. 77, pp. 67–82, 6 2018, doi: 10.1016/J.AST.2018.02.033.

[25] E. Torenbeek, *Advanced Aircraft Design*. John Wiley and Sons, 2013, ISBN: 9781118568101.

[26] ——, *Synthesis of Subsonic Airplane Design*. Delft University Press, 1982, ISBN: 90-247-2724-3.

[27] A. Sgueglia, P. Schmollgruber, N. Bartoli, O. Atinault, E. Benard, and J. Morlier, "Exploration and sizing of a large passenger aircraft with distributed ducted electric fans," in *AIAA Aerospace Sciences Meeting 2018*, 2018, doi: 10.2514/6.2018-1745.

[28] F. Beltrame, D. Krempus, P. Colonna, and C. M. De Servi, "Reduced order modelling of optimized heat exchangers for maximum mass-specific performance of airborne ORC waste heat recovery units," in *7th International Seminar on ORC Power Systems*, Seville, Spain, 2023.

[29] GREThh, "Echtherm version 3.2," 2023, software.

[30] M. R. Nichols, "Investigation of flow through an intercooler set at various angles to the supply duct," NASA Langley Research Center, Tech. Rep., 1942.

[31] Kaltra GmbH, "Microchannel condensers: Heat exchangers for condenser applications," 2020, accessed on 16 June 2023. [Online]. Available: https://www.kaltra.com/wp-content/uploads/2020/04/TM_Microchannel-Condensers_Ver.3.0_EN.pdf

[32] J. Blank and K. Deb, "Pymoo: Multi-objective optimization in Python," *IEEE Access*, vol. 8, pp. 89 497–89 509, 2020, doi: 10.1109/ACCESS.2020.2990567.

[33] C. M. Invernizzi, *Closed Power Cycles*. Springer, 2013, ISBN: 978-1-4471-5140-1.

[34] J. Felder, H. Kim, and G. Brown, "Turboelectric distributed propulsion engine cycle analysis for hybrid-wing-body aircraft," in *47th AIAA Aerospace Sciences Meeting including The New Horizons Forum and Aerospace Exposition*, 2009, doi: 10.2514/6.2009-1132.

[35] B. T. Schiltgen and J. Freeman, "Aeropropulsive interaction and thermal system integration within the ECO-150: A turboelectric distributed propulsion airliner with conventional electric machines," in *16th AIAA Aviation Technology, Integration, and Operations Conference*, 2016, doi: 10.2514/6.2016-4064.

[36] G. C. Oates, "Aerothermodynamics of aircraft gas turbine engines," US Air Force Aero Propulsion Laboratory, Tech. Rep., 1987, aFAPL-TR-78-52.

[37] D. Lee, D. Fahey, A. Skowron, M. Allen, U. Burkhardt, Q. Chen, S. Doherty, S. Freeman, P. Forster, J. Fuglestvedt, A. Gettelman, R. De León, L. Lim, M. Lund, R. Millar, B. Owen, J. Penner, G. Pitari, M. Prather, R. Sausen, and L. Wilcox, "The contribution of global aviation to anthropogenic climate forcing for 2000 to 2018," *Atmospheric Environment*, vol. 244, p. 117834, 2021, doi: 10.1016/j.atmosenv.2020.117834.

[38] E. S. Dallara, I. M. Kroo, and I. A. Waitz, "Metric for comparing lifetime average climate impact of aircraft," *AIAA Journal*, vol. 49, no. 8, pp. 1600–1613, 2011, doi: 10.2514/1.J050763.

[39] P. Proesmans and R. Vos, "Airplane design optimization for minimal global warming impact," *Journal of Aircraft*, vol. 59, no. 5, pp. 1363–1381, 2022, doi: 10.2514/1.C036529.

7

Weight Estimation of Aeronautical Gas Turbine Engines

Parts of the methods and some charts of this chapter have been published in:

I. Boersma, "Weight estimation of gas turbine engines," Master Thesis, Delft University of Technology, 2022, url: https://repository.tudelft.nl/islandora/object/uuid:20f02be0-e9db-484b-b487-ef1e087ad894?collection=education, accessed on 19 April 2024.

and

F. Verweij, "Weight estimation of turboshaft engines," Master Thesis, Delft University of Technology, 2023, url: https://repository.tudelft.nl/islandora/object/uuid:54d8ba82-7104-4f40-9ae6-8b81f364912c?collection=education, accessed on 19 April 2024.

ABSTRACT

To identify the impact of a novel engine concept on aircraft performance it is of paramount importance to estimate its size and mass. For conventional engine architectures, empirically derived correlations can estimate engine dimensions and mass with sufficient accuracy for conceptual aircraft design. However, these empirical models may not be applicable for estimating the mass of novel engine architectures. Therefore, there is a need for a tool to perform size and mass estimation of engines based on unconventional cycle concepts. The WATE++ software developed by NASA can perform this task, however, it is not easily available to non-US citizens. For this purpose, a new software for engine size and mass estimation is developed. This tool performs component sizing based on mechanical considerations. The name of this tool is "weight estimation for aeronautical gas turbine engines" (WEST). The aim is to release WEST open-source once development is finished. The current capabilities of WEST are presented by applying it to model a direct-drive turbofan engine. The results are subsequently compared with publicly available data produced using WATE++. This comparison shows that the developed tool can provide major engine dimensions, but underestimates overall engine mass by 15%. Finally, suggestions for further improvement of WEST are given.

7.1. INTRODUCTION

Future aircraft designs, based on turboelectric or hybrid-electric architectures, will exhibit a higher degree of propulsion system airframe integration than current-day aircraft. This requires multidisciplinary design approaches and software frameworks that can simulate the mutual interaction between aircraft sub-systems. To assess the feasibility of novel gas turbine engine concepts within such frameworks, the ability to predict engine mass and dimensions is crucial. Traditionally, the conceptual design of tube-and-wing aircraft is conducted using statistically derived laws as presented by Torenbeek [1]. The single-equation models used to estimate engine mass usually correlate values of published mass to inlet mass flow rate, thrust, overall pressure ratio, and bypass ratio. Torenbeek [1] presents a simple model to predict turboshaft and turboprop mass based on mass flow rate alone. Lolis [2] provides a literature overview of equations for turbofan mass estimation. As these correlations are based on engine data spanning multiple decades, larger errors have to be expected for engine designs adopting modern technology, and their application to engines based on unconventional thermodynamic cycles should be carefully considered.

More detailed methods are arguably needed for the size and mass estimation of unconventional engines. Sagerser et al. [3] were the first to propose a component-based weight estimation method. In this approach, the engine is subdivided into its major components. The size and mass of these components may be estimated by applying empirical, semi-empirical, or physics-based models. Onat and Klees [4] further developed this approach and NASA implemented it into the first version of their weight analysis of turbine engines (WATE) code. Similar to empirical single-equation methods, the work of Sagerser et al. [3] and Onat and Klees [4] rely on empirical data. WATE was further developed to incorporate physics-based modeling of axial turbomachinery discs [5]. The latest version based on an object-oriented programming approach is called WATE++ [6]

and promises to predict engine mass with an error in the range of +/-10% with respect to published data. Similar software was developed at Cranfield University [2] and by the German Aerospace Center (DLR) [7]. Furthermore, the commercially available engine performance and design tool GasTurb [8] incorporates some capabilities to perform engine mechanical design. The tools presented in Refs. [6, 2, 7] share the same limitation, i.e., their availability. WATE++ is only available to US citizens and the codes of Cranfield University and DLR are proprietary. GasTurb is available to the open public, but cannot be efficiently integrated into a larger simulation environment and only provides weight estimation for predefined engine architectures.

To address these shortcomings, a new component-based weight estimation code is developed. The name of this tool is "weight estimation of aeronautical gas turbine engines" (WEST). The main purpose of this development effort is to provide the research community with an open-source tool for engine mass and size estimation that can be easily integrated within existing simulation frameworks. The software is implemented in the Python programming language using a modular structure based on object-oriented programming. As a secondary purpose, WEST can serve as an educational tool. For example, it can complement aircraft engine courses that typically focus on the thermodynamic cycle. By using WEST students can learn about the implications of thermodynamic design choices on the engine's mechanical design. To this end, students are actively involved in developing WEST.

The development of this tool is still ongoing. The following sections describe the implemented methodology and present its capabilities by comparison with results openly available obtained with the WATE++ code.

7.2. METHODOLOGY

WEST can model single-stage fans, multi-stage axial compressors and turbines, multi-stage radial compressors, axial flow annular combustors, reverse flow combustors, shafts, ducts, gearboxes, and frames. Air intakes and nozzles are not included in the current methodology. The methods used to size these components differ in the level of modeling fidelity. Figure 7.1 gives an overview of the components used to model a single-spool gas generator that employs an axial-radial compressor consisting of axial stages followed by a single radial stage. To facilitate the model implementation, the main engine components are broken down into sub-components representing different parts or aspects being modeled. The color code and symbols (++, +, -) in this figure encode the degree of fidelity applied to model components and sub-components. The highest degree of modeling fidelity (green, ++) refers to one-dimensional numerical schemes, such as those for stress analysis. These methods are applied to model the mechanical stresses in the rotor blades, the stator blades, and the disks. The combined mass of these components makes up approximately 40% of the engine weight [9]. Components with a semi-empirical modeling approach (blue, +) use a mix of physics-based methods and empirical correlations. The physics-based and semi-empirical models provide component dimensions from which the mass is determined by multiplying the material volume by its density. Empirical correlation-based models (orange, -) directly provide component mass and are based on the methods presented in Ref. [4].

The sizing of an engine requires thermodynamic cycle data, turbomachinery per-

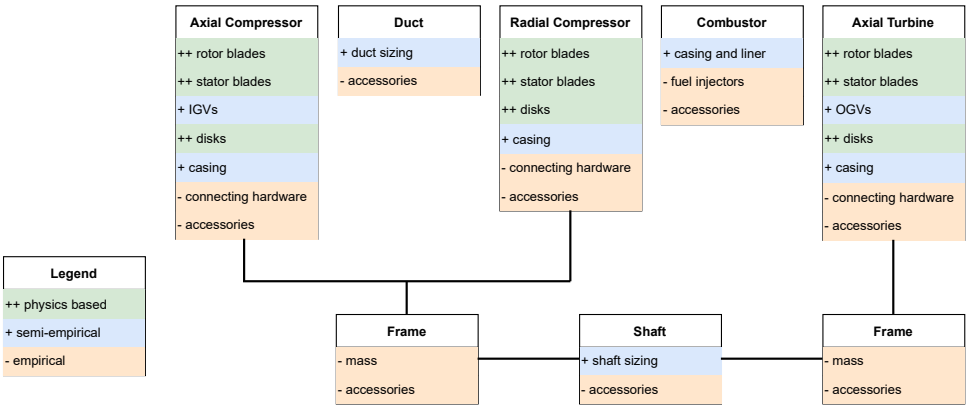

Figure 7.1: Component breakdown of a single-spool gas generator employing an axial-radial compressor. The color code and symbols (++, +, -) indicate the level of modeling fidelity.

formance coefficients, and geometrical design variables as input. Figure 7.2 shows an extended design structure matrix (XDSM) of a single-spool gas generator incorporating axial turbomachines and an axial flow annular combustor. In the XDSM, the thick gray lines indicate dependencies between the components, and the thin black line indicates the computational execution order. The gray boxes indicate the exchange of dependent variables between the components. User input data is indicated by the white boxes in the top row of the diagram. According to Onat and Klees [4] the mass of the accessories can be assumed to be 17% of overall mass. Furthermore, connecting hardware refers to components used to connect multi-stage machines. Its weight is evaluated based on an empirical correlation of Onat and Klees [4]. The main outputs of the model are engine mass and engine size.

7.2.1. AXIAL TURBOMACHINERY DESIGN

The axial turbomachinery design module sizes multi-stage axial compressors and turbines, and single-stage fans. Figure 7.3 gives an overview of the design process of a multi-stage axial turbomachine component. First, the main gas path design is conducted with a meanline method to define the dimensions of each stage. Second, based on these dimensions, three-dimensional rotor and stator blade design is performed. Third, the disks are sized by imposing the rotor blade root stress as a boundary condition at each disk rim. Fourth, the casing is sized for pressure and blade containment.

GAS PATH DESIGN

The gas path design procedure determines the dimensions of the axial turbomachine flow channel which includes, for example, the span and the chord of the blades of each row. The meridional flow channel can be designed to have 1) a constant meanline radius, 2) a constant hub radius, or 3) a constant tip radius. Figure 7.4 gives a sketch of the gas path of a two-stage compressor with a constant hub radius design. The stator and rotor blade velocity triangles at the meanline radius (r_m) are determined assuming a repeated stage design with equal specific work per stage. The thermodynamic properties

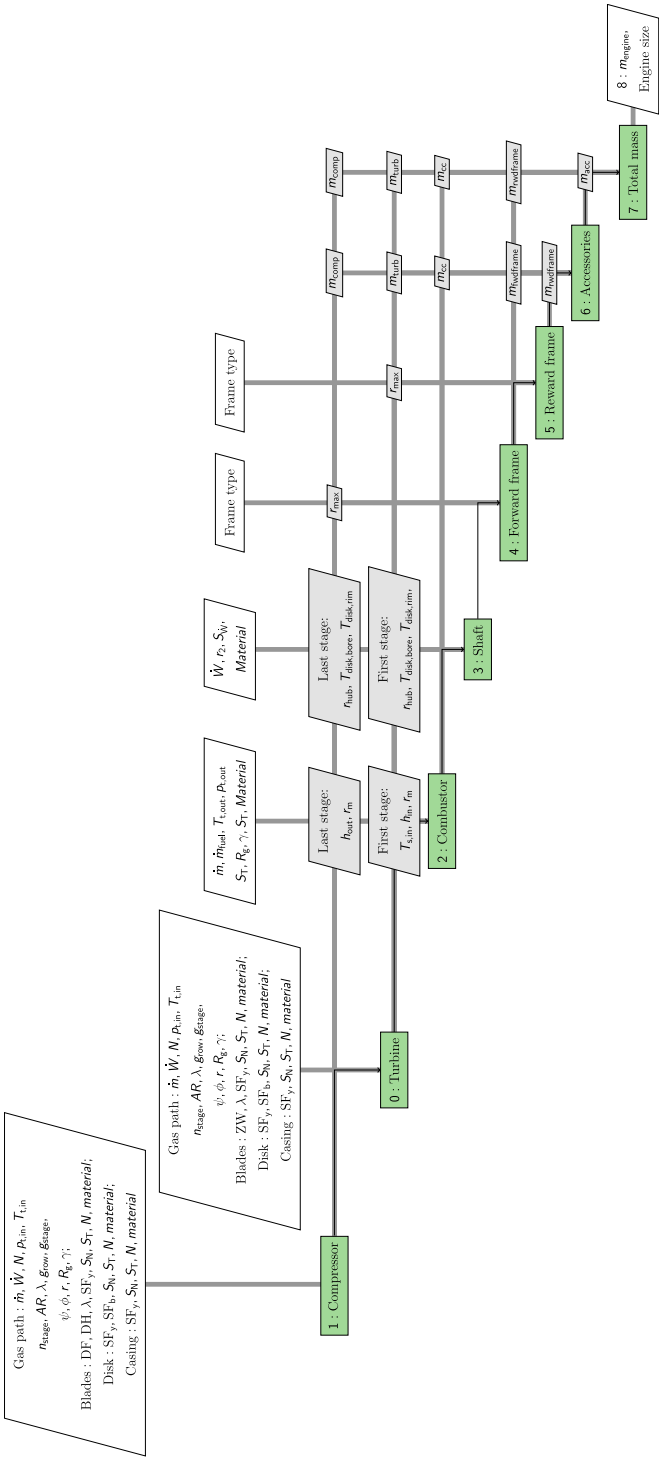

Figure 7.2: XDSM of a gas generator model.

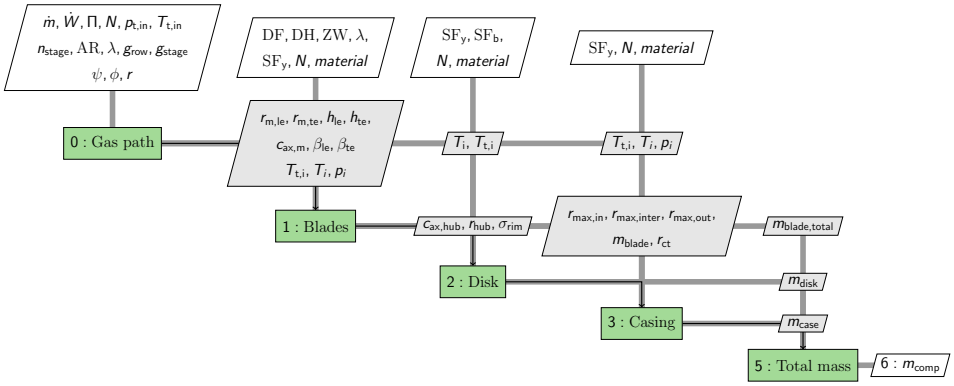

Figure 7.3: XDSM of a compressor model.

along the gas path are calculated assuming calorically perfect gas behavior. Turbomachinery efficiency estimation using loss models is not implemented at this point and the procedure requires polytropic efficiency as an input. The same efficiency is applied to each stage. The blade heights at the leading edge (h_{le}) and trailing edge (h_{te}) are determined based on the conservation of mass, the meanline velocity, and blockage factors taking into account boundary layer blockage. The blade axial chord at the meanline radius ($c_{ax,m}$) is determined based on the blade aspect ratio (AR). AR is defined as the mean of h_{le} and h_{te} divided by $c_{ax,m}$. Appropriate values for AR can be selected based on measured values and correlations given in Ref. [10, Ch. 5] and Ref. [9]. The axial chord at the blade root and tip is determined as a function of the blade taper ratio (λ). The non-dimensional row gap (g_{row}) and stage gap (g_{stage}) parameters define the distance between blade rows and stages, respectively. The non-dimensional gaps are defined as the dimensional gap (l_{row}, l_{stage}) divided by $c_{ax,m}$ of the blade placed upstream of the gap. The stage number (n_{stages}) can be provided as an input. If not provided, WEST uses a simplified method to determine the stage number based on the pressure ratio (Π) and default stage pressure ratio values of 1.3 for the compressor and 4.0 for the turbine. An alternative approach not implemented in WEST, evaluates the stage number assuming a constant specific work per stage, that combined with the duty coefficients results in a design that complies with mechanical design constraints (maximum circumferential speed) and fluid mechanic constraints (maximum Mach numbers).

Table 7.1 summarizes the required input parameters for the design of the turbomachine gas path. WEST requires turbomachinery duty coefficients as an input to define the velocity triangles and, thus, gas path shape. The same duty coefficients are applied to all stages. This approach differs from the one chosen for the tools presented in Refs. [2, 7, 5], where hub-to-tip ratios and axial Mach numbers at the component inlet and outlet need to be specified. The use of duty coefficients can be preferential especially when considering novel engine technologies, that might adopt values of hub-to-tip ratios and axial Mach numbers different than those recommended for conventional engines.

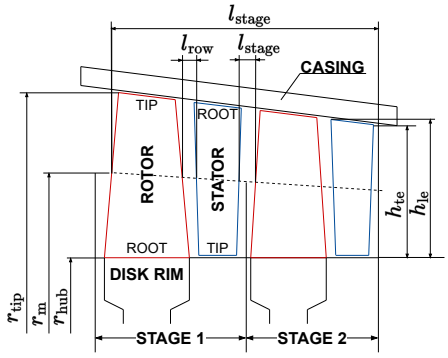

Figure 7.4: Sketch of the gas path of a two-stage compressor indicating major dimensions.

Table 7.1: Input parameters for gas path design.

Category	Input Parameter	Symbol	Units
Performance	Mass flow rate	$\dot{m}$	kg/s
	Pressure ratio	Π	-
	Power	$\dot{W}$	W
	Rotational speed	N	rpm
	Inlet total pressure	$p_{t,in}$	Pa
	Inlet total temperature	$T_{t,in}$	K
Duty Coefficients	Flow coefficient	ϕ	-
	Work coefficient	ψ	-
	Degree of reaction	r	-
Working fluid	Specific gas constant	R_g	J/(kgK)
	Ratio of specific heats	γ	-
Geometry	Number of stages	n_{stage}	-
	Annulus type	-	-
	Blade aspect ratio	AR	-
	Blade taper ratio	λ	-
	Row gap	g_{row}	-
	Stage gap	g_{stage}	-

BLADE DESIGN

The enthalpy of the working fluid is increased or decreased as a result of its interaction with the blades via shear and pressure forces. The blade design procedure determines 1) the three-dimensional shape of the blades that fulfills mechanical requirements, 2) the number of blades for each row, and 3) the mass of the blades.

The three-dimensional shape of the blade is defined by its height at the leading (h_{le}) and trailing edge (h_{te}), the meanline radii at the leading ($r_{m,le}$) and trailing edge ($r_{m,te}$), the meanline axial chord ($c_{ax,m}$), the taper ratio (λ), the blade angles at the leading (β_{le}) and trailing edge (β_{te}), the airfoil profile and the thickness distribution along its span. The required input parameters are summarized in Tab. 7.2.

The velocity triangles at the blade hub (r_{hub}) and tip radius (r_{tip}) are determined assuming a free vortex blade design. Free vortex design leads to highly twisted blade designs which are uncommon in modern engines. However, the error made has a marginal impact on blade mass estimates. For stress analysis and mass estimation, the blade is discretized along its span into two sections that are divided by r_m. The camber line of the compressor blades is defined by a circular arc that matches the angles β_{le} and β_{te}, and c_{ax} at each spanwise position. The thickness distribution of compressor blades is that of a NACA 65-series airfoil. In the case of the turbine, the camber line is defined by a class-shape-transformation (CST) function. This is necessary as a circular arc cannot represent the shape of highly cambered turbine blades. The thickness distribution is determined with a function proposed by Ref. [11]. The thickness-to-chord ratio (t/c) at the tip of the compressor rotor and stator blades is fixed to 7.5% and 10%, respectively. In the case of the turbine, t/c at the tip of the rotor and stator blades is fixed to 20.0% and 22.5%, respectively. The value of t/c_{root} of both compressor and turbine blades is determined during stress analysis. The highest stress occurs at the blade root and is expressed as the von Mises stress ($\sigma_{e,root}$), which is the combination of stresses due to centrifugal forces, bending forces, and shear forces. By default, to provide a safety margin

Table 7.2: Input parameters for blade design. The acronyms LE and TE indicate the property at the leading and trailing edge, respectively.

Category	Input Parameter	Symbol	Units
Performance	Total temperature at row inlet	$T_{t,i}$	K
	Static temperature at row inlet	T_i	K
	Static pressure at row inlet	p_i	Pa
	Shaft speed	N	rpm
Geometry ring disk	Blade LE angle	β_{le}	°
	Blade TE angle	β_{te}	°
	Blade LE height	h_{le}	m
	Blade TE height	h_{te}	m
	Blade mean radius at LE	$r_{m,le}$	m
	Blade mean radius at TE	$r_{m,te}$	m
	Meanline axial chord	$c_{ax,m}$	m
	Blade taper ratio	λ	-
Mechanical	Material	-	-
	Yield criterion	SF_y	-
	Diffusion factor	DF	-
	De Haller number	DH	-
	Zweifel coefficient	ZW	-

for high-cycle fatigue, the value of $\sigma_{e,root}$ is limited to 70% of the material yield strength as proposed by Saravanamuttoo et al. [12, Ch. 8]. The resulting safety factor (SF_y) which is defined as the ratio of material yield strength to maximum allowable $\sigma_{e,root}$ has a value of 1.43. The value of t/c_{root} corresponds to the one that fulfills this mechanical requirement. In the case of cooled turbine blades, data of Grieb [10, Ch. 5] suggests that the cross-sectional area can be reduced by 25% for the calculation of stresses and the blade mass. In the case of shrouded turbines, a multiplier is applied to $\sigma_{e,root}$ to take account of the increase in blade mass. However, the actual mass of the shroud is not estimated in the current implementation. The data presented by Grieb [10, Ch. 5] suggests multiplication factors of 1.25 and 1.5 for uncooled and cooled blades, respectively.

The blade bulk temperature is set equal to the adiabatic wall temperature (T_{aw}). The recovery factor for air is estimated to be 0.89. For the rotor blade, T_{aw} is calculated based on the total temperature in the relative reference frame.

Two methods are implemented to calculate the number of blades in a row. The first method is based on the methodology of Becker et al. [7]. In this case, the number of compressor blades is determined based on a calculated blade solidity. Blade solidity (σ_{bl}) is defined as

$$\sigma_{bl} = c_{ax}/p, \tag{7.1}$$

where the variable p is the pitch between adjacent blades. σ_{bl} is determined as a function of the De Haller number (DH) and the diffusion factor (DF) at the blade root and tip. Subsequently, the value of σ_{bl} that results in the minimum number of blades is selected. The number of blades is computed by dividing the circumference at which σ_{bl} is defined by the value of p, rounding to the next integer. The number of turbine blades in a row is determined according to the method of Ref. [7] as a function of blade angles, $c_{ax,m}$,

and the Zweifel coefficient (ZW). The second method allows the direct specification of solidity values at the meanline radius of the stator and rotor blades of both compressors and turbines.

DISK DESIGN

The purpose of a disk is to hold the blades in place and transfer torque to the shaft. Two different disk types are implemented in WEST. These are 1) the web disk (Fig. 7.5), and 2) the ring disk (Fig. 7.6). A disk is geometrically divided into 6 sections, each defined with a radius and a thickness.

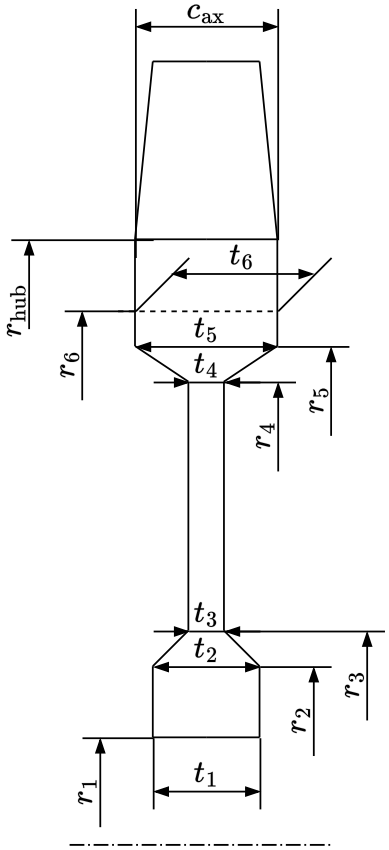

Figure 7.5: Sketch of a web disk indicating major dimensions.

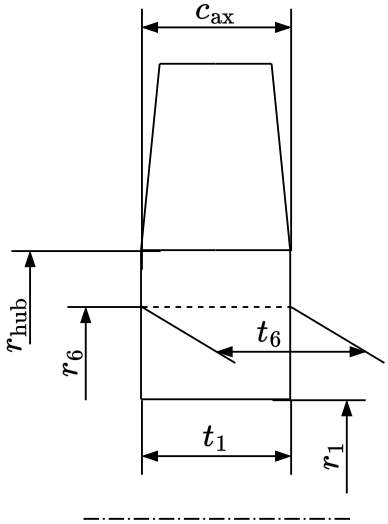

Figure 7.6: Sketch of a ring disk indicating major dimensions.

The disk design procedure is coupled with a gradient-based optimizer to find the geometry that minimizes disk mass while fulfilling mechanical design criteria. To reduce the number of optimization variables, simplifications are applied to the disk geometry. These simplifications are based on recommendations outlined by Lolis [2] and Tong et al. [5], and are detailed in Ref. [13]. For both disk types, the assumption is made that the disk includes the volume and mass of the blade platform and root. The same approach

is applied in the work documented in Ref. [2]. Therefore, the radius r_6 and the blade hub radius (r_{hub}) are set equal. This is contrary to the approaches chosen by Tong and Naylor [6] and Becker et al. [7], where the blade root is modeled [7] or estimated based on empirical correlations [5]. In the case of the ring disk, all thicknesses are taken to be equal to the blade axial chord at the root. Furthermore, besides r_6 only the disk bore radius (r_1) is required to define the disk geometry. In the case of the web disk, the number of geometrical variables is reduced to five, which are the radii r_1, r_2, r_6, and the thicknesses t_2 and t_4. Additional constraints are applied to the minimum value of the rim thickness ($h_{\text{rim}} = r_6 - r_5$) if bladed disks or disks of single-stage fans are modeled. A summary of the required input data for disk modeling is given in Tab. 7.3.

Table 7.3: Input parameters for disk design.

Category	Input Parameter	Symbol	Units
Performance	Temperature rim	T_6	K
	Temperature bore	T_1	K
Geometry ring disk	Radius section 1	r_1	m
	Radius section 6	r_6	m
	Thickness section 6	t_6	m
Geometry web disk	Radius section 1	r_1	m
	Radius section 2	r_2	m
	Thickness section 2	t_2	m
	Thickness section 4	t_4	m
	Thickness section 6	t_6	m
Mechanical	Rim stress	σ_{rim}	Pa
	Yield criterion	SF_y	-
	Burst criterion	SF_b	-
	Radial temp. dist.	-	-
	Material	-	-

The stress analysis considers axial, radial, tangential, and thermal expansion stresses. Details on the mathematical procedure are provided in Ref. [13]. The optimization variables employed to minimize disk mass are the geometrical variables reported in Tab. 7.3. Two optimization constraints are employed to ensure mechanical integrity. These are the burst criterion and the yield criterion. The burst criterion ensures sufficient safety margin to bursting of the disc due to overspeed (SF_b). In WEST, the definition reported in Ref. [10, Ch. 5] is implemented

$$\frac{N_{\text{burst}}}{N_{\text{max}}} = \sqrt{\frac{\bar{\sigma}_{\text{uts}}}{\bar{\sigma}_\phi}} > \text{SF}_\text{b}, \tag{7.2}$$

where N_{burst} is the burst speed, N_{max} is the maximum allowable operating speed, $\bar{\sigma}_{\text{uts}}$ is the ultimate stress of the material evaluated at the average disk temperature, and $\bar{\sigma}_\phi$ is the area-averaged tangential stress. Grieb [10, Ch. 5] suggests a value of SF_b in the range of 1.25 to 1.30 for disks of gas generators, and a value in the range of 1.40 to 1.50 for disks of free power turbines.

The yield criterion ensures sufficient safety margin to low-cycle fatigue (SF_y). Grieb [10, Ch. 5] shows that for a typical cycle number of 10^4 and common disk materials fatigue stress equals approximately the material yield stress (σ_y). The yield criterion is defined as

$$\frac{\sigma_y}{\sigma_{e,max}} > SF_y, \tag{7.3}$$

where $\sigma_{e,max}$ is the maximum von Mises stress that occurs at the disk bore radius (r_1). σ_y is evaluated based on the temperature at the same position. In Tong et al. [5], a value of $SF_y = 1.1$ is suggested.

To account for temperature effects on material properties and stress, WEST provides three different temperature distributions along the disk's radial direction. In the case of compressor disks, a constant temperature equal to the adiabatic wall temperature of the rotor blade is applied along the disk radius. In the case of turbine disks, a linear or a quadratic distribution can be selected. The linear temperature profile is proposed by Ref. [14, Part B, Ch.4] and applies the compressor discharge total temperature at the disk bore and the turbine rotor blade adiabatic wall temperature at the disk rim. The quadratic temperature profile is a model developed by Grieb [10, Ch. 5], based on statistical data.

CASING DESIGN

The casing consists of the outer shell of the gas path and is the attachment point of stator blades. It must be able to withstand high pressures and contain blade fragments in case of blade failure. Table 7.4 gives the required input parameters for casing design. The inner contour of the casing is defined by the blade radii at the stage inlet ($r_{max,in}$), interstage ($r_{max,inter}$), and stage exit positions ($r_{max,out}$). The casing thickness is calculated on a stage-by-stage basis employing the semi-empirical method presented by Bretschneider et al. [15]. This method considers requirements for pressure and blade containment. The thickness necessary to contain blade failure is a function of the kinetic energy of a single-blade fragment ($E_{kin,bl}$) and material yield strength. $E_{kin,bl}$ is determined based on the mass of the rotor blade (m_{blade}), its centroid radius (r_{ct}), and the shaft rotational speed (N). The thickness required for pressure containment is a function of maximum static pressure occurring along the stage (p_{max}) and material yield strength. By default, a safety factor against plastic deformation (SF_y) of 1.1 is applied. Material properties are evaluated at the adiabatic wall temperature calculated based on stage inlet conditions and assuming a recovery factor for air of 0.89.

FAN DESIGN

The design procedure of single-stage fans differs from multi-stage compressors in that the gas path is split after the rotor into a core and a bypass channel. The design of the fan rotor and stator blades, disk, and casing follows the same methodology as outlined in the preceding sections. Additionally, the fan component includes the design of the spinner. Figure 7.7 shows a sketch of the singe-stage fan including the disk, the casing, and the spinner. The design incorporates separate stator rows for the core and bypass streams, highlighted in blue.

Table 7.4: Input parameters for casing design.

Category	Input Parameter	Symbol	Units
Performance	Total temperature at stage inlet	$T_{t,i}$	K
	Static temperature at stage inlet	$T_{t,i}$	K
	Static pressure at stage inlet	p_i	Pa
	Shaft speed	N	rpm
Geometry	Stage inlet outer radius	$r_{max,in}$	m
	Inter-stage outer radius	$r_{max,inter}$	m
	Stage exit outer radius	$r_{max,out}$	m
	Blade centroid radius	r_{ct}	m
Mechanical	Material	-	-
	Safety factor	SF	-

The core and bypass channels are divided by a splitter. The radius of the splitter leading edge ($r_{splitter}$) is calculated, to a first approximation, as

$$r_{splitter} = \sqrt{\frac{\dot{m}_{core}}{\rho_m V_m \pi} + r_{core,hub}^2}, \tag{7.4}$$

where $\dot{m}_{core}$ is the core mass flow rate, ρ_m is the rotor meanline air density, V_m is the rotor meanline velocity, and $r_{core,hub}$ is the hub-radius at the inlet of the core channel. $r_{core,hub}$ is set equal to the rotor blade trailing edge hub radius. The distance of the core and bypass stator leading edges to the splitter leading edge (l_2, l_3) is determined by multiplication of the non-dimensional gap parameters $g_{core,stator}$ and $g_{byp,stator}$ with the height of the inlet of the respective channel (h_{core}, h_{byp}). $g_{core,stator}$ and $g_{byp,stator}$ are required user input. The gap between the rotor trailing edge and the splitter leading edge (l_1) is determined based on the row gap parameter defined in Section 7.2.1. The height of the core and bypass stator blade leading edges is determined based on mass conservation and assuming V_m as the inlet speed. The splitter angle ($\alpha_{splitter}$) is set to 15 deg by default. This method assumes a free vortex design where the value of V_m is equal along the rotor blade trailing edge. However, this results in a very low value of the degree of reaction at the hub of the rotor blade, which leads to very large blade angles and absolute velocities. Furthermore, fan stages are usually designed for axial inflow and axial outflow. This design feature cannot be fulfilled using the current design method for sizing the gas path of axial turbomachines. Therefore, while the procedure can define a suitable gas path for the fan stage, it does not result in realistic blade angles and the identified value of $D_{splitter}$ should be seen as a guess value as it is not calculated with the correct value of V_m at the core channel entry. Nevertheless, as shown in Section 7.3 the current method can reproduce the geometry of an existing fan. The impact of wrong blade angles on blade mass is found to be marginal.

The spinner is modeled as a cone. Its outer diameter is set equal to the rotor blade hub diameter ($r_{fan,hub}$) at the leading edge. The cone angle is set equal to the angle of the rotor blade hub contour, in case the resulting spinner length ($l_{spinner}$) is below or

equal to 1.5 times the fan hub axial chord ($c_{\text{ax,hub}}$). If $l_{\text{spinner}} > 1.5c_{\text{ax,hub}}$, then l_{spinner} is set to $1.5c_{\text{ax,hub}}$. The value of 1.5 is derived from measurements of spinner geometries of various turbofan engines. According to Lolis [2] a spinner wall thickness of 5 mm is suitable.

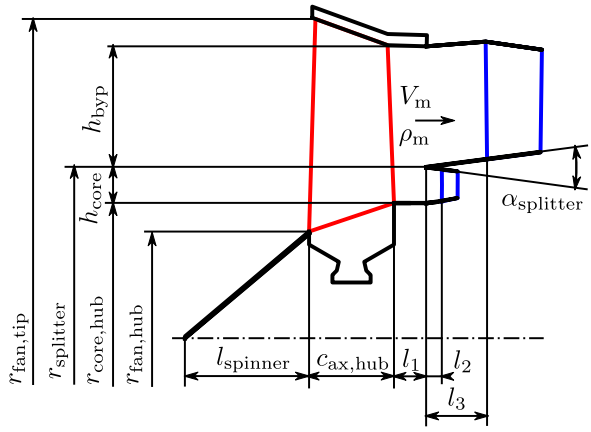

Figure 7.7: Sketch of the fan including spinner, casing, and disk, as well as indicating major dimensions.

7.2.2. RADIAL TURBOMACHINERY DESIGN

The radial turbomachinery design module can model single or multi-stage radial compressors. A radial compressor consists of the impeller, the diffuser, and the casing. Splitter blades are optional. In the case of multi-stage configurations return channels are modeled. As for axial turbomachines, the design procedure consists of four steps: 1) gas path design, 2) blade design, 3) impeller design, and 4) casing design.

GAS PATH DESIGN

The gas path design procedure determines the dimensions of the flow channel and the blades and is based on the procedure detailed in Ref. [16]. Figure 7.8 gives an overview of the gas path and the main components of a radial compressor. Table 7.5 lists the required input data. In case no isentropic efficiency is provided, its value is evaluated based on the loss models presented in Ref. [16]. In case splitter blades are included, the ratio of splitter blade length to gas path length (ll_{splitter}) needs to be specified. The impeller shape factor (k) relates the hub diameter ($D_{1,\text{h}}$) to the tip diameter ($D_{1,\text{t}}$) at the inlet of the impeller. Based on k and the duty coefficients the velocity triangles at the meanline radius of the inlet section and at the outlet of the impeller are determined. The thermodynamic properties at the outlet of the impeller and diffuser are calculated assuming that the working fluid behaves as an ideal gas. The diffuser can be of the vaned or vaneless type. In case the diffuser inlet diameter ratio ($\frac{D_{2,s}}{D_2}$) and the vaned diffuser exit diameter ratio ($\frac{D_3}{D_2}$) are not specified, these ratios are determined based on regression of

Table 7.5: Input parameters for the gas path design of radial compressors.

Category	Input Parameter	Symbol	Units
Performance	Mass flow rate	$\dot{m}$	kg/s
	Pressure ratio	Π	-
	Rotational speed	N	rpm
	Inlet total pressure	$p_{t,in}$	Pa
	Inlet total temperature	$T_{t,in}$	K
	Isentropic efficiency	η_{is}	-
Duty Coefficients	Flow coefficient	ϕ	-
	Work coefficient	ψ	-
	Degree of reaction	r	-
Working fluid	Specific gas constant	R_g	J/kg/K
	Ratio of specific heats	γ	-
Geometry	Rotor inlet flow angle	α_1	-
	Impeller shape factor	k	-
	Splitter length ratio	$k_{splitter}$	-
	Vaned diffuser exit diameter ratio	$\frac{D_3}{D_2}$	-
	Diffuser inlet diameter ratio	$\frac{D_{2,s}}{D_2}$	-

statistical data provided in Ref. [10, Ch. 5]. The resulting equations are

$$\frac{D_{2,s}}{D_2} = 1.05 \tag{7.5}$$

and

$$\frac{D_3}{D_2} = (1.575 - 0.05\Pi). \tag{7.6}$$

Due to a lack of data, the same equations are applied to the vaneless diffuser design. This simplification is expected to have a minor impact on mass estimation. Typically, the vaneless diffuser dimensions are determined based on energy conservation to obtain a desired exit static pressure. The gas path contour of the impeller hub and tip is generated using a set of Bezier curves based on four control points similar to the method described by Smith and Merryweather [17].

BLADE DESIGN

The blade design procedure determines the blade angle distribution along the impeller gas path, the number of blades, and the rotor and stator blade thicknesses. Mechanical analysis of the blades is not conducted and they are sized based on empirical correlations. No dedicated inputs are required for the blade design procedure.

The velocity triangles at positions other than the meanline are calculated based on the free vortex assumption. The blade angle distribution along the hub ($\beta_{h,x}$), the meanline ($\beta_{m,x}$), and the tip ($\beta_{t,x}$) are defined by sets of Bezier curves using four control points that are equally spaced and of which two are located at the inlet and exit of the gas path. The number of rotor blades is calculated according to Ref. [18] as a function of the blade

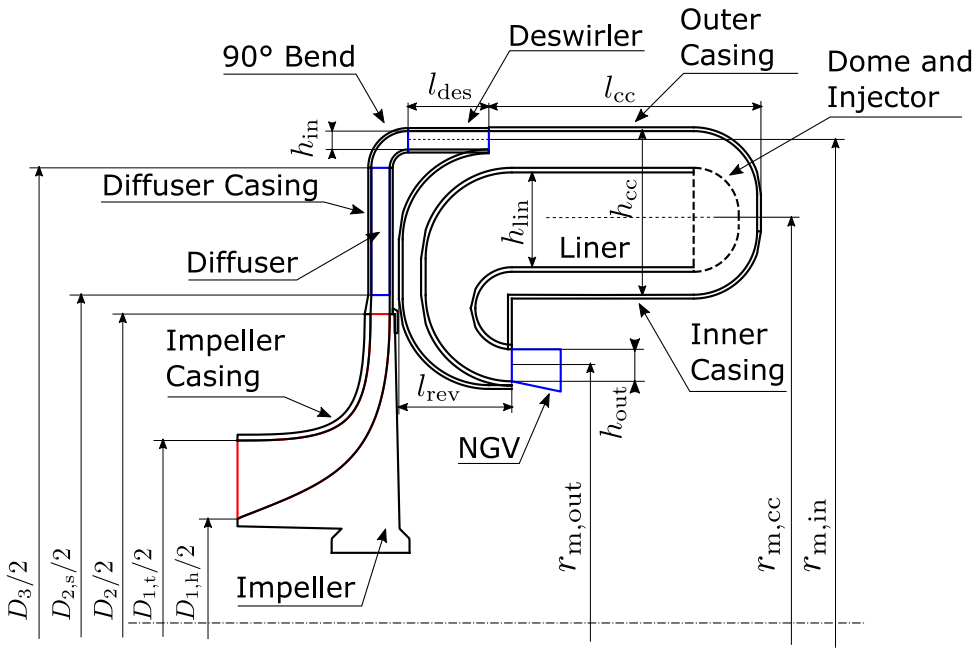

Figure 7.8: Sketch of a radial compressor connected to a reverse flow combustor indicating major components and dimensions.

angles at the impeller inlet and outlet, and the diameter ratio $\frac{D_{1,\mathrm{t}}}{D_2}$. The number of diffuser blades equals the number of rotor blades plus eight. This is to avoid resonance phenomena as described by Aungier [16]. The thickness of the rotor blades linearly increases along the meridional channel. The inlet ($t_{\mathrm{bl},1}$) and outlet thicknesses ($t_{\mathrm{bl},2}$) are determined as a function of blade height at the respective location based on data presented in Ref. [19]. The thickness of the diffuser blades follows the distribution suggested by Aungier [16]. The maximum blade thickness equals $t_{\mathrm{bl},2}$.

DISK DESIGN

The purpose of the disk is to hold the blades in place and to transfer the torque to the shaft. Two radial disk types are implemented in WEST as shown in Fig. 7.9. Table 7.6 gives the required input data. Contrary to the design of axial disks the blade root stress is not an input but is calculated as part of the radial disk design routine. The main dimensions defining a radial impeller are the hub radius at the inlet ($D_{1,\mathrm{h}}/2$), the tip radius at the inlet ($D_{1,\mathrm{t}}/2$), the tip radius at the outlet (D_2), the impeller axial length ratio (L_{ax}/D_2), and the shape of the impeller flow path along the hub and tip that is defined by the vectors $\boldsymbol{D}_{\mathrm{h,x}}$ and $\boldsymbol{D}_{\mathrm{t,x}}$.

The radial disk design procedure is coupled with a gradient-based optimization algorithm to determine the disk geometry that yields minimum mass while fulfilling the mechanical design criteria. The same criteria as for the axial disk design are applied (see Section 7.2.1). For this purpose, a set of geometrical constraints detailed in Ref. [20] are

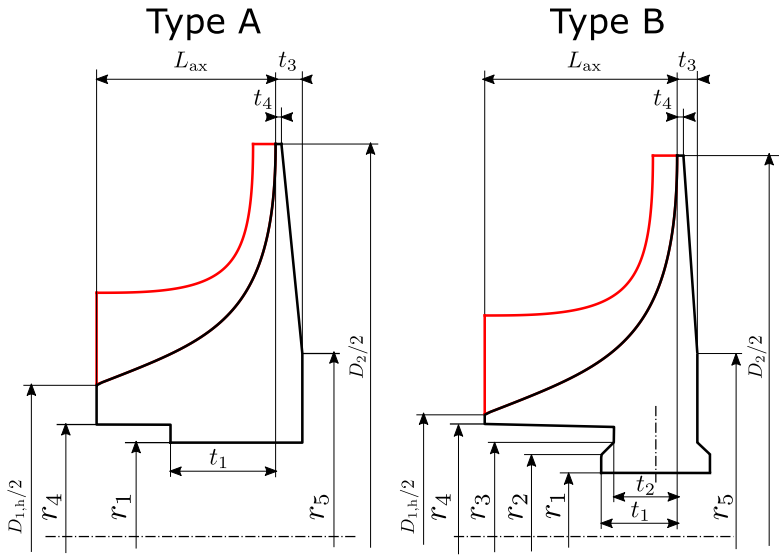

Figure 7.9: Sketch of the radial disk types A and B indicating major dimensions.

7

Table 7.6: Input parameters for radial disk design.

Category	Input Parameter	Symbol	Units
Performance	Total gas temperature impeller inlet	$T_{t,1}$	K
	Total gas temperature impeller exit	$T_{t,2}$	K
	Rotational speed	N	rpm
Geometry	Disk type	-	-
	Impeller hub radius at inlet	$D_{h,1}/2$	m
	Impeller tip radius at inlet	$D_{t,1}/2$	m
	Impeller tip radius	$D_2/2$	m
	Rotor blade tip radius at impeller inlet	$D_t/2$	m
	Impeller axial length ratio	$\frac{L_{ax}}{D_2}$	-
	Rotor blade thickness impeller inlet	$t_{bl,1}$	m
	Rotor blade thickness impeller exit	$t_{bl,2}$	m
	Number of rotor blades	n_{bl}	-
	Impeller flow path shape along the hub	$D_{h,x}$	m
	Impeller flow path shape along the tip	$D_{t,x}$	m
	Blade angle distribution along the flow path	β_x	°
Mechanical	Yield criterion	SF_y	-
	Burst criterion	SF_b	-
	Radial temp. dist.	-	-
	Material	-	-

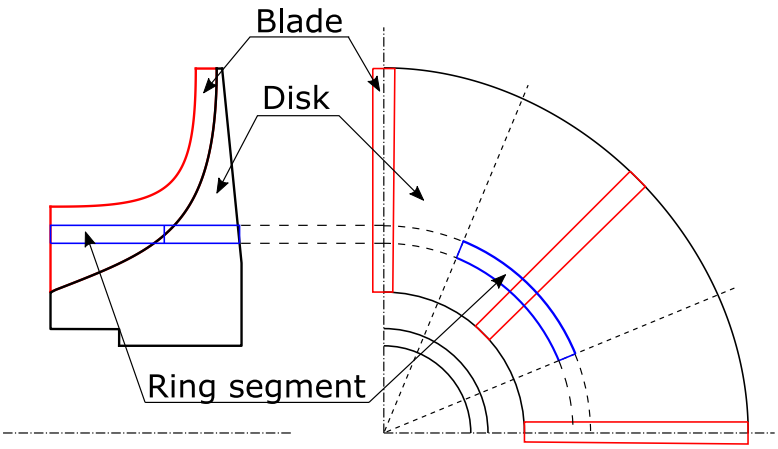

Figure 7.10: Discretization of the radial impeller into ring segments.

imposed.

A novel algorithm developed by Verweij [20] is used for disk stress analysis. This method extends the stress analysis procedure explained in Ref. [21] by including the effect of thermal stresses. For this purpose, the geometry of the impeller is discretized into ring segments as shown in Fig. 7.10. Under the assumption that each segment covers a single radially aligned blade, its width is determined by dividing the perimeter based on the element radius with the number of rotor blades (n_{bl}). Since the actual blades are not radially aligned, a corrected blade thickness is determined. Its value is a function of the thickness distribution and the blade angle distribution (β_{x}) of all blades crossing the respective segment. This corrected thickness is applied to the radial blades used for stress analysis. For each ring segment, a linear system of equations is formulated, accounting for the balance of forces and moments, as well as the displacement in the radial direction and the deformation of the ring element. This system of equations is evaluated for each element starting from the hub and going to the tip of the impeller. Boundary conditions for forces and moments at the impeller hub and tip need to be prescribed. The solution of this boundary value problem does not require iteration. The radial temperature distribution is assumed to be constant and equal to the air inlet total temperature between the radii r_1 and $D_{1,\mathrm{h}}/2$ and to increase linearly between the radii $D_{1,\mathrm{h}}/2$ and $D_2/2$ to the value of the air exit total temperature. No data on the radial temperature distributions of radial impellers was found in the literature. The mathematical details of the procedure sketched in the preceding paragraph are given in Ref. [20]. Application of this method for the design of axisymmetric disks of axial turbomachines is possible and can reduce computational time due to its non-iterative nature.

RETURN CHANNEL DESIGN

Return channels guide the flow between stages in the case of multi-stage radial compressors. The channel incorporates vanes to achieve a desired flow angle at the outlet (β_2). Figure 7.11 provides a sketch of a multi-stage compressor indicating the main dimensions of the return channel and Tab. 7.7 gives the required input parameters. The

design procedure of the return channel is a simplified version of the procedure outlined in Refs. [22, 23].

The inlet and outlet meanline radii and heights are given by the compressor stages that the channel connects to. Following design guidelines of Aungier [22], β_2 is set equal to the inlet absolute flow angle of the downstream compressor, and the vane inlet angle (β_1) is set equal to the diffuser outlet angle of the upstream compressor. Furthermore, the radius r_1 is set equal to 1.5 times the inlet channel height (h_1), and the radius r_2 is set equal to the outlet height of the return channel (h_{out}). The vane inlet and outlet heights (h_1, h_2) are calculated based on the conservation of mass. The vane profiles are generated with the same procedure applied to model diffuser blades and outlined in Section 7.2.2. The number of vanes is equal to the number of impeller blades of the downstream compressor incremented by one. The wall thicknesses are determined based on the same procedure outlined in Section 7.2.1.

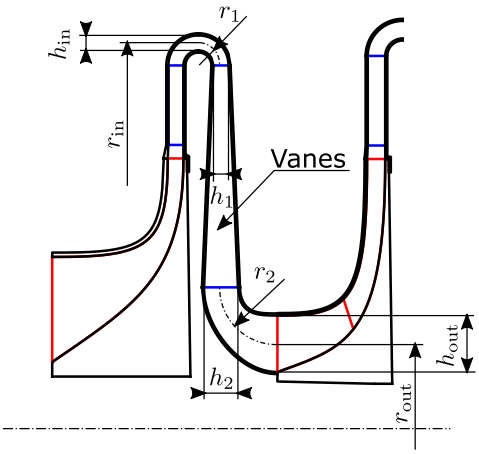

Figure 7.11: Sketch of a two-stage radial compressor indicating the main dimensions of the return channel.

Table 7.7: Input parameters for return channel.

Category	Input Parameter	Symbol	Units
Performance	Adiabatic wall temperature	T_{aw}	K
	Inlet static pressure	p_1	Pa
Geometry	Mean radius inlet	$r_{\text{m,in}}$	m
	Inlet duct height	h_{in}	m
	Mean radius outlet	$r_{\text{m,out}}$	m
	Outlet duct height	h_{out}	m
	Inlet bend radius	r_1	m
	Vane inlet duct height	h_1	m
	Outlet bend radius	r_2	m
	Vane outlet duct height	h_2	m
	Vane inlet blade angle	β_1	°
	Vane outlet blade angle	β_2	°
Mechanical	Material	-	-
	Safety factor	SF	-

CASING DESIGN

The casing of the radial compressor forms the outer shell of the radial compressor gas path. Its purpose is to guide the flow, withstand pressure, and contain debris of rotor blades in case of failure. As shown in Fig. 7.8 the casing is divided into three sections: 1) the impeller casing, 2) the diffuser casing, and 3) a 90-degree bend which is required to connect to downstream components. The thickness of the impeller casing is determined based on the same pressure and blade containment requirements applied for the sizing of the casing of axial machines (see Section 7.2.1). The thickness of the diffuser casing and the 90-degree bend are determined based on the pressure containment requirement only.

VALIDATION

The developed stress analysis procedure is validated by comparison with the results of a FEM model of a radial compressor similar to the one presented by Giuffre' et al. [24].

The same geometries and mechanical boundary conditions are applied to both models. Furthermore, the temperature distribution resulting from the FEM model is extracted and used as input for the procedure implemented in WEST. Figures 7.12 and 7.13 give an overview of the von Mises stress distribution within the impeller as calculated with WEST and resulting from the FEM simulation, respectively. In the case of the WEST, which only employs a one-dimensional discretization, the stress contours are extrapolated from the resulting stress values at the front and back sides of the impeller. Nevertheless, the simplified method implemented in WEST can accurately predict the locations of minimum and maximum stresses. A comparison of the resulting von Mises stress along the disk front and back sides is presented in Fig. 7.14. Despite the lower fidelity when compared to the three-dimensional FEM, WEST can capture the main stress distribution reasonably well. Discrepancies are mainly observed in the disk bore region at the front side and the disk tip at the backside.

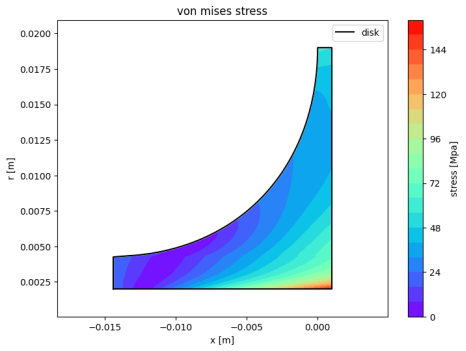

Figure 7.12: Contour plot of the impeller von Mises stress distribution calculated with WEST.

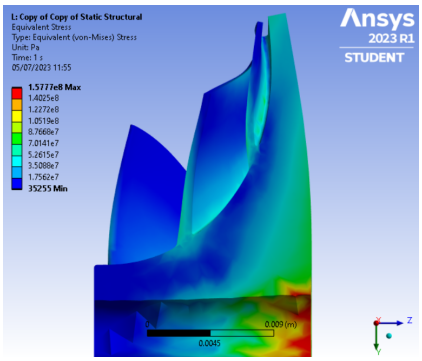

Figure 7.13: Contour plot of the impeller von Mises stress distribution as calculated with the FEM model.

7.2.3. COMBUSTOR DESIGN

The combustion chamber (CC) design procedure conducts the sizing of the combustor casing and flame tube. Two combustor designs are implemented: 1) an axial flow annular combustor model which is based on the methods of Refs. [4, 7], and 2) a reverse flow combustor model which is based on the method of Ref. [25]. Figure 7.15 and 7.8 show the schematics of the annular and reverse flow combustor, respectively. Table 7.8 lists the required input parameters. The design of both combustor types requires knowledge of the compressor exit meanline radius ($r_{\mathrm{m,in}}$) and channel height (h_{in}), and the turbine inlet meanline radius ($r_{\mathrm{m,out}}$) and channel height (h_{out}).

In the case of the annular combustor, the length of the combustor (l_{cc}) is by default determined as the product of a flow residence time of 5 ms and a reference speed (V_{ref}). V_{ref} is determined as

$$V_{\mathrm{ref}} = \sqrt{0.006 R T_4}, \tag{7.7}$$

where R is the specific gas constant of the exhaust gas and T_4 is the static turbine in-

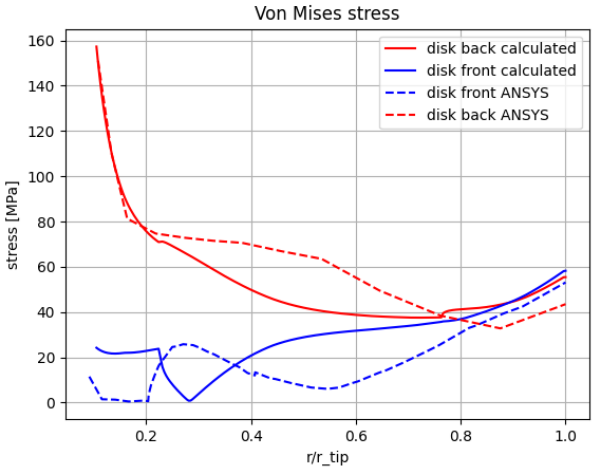

Figure 7.14: Comparison of the von Mises stress distribution along the front and back sides of the disk resulting from the FEM analysis and the procedure implemented in WEST.

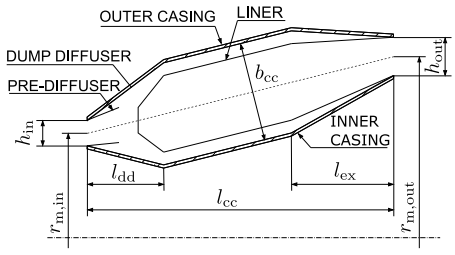

Figure 7.15: Sketch of annular combustor including major dimensions.

Table 7.8: Input parameters for combustor design.

Category	Input Parameter	Symbol	Units
Performance	Air mass flow rate	$\dot{m}$	kg/s
	Fuel mass flow rate	$\dot{m}_{fuel}$	kg/s
	Outlet total pressure	$p_{t,out}$	Pa
	Outlet total temperature	$T_{t,out}$	K
Working fluid	Specific gas constant	R_g	J/(kgK)
	Ratio of specific heats	γ	-
Geometry	Inlet mean radius	$r_{m,in}$	m
	Outlet mean radius	$r_{m,out}$	m
	Inlet channel height	h_{in}	m
	Outlet channel height	h_{out}	m
	Reverse CC height ratio	k_h	-
	Reverse CC length ratio	k_{cc}	-
	Reverse channel ratio	k_{rev}	-

let temperature. Becker et al. [7] evaluate this equation using the compressor exit static temperature (T_3) instead of T_4. However, as shown in Section 7.3 combustor length is underpredicted when using T_3. The required cross-sectional area of the combustor (A_{cc}) is evaluated based on the thermodynamic properties at the combustor exit and V_{ref}. Subsequently, the width of the combustor (b_{cc}) is determined based on A_{cc} and at the radius $\frac{r_{m,in}+r_{m,out}}{2}$. The length of the combustor dump diffuser (l_{dd}) is taken to be a quarter of l_{cc} and the combustor exit channel length (l_{ex}) is one-third of l_{cc}. The width of the liner is taken to be 60% of b_{cc}.

Contrary to the annular combustor design procedure, the geometry of the reverse flow combustor is determined using geometrical ratios specified as inputs by the user. The annular casing height (h_{cc}) is determined by specifying the combustor height ratio $k_h = \frac{h_{cc}}{r_{m,in}-r_{m,out}}$. The value of h_{cc} in combination with the combustor total length ratio ($k_{cc} = \frac{l_{cc}}{h_{cc}}$) and the reverse channel length ratio ($k_{rev} = \frac{l_{rev}}{h_{cc}}$), allows the evaluation of the combustor total length (l_{cc}) and reverse channel length (l_{rev}), respectively. The liner width (h_{liner}) is calculated as

$$h_{liner} = h_{cc} - 3h_{in}, \tag{7.8}$$

and the combustor mean radius ($r_{m,cc}$) is defined as

$$r_{m,cc} = r_{m,in} - h_{cc}/2. \tag{7.9}$$

The de-swirler length l_{des} is set to prevent geometrical interference with the radial compressor stage as

$$l_{des} = l_{rev} - 1.5h_{in}. \tag{7.10}$$

In the case of both the annular and reverse flow combustor, the thickness of the inner and outer casing is determined based on pressure containment considerations as described in Section 7.2.1. Steel is assumed as the combustor material and a yield strength of 480 MPa is selected. The flame tube thickness is set to 1.5 mm. The weight of the injector and dome assembly is evaluated with the empirical correlations given in Ref. [4].

7.2.4. SHAFT DESIGN

Shafts are used to transmit power from the turbine to the compressor and accessory drives. The method to predict shaft dimensions is largely based on the work of Becker et al. [7]. The shaft is split into three sections as shown in Fig. 7.16. Section 1 connects the shaft to the last compressor disk. Section 3 connects the shaft to the first turbine disk. Table 7.9 reports the required input data. The user must provide the radius of Section 2 (r_2). The radii r_1 and r_3 define the connection points with the compressor and turbine, respectively. By default, r_1 is set to 75% of the last stage compressor hub radius, and r_3 is set to the bore radius of the first stage turbine disk, or in case this value is lower than r_2, r_3 is set equal to r_2. A default value of 60 deg is applied to the cone angles of Sections 1 (α_1) and 3 (α_3). In case $r_3 = r_2$, α_3 is set to zero. The total length of the shaft (l_{sh}) is defined as the difference between the coordinates x_1 and x_3, which define the connection points to the compressor and turbine, respectively. The material thickness of each section (t_1, t_2, t_3) is determined based on stress analysis and a safety factor (SF) that relates material yield stress to the maximum von Mises stress (see Ref. [7]). A default value of 1.1 is set

for the safety factor and a minimum material thickness of 2 mm is applied. The applied torque and axial force are inputs and result from the compressor and turbine design. The temperature dependency of the material properties is considered. The temperature of shaft Section 1 is set equal to the hub temperature of the compressor disk to which it is connected. The temperature of shaft Section 3 is set equal to the prevailing disk temperature at the connection point r_3. The temperature of shaft Section 2 is the mean of the temperature evaluated at Sections 1 and 3.

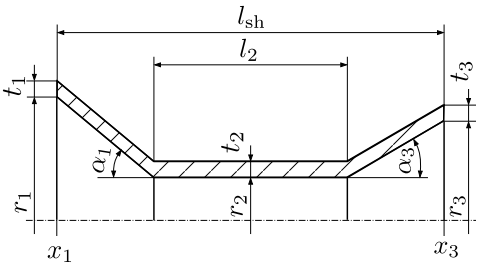

Figure 7.16: Sketch of the shaft including major dimensions.

Table 7.9: Input parameters for shaft design.

Category	Input Parameter	Symbol	Units
Performance	Power	$\dot{W}$	W
	Speed	N	rpm
	Axial force	F_{ax}	N
	Temperature of Section 1	T_1	K
	Temperature of Section 3	T_3	K
Geometry	Inner radius Section 1	r_1	m
	Inner radius Section 2	r_2	m
	Inner radius Section 3	r_3	m
	Axial location Section 1	x_1	m
	Axial location Section 3	x_3	m
	Cone angle Section 1	α_1	°
	Cone angle Section 3	α_3	°
Mechanical	Material	-	-
	Safety factor	SF	-

7

7.2.5. DUCT DESIGN

Ducts are the flow passages that connect turbomachines. A duct consists of two concentrically arranged conical structures as shown in Fig. 7.17. Table 7.10 gives the required input parameters. The inlet and outlet meanline radii ($r_{m,in}$, $r_{m,out}$) and channel heights (h_{in}, h_{out}) are provided by the turbomachinery design. Furthermore, either the length of the duct (l_{duct}) or its flare angle (α_{duct}) needs to be provided. The thickness of the inner and outer walls (t_1, t_2) is determined based on the pressure containment requirement that is also employed for casing sizing (see Section 7.2.1). Therefore, the static pressure at the inlet of the duct (p_{in}) is required. The material yield strength is evaluated based on the adiabatic wall temperature (T_{aw}) at the inlet of the duct. For this purpose, a recovery factor for air of 0.89 is assumed. A default value for the safety factor (SF) relating material yield strength to the von Mises stress of 1.1 and a minimum wall thickness of 1 mm is applied.

7.2.6. FRAME MASS

A frame is a structural component that holds the engine shafts and transmits the produced thrust to the airframe. The frame consists of struts that support the bearing chamber. These struts are aerodynamically shaped and located in the connection ducts between LPC and HPC, and HPT and LPT. Figure 7.18 depicts a possible arrangement of the forward and reward frames of a direct-drive turbofan engine.

The mass of the frame is estimated based on empirical correlations derived by Onat

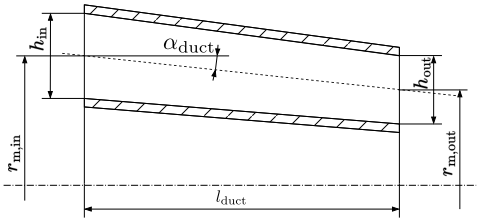

Figure 7.17: Sketch of the duct including major dimensions.

Table 7.10: Input parameters for duct design.

Category	Input Parameter	Symbol	Units
Performance	Adiabatic wall temperature	T_{aw}	K
	Inlet static pressure	p_1	Pa
Geometry	Mean radius inlet	$r_{m,in}$	m
	Mean radius outlet	$r_{m,out}$	m
	Channel height inlet	h_{in}	m
	Channel height outlet	h_{out}	m
	Channel length	l_{duct}	m
	Flare angle	α_{duct}	°
Mechanical	Material	-	-
	Safety factor	SF	-

and Klees [4]. They present correlations for four different types of frames. These types are distinguished by their location in the engine, the number of bearings, and if they allow for power off-takes. The available types are 1) single fixed-bearing frame without power off-take, 2) single fixed-bearing frame with power off-take, 3) single loose-bearing turbine frame, and 4) dual fixed/loose-bearing frame or intermediate single loose-bearing frame located below the combustor.

The frame model requires as input the frame type and the maximum radius of the turbomachine it supports. The methodology of Onat and Klees [4] is not clear which radius to take in case the frame supports two turbomachines. Furthermore, the correlations they developed are based on turbojet and low-bypass ratio engine data. No suitable frame type is provided that matches the architecture of the forward frames of high-bypass ratio engines. A possible solution can be to use one Type 1 frame to support the fan and LPC and one Type 2 frame for the HPC.

7.2.7. GEARBOX MASS

Turboshaft and turboprop engines employ reduction gearboxes to drive a load. In WEST three methods are implemented that use empirical correlations to estimate gearbox mass. All methods relate gearbox mass to power, and input and output speed. The method of Grieb [10, Ch. 5] additionally requires the gas generator mass as an input. The methods of Hendricks and Tong [26] and Brown et al. [27] are both based on a similar database for gearbox masses and include the mass of the lubricant. Additionally, Brown et al. [27] introduces a factor to take the technology level into account. The method documented in Ref. [4] is disregarded, as their documentation is unclear whether it requires gearbox input or output speed as a variable. The applicability of these correlations to gearboxes of geared turbofan engines is questionable, as they are based on designs for lower power levels and higher reduction ratios than is the case for turbofan engines. However, Hendricks and Tong [26] used their correlation to estimate the gearbox mass of an open-rotor engine.

7.2.8. DESIGN POINT SCALARS

Design point scalars enable using a single thermodynamic dataset to design components at different operating conditions. This is necessary, as the thermodynamic, aero-

dynamic, and mechanical design points of the engine can differ. The thermodynamic design determines the size of the gas path, and for civil turbofan engines, it is often determined at the top-of-climb (TOC) operating point. The aerodynamic design point relates to the aerodynamic design of the turbomachines. To achieve optimum efficiency the aerodynamic design point of the turbomachines of civil turbofan engines is often cruise. The mechanical design point corresponds to the operating point where the highest temperatures and shaft speeds are encountered. For a civil turbofan engine, this occurs at the rolling-take-off (RTO) operating point. Since the purpose of the current version of WEST is not to provide estimates of turbomachinery efficiencies, the aerodynamic design point is disregarded.

WEST requires as input engine cycle data at the thermodynamic design point to size the gas path. Design point scalars (S) are used to enable the design of the mechanical components (mechanical design point) using the same thermodynamic dataset. These scalars relate conditions at the mechanical design point to those at the thermodynamic design point. Three scalars are employed in WEST: 1) a temperature scalar, 2) a speed scalar, and 3) a power scalar. The scalars are defined as $S = \frac{k_{\text{mech}}}{k_{\text{thermo}}}$, where k is the respective property at the mechanical or thermodynamic design point. The values of these scalars must be determined from engine performance simulations. The scalars are provided with the thermodynamic dataset of the thermodynamic design point to components designed at the mechanical design point. The required properties at this design point are obtained by multiplying the scalars with the respective properties of the thermodynamic dataset.

7.2.9. MATERIAL DATABASE

WEST includes a material database consisting of commonly used materials for the design of gas turbine engines. Table 7.11 shows the available materials in the database and Tab. 7.12 gives an overview of the stored material properties. Temperature-dependent data is available for most materials.

Table 7.11: Available materials in the database of WEST.

Category	Designation
Steel alloys	17-4PH AISI 4340*
Titanium alloys	Ti-17 Ti-6242 Ti-6Al-4V
Nickel base alloys	HASTELLOY S INCONEL 600 INCONEL 718 NIMONIC 105
Single crystal alloys	CMSX-4 CMSX-10 TMS-196 TMS-238

* Temperature dependency not accounted for.

Table 7.12: Material properties accessible through the WEST material database.

Property	Temp. dependency	Symbol	Units
Density	No	ρ	kg/m^3
Young's Modulus*	Yes	E	Pa
Ultimate tensile strength	Yes	σ_{uts}	Pa
Yield strength	Yes	σ_y	Pa
Poisson's ratio*	Yes	ν	-
Coefficient of thermal expansion*	Yes	α	K^{-1}
Thermal conductivity*	Yes	k	W/mK
Specific heat capacity*	Yes	c	J/kgK

* Not available for single crystal alloys.

7.3. RESULTS

This section presents the initial results of applying WEST to model a two-spool direct-drive turbofan engine. The sizing of the CFM56-7B engine is taken as the test case. A thermodynamic model of the engine is generated and used as input for WEST. Geometrical design variables, such as blade aspect ratios and row and stage gaps, are selected to match the geometry of the CFM56 engine. Subsequently, the resulting component masses are compared with data obtained with the WATE++ code for the same engine.

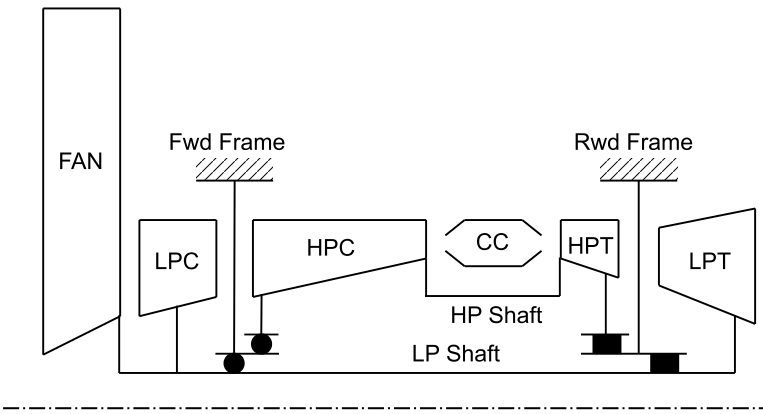

Figure 7.18: Mechanical configuration of a direct-drive turbofan engine. The forward (fwd) frame supports the high-pressure (HP) and low-pressure (LP) shafts via two fixed-bearings indicated with filled circles. The rearward (rwd) frame supports the HP and LP shaft via loose-bearings indicated with filled rectangles.

7.3.1. WEST SETUP

Figure 7.18 shows a schematic of the mechanical configuration of this engine. The gas generator consists of the high-pressure compressor (HPC) that is driven by the high-pressure turbine (HPT) via the high-pressure (HP) shaft. The fan (FAN) and the low-pressure compressor (LPC) are driven by the low-pressure turbine (LPT) via the low-pressure (LP) shaft. All turbomachines are of the axial type and the combustor is of the axial flow annular type. The forward frame is modeled using two single frames, one of Type 1 and one of Type 2, as suggested in Section 7.2.6.

A thermodynamic model to predict the performance of the CFM56 engine during on-design and off-design operations is set up using the modeling software GSP [28]. The turbomachine off-design performance is computed using generic turbomachinery maps provided within GSP. The thermodynamic design point is at TOC at an altitude of 11 km and a Mach number of 0.78. The mechanical design point is at RTO at sea level conditions and a Mach number of 0.3. According to published data at sea-level-static (SLS) conditions the engine produces 121 kN of thrust, has a high-pressure spool speed of 15 183 rpm, and a low-pressure spool speed of 5380 rpm [29]. The thrust at RTO is calculated by multiplying the SLS thrust with a thrust lapse value of 0.77. The thrust lapse is determined using the method presented in Ref. [30]. Assuming that the engine operates on an Airbus A320, the thrust required at the start of cruise (F_{crz}) is approximately 20 kN. The thrust at TOC (F_{toc}) is determined based on the thrust ratio $\frac{F_{\text{toc}}}{F_{\text{crz}}} = 1.20$. The value of this ratio is derived based on the requirement to achieve a 1.1% climb gradient at TOC [10, Ch. 4]. The turbomachinery isentropic efficiencies, the turbine cooling air requirement, air intake pressure loss, the nozzle discharge coefficients, and mechanical efficiencies are assumed to be equal to the values suggested for this engine by Kurzke and Halliwell [14, Part A, Ch. 4]. The simulation of the cruise operation point using this model results in a thrust-specific fuel consumption approximately 3.5% higher than published data [29].

The shape of the gas path and therefore the size and mass of the engine highly depend on the selected turbomachinery duty coefficients. Grieb [10, Ch. 5] presents data for the duty coefficients of the considered turbomachines as a function of entry-into-service and stage-loading. First estimate values of the load coefficients (ψ) and flow coefficients (ϕ) are set based on these data. Their values are further refined by trial and error to improve the geometrical similarity of the gas path produced with WEST and the gas path of the CFM56 engine. The engine design is less sensitive to the value of the degree of reaction. Therefore, for all turbomachines except for the fan, a value of 0.5 is adopted. For the fan, a value of 0.75 is used, which, for the selected work coefficient, results in zero swirl at the exit of the fan stator vanes. The HPT blades are assumed to be cooled. The number of all turbomachine stages is equal to those of the CFM56-7B. Solid fan rotor blades are assumed, as it is the case for the CFM56-7B [1]. Appropriate values for blade aspect ratios, row and stage gaps are obtained by measurements from a CFM56-7B cutaway drawing [29]. The same values for stator and rotor blade solidity as used for the WATE++ model of Greitzer et al. [9] are applied. Furthermore, a value of the burst criterion $SF_{\text{b}} = 1.46$ (see Eq. 7.2) as suggested by Tong et al. [5] and used by Greitzer

[1] https://www.cfmaeroengines.com/press-articles/tech56-swept-fan-blade-successfully-completes-blade-out-rig-test/

et al. [9] is employed. This value is larger than the range specified in Section 7.2.1 and it is only used for the sake of comparison with the WATE++ results. Furthermore, Tong et al. [5] do not justify their value of the burst criterion. Therefore, it is recommended to use the range of values specified in Section 7.2.1 which are based on engine certification requirements.

Table 7.13 summarizes the required input data, the thermodynamic cycle data at TOC, the design point scalars relating RTO to TOC conditions at the inlet of the respective component, the turbomachinery duty coefficients, and the selected materials.

Table 7.13: Input parameters used to model the CFM56 engine in WEST. The symbols $\dot{m}_{in}$, $p_{t,in}$, and $T_{t,in}$, refer to the mass flow rate, total pressure and total temperature at the inlet of the respective component. The symbols S_N, S_T, and $S_{\dot{W}}$, refer to the design point scalars for speed, temperature, and power, respectively. Materials are referred to using the designation of the WEST material database.

Category	Parameter	FAN	LPC	HPC	CC	HPT	LPT
Performance	$\dot{m}_{in}$ (kg/s)	157	26	26	22	22	26
	$p_{t,in}$ (bar)	0.34	0.58	1.0	11.0	10.3	2.36
	$T_{t,in}$ (K)	243	289	343	717	1450	1040
	S_N (-)	1.04	1.04	1.08	-	1.08	1.04
	S_T (-)	1.27	1.23	1.2	1.17	1.17	1.19
	$S_{\dot{W}}$ (-)	-	-	-	-	2.85	2.81
Duty coeff.	ψ	0.5	0.3	0.4	-	1.7	1.9
	ϕ	0.8	0.7	0.6	-	0.5	1.0
	r	0.75	0.5	0.5	-	0.5	0.5
Geometry	AR first rotor	2.35	2.2	2.6	-	1.8	3.5
	AR last rotor	-	2.2	1.9	-	-	8.0
	AR first stator	2.8/3.2*	2.9	3.6	-	1.1	2.5
	AR last stator	-	1.8	1.5	-	-	5.0
	taper ratio rotor	0.85	0.8	0.85	-	0.8	0.8
	taper ratio stator	1.0/1.0*	1.0	1.0	-	1.0	1.0
	row gap param.	0.25	0.25	0.25	-	0.57	0.5
	stage gap param.	0.01/0.5**	0.45	0.45	-	0.57	0.15
Materials	Rotor blades	Ti-17	Ti-17	Ti-17/Inconel 718	-	CMSX-4	CMSX-4
	Stator blades	17-4PH	Ti-17	Ti-17	-	Nimonic 105	Nimonic 105
	Disks	Ti-17	Ti-17	Ti-17/Inconel 718	-	Inconel 718	Inconel 718
	Casing	17-4PH	17-4PH	17-4PH	17-4PH	Nimonic 105	17-4PH
	Shaft	-	-	-	-	Inconel 718	17-4PH

* The first value is for the core stator and the second value is for the bypass stator.

** Non-dimensional gap parameters of the core ($g_{core,stator}$) and bypass stator ($g_{byp,stator}$) leading edges to the splitter leading edge.

7.3.2. WEST RESULTS

Figure 7.19 shows the design of the engine on the meridional plane resulting from WEST overlapped with the cutaway drawing of the CFM56-7B engine. Despite the simplified gas path architectures integrated in WEST, satisfactory geometrical agreement is achieved for the gas path shape of all components. The fan core channel exhibits poor matching with the LPC. This is the result of the simplified fan modeling approach, where the variation of V_m along the rotor blade is not considered (see Section 7.2.1). Therefore,

the splitter leading edge radius is underpredicted (see r_{splitter} in Fig. 7.7). The combustor length is in good agreement with the actual engine dimensions. Sizing the combustor based on the HPC exit temperature as proposed by Becker et al. [7] and explained in Section 7.2.3 results in a 30% shorter combustor. It can be further observed, that the optimized disk shapes of the HPC do not match those of the actual engine. Reasons for this could be related to manufacturing or assembly aspects that cannot be considered with the simplified methodology implemented in WEST.

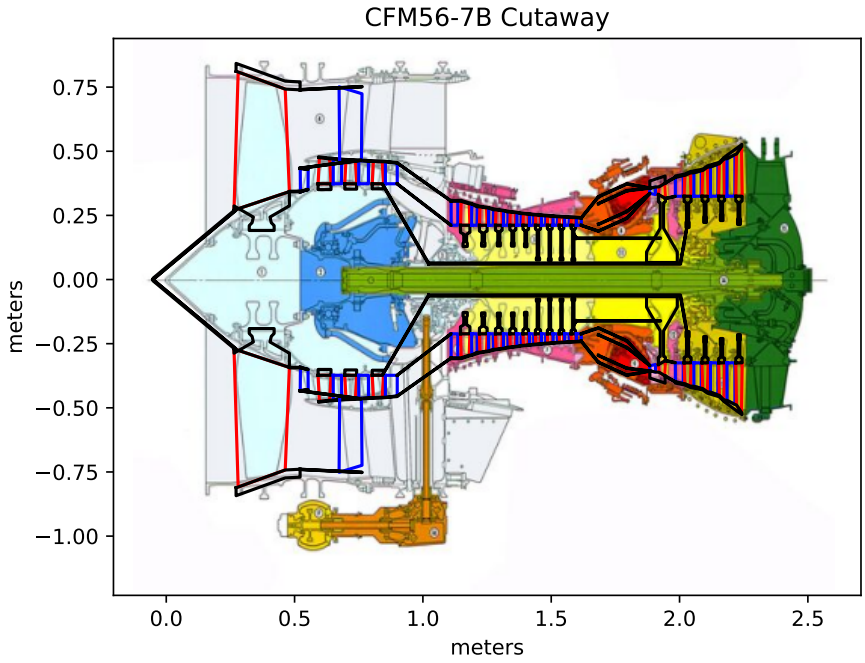

Figure 7.19: Comparison of the cutaway drawing produced with WEST with the cutaway drawing of the CFM56-7B engine.

Table 7.14 presents the resulting mass breakdown of the engine designed with WEST and WATE++ as provided in Ref. [9]. Greitzer et al. [9] do not provide thermodynamic cycle data and the resulting geometry of the WATE++ model is not known. Furthermore, only an overview of the used material types is given without specifying the exact alloy. Similar materials are applied for the WEST model. Additionally, modeling methodologies and assumptions may differ. These aspects introduce uncertainty in the comparison of the results. In general, WEST underpredicts the masses of most components and the engine total mass is 15% lower than the result obtained with WATE++. This number doubles to 30% when compared to the published engine dry mass of 2400 kg [29].

A detailed mass breakdown of the turbomachinery components obtained with WEST and WATE++ is given in Tab. 7.15. The results show that WEST in general underestimates

Table 7.14: Mass breakdown of a turbofan engine with similar specifications to a CFM56-7B engine modeled with WEST, and compared with data presented in Ref. [9] using the WATE++ program.

Component	WATE++	WEST	Delta
Fan (kg)	494	512	4%
LPC (kg)	97	77	-21%
HPC (kg)	184	101	-45%
CC (kg)	107	102	-5%
HPT (kg)	160	134	-16%
LPT (kg)	307	225	-27%
HP Shaft (kg)	11	6	-46%
LP Shaft (kg)	67	20	-70%
Ducts (kg)	30	8	-73%
Frames (kg)	145	205	41%
Accessories (kg)	317	285	-10%
Other (kg)	40	-	-
Total (kg)	1959	1675	-15%

blade masses. This is expected due to the different approaches of blade mass accounting implemented in WEST and WATE++. In WATE++ blade mass includes the mass of the airfoil, the platform, and the root and is estimated using the method of Ref. [4]. This method uses an empirically determined blade volume factor (K) that relates the blade height (h_{bl}) and aspect ratio (AR) to the combined volume of the airfoil, the platform, and the root (V_{bl}) according to the following equation

$$V_{\text{bl}} = \frac{K \times h_{\text{bl}}^3}{AR^2}. \tag{7.11}$$

The product of V_{bl} and the blade material density yields its mass. In contrast, the blade mass estimate of WEST only relates to the airfoil mass, and the blade platform and root masses are considered to be part of the disk mass (see Section 7.2.1). The observed error in blade mass estimates can also be due to different design assumptions in WEST and WATE++. For example, the overestimation of LPT stator and rotor blades might be due to too large values for the thickness-to-chord ratios. Similar reasoning may apply to the fan rotor blades. The mass of the fan rotor blades is overestimated with WEST, especially when considering that only airfoil mass is included. Fan stator mass is highly underestimated when compared to WATE++. The mass estimate of WATE++ seems to include masses of structural struts placed in the bypass duct. This hypothesis is supported by the high value of K for the fan stator reported by Greitzer et al. [9]. Given the difference in blade mass estimation methods, comparing the combined blade and disk mass seems most appropriate. This comparison results in errors ranging from -10 to 10% for the FAN, LPC, HPT, and LPT and of -36% for the HPC if compared to the WATE++ results.

The same disk modeling methodology is applied in WEST and WATE++ and differing modeling assumptions may cause the observed discrepancies. For example, as previously mentioned differences in blade modeling impact the comparability of the results obtained with WEST and WATE++. Similarly, the geometrical simplifications applied to the disk design and assumptions regarding disk rim thickness to accommodate for the blade root can impact the mass estimates. Furthermore, it is not specified what disk radial temperature distribution is applied in WATE++.

The combined mass of the frames is 41% higher than the mass estimated with WATE++. It is not specified what frame configuration was assumed for the WATE++ model. In Tab. 7.15, the component labeled Other in the case of WEST refers to the hardware used to connect stages of multi-stage machines. In the case of WATE++, it is not specified what component masses are considered.

Table 7.15: Mass breakdown of the LPC, HPC, HPT, and LPT as estimated with WEST and WATE++ for the CFM56-7B engine. The WATE++ data is taken from Ref. [9].

Component	**HPC**			**HPT**		
	WATE++	**WEST**	**Delta**	**WATE++**	**WEST**	**Delta**
Rotor blades (kg)	16	6	-63%	13	2	-85%
Stator blades (kg)	22	10	-55%	31	3	-90%
Disks (kg)	85	63	-26%	48	94	96%
Casing (kg)	41	15	-63%	22	35	59%
Other (kg)	19	6	-68%	48	-	-
Total (kg)	184	101	-45%	160	134	-16%
Component	**LPC**			**LPT**		
	WATE++	**WEST**	**Delta**	**WATE++**	**WEST**	**Delta**
Rotor blades (kg)	11	9	-18%	35	51	46%
Stator blades (kg)	14	15	7%	36	46	28%
Disks (kg)	26	32	23%	81	72	-11%
Casing (kg)	26	17	-35%	54	49	-9%
Other (kg)	19	5	-74%	100	6	-94%
Total (kg)	97	77	-21%	307	225	-27%
Component	**FAN**					
	WATE++	**WEST**	**Delta**			
Rotor blades (kg)	153	149	-3%			
Stator blades (kg)	130	55	-58%			
Disks (kg)	47	116	147%			
Casing (kg)	159	176	11%			
Other (kg)	6	-	-			
Total (kg)	494	512	4%			

Boersma [13] provides an additional example of the application of WEST to model the gas generator of the Pratt & Whitney PW2037 turbofan engine. A comparison of

these results with data produced with WATE++ shows that gas generator mass is underpredicted by 18%. Furthermore, Verweij [20] presents the application of WEST to model the General Electric T700 and MTU Turbomeca Rolls Royce MTR390 turboshaft engines. In this case, no component data of the analyzed engines was available. However, WEST can provide a fairly accurate gas path shape of both engines and the mass estimate is approximately 30% lower than the published masses of these engines. This accuracy is in line with that currently achieved for turbofan mass estimation. In the case of turboshaft engines, the estimation of the masses of the gearbox and accessories, such as the commonly employed particle separator, increases the degree of uncertainty further.

Generation of the results presented in this section took approximately 90 seconds on a single core of an AMD Ryzen 7 PRO 4750U processor. For comparison, the generation of the engine gas path takes roughly one second. At this point of the development, the code cannot be parallelized. The disk design procedure takes the longest time and is driven by the number of discretization points. The presented results use disks discretized with an equispaced one-dimensional grid of 100 nodes. A grid sensitivity study has shown no appreciable changes in the results for a finer discretization. A sufficient grid density is especially important in regions of geometrical discontinuity. This is highlighted by results of Ref. [31] that show the grid sensitivity of the computed von Mises stress distribution to the grid density and node distribution. It is shown, that equispaced grids require an order of magnitude more nodes to match the results of an unevenly spaced grid. Gutzwiller and Turner [31] developed the T-AXI disk software that employs a method with an adaptive grid. Therefore, implementing a more advanced disk stress analysis algorithm can drastically reduce computational time.

7.4. CONCLUSIONS

This chapter describes the development status of a new component-based engine weight estimation tool named WEST. A comparison of the mass estimation obtained with WEST and WATE++ for a direct-drive turbofan engine shows that WEST tends to underpredict masses. Overall, WEST outputs a total engine mass that is 15% lower than the result obtained with WATE++.

The largest discrepancies are identified in predicting turbomachinery disk and blade masses. This may be due to different modeling approaches and assumptions employed in the two computer programs. In particular, the methods used to model blade masses differ. An accurate estimation of rotor blade mass is crucial, as it serves as an input for the design of the disk and the casing. In this respect, further research and development is required to improve the predictive capabilities of WEST. It is also found that the computational time needed to conduct a full engine design can be prohibitive when repeated execution is necessary, as can be the case during optimization studies. This problem may be circumvented by using WEST to train a surrogate model that could be efficiently employed as part of a larger simulation framework.

At this stage of the development, WEST incorporates methods to model all major components of turboshaft and turbofan engines. However, further improvements are needed to increase the accuracy of estimating engine mass. The following points are identified for future work:

- Improvement of the blade design methodology and re-evaluation of the validity and accuracy of considering blade platform and root mass as part of the disk mass. Possible methods to consider are the method of Sawyer [32] for the preliminary design of turbine blade fir-tree attachments, and a more simplified method for the estimation of blade platform and root size and mass as detailed in the technical user manual of GasTurb [8][2]. Furthermore, default values employed for blade thickness-to-chord ratios should be re-assessed and adapted based on the type of turbomachine.

- Improvement of the disk design methodology to reduce the needed computational time. In the case of axial disks adopting the radial disk design routine can reduce computational time due to its non-iterative nature. Alternatively, implementing an adaptive grid method, such as the one presented by Gutzwiller and Turner [31], can improve computational time for both axial and radial disks. Additionally, the axial disk model implemented in WEST should be compared against results obtained with the T-AXI disk sizing program [31]. Furthermore, the hyperbolic axial disk type commonly used for high-pressure turbines should be implemented.

- At the moment WEST requires turbomachinery duty coefficients for gas path sizing. The effect these coefficients have on the gas path shape is not immediately obvious to the user. Therefore, it is recommended to modify the present design methodology to allow the specification of axial Mach number and hub-to-tip ratio at the entry of the turbomachine as an alternative method.

- The current version of WEST requires the shaft speed as an input. The shaft speed influences the diameter of the turbomachines. However, for optimization studies including engine design, it can be argued that a method enabling the shaft speed to be automatically determined based on mechanical design criteria is advantageous. Therefore, the implementation of a physics-based method or a method using a speed scaling parameter that is based on a reference engine design (see Walsh and Fletcher [33, Ch. 4]) is suggested.

- Improvement of the fan design methodology by adopting a controlled vortex method, namely a method in which the degree of reaction is controlled along the blade span, for three-dimensional blade design. This can improve the splitter leading edge radius estimation and therefore the matching with the LPC. Furthermore, the assumptions employed for the modeling of the fan disk need to be re-evaluated as the current results overpredict disk mass when compared to the results of WATE++.

- Currently, WEST requires rotor and stator blade aspect ratios as input. The value of the selected aspect ratios affects engine length and the masses of multiple components such as disks and shafts. Therefore, the predictive capabilities of WEST can be improved by implementing a semi-empirical or physics-based method determining aspect ratios based on mechanical and aerodynamic design considerations. A first attempt at identifying a relation between compressor rotor blade

[2] GasTurb Details 6, https://www.gasturb.com/Downloads/Manuals/GasTurbDetails6.pdf, accessed on 17 May 2024

aspect ratio and work coefficient is documented in the work of Verweij [20]. Alternatively, an empirical method can be implemented using data presented in Ref. [9] relating blade aspect ratios to engine dimensions.

- Extension of WEST with models to predict the size and mass of the inlet, nozzle, and nacelle, and a method to estimate the mass of lubricants.

The lack of publicly available data on actual engine component masses hinders the development of accurate mass prediction tools. On that note, large benefits for model improvement are envisioned from collaboration with engine manufacturers or maintenance, repair, and overhaul (MRO) shops.

BIBLIOGRAPHY

[1] E. Torenbeek, *Synthesis of Subsonic Airplane Design*. Delft University Press, 1982, ISBN: 90-247-2724-3.

[2] P. Lolis, "Developoment of a preliminary weight estimation method for advanced turbofan engines," Ph.D. dissertation, Cranfield University, 2014.

[3] D. A. Sagerser, S. Lieblein, and R. P. Krebs, "Empirical expressions for estimating length and weight of axial-flow components of VTOL powerplants," NASA Lewis Research Centre, Tech. Rep., 1971, NASA-TM-X-2406.

[4] E. A. Onat and G. W. Klees, "A method to estimate weight and dimensions of large and small gas turbine engines," NASA Lewis Research Centre, Tech. Rep., 1979, NASA-CR-159481.

[5] M. T. Tong, I. Halliwell, and L. J. Ghosn, "A computer code for gas turbine engine weight and disk life estimation," *Journal of Engineering for Gas Turbines and Power*, vol. 126, no. 2, pp. 265–270, 06 2004, doi: 10.1115/1.1691980.

[6] M. T. Tong and B. A. Naylor, "An object-oriented computer code for aircraft engine weight estimation," in *Proceedings of the ASME Turbo Expo*, 2008, doi: 10.1115/GT2008-50062.

[7] R. Becker, S. Reitenbach, C. Klein, T. Otten, M. Nauroz, and M. Siggel, "An integrated method for propulsion system conceptual design," in *Proceedings of the ASME Turbo Expo*, 2015, doi: 10.1115/GT2015-43251.

[8] GasTurb GmbH, "Design and off-design performance of gas turbines," 2024, software. [Online]. Available: https://www.gasturb.com/

[9] E. M. Greitzer, P. Bonnefoy, E. De la Rosa Blanco, C. Dorbian, M. Drela, D. Hall, R. Hansman, J. Hileman, R. Liebeck, J. Lovegren *et al.*, "N+3 aircraft concept designs and trade studies, final report," NASA Glenn Research Center, Tech. Rep., 2010, NASA-CR-2010-216794/vol2.

[10] H. Grieb, *Projektierung von Turboflugtriebwerken*. Birkhäuser Basel, 2004, ISBN: 978-3-0348-7938-5, doi: 10.1007/978-3-0348-7938-5.

[11] J. Dunham, "A parametric method of turbine blade profile design," in *Proceedings of the ASME Turbo Expo*, 1974, doi: 10.1115/74-GT-119.

[12] H. I. H. Saravanamuttoo, G. F. C. Rogers, H. Cohen, P. V. Straznicky, and A. C. Nix, *Gas Turbine Theory*, 7th ed. Pearson Education, 2017, ISBN: 0132224372.

[13] I. Boersma, "Weight estimation of gas turbine engines," Master's thesis, Delft University of Technology, 2022. [Online]. Available: https://repository.tudelft.nl/islandora/object/uuid:20f02be0-e9db-484b-b487-ef1e087ad894?collection=education

[14] J. Kurzke and I. Halliwell, *Propulsion and Power: An Exploration of Gas Turbine Performance Modeling*. Springer International Publishing, 2018, ISBN: 978-3-319-75979-1, doi: 10.1007/978-3-319-75979-1.

[15] S. Bretschneider, F. Rothe, M. G. Rose, and S. Staudacher, "Compressor casing preliminary design based on features," in *Proceedings of the ASME Turbo Expo*, 2008, doi: 10.1115/GT2008-50102.

[16] R. H. Aungier, *Centrifugal Compressors: A Strategy for Aerodynamic Design and Analysis*. ASME Press, 01 2000, doi: 10.1115/1.800938.

[17] D. J. L. Smith and H. Merryweather, "The use of analytic surfaces for the design of centrifugal impellers by computer graphics," *International Journal for Numerical Methods in Engineering*, vol. 7, no. 2, pp. 137–154, 1973, doi: 10.1002/nme.1620070205.

[18] B. Eckert and B. Schnell, *Axial- und Radialkompressoren*. Springer, 1961, ISBN: 978-3-642-80543-1.

[19] C. Xu, "Design experience and considerations for centrifugal compressor development," *Proceedings of the Institution of Mechanical Engineers, Part G: Journal of Aerospace Engineering*, vol. 221, no. 2, pp. 273–287, 2007, doi: 10.1243/09544100JAERO103.

[20] F. Verweij, "Weight estimation of turboshaft engines," Master's thesis, Delft University of Technology, 2023. [Online]. Available: https://repository.tudelft.nl/islandora/object/uuid:54d8ba82-7104-4f40-9ae6-8b81f364912c?collection=education

[21] G. Ray and B. Sinha, "Computation of centrifugal stresses in a radial-flow impeller," *Computers Structures*, vol. 40, no. 3, pp. 731–740, 1991, doi: 10.1016/0045-7949(91)90240-M.

[22] R. H. Aungier, "Aerodynamic design and analysis of vaneless diffusers and return channels," in *Proceedings of the ASME Turbo Expo*, 1993, doi: 10.1115/93-GT-101.

[23] ——, "Centrifugal compressor stage preliminary aerodynamic design and component sizing," in *Proceedings of the ASME Turbo Expo*, vol. Volume 1: Turbomachinery, 1995, doi: 10.1115/95-GT-078.

[24] A. Giuffre', P. Colonna, and M. Pini, "Design optimization of a high-speed twin-stage compressor for next-gen aircraft environmental control system," *Journal of Engineering for Gas Turbines and Power*, vol. 145, no. 3, 12 2022, doi: 10.1115/1.4056022.

[25] B. Khandelwal, M. Yan, G. Hegde, V. Sethi, and R. Singh, "Design procedure of a reverse flow combustor for a helicopter engine with high temperature rise," in *Aerospace Technology Conference and Exposition*, 2011, doi: 10.4271/2011-01-2562.

[26] E. Hendricks and M. Tong, "Performance and weight estimates for an advanced open rotor engine," in *48th AIAA/ASME/SAE/ASEE Joint Propulsion Conference*, 2012, doi: 10.2514/6.2012-3911.

[27] G. V. Brown, A. Kascak, B. T. Ebihara, D. Johnson, B. B. Choi, M. W. Siebert, and C. J. Buccieri, "NASA Glenn Research Center program in high power density motors for aeropropulsion," NASA Lewis Research Centre, Tech. Rep., 2005, tM-2005-213800.

[28] W. Visser, "Generic analysis methods for gas turbine engine performance: The development of the gas turbine simulation program GSP," Ph.D. dissertation, Delft University of Technology, 2015.

[29] Jane's Information Group, "Jane's aero-engines," 2022. [Online]. Available: https://shop.janes.com/products/air-space/janes-aero-engines

[30] J. D. Mattingly, W. H. Heiser, K. M. Boyer, B. A. Haven, and D. T. Pratt, *Aircraft Engine Design*, 3rd ed. AIAA, 2018, ISBN: 978-1-62410-650-7.

[31] D. P. Gutzwiller and M. G. Turner, "Rapid low fidelity turbomachinery disk optimization," *Advances in Engineering Software*, vol. 41, no. 5, pp. 779–791, 2010, doi: 10.1016/j.advengsoft.2009.12.019.

[32] J. W. Sawyer, *Sawyer's Gas Turbine Engineering Handbook, Volume 1: Theory & Design*, 3rd ed. Turbomachinery International Publications, 1985, ISBN: 0-937506-14-1.

[33] P. P. Walsh and P. Fletcher, *Gas Turbine Performance*, 2nd ed. Blackwell Science, 2004, ISBN: 978-0-632-06434-2.

8

CONCLUSIONS AND RECOMMENDATIONS

The design of organic Rankine cycle (ORC) bottoming units for aircraft gas turbine engines differs from that of stationary systems due to the trade-off between thermodynamic benefits on mission fuel consumption and the penalties of increased aircraft mass and drag. Airborne systems are inherently more complex and face drastically different and continuously changing environmental conditions compared to stationary systems. For these reasons, common design guidelines devised for stationary ORC systems no longer apply, and the optimal design of combined-cycle engines requires a novel and complex multidisciplinary approach.

The work documented in this dissertation aims to advance knowledge about airborne ORC waste-heat-recovery (WHR) systems by employing numerical modeling to identify optimal design choices and formulate a first set of design guidelines. For this purpose, an advanced simulation framework was developed, incorporating models for the gas turbine engine, the ORC unit, the ORC turbine and heat exchanger preliminary sizing, and aircraft design and performance estimation. This software was named the *ARENA* framework, and it can be used to design combined-cycle engines optimized for minimized fuel consumption while considering their impact on aircraft design and performance.

8.1. CONCLUSIONS

The ARENA framework is coded in Python. The choice of this programming language enables simple integration of external software packages and therefore a high degree of flexibility. The Python library *openMDAO*, which provides standardized methods for implementing models using an object-oriented approach and simple integration of different solver types and optimizers, is used. As a result, system models with a high degree of adaptability, maintainability, and reusability can be generated. This philosophy allows for a straightforward extension of the ARENA framework with additional capabilities for

future research.

The ARENA framework was applied to model and simulate three cases with differing combined-cycle configurations and missions. These cases are 1) a combined-cycle auxiliary power unit (CC-APU) instead of a conventional APU to provide a medium-range aircraft power on the ground (Chapter 3), 2) combined-cycle turboshaft engines (CC-TS) replacing the conventional turboshaft engines of a medium-range turboelectric aircraft (Chapter 5), and 3) combined-cycle turbofan engines (CC-TF) in place of the conventional turbofan engines of a medium-range partial-turboelectric aircraft (Chapter 6). The modeling assumptions relate to currently available heat exchanger technology and values for gas turbine turbomachinery efficiencies predicted for the year 2035. Considering possible heat exchanger performance improvements due to advanced manufacturing technologies such as additive manufacturing, the presented results may underestimate the potential of the investigated systems. The results are also affected by uncertainties regarding engine mass estimation and the aerodynamic performance of ducts housing the heat exchangers.

Based on the results obtained from these simulation studies, the following conclusions are drawn:

- The augmentation of thermodynamic efficiency of an aircraft gas turbine engine due to waste heat recovery via an ORC bottoming unit can outweigh the penalty of increased aircraft mass and drag on mission fuel consumption. However, the fuel-saving potential of this new technology depends on the combined-cycle configuration and the mission scenario.

- The CC-APU system consumes approximately 50% less fuel for providing ground power than a conventional APU. This efficiency increase translates into mission fuel savings of 0.6%. However, operating the CC-APU during cruise to provide secondary power is less fuel efficient than using power off-takes from the main engines (see Chapter 2).

- Replacing the gas turbine engines of a turboelectric aircraft with CC-TS or CC-TF engines may result in fuel savings of 1.5% and 4%, respectively. Fuel savings of 2.3% are achieved with the CC-TS Mark II engine concept (see Section 6.3.5) that employs the condenser arrangement of the CC-TF engine. Integrating the condensers into the bypass duct of the CC-TF results in an advantage over the CC-TS configuration where they are integrated into ram-air ducts. The combination of pressure rise and thermal energy addition to the bypass air increases the bypass propulsive efficiency by 13% and the specific thrust of the engine during cruise by 30%. The bypass propulsive efficiency is defined as the bypass net thrust divided by the power required to compress the bypass air. The optimal value of the fan pressure ratio of the CC-TF is 10% higher than that of a conventional turbofan engine.

- The optimal design of the gas turbine of a combined-cycle engine employed on aircraft is characterized by a higher turbine inlet temperature and a lower overall pressure ratio during cruise if compared to a simple-cycle aircraft gas turbine engine. The pressure drop over the exhaust duct of the gas turbine caused by the

evaporator increases the back pressure of the turbine. This results in a lower specific power or specific thrust and lower thermal efficiency. Given a fixed power requirement, the power capacity of the gas turbine engine is reduced due to the contribution of the ORC unit in providing shaft power. As a result, the gas turbine engine is shorter and smaller in diameter than a simple-cycle engine, which produces the same power as the combined-cycle engine. The reduction in gas turbine power capacity can negatively impact the performance of the engine at operating points where the WHR system may contribute less power, such as at take-off.

- The optimal configuration for integrating the condenser into the engine assembly is such that it is tilted by an angle of approximately 75 degrees with respect to the radial direction and placed downstream of the fan. This configuration allows for thrust augmentation due to thermal energy input into the air stream at elevated pressure. Tilting the condenser increases the heat transfer area while reducing the frontal area of the engine. Integrating the condenser into a ram-air duct and transferring thermal power from the condensing working fluid to the air stream generates sufficient thrust to balance the drag caused by the ram-air duct and the condenser. The optimal configuration for integrating the evaporator into the engine assembly is such that it is of annular shape and integrated into the S-shaped exhaust duct of the gas turbine engine. This configuration maximizes the heat transfer area while keeping the frontal area of the engine within feasible limits. However, an aerodynamically optimized exhaust duct is required to minimize the pressure loss due to flow turning.

- It is estimated that adopting combined-cycle engines as the prime movers of medium-range turboelectric aircraft increases maximum take-off mass and operating empty mass by 0.5% and 1% in the case of the CC-TS configuration, and by 2% and 4% in the case of the CC-TF concept. The lift-to-drag ratio of an aircraft employing optimized combined-cycle engines does not change significantly compared to an aircraft using conventional gas turbine engines. In the case of the CC-TF engine, the reason for little change in lift-to-drag ratio is, that the shorter engine combined with the larger nacelle diameter results in no appreciable change in nacelle wetted area and drag compared to a conventional turbofan engine. In the case of the CC-TS engine, the lift-to-drag ratio is not affected as the ram-air duct causes zero net force resulting from the thrust production due to the heating of the ram air.

- Employing mixtures of organic compounds as the working fluid of air-cooled ORC bottoming units of stationary gas turbines in the 50 MW power range has no beneficial effect on the combined-cycle power output. However, mixtures can result in a more compact and thus cost-effective ORC turbine design. This can be beneficial for the design of ORC systems for vehicular applications. Additional research is required to understand the impact of working fluid selection on the combined-cycle engine and aircraft performance.

- The following design guidelines for airborne ORC WHR units are devised:

    1. For first-order analysis (see Chapter 2), values for ORC unit mass-specific power in the range of 1 to 1.7 kW/kg and for net efficiency of the ORC system

in the range of 15 to 18% are suitable. Furthermore, a conservative estimate for the ORC heat recovery factor is 60%. These values result from the analyzed configurations presented in Chapters 4 to 6 and are based on the assumption of current-day heat exchanger technology and predicted gas turbine turbomachinery efficiencies for the year 2035.

2. From a thermodynamic point of view, ORC systems can be optimized for efficiency or power output. The power output of airborne ORC systems is affected by 1) the space constraints that effectively limit heat exchanger size, 2) the penalty of the evaporator pressure drop on gas turbine performance, and 3) the penalty of the condenser pressure drop on aircraft drag. Therefore, contrary to stationary ORC power plants, airborne ORC systems are optimized for thermal efficiency. Hence, the cycle temperature must be the highest possible. The supercritical configuration makes ORC efficiency less sensitive to the maximum cycle pressure. Its value can be selected based on component design and control considerations.
3. ORC turbine maximum total-total efficiency coincides with ORC turbogenerator maximum mass-specific power (see Chapter 4) and design variables should be selected accordingly.
4. Tilting the condenser by an angle of 60 to 75 degrees with respect to the radial direction increases the heat transfer area while keeping the frontal area of the engine small. The benefit of a smaller engine frontal area in reducing aircraft drag outweighs the penalty of increased pressure loss due to flow turning.
5. In the case of a flat-tube louvered fin condenser, the optimal design features a high ratio of fin area to flat-tube area to keep the heat transfer area large and pressure drop over the cold side low.
6. In the case of a bare-tube evaporator, the best topology is an in-line configuration with a non-dimensional transversal pitch of 3 and a non-dimensional longitudinal pitch of 1.25. This limits the hot side pressure drop. The non-dimensional pitches are defined as the dimensional length divided by the outer diameter of the tube.
7. In the case of a fan-air-cooled configuration such as used for the CC-APU concept, employing an aerodynamically optimized fan is crucial to achieve maximum performance. Furthermore, using mixtures of organic compounds as working fluids can reduce fan power consumption.

Considering the uncertainty introduced by modeling restrictions and simplifying assumptions, and the limited number of case studies described in this dissertation, the predicted mission fuel savings of a few percent may not justify the development of the analyzed concepts. Hence, it is advisable to enhance the ARENA framework and explore alternative configurations, the adoption of optimal working fluids, and other scenarios.

8.2. RECOMMENDATIONS

Suggestions on the extension of the ARENA framework to support further research on more advanced combined-cycle engine architectures are as follows:

1. Currently, the framework only allows performing ORC on-design simulations. The results presented on the CC-TF concept highlighted that the reduced power capacity of the gas turbine engine resulting from adding a WHR system negatively affects the gas turbine performance at take-off. Therefore, the ability to perform off-design simulations of the ORC system is required to assess the performance of the combined-cycle engine throughout the entire aircraft mission. Furthermore, the capability of performing multipoint design optimization of the combined-cycle engine may allow for improved system performance.

2. To improve the computational efficiency of the ARENA framework it is recommended to develop a new ORC performance analysis tool using the standardized methods provided by the Python library *openMDAO* [1]. In particular, the code used to model turbomachines and ducts implemented in the Python library *pycycle* [2], can be reused. pycycle is a software tool for gas turbine performance analysis based on openMDAO. However, the code should be linked to a suitable library for the estimation of thermodynamic and transport properties of organic compounds. Alternatively, the look-up-table method implemented into pycycle can be provided with pre-tabulated data for the organic compounds of interest.

3. The aircraft design and performance methods implemented in the ARENA framework rely on previously computed estimates of airframe masses and aerodynamic coefficients and only consider resizing of the wing and the variation of engine nacelle drag. Aircraft constraints analysis is not performed, and fixed values for wing-loading and power-loading need to be provided. As a result, the impact of the propulsion system on aircraft size and performance is only partially evaluated. Therefore, extending the framework with a module for aircraft conceptual design is suggested. In this regard, reuse or integration of the openMDAO-based aircraft conceptual design libraries *openconcept* [3] and *fast-oad* [4] could be of interest.

4. Currently, the ARENA framework employs separate methods to determine the mass of different gas turbine configurations. The implementation of a common methodology for engine mass estimation is desirable. WEST (Chapter 7) is capable of this task, however, its integration is not suggested at this point due to the long execution time. Alternatively, as explained in Chapter 7, surrogate models of specific engine configurations could be generated with WEST and integrated into the ARENA framework. These surrogate models use thermodynamic cycle data and design assumptions as input and compute overall engine dimensions and mass as output.

5. The objective of the work presented in this dissertation is to obtain the preliminary design of an aircraft propulsion system that reduces mission fuel consumption and, therefore, the emission of the long-lived greenhouse gas CO_2. However, as outlined in Chapter 1 there is a clear consent in research that a significant part of the contribution of aviation to global warming is associated with non-CO_2 effects caused by the emissions of NO_x and water vapor at high altitudes. To identify propulsion system configurations that minimize overall environmental impact, methods need to be implemented that estimate the emission of NO_x and water and their effect on radiative forcing. For testing purposes, the emissions model

developed by Proesmans and Vos [5] was implemented in the ARENA framework. These tests showed that minimization of aircraft environmental impact requires the simultaneous optimization of airframe and propulsion system design variables. This calls for integrating an aircraft conceptual design module into the ARENA framework as outlined in point 2).

Building upon the work described in this dissertation, the following topics are recommended for further research:

1. While this work concerns the study of aircraft gas turbine engines adopting ORC WHR systems optimized for minimum fuel burn, the technology may have an even more relevant impact if the design is optimized for minimum environmental impact. These aircraft employ gas turbine engines with lower thermal efficiency to reduce the emissions of NO_x [5, 6], and thus the gas turbine discharges a larger amount of heat. A WHR system may therefore improve the thermal efficiency of these engines and at the same time lower the overall environmental impact.

2. To identify the performance improvement potential of the CC-TF concept, a design space exploration can be performed, whereby the analysis is based on assumptions related to more advanced component technology than those adopted in this work. For example, the impact of using next-generation heat exchangers made of more advanced materials and featuring optimized three-dimensional shapes obtained using additive manufacturing on mass and effectiveness can be studied. A first estimate of the potential benefits may be obtained by analyzing combined-cycle engine performance under the assumption of a reduction of gas-side pressure drop by up to 30%, an increase of gas-side heat transfer coefficient by up to 30%, and a reduction of evaporator mass by up to 60%. A pressure drop reduction of 25% for an optimized bare-tube heat exchanger geometry was identified by Raikar et al. [7]. The mass reduction potential results from the assumption of using silicone carbide as the construction material of the evaporator instead of Inconel.

3. The working fluid of the ORC system is a major degree of freedom for the design of such systems and its optimal selection for airborne applications has not been analyzed in this work. From a thermodynamic point of view, its optimal selection depends on the temperature and heat capacity of the heat source and heat sink and its impact on the turbine and heat exchanger design. Fluid characteristics that must be considered are the thermal stability limit depending on the containing material and sealings, toxicity, and flammability. As presented in Chapter 3 the working fluid selected for the analyses presented in this dissertation is appropriate for high-temperature applications due to its high thermal stability. As the results documented in Chapters 3 to 6 show, the optimal thermodynamic cycle for the considered configurations always adopts the highest possible cycle temperature constrained by the thermal stability limit of the working fluid. A further increase in ORC thermal efficiency may be possible with working fluids featuring higher thermal stability limits. Moreover, in the case of airborne ORC systems, the minimum cycle temperature is constrained by the limit on the pressure drop over

the condenser air-side. The non-isothermal isobaric condensation of mixtures of working fluids may allow a reduction of the required air mass flow rate and therefore pressure drop for the rejection of a given heat load. Furthermore, the findings presented in Chapter 3 indicate that the working fluid can impact the volume and mass of the components of the ORC system. These are important figures of merit in the design of airborne systems. Therefore, it is recommended to investigate the impact of working fluids on the design of ORC components and aircraft performance.

4. All the investigated combined-cycle configurations assume that a dedicated electrical generator is mounted on the shaft of the ORC turbine. Alternatively, the ORC turbine could be mechanically coupled with a gas turbine shaft or the shaft of the air compressor of a bleedless environmental control system or vapor compression cycle. In the case of the CC-TF concept for conventional or partial-turboelectric aircraft architectures, coupling the ORC turbine with the low-pressure shaft of the gas turbine may reduce the overall mass and increase the efficiency of the combined-cycle engine. This configuration might require a gearbox, therefore the possibility of modeling the gearbox to obtain its size and mass should be added to the ARENA framework. However, it may be possible to design an efficient ORC turbine for a rotational speed that is the same as that of the gas turbine shaft by selecting a suitable working fluid and turbine design variables.

5. The first-order analysis presented in Chapter 2 on the CC-APU concept to provide secondary power during cruise showed that the main engines provide shaft power more efficiently. However, advantages on fuel consumption or benefits on gas turbine design may still be possible from operating a CC-APU in other flight phases. For instance, during descent, the provision of secondary power requires operating the main engines at a higher thrust setting than necessary in case of no power off-takes. It may be possible to reduce mission fuel consumption if the CC-APU is operated during descent to provide onboard systems with electricity. The analysis of this concept requires the possibility of computing the turbofan performance in conditions close to idle. Simulation results at this operating point strongly depend on the relations underlying the turbomachinery maps. The lack of reliable engine maps and data on engine performance close to idle conditions is therefore a challenge that needs to be overcome to perform such a study.

6. Besides reducing mission fuel consumption, other benefits may derive from adopting ORC bottoming units. For example, reducing engine exhaust temperature lowers the noise and the thermal signature of the aircraft. A reduction of jet noise of aircraft APUs operated on the ground is of general interest to airport operators. The reduction in thermal signature is of interest for military aircraft to avoid detection by heat-seeking missiles. The attractiveness of employing ORC WHR systems on aircraft may increase if methods are implemented to quantify these effects.

BIBLIOGRAPHY

[1] J. S. Gray, J. T. Hwang, J. R. R. A. Martins, K. T. Moore, and B. A. Naylor, "OpenMDAO: An open-source framework for multidisciplinary design, analysis, and optimization," *Structural and Multidisciplinary Optimization*, vol. 59, no. 4, pp. 1075–1104, April 2019, doi: 10.1007/s00158-019-02211-z.

[2] E. S. Hendricks and J. S. Gray, "pyCycle: A tool for efficient optimization of gas turbine engine cycles," *Aerospace 2019*, vol. 6, p. 87, 8 2019, doi: 10.3390/AEROSPACE6080087.

[3] B. J. Brelje and J. R. Martins, "Electric, hybrid, and turboelectric fixed-wing aircraft: A review of concepts, models, and design approaches," *Progress in Aerospace Sciences*, vol. 104, pp. 1–19, 2019, doi: j.paerosci.2018.06.004.

[4] C. David, S. Delbecq, S. Defoort, P. Schmollgruber, E. Benard, and V. Pommier-Budinger, "From FAST to FAST-OAD: An open source framework for rapid overall aircraft design," *IOP Conference Series: Materials Science and Engineering*, vol. 1024, no. 1, p. 012062, jan 2021, doi: 10.1088/1757-899x/1024/1/012062.

[5] P. Proesmans and R. Vos, "Airplane design optimization for minimal global warming impact," *Journal of Aircraft*, vol. 59, no. 5, pp. 1363–1381, 2022, doi: 10.2514/1.C036529.

[6] H. S. Saluja, F. Yin, A. Gangoli Rao, and V. Grewe, "Effect of engine design parameters on the climate impact of aircraft: A case study based on short-medium range mission," *Aerospace*, vol. 10, no. 12, 2023, doi: 10.3390/aerospace10121004.

[7] P. P. Raikar, N. Anand, M. Pini, and C. M. De Servi, "Concurrent optimization of multiple heat transfer surfaces using adjoint-based optimization with a CAD-based parametrization," *International Journal of Heat and Mass Transfer*, vol. 236, p. 126230, 2025.

CURRICULUM VITÆ

Dabo KREMPUS

Born 2 April 1991 in Vienna, Austria

EXPERIENCE

PhD Candidate at TU Delft **Sept.2020–Sept.2024**
Aerospace Faculty, Flight Performance & Propulsion Section

Systems Engineer at RUAG Space (Vienna/Zurich) **Sept.2018–Sept.2020**
Thermal Spacecraft Systems, Vienna
Spacecraft Mechanisms, Zurich (3 months)

Intern at Austrian Institute of Technology (Vienna) **Apr.2018–Jul.2018**
Research on low-Speed aerodynamics, experimental and numerical

MSc Thesis Student at ESA ESTEC (Noordwijk, NL) **Oct.2016–Apr.2017**
Research on aerothermodynamics of civil hypersonic aircraft, numerical

BSc Thesis Student at Airbus (Hamburg) **Apr.2014–Aug.2014**
Research on the performance impact of aircraft icing, numerical

Paramedic at Austrian Red Cross (Ziersdorf, AT) **Jan.2011–Oct.2011**
Conducting ambulance service and rescue missions

EDUCATION

MSc Degree in Aerospace Engineering **Oct. 2014–June 2017**
University of Stuttgart/TU Berlin, Graduated with distinction
Thesis title: *Evaluation of the Aero-propulsive Performance of a Hypersonic Aircraft during the Acceleration Phase*

BSc Degree in Aeronautical Engineering **Oct. 2011–Oct. 2014**
FH Joanneum (Graz, AT), Graduated with distinction
Thesis title: *Airbus A320 Performance Degradation due to Icing-induced Surface Roughness*

Exchange Semester in Aerospace Engineering **Oct. 2013–Feb. 2014**
University of Bath (Bath, UK), passed all courses with an A

A-levels in Aeronautical Engineering **Sept. 2006–May 2011**
Bundesfachschule für Flugtechnik (Langenlebarn, AT), Graduated with distinction

List of Publications

1. **D. Krempus**, S. Bahamonde, T. P. van der Stelt, W. Klink, P. Colonna, C. M. De Servi, On mixtures as working fluids of air-cooled ORC bottoming power plants of gas turbines, *Applied Thermal Engineering*, Volume 236, Part D, 2024, 121730, DOI: j.applthermaleng.2023.121730.

2. **D. Krempus**, F. Beltrame, M. Majer, C. M. De Servi, R. Vos, P. Colonna, ORC Waste Heat Recovery System for the Turboshaft Engines of Tuboelectric Aircraft *Aerospace Europe Conference 2023 - 10th EUCASS - 9th CEAS*, 2023.

3. **D. Krempus**, F. Beltrame, M. Majer, C. M. De Servi, M. Pini, R. Vos, P. Colonna, Organic Rankine Cycle Waste Heat Recovery Systems for Aircraft Auxiliary Power Units, *Journal of the Global Power and Propulsion Society*, 2024. (Submitted)

4. **D. Krempus**, F. Beltrame, C. M. De Servi, R. Vos, P. Colonna, Organic Rankine cycle Waste Heat Recovery System for the Turbofan Engines of a Partial-turboelectric Aircraft, *Journal of Propulsion and Power*, 2024. (Submitted)